

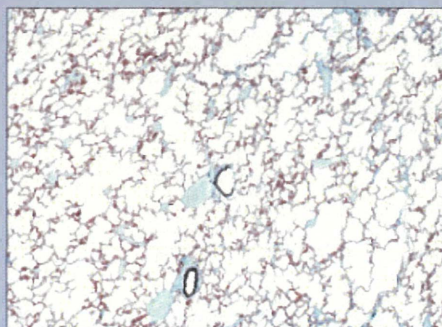
# Pathology of Organ Structure by Analysis and Interpretation of Image

出版年月日	2005
URL	<a href="http://hdl.handle.net/10097/00125403">http://hdl.handle.net/10097/00125403</a>

# Pathology of Organ Structure by Analysis and Interpretation of Images

Tohru Takahashi

*Department of Pathology, Ishinomaki Red Cross Hospital  
Professor Emeritus, Tohoku University*



SciPress, Tokyo



## Pathology of Organ Structure by Analysis and Interpretation of Images



# Pathology of Organ Structure by Analysis and Interpretation of Images

Tohru Takahashi

*Department of Pathology, Ishinomaki Red Cross Hospital  
Professor Emeritus, Tohoku University*



SciPress, Tokyo

## **Pathology of Organ Structure by Analysis and Interpretation of Images**

Tohru Takahashi

ISBN No. 4-87677-109-X

Published by SciPress, 2005 Sansei Jiyuugaoka Haimu, 27-19 Okusawa 5-chome, Setagaya-ku, Tokyo 158-0083, Japan.

Tel: +81-3-3718-7500 Fax: +81-3-3718-4406

URL <http://www.scipress.org/>

All rights reserved

© 2005 (First Edition), 2011 (Second Edition) by SciPress, Tokyo

No part of the material protected by this copyright notice may be reproduced or utilized in any form or by any means, electronic or mechanical, including photo-copying, recording or by any information storage and retrieval system, without written permission from the copyright owner.

This book is partly supported by Grant-in-Aid for Publication of Scientific Research Results of the Japan Society for the Promotion of Science (No. 155310).

Printed in Japan

# Contents

Foreword .....	vii
Introduction .....	ix
Co-workers and Associates .....	xiii
1. Measurements on Microscopic Images .....	1
a) Morphometry of arteries on microscopic images .....	1
b) Morphometry of airways — what part of bronchial tree constricts in asthmatic attack? .....	12
c) Standardized morphometry of airways in normal and diseased lungs .....	18
2. Stereology and Its Application to Pathology .....	25
a) Evaluation of paraquat-induced atelectasis .....	26
b) Langerhans islets of the pancreas in diabetics .....	30
c) Morphometry of metastatic tumor nodules in the liver .....	37
d) Alveolar surface area of normal and emphysematous lungs .....	42
e) Remodeling of alveolar structure in paraquat lung .....	47
f) Changes of bone trabeculae in osteoporosis — a cylindrical model .....	54
g) The mean radius of hepatic lobules — another cylindrical model .....	60
h) Problems that cannot be solved by stereology .....	66
3. The Basic Structure of Human Liver from the Viewpoint of Vascular Architecture .....	69
a) The unitary structure — different concepts .....	69
b) The microvasculature of human liver and its functional significance .....	74
c) Quantitative expression of vasculature pattern .....	82
d) Why does the vascular pattern differ among the organs ? .....	87
e) Pathogenesis of hepatic failure in cirrhosis .....	93
4. Three-D Structural Analysis. Method and Examples of Application .....	97
1) Preparation of serial sections .....	97
2) Abstraction of 2-D images from serial sections .....	98
3) Manual reconstruction .....	101
4) Computer-assisted reconstruction .....	103
5) Examples of 3-D reconstruction .....	105
a) The vasa vasorum of aortic wall .....	105
b) Three-D mapping of vascular lesions of lungs in pulmonary hypertension .....	108

c) Hypoplastic zone of myenteric plexus in Hirschsprung's disease . . . . .	119
d) Three-D mapping of airway obstruction in bronchiolitis obliterans . . . .	125
e) Multistep carcinogenesis of the large intestine . . . . .	126
f) The development and extension of hepatohilar bile duct carcinoma . . . .	131
g) Intraductal papilloma of breast: extension and cancer development . . .	136
h) Three-D microanatomy and pathology of human pancreas . . . . .	140
i) The microanatomy of terminal liver vessels and bile ducts . . . . .	149
5. The Structure of Adenocarcinoma and the Structural Differentiation . . . . .	153
6. Morphogenesis of Cirrhosis from Chronic Hepatitis . . . . .	171
7. Some Other Topological Problems in Microscopic Pathology . . . . .	195
a) Changes of pattern from chronic hepatitis to cirrhosis . . . . .	195
b) Two types of glandular tumors: papillary and tubular . . . . .	202
c) Hepatocellular carcinoma: two different types . . . . .	208
d) The pattern of zonal hepatocellular necrosis: Is the acinar theory tenable? .	210
8. The Adequate Classification of Form in Pathology . . . . .	225
a) Adequate classification of liver cirrhosis . . . . .	227
b) Adequate classification of carcinomatous and precarcinomatous cells . .	235
i) Adenocarcinoma of lung and its precursor . . . . .	235
ii) Carcinoma and dysplasia of the pancreatic duct . . . . .	240
Appendix . . . . .	249
Literature . . . . .	257
Acknowledgment . . . . .	265

## Foreword

While engaged for many years in the study and practice of human pathology, my interest has always centered around the organ structure and its changes. Undoubtedly, I led myself along this path under the profound influence of my teacher, Prof. Norio Suwa (1915 - 1996). He was a figure who was not so much a diagnostic pathologist as a philosopher, always asking what a significance the form of biostructure may have on its function. In contrast, I am rather an ordinary pathologist, spending a larger part of my time studying problems much closer to the practice of pathology. However I have to acknowledge there is also some peculiarity in my own way of thinking as pathologist. Coming to encounter a huge variety of pictures every day, I used to look for problems that seemed accessible to studies from a "structure and form" point of view.

Today, the frontiers of pathology seem growingly assisted by molecular studies. I think this may be a natural course of event in the history of science, but cannot help asking a question. The knowledge about, perspectives in, and technique to study the structure and form of organs—aren't these another indispensable and invaluable weapon of pathologists? Don't they belong to our own expertise where we can identify ourselves? Isn't the science of structure and form the very aspect of biomedical science where no workers in other fields can compete with us? To me, it seems to be of profound significance for the future advancement of pathological research if we manage to synthesize the molecular and structural studies. There is however a problem. While one can find plenty of textbooks for molecular biology, in morphology there is none that provides us with the ABC of research. And this may be the reason why, as stated above, problems of form still abound in human pathology.

As a matter of course, my study has taken a meandering course, with plenty of trials and errors. It was not until about twenty years ago that our studies began taking a more straight course. In one aspect, I owe the acceleration of studies to the introduction of computers which then became available in our laboratory, and this greatly assisted in analyzing organ structure. Also, for the academic influence I am indebted to researchers working in other fields, many of whom I came to know through Science on Form Japan, an interdisciplinary forum established in 1985. And of course, I have to thank my young coworkers, many of whom came to my laboratory to study problems they embraced during their activities as clinicians. Preparing this manuscript, I was struck by the affluence of works performed and left by them.

In this book I intended to compile the studies of my team and of myself. Because the works were all based on analysis of form, I made it an editing principle that in introducing every subject of study, all the context, including the motive, methodological considerations and the understanding reached, be illustrated with an image. What I am afraid is that the geometric rationale given at some places may seem, particularly to non-biomedical workers, too much lengthy and presenting only intuitive descrip-

tion. Please let me say that working in biomedical domain, I myself, and perhaps most of the readers, may not be much skilled in mathematical thinking.

Taking this opportunity, I would like to express my gratitude to Prof. R. Takaki of Tokyo University of Agriculture and Technology (physics), who, as president of Society for Science on Form, has helped me getting acquainted with methods and knowledge in the study of form. Profound thanks to Dr. James P. Butler, Associate Professor of Medicine, Harvard University Medical School, for his sincere discussion over the manuscript and kind advice on English wording. Last but not least, my gratitude to Mr. K. Oshida, SciPress, who undertook to publish this book. Without his help and encouragements, I would not have managed to put into arrangement our studies that all had been left in a mess.

December 2003  
Tohru Takahashi, M.D., PhD.



# Introduction

Human pathology is a science dealing with organs, tissue specimens or cells, all taken from patients through biopsy, surgery or autopsy. Undoubtedly, the fruits born by the studies of human pathology contribute greatly, not only to better diagnosis and therapy of diseases but to elucidation of their mechanism. In performing the study, pathologists resort predominantly to the analysis of biostructure and its form. While various knowledge and technique have been introduced to pathology from other fields like biochemistry, immunology or molecular biology, it is the science of form that has been and still remains the core of research in pathology. What are the principles underlying the normal structure of an organ? In diseases, what deviation from the norm do the organs undergo and how does it explain the abnormal organ function? And how can we better recognize the changes of structure and form, with which to improve the diagnosis of diseases? These are problems pathologists have been engaged in, all of which, if solvable at all, should be solved mainly by studies of form. What a pathologist encounters throughout life amounts to a vast accumulation of widely varying form. In a sense, human pathology is a treasury of forms and of problems about the form.

However, this does not mean that so far, pathology as a science of form has managed to establish a methodological basis of its own, and many problems of form are being left unsolved. Yet recently, the studies of form have attained a dramatic extension by the hand of non-biomedical scientists including image engineers, mathematicians and statisticians, giving us an impetus, influence and stimuli. In this book, I intend to compile the studies of my team and my own, which were mostly performed resorting to analysis of form. Particularly it seems essential to demonstrate, in what aspect of study we came to face a bar, and how we were assisted in overcoming it with new methodology, technology and way of thinking. Also, it will be shown how much our studies have been assisted by the recent advancement of computer technology. Listed below are the main problems to be discussed.

## 1. The quantification of form

Consider the diagnosis of cancer. There is no doubt that today, the final diagnosis of this disease is given mainly by pathologists. New methods like analysis of DNA from tumor cells or of specific molecules of patients' serum still remain as an auxiliary measure, while in the medical scene, decision-making about a patient mostly relies upon form-related information, including clinical images, macroscopic organ changes and microscopy of specimens. Yet strictly speaking, a form-based diagnosis made by pathologists cannot be exempted from having a streak of ambiguity. The microscopic diagnosis of cancer differs from biochemical analysis, in the latter of which the result is given in the form of titer for a specific molecule in the serum. In evaluating the form of tissue and cells, the examiner cannot but depend upon one's own experience, which

brings about a limitation upon the reproducibility of diagnosis. Moreover, the object of pathological analysis mostly assume a shape that is irregular, variable, far from geometric, and seemingly least accessible to quantification. Still, it is imperative to introduce quantitative methods to this domain if we try to bring the morphological pathology closer to the level of science.

## 2. Three-D quantities and their estimation

Another difficulty awaiting us is the need to obtain quantitative information about the 3-D structure. On most occasions, what we can access is only 2-D section. Whether light or electron microscopic, the sections available are thin enough for disregarding their thickness. However, the real object of observation is always a 3-D parenchyma that continues behind the sectional plane. On account of this, the need often arises to know the 3-D structure and geometry. When the need is of such a nature as to be satisfied if 3-D quantities are provided, one might sometimes be able to resort to stereology. This is a generic term for the principles and technique with which one can estimate the quantities characterizing the 3-D structure through measurement or sampling upon small number of 2-D sections. As one may expect, principles of stereology are mostly deduced from statistics and geometric probability. Consider, for example, how the total surface area of alveolar septa was estimated for the human lung, the right and left combined together. This is a problem solved by Weibel (1963) who developed a new theorem of stereology to apply to this task. Also there are other problems in human pathology in which stereology can work as an effective tool, but unfortunately, we cannot say that the knowledge about stereology is being widely distributed among researchers working in pathology.

## 3. Problems that require 3-D reconstruction

Though stereology is a "bright" method of morphometry, its applicability to real problems is not free from limitation, as will be shown. When the problem one is facing has proved to be beyond the reach of stereology, there is no other way than to perform 3-D reconstruction from serial sections, i.e., to have direct access to the space by reproducing the 3-D structure. Problems that need reconstruction are found in every sector of pathology, and it is in these problems that my colleagues and I have been engaged for many years. After having consumed much time and energy in performing this, we recently managed to introduce computer-assist, which greatly helped expand the scope of 3-D analysis. Problems that require 3-D reconstruction are mostly those dealing with either the connectivity of structure or the spatial distribution of lesions. A series of such examples will be shown.

Sometimes the author performed what may be called 3-D measurement. When one needs to obtain at any cost 3-D quantities that apparently are not susceptible of stereological approach, direct 3-D measurement upon serial sections may be the last resort. Today, in this aspect too, we can expect computer assist in the form of computational geometry.

## 4. Topological problems in pathology

Not rarely we face lesions of such a character as to be studied from a structural connectivity point of view. How the structural components are connected in space is a

problem of topology and therefore is beyond the scope of stereology. This is symbolized by the history of computer-aided 3-D reconstruction, which in the earliest stage of development was designed exclusively to visualize the connectivity of neuronal network (Capowski, 1977). To put it in other words, structural connectivity is a problem studied most effectively by applying topological parameters. Several examples will be shown in the following, in all of which, approach to the problems was guided along the topological way of thinking. Particularly, in studying the morphogenesis of various lesions, one never fails to find connectivity and its changes defining the way of development. An appropriate example may be found in the development of cirrhosis from chronic hepatitis, where the advancement of disease involves a series of radical transformation in the skeleton, which can be described only in topological terms.

The experience obtained through the study of cirrhogenesis helped characterize the structure of adenocarcinoma and adenoma with various grades of differentiation. It will be shown that the concept of differentiation, hitherto applied only to the individual cells, can also be extended to the structural aspect, allowing us to define "structural differentiation" or "structural atypism."

#### 5. The adequate classification of form

Classification is a method widely applied in pathological research. However, no attempt has been made at examining whether the object under study is classifiable at all, or when it really is, how one can define the most adequate and therefore reproducible classification. These are questions accessible to the method called cluster analysis, an application of multivariate statistics. This is a way of thinking, for the application of which, one can find a fertile soil in the domain of pathology. In this book, several of our attempts will be presented: the classification of liver cirrhosis, and that of atypical cells found in carcinomas and pre-carcinomatous lesions.

In writing the manuscript, my attention has been focused on making this book accessible not only for researchers working in pathology but for those in other fields, including non-biomedical scientists. It is for this reason that for each of the studies introduced, efforts have been made to shed light on its biological background or clinical significance. To pathologists, sometimes such explanations might appear redundant, but if the readers could be kind enough to tolerate the boredom, I would be much grateful.

## Co-workers and Associates

Dr. Shigeru ARAI

Professor Emeritus of Pathology, Yamagata University School of Medicine, Yamagata,  
Japan

Dr. Ryohji CHIBA

Chief Pathologist, Dept. of Pathology, Sendai Kohsei Hospital, Sendai, Japan

Dr. Tamihiko CHIBA

Director, National Hospital Organization Yonezawa Medical Center, Yonezawa, Japan

Dr. Masahito EBINA

Associate Professor, Dept. of Respiratory Medicine, Tohoku University Graduate School  
of Medicine, Sendai, Japan

Dr. Mareyuki ENDOH

Chief Pathologist, Dept. of Pathology, Sendai Kohsei Hospital, Sendai, Japan

Dr. Hitoshi FUKASAWA

Late Director, Akita Prefectural Institute for Brain and Blood Vessel Research, Akita,  
Japan

Dr. Tohru FURUKAWA

Professor, International Research & Educational Institute for Integrated Medical Sciences,  
Tokyo Women's Medical University, Tokyo, Japan

Dr. Michiko FURUYAMA

Dept. of Medicine, Fukujuen Hospital, Sendai, Japan

Mr. Masazumi ITOH

Rise Corporation, Sendai, Japan

Dr. Noriyuki IWAMA

Director, Dept. of Pathology, Sendai Rousai Hospital, Sendai, Japan

Dr. Tsuneo KAIHOH

Director, Yuri-Honjoh Medical Association Hospital, Honjoh, Japan

Dr. Katsuo MATSUKI

Director, Dept. of Cardiac Surgery, Hachinohe City Hospital, Hachinohe, Japan

Dr. Jun MATSUMOTO

Director, Ohizumi-kinen Hospital, Zaoh, Miyagi, Japan

Dr. Hiromitsu MIURA

Miura Clinic (pediatric surgery), Hachinohe, Aomori, Japan

Dr. Masuko MORI

Miyagi Medical Association, Sendai, Japan

Dr. Megumi NAKAMURA

Senior Lecturer, Dept. of Pediatric Surgery, Yamagata University School of Medicine,  
Yamagata, Japan

Dr. Yasuyuki NAKAMURA

Director of Pathology, Iwate Prefectural Ohfunato Hospital, Ohfunato, Japan

Dr. Masaki NIO

Professor of Pediatric Surgery, Tohoku University Graduate School of Medicine, Sendai,  
Japan

Dr. Ryohji OHI

Professor Emeritus of Pediatric Surgery, Tohoku University Graduate School of Medicine,  
Sendai, Japan

Dr. Noriaki OHUCHI

Dean, and Professor of Surgery, Tohoku University Graduate School of Medicine, Sendai,  
Japan

Dr. Kichiya OKUYAMA

Vice Director, Kurihara Central Hospital, Kurihara, Miyagi, Japan

Dr. Kiyoko SASAKI

Dept. of Surgery, Tohoku University Graduate School of Medicine, Sendai, Japan

Dr. Yasuhiko SASAKI

Director Emeritus, Ishinomaki Red Cross Hospital, Ishinomaki, Japan

Dr. Takashi SAWAI

Professor of Pathology, Iwate Medical University, Morioka, Japan

Dr. Ken SAITOH

Director, Dept. of Pathology, Akita Red Cross Hospital, Akita, Japan

Mr. Isao SUGAWARA

Chief Laboratory Technician, Dept. of Pathology, Ishinomaki Red Cross Hospital,  
Ishinomaki, Japan

Dr. Masanori SUZUKI

Director, Kanma General Hospital, Kuroiso, Japan

Dr. Masanobu TAKEMURA

Director, Dept. of Surgery, Shiomi General Hospital, Yokohama, Japan

Dr. Nobuaki TAMAHASHI

CEO, Japan Pathology Laboratory, Inc. Sendai, Japan

Dr. Fumiaki TEZUKA

Director, Dept. of Pathology, Sendai Red Cross Hospital, Sendai, Japan

Dr. Tadashi WATANABE

Dept. of Medicine, Katta Municipal Hospital, Shiroishi, Miyagi, Japan

Dr. Hiroshi YAEGASHI

Dept. of Pathology, Iwate Prefecture Central Hospital, Morioka, Japan

Dr. Genya YAGINUMA

Director of Cardiac Surgery, Sendai Kohsei Hospital, Sendai, Japan

Dr. Nobuhisa YAGINUMA

Director, Dept. of Gastroenterology, Fukushima Dai-ichi Hospital, Fukushima, Japan

Dr. Hideaki YAMANAMI

Director, Dept. of Surgery, Miyagi Cancer Center, Natori, Japan

Dr. Yuande ZHANG

Professor of Pathology, Jilin University School of Medicine, Changchun, China

## Measurements on Microscopic Images

### a) Morphometry of Arteries on Microscopic Images

It seems pertinent to begin with an example of 2-dimensional micromorphometry which was performed in the early 1960s by the team of Prof. Suwa as a part of systematized study of arteries (Suwa and Takahashi, 1971). This is for the following three reasons. First, the study presents in a typical way how, in dealing with a real biostructure, one can apply a simplified model. Usually, organs or tissues we face in a living matter have a structure too much complicated to allow direct 2-D morphometry.

Second, this study of arteries introduces a viewpoint from which one can see that the structure of an organ primarily depends on its tissue circulation. How it does, will be discussed in Chapter 3, where we deal with the structure of the liver. This led me to regard the vasculature of the liver as an adequate design that allows this organ to carry out its manifold functions. And I owe all this idea to what I previously experienced while being engaged in the morphometric studies of arteries.

Third, a brief look at the history of measurement technique is to be given. Only two measurements were involved in the study of arteries: to obtain the length and the area on microscopic level. It will be shown that all necessary measurements were practicable even in the early 60s, when no computer assist was available.

### Changes of arteries in hypertension (Figs. 1-1, 1-2)

Figure 1-1 demonstrates a pair of cross-sectioned muscular arteries. Each was taken from a medium-sized subbranch of the superior mesenteric artery of an adult, about 300  $\mu\text{m}$  in external diameter. The left was obtained from the autopsy of a normotensive subject, and the right, from a hypertensive of about the same age. The mean blood pressure ante mortem of the latter had been elevated by about two times the norm. Here, worthy of attention is the thickness of the media, the muscular layer of the arterial wall where smooth muscle cells are arranged so as to encircle the arterial lumen. It is obviously thickened in the hypertensive, and here too, the medial thickness appears to be about two times that of the normotensive. As will be shown, this is not considered a mere coincidence.

It is well known that systemic hypertension, when sustained for a long time, can lead to a fatal outcome of the patient such as cerebral hemorrhage, renal failure or cardiac failure. Of these, the first two diseases occur in patients in whom cerebral or renal arteries are not normal but involved beforehand in a change generally called hypertensive arterial lesion. Figure 1-2 exhibits changes of small artery found in the



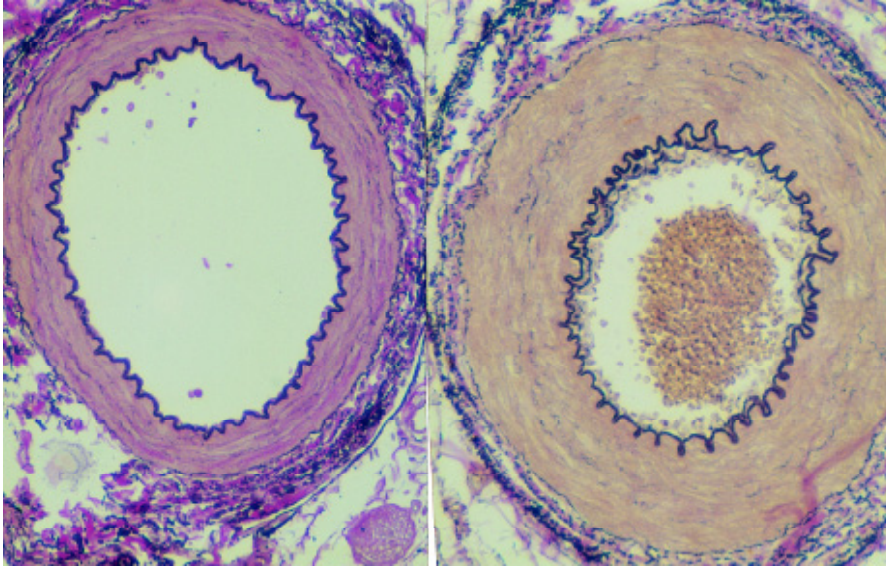


Fig. 1-1. Hypertrophy of medial smooth muscles in a systemic artery of hypertensive subject. Arterial cross sections, both from a peripheral branch of the superior mesenteric artery, about 0.3 mm in external diameter. The left is from a normotensive, and the right, from a hypertensive subject. Note the remarkably thickened medial smooth muscles in the latter. Elastica van Giesson stain.

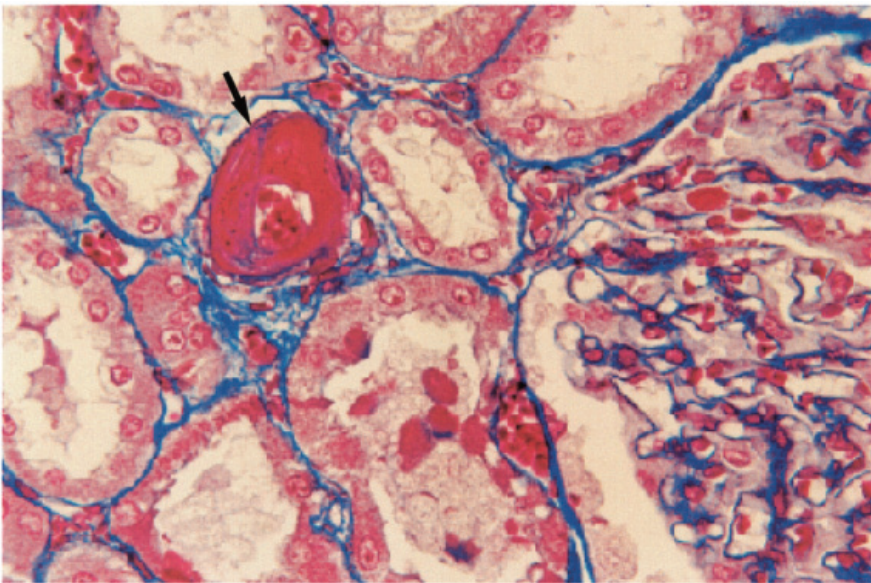


Fig. 1-2. Hypertensive arteriolar lesion (arrow) found in a glomerular vas afferens of kidney from a patient with malignant hypertension. Necrosis of vascular wall with infiltration of fibrinoid material (red). Azan-Mallory stain.



kidney of hypertensive patient, where the medial layer, uniformly reddened on Mallory's stain due to infiltration of fibrin-containing serum component, has undergone diffuse necrosis of smooth muscle cells. In the kidney of hypertensive this sort of lesion leads to luminal obstruction where the blood flow is seriously blocked. Therefore if the lesion involves a number of small arteries of the kidney, the vascular bed of the organ is significantly narrowed and chronic renal failure develops. If a hypertensive patient harbors similar lesions in the brain arteries, it means that the arteries are more or less apt to rupture at the site, resulting in cerebral hemorrhage. Now the problem we face is what hemodynamical changes dominate over the arterial circulation of hypertensives, creating such necrotic lesions in the peripheral small arteries and arterioles.

### Analysis of arterial hemodynamics applying Laplace formula (Fig. 1-3)

The mechanical conditions dominating a muscular artery can be analyzed by applying Laplace formula. In Fig. 1-3, a segment of artery is represented by a thin-walled cylinder of uniform radius  $R$ . The inner pressure of the artery corresponding to the mean blood pressure is  $P$ , and this generates a tension  $T$  upon the wall along the direction vertical to the arterial axis. Then,

$$T = PR \quad (1-1)$$

which shows that the wall tension  $T$  increases in proportion to  $P$ , the inner blood pressure. Therefore when the mean pressure is elevated to two times its normotensive level, also the wall tension is doubled, so long as the arterial radius  $R$  remains unchanged. It would be reasonable to assume that in this situation, the circularly arranged smooth muscles of the media become strengthened by thickening themselves so as to antagonize the increased tension load. This explains why in hypertension, arterial changes occur in the form as in Fig. 1-1. In other words, this is an adaptation process of medial smooth muscles to elevated pressure load. The situation may be quite the same as in the left ventricular wall of hypertensive patient, where, in the form of ventricular hypertrophy, the heart muscles attain adaptation to increased mechanical load. Medial hypertrophy in arteries exposed to elevated inner pressure is also found in the expression of the third law of Thoma (1911) who says that the thickness of vascular wall is determined by tension acting transversely on the wall.

This consideration provides a rationale for analyzing the hemodynamical changes

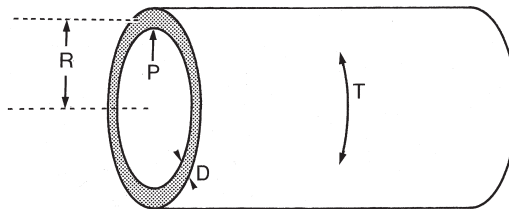


Fig. 1-3. A schema showing the application of Laplace formula to artery.  $P$ : mean arterial pressure dominating in the lumen.  $r$ : the radius of the artery.  $T$ : the tension exerted upon the wall.  $D$ : the thickness of media.

of arterial circulation in hypertensive subjects. Suppose that in normotensive subjects, we can determine in quantitative terms the medial thickness and radius of arteries supplying an organ. This is done by performing measurement at various levels from the trunk to middle to small arteries to arterioles. Then the analysis is extended to hypertensives, and if, at a level of artery, the media proved to be significantly thickened compared with the normotensive, we can conclude that at the level, the arterial wall had been exposed to an elevated pressure. Thus, the goal of this study has been to visualize how the medial hypertrophy is distributed over the arterial tree, and from this viewpoint to understand the mechanism that can produce hypertensive arterial injuries.

### Standardized morphometry of arteries (Fig. 1-4)

An artery can actively change its luminal width according to the situation in which it is placed, by either constricting or relaxing its medial smooth muscles. Therefore, in cross section, an artery presents various forms between the two extremes, tightly constricted and fully dilated states. The more constricted, the thicker is its media, and vice versa, as in Fig. 1-4. The artery in the right picture corresponds to the dilated state of the non-dilated artery in the left, both with the same medial area  $S$  and the same perimeter length  $L$  of the inner elastic membrane. Therefore, if measurement is performed directly on a non-dilated artery, we obtain a medial thickness more or less larger than its dilated state. Also the measurement of radius, if performed directly, will give a varying result, depending on the state in which the artery was fixed. Thus, both the anatomical radius and medial thickness have to be defined in a state of artery standardized somehow. In this study, a given cross-sectioned artery was submitted to measurement of two quantities: the perimeter length  $L$  of the inner elastic lamina and the sectional area  $S$  of the media, as in the left figure. Then we assume that the artery was transformed into a circular state, as in the right, without changing  $L$  or  $S$ , where the media forms a circular belt of uniform thickness along the entire circumference. The anatomical radius  $R$  and medial thickness  $D$  were defined in this state, namely,

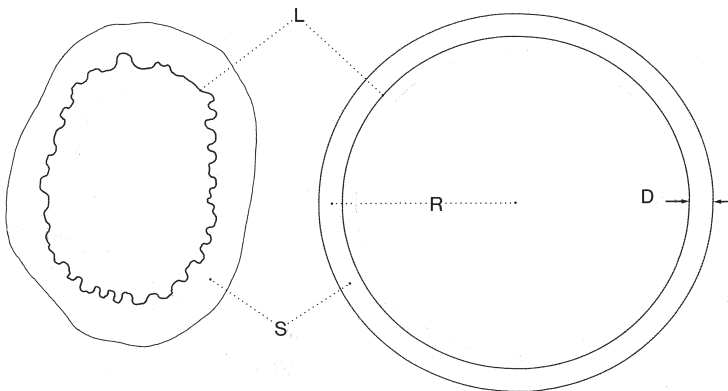


Fig. 1-4. Standardized measurement of artery. Arteries found in a real microscopic section are constricted, irregularly and to varying degree, as in the left. Here the medial area  $S$  and the perimeter length  $L$  of elastic lamina are measured, and the anatomical radius  $R$  and medial thickness  $D$  of this artery are defined in a circularly dilated state as in the right, a transformation, through which,  $S$  as well as  $L$  is kept unchanged.

$$S = 2\pi RD$$

$$L = 2\pi(R - D/2).$$

The solutions of the equations are:

$$R = \frac{S}{\sqrt{L^2 + 4\pi S} - L}$$

$$D = \frac{\sqrt{L^2 + 4\pi S} - L}{2\pi}.$$

This standardized morphometry, published by Furuyama (1962), serves as a simple geometric model of cross-sectioned arteries and found several applications. It has been employed particularly often by Yamaki (1981) who published a number of papers dealing with pulmonary vasculature and its changes in pulmonary hypertension.

#### **Micromorphometry of arteries: measurement technique (Figs. 1-5, 1-6)**

In the early 60s when our studies of arterial changes in hypertensives were under progress, we had technical difficulties in measuring the perimeter length  $L$  of the inner elastic membrane. In measuring  $S$ , the area of the medial layer, a classic-type manual

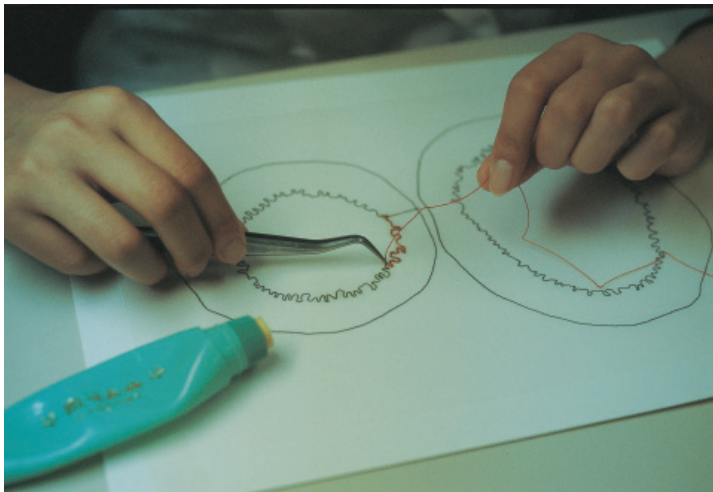


Fig. 1-5. Manual measurement of perimeter length for irregularly meandering elastic lamina. Cotton thread is stuck on the contour of elastic lamina in a drawing of arterial cross section, a laborious method employed in the 1960s when computer assist was not available.

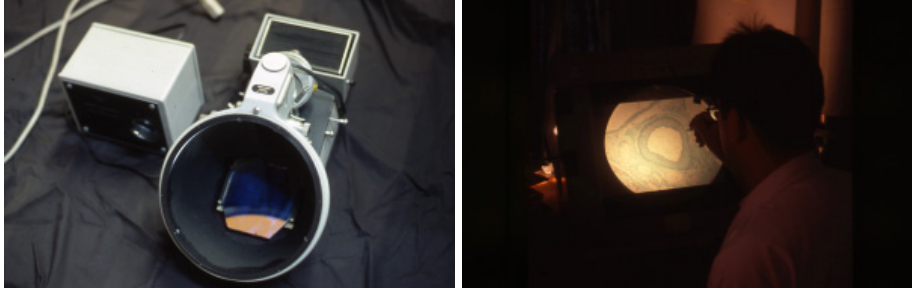


Fig. 1-6. Profile abstraction of elastic lamina from an arterial cross section (right) using a microprojector (Visopan-model, Reichert, left).

planimeter was available, though exacting time and labor. On the other hand, the irregularly indented course of the elastic lamina on cross-section of an artery refused easy determination of its perimeter length. What we employed after various attempts was a direct measurement as shown in Fig. 1-5; cotton thread was stuck on a drawing of an arterial cross section, where the finely undulating elastic lamina was faithfully followed. Today, these measurements are easily performed upon a digitizer connected with a desktop computer; a drawing of arterial profile is placed on a digitizer, where the profiles are inputted by tracing with a cursor. Figure 1-6 presents how the profile of a cross-sectioned artery was drawn on a sheet of tracing paper on which the picture was projected at an adequate magnification. Various types of microscopic projectors were used. In the figure, an artery is being drawn using a Visopan-type microprojector (Reichert). Drawing can be omitted if one manages somehow to project the image of artery directly on the digitizer. One can also make use of a software that allows to project microscopic images through CCD camera onto a computer display, and measure the length of meandering curve by following with a mouse-linked cursor.

### Arterial hemodynamics in hypertension (Figs. 1-7, 1-8)

Figure 1-7 presents an example of measurement. This is from an autopsy material of a girl, aged 1 year and 4 months, dying from rotavirus enteritis, then called pseudocholera infantum. Both  $R$ , the radius, and  $D$ , the medial thickness, were determined on the renal and superior mesenteric arteries, and the results were presented on bilogarithmic coordinates. The level of arteries subjected to measurement ranged in both arterial systems from the trunk down to the precapillary arterioles. One can see that there is a close linear regression between  $R$  and  $D$ , namely,

$$\log D = a \log R + b$$

where  $a$  and  $b$  are constants.

However, the slope appears much gentler in the range of radius smaller than 0.1 mm than in the larger arteries, requiring to define the regression separately for the proximal and distal regions of  $R$ . This implies that in the peripheral region, small arteries and arterioles are equipped with a medial layer that is significantly hypertrophic compared with the larger arteries. In other words, the  $D/R$  ratio becomes higher

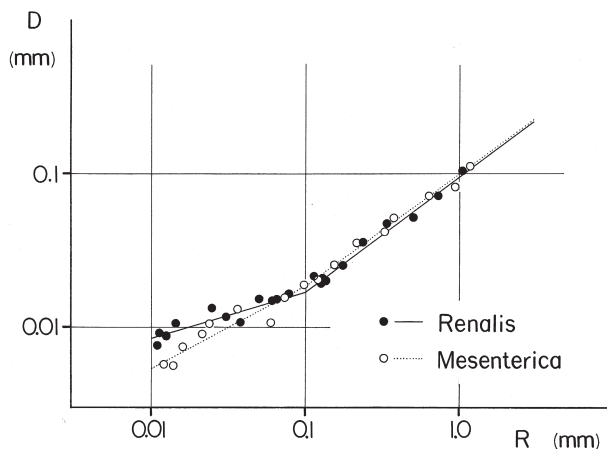


Fig. 1-7. The medial thickness  $D$  and the radius  $R$  are determined on the renal and mesenteric arteries in an autopsy case of a girl 1 year and 4 months old. The results are presented on bilogarithmic coordinates. In both the renal and mesenteric arteries there is a close linear regression, but the regression lines are gentler in the region of  $R < 0.1$  mm. Reproduced from Suwa and Takahashi (1971): Morphological and morphometrical analysis of circulation in hypertension and ischemic kidney. Urban & Schwarzenberg, München, pp. 45.

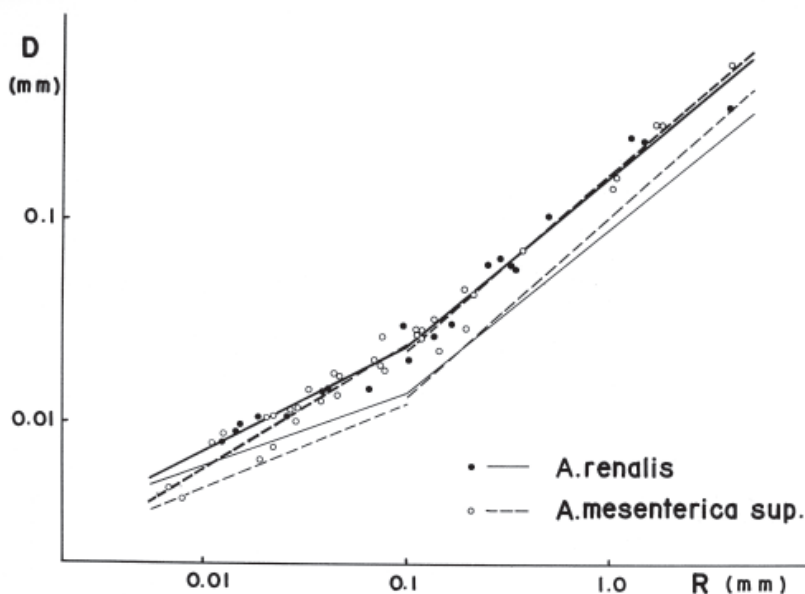


Fig. 1-8. The change of medial thickness in arterial hypertension in an autopsy case of male aged 55 years. He died of cerebral hemorrhage and his mean blood pressure was 175 mmHg. The thinner lines, solid and broken, are the regression lines from 17 normotensives of the same age group. There is a distinct medial hypertrophy in the region of  $R > 0.1$  mm, whereas in the smaller arteries,  $D$  becomes growingly normalized toward the terminal region. Reproduced from Suwa and Takahashi (1971): Morphological and morphometrical analysis of circulation in hypertension and ischemic kidney. Urban & Schwarzenberg, München, pp. 52.

toward the arterial periphery.

The measurements were performed on autopsy materials from 45 normotensive subjects so as to include various age classes as uniformly as possible. This gave us a basic data with which to compare the hypertensive cases. Shown as an example in Figure 1-8 is the result of measurement from a hypertensive patient, a male aged 55 years, who died of cerebral hemorrhage. His mean blood pressure was 175 mmHg, nearly two times higher than the control of the corresponding age group. Both the renal and mesenteric arteries are shown to have a media thickened almost double the normotensive level, at least in the range of  $R$  larger than 0.1 mm. Of the thinner lines, the solid are the regression lines with regard to renal arteries and the broken lines are those of mesenteric arteries, both calculated from the pooled data from 17 normotensive subjects of the same age group. However, the medial hypertrophy becomes ambiguous toward the arterial periphery. In the arteriolar region where  $R$  is about 0.01 mm, there is practically no medial thickening.

The result discloses a significant aspect of blood flow dynamics in hypertension. In the range of  $R$  larger than 0.1 mm, the media is uniformly thickened. This means that in this region, the media had been antagonizing a mean blood pressure elevated as high as double the normotensive level. However, at the arteriolar level of  $R = 0.01$  mm, the mean blood pressure appears to have been already normalized, probably thanks to vasoconstriction of the proximal larger arteries. Now let us recall that it is in this very region of small arteries that hypertensive arterial lesions develop. Thus, development of the lesions seems to have some bearing with elevated blood pressure, but it may be safe to say that at least, the lesions are not the result of direct exposure of arterial wall to high pressure itself. We think that possibly, the development of hypertensive arterial injuries may be attributable to fluctuated blood flow and repeated ischemia in the periphery resulting from arterial constriction taking place in the proximal region.

### Higher $D/R$ in the arterioles and its physiological significance (Fig. 1-9)

Now let us come back to the normal arteries and consider the "physiological hypertrophy" of media in the peripheral region. In Fig. 1-9, the values of  $D/R$  ratio obtained from a normotensive adult is plotted against the radius  $R$ . There is a marked elevation of this ratio in the arterial periphery, particularly in the range of  $R$  smaller than 0.1mm.

Based on the Laplace formula we assumed that when  $P$ , the mean blood pressure, is elevated to two times the normal level, the tension load  $T$  upon the wall will be doubled. Consider that in this situation, the smooth muscle cells hypertrophy so as to double the medial thickness. Then an adaptation to the increased load will be attained by the medial layer now sufficiently strengthened to antagonize the wall tension  $T$  with a doubled muscular mass. Therefore, once a state of adaptation is reached, we can assume that the medial thickness  $D$  is parallel with the quantity of physical work done in a certain period by the smooth muscle cells. Thus, not only for hypertensives but for arteries in general, we can write

$$D = B \cdot T$$

where  $B$  is a constant. With this, the Laplace formula (1-1) can be re-written into

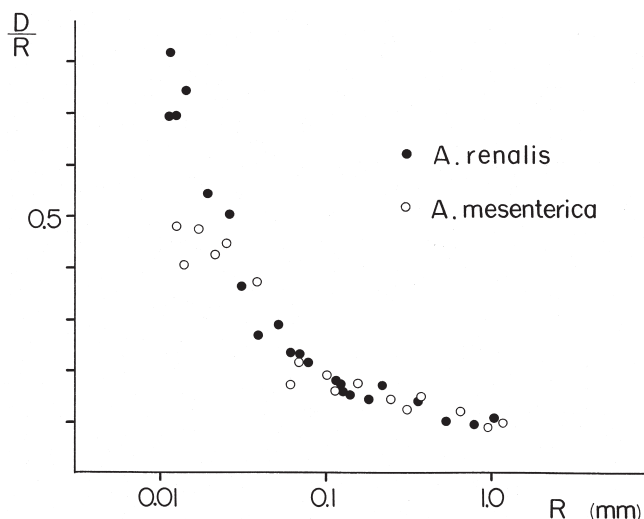


Fig. 1-9.  $D/R$ , the comparative thickness of media, rapidly rises in the arteriolar region toward the periphery, particularly in the renal artery. This physiological hypertrophy of media in the periphery cannot be understood from the quantity of physical work performed by the smooth muscle cells to antagonize the blood pressure, because the pressure must be far lowered in the peripheral region. Reproduced from Suwa and Takahashi (1971): Morphological and morphometrical analysis of circulation in hypertension and ischemic kidney. Urban & Schwarzenberg, München, pp. 46.

$$D/R = BP.$$

According to this, the ratio  $D/R$  must be proportional to the inner blood pressure. However, of course the mean arterial pressure falls as the artery becomes smaller toward the periphery. If so, the ratio  $D/R$  might also be expected to drop from the middle to small arteries to arterioles. In reality, however, we have found quite the opposite. The ratio  $D/R$  rises with thinning arterial radius, and the highest ratio is attained at the most peripheral level of the arterial tree. Consequently, so long as the pressure-sustaining aspect of arteries is concerned, it seems as if the terminal region of arteries were equipped with a meaningless mass of extremely hypertrophic smooth muscles.

This luxury is to be interpreted in another way; it reflects the extraordinarily vigorous activities assigned to small arteries and arterioles. As well known in the domain of circulatory physiology, the peripheral arteries repeat constricting so as to regulate blood flow and distribution of blood into the tissue. Thus we realize that there are at least two different aspects in the function of arterial muscular coat, that is, to bear the tension load, and to regulate the blood flow. In the media of an artery we cannot separately assess the quantity of work done to achieve each of the two functions. However, what an unexpectedly large work is undertaken by arteries in regulating blood flow may be understood if we compare among arteries supplying different organs, as in the following.

### Organ difference in arterial circulation (Fig. 1-10)

In Fig. 1-10, arteries supplying different organs are compared. This is from the

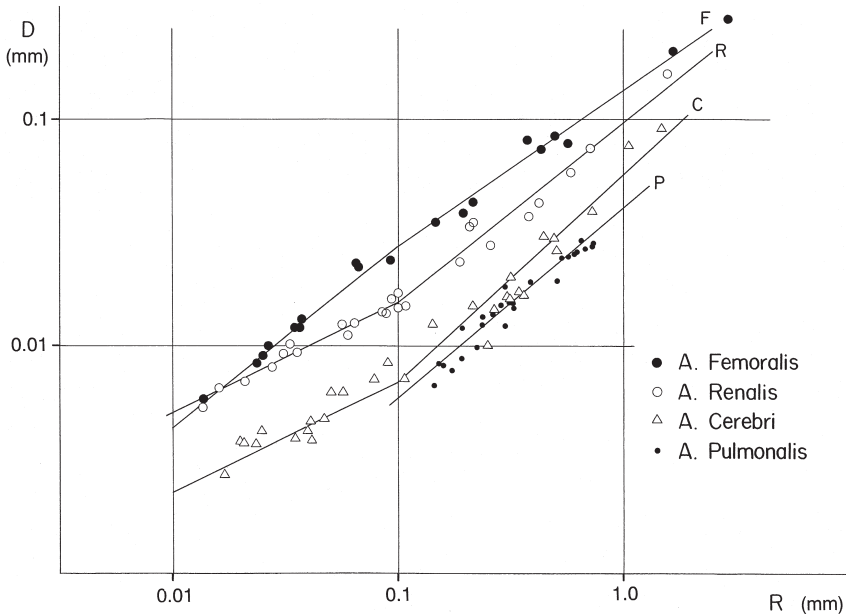


Fig. 1-10. The organ difference in the development of media is examined among the femoral (F), renal (R), cerebral (C) and pulmonary (P) arteries from autopsy material of a young male. The femoral arteries were sampled from the branches running in the quadriceps, so as to represent the arteries of skeletal muscles. Note that there is a remarkable between-organs difference. Reproduced from Suwa and Takahashi (1971): Morphological and morphometrical analysis of circulation in hypertension and ischemic kidney. Urban & Schwarzenberg, München, pp. 46.

autopsy material of a young male aged 16 years who died of cerebral trauma. The femoral arteries are taken from arteries supplying the quadriceps muscles and represent arteries feeding the skeletal muscles; added to this are the renal, cerebral and pulmonary arteries. It may be clear at a glance that there is a great organ difference. In the pulmonary arteries,  $D$  remains at the lowest level. In this artery, the values of  $D$  keep an almost equal distance downward from the renal arteries along the entire range of  $R$ . The distance in  $D$  between the renal and pulmonary arteries corresponds, on a logarithmic scaling, to a difference of 4 to 1 along the entire range of  $R$ , and this appears to be reflecting approximately the difference of mean blood pressure between these arterial systems. Aside from this, however, the medial thickness greatly differs within arteries belonging to the systemic circulation. In the femoral artery, the arteries of skeletal muscles,  $D$  remains the highest in the middle and larger arteries, and at  $R = 0.1$  mm, the medial thickness is about five times larger than in the cerebral arteries. Because the skeletal muscles, kidneys and the brain are belonging to the systemic circulation, it may be unthinkable that among these organs, a difference in blood pressure maximally as large as 5 to 1 should exist. From the above discussion it seems most likely that the pattern of  $D$ , which is specific of each organ, reflects different regulatory activity of arteries. For example, the extraordinarily thickened media in the arteries of skeletal muscles may be supposed to be showing that in a human who usually leads a "normal" state of living, the arteries are kept in a constricted state in most



of the time. It may be only on rare occasions that the subject is engaged in such an intensive muscular work as running full-power for a while, when the arteries may be fully open, supplying blood at a flow rate higher than 10 times "normal." On the other hand, arteries of the brain have the lowest  $D$  in the organs of the systemic circulation. This may be interpreted to imply that the brain comprises nerve cells so "tachyphoric" as to be vulnerable to ischemic injuries if they are placed in an environment where blood flow can greatly fluctuate as in the skeletal muscles. In the kidney, attention should be paid to the terminal region of renal arteries. Here  $D$  of vas afferens-class arteries is higher than in any of the other organs. Presumably, this may be related with the particularly active regulation of renal blood flow which is assumed to take place at the preglomerular arterioles. From the anatomical pattern of renal vasculature, Suwa and Takahashi (1971) theoretically concluded that in the kidney, the adequate site for blood flow regulation must be at the vasa afferentia. This is because the normal blood pressure in the glomerular capillaries is incomparably higher than in capillaries of common organs. Consider what if vasoconstriction has occurred at a proximal level, for example at the interlobular or larger arteries. The blood pressure of glomerular capillaries would fall simultaneously in a number of glomeruli below 80 mmHg, the critical height required for urine filtration, thus suspending the urine production in the area supplied by the artery. Only by alternating and intermittent constriction of vasa afferentia taking place among a large group of glomeruli, regulation of renal blood flow can be achieved while avoiding suspended urine production all at once.

The morphology of arteries, when submitted to metric analysis of radius and media, can bring about a series of insights into the functional aspects of microcirculation. This will be revisited again in Chapter 3 where the microstructure of the liver is to be related with the tissue circulation of the organ.

### **Application to pulmonary arteries in pulmonary hypertension**

The morphometry of arteries has found other applications, of which, two studies are to be introduced.

It has been known that in interstitial lung diseases such as idiopathic pulmonary fibrosis, the vascular resistance of lung rises more or less. Although this usually has been attributed to collapse of capillary bed due to fibrosis, vasoconstriction of pulmonary arteries may be another important mechanism. On the other hand, the segments of pulmonary arteries supplying lung areas poorly ventilated due to various changes tend to constrict and suppress the blood supply to such areas. This is a mechanism called the hypoxic vasoconstriction, a response that can also occur in arteries supplying fibrotic areas of lung where ventilation is impeded. If so, overstraining of arterial wall may precipitate thickening of media in the constricted segments. Therefore if subjected to the above measurement, medial hypertrophy will reveal when and where vasoconstriction has taken place. This was undertaken by Sawai *et al.* (1994), who performed morphometry of pulmonary arteries in autopsy lungs from 21 patients dying in various stages of fibrosis due to paraquat intoxication, together with five normal lungs as control. (The paraquat-associated lung changes will be shown in the next chapter.) The standardized morphometry described above was employed, where arteries were sampled in each case so as to cover a wide range of  $R$  from 0.05 to 1.0 mm. It was shown that the medial thickness  $D$  began to rise as early as on the 8th day of

intoxication, when, as yet, there were little fibrotic changes. Interestingly, this dating almost exactly coincides with the beginning deposition of fibrogenic matrix on alveolar wall, which will be shown in Chapter 2 (Figs. 2-25 and 2-27). Thus it seems that the medial hypertrophy is the result of hypoxic vasoconstriction triggered by the formation of matrix layer upon the alveolar septa, which causes alveolar-capillary block. In all the cases, the maximum thickening of media was found in small arteries of intracinacinar level. The conclusion: hypoxic vasoconstriction of pulmonary arteries occurs in an early, pre-fibrotic stage of interstitial lung disease and contributes to elevated vascular resistance.

### **Application to portal veins**

Another example is application to the changes of intrahepatic portal veins in patients having congenital biliary atresia with portal hypertension (also see Chapter 2). During the past decades, progress in the surgical treatment for this disease contributed to a dramatic increase in the number of long-term survivors. However, some postsurgical problems still remain, including the development of portal hypertension, a sometimes threatening complication. Nio *et al.* (1987) found that in infants with biliary atresia, smooth muscle layer emerges in the wall of medium-sized and smaller intrahepatic portal veins which normally are muscle-free. The muscular layer seemed to thicken and extend toward the periphery as portal hypertension progresses. In view of this, surgical biopsy and autopsy specimens of liver from 41 patients with biliary atresia were submitted to morphometry of intrahepatic portal veins. It was disclosed that with the persistence of portal hypertension, not only does the medial layer of proximal portal veins thicken, but extends to the periphery. In patients in whom biopsy specimens were taken at the second or third laparotomy three to five years after the corrective operation, the degree of medial hypertrophy proved to significantly correlate with the portal vein pressure intrasurgically measured. Thus, in a venous system too, medial thickening serves as a criterion for judging whether or not there is hypertension, and if there is, to what degree.

### **b) Morphometry of airways—what part of bronchial tree constricts in asthmatic attack ?**

#### **Bronchial smooth muscles in 3-D (Fig. 1-11)**

The morphometric study of arteries and the methods we developed have found another application, i.e., to the analysis of airway changes in patients of bronchial asthma. Like an artery, a segment of bronchus is a contractile tube which changes its luminal width by contracting or relaxing the smooth muscle cells circularly embedded in the wall. Figure 1-11 is a computer-aided 3-D reconstruction of a membranous bronchiole about 1mm in diameter. In reality, this is one of the images produced for the first time with the aid of the first trial system we managed to develop with which to assist serial sections technique (Takahashi *et al.*, 1986; Yaegashi, Takahashi *et al.*, 1987). Despite the somewhat coarse texture of image, the arrangement of smooth muscles in the bronchiolar wall is clearly visible, with the bundles of smooth muscles (shown red) surrounding in circular orientation, but strictly speaking, taking a slightly spiral course. The attack of bronchial asthma, a paroxysmal dyspnea that asthmatic

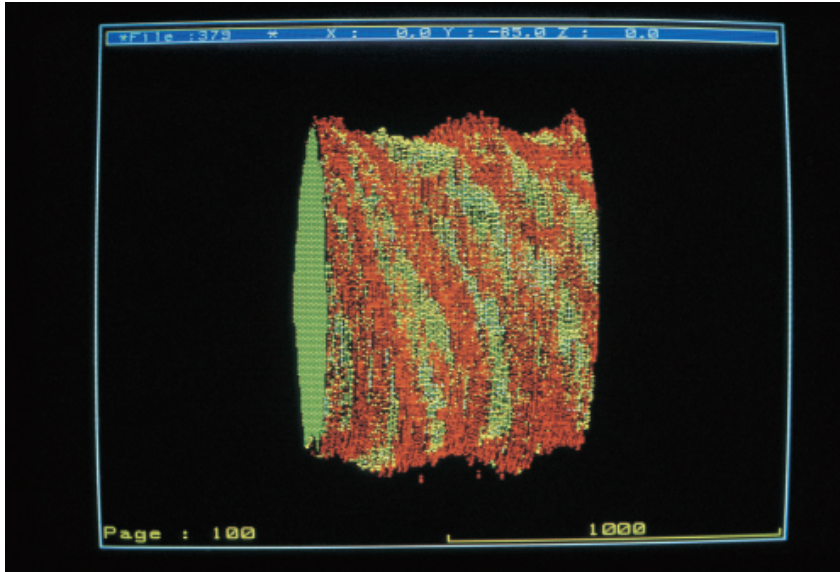


Fig. 1-11. A computer-assisted 3-D reconstruction of membranous bronchiole, about 1 mm in diameter. The lateral view is presented to demonstrate the distribution of smooth muscles in the wall (also see Fig. 4-7). The smooth muscles (red) are winding round the bronchiole, forming a gentle spiral. Reproduced from Yaegashi, Takahashi *et al.* (1986): *J. Microscopy* 146, pp. 57.

patients frequently suffer from, is considered to be resulting from bronchial convulsion, a tight constriction of these muscular bundles. All bronchial segments within a certain range of diameter are thought to take part in constriction more or less, but what level of airways in the bronchial tree are chiefly involved has not been clear.

#### **Application of Laplace formula to airways (Fig. 1-12)**

Also to this problem we can apply the discussion extended for the blood vessels, and here too, the mechanical forces that work on and around the bronchial wall are related in the form of Laplace formula

$$T = PR$$

where  $T$  is the circumferential tension exerted on the bronchial wall and  $R$ , the radius of a bronchial segment. However, in the case of bronchi, there is a difference from blood vessels. In this case, the pressure  $P$  does not imply the inner pressure of bronchus but denotes the force working on its wall as the elastic recoil from outside (Fig. 1-12). A segment of bronchus can keep its cylindrical shape from being collapsed, mostly with the help of the "recoil pressure." This is the force exerted upon the bronchial wall from the outside through multiple alveolar septa that contain elastic fibers and are attached at the outer surface of the bronchus, pulling it outward. The tension  $T$  generated upon the wall on account of this "elastic recoil"  $P$  is counterbalanced by the circular smooth muscles, which antagonize the recoil, keeping the bronchus from being

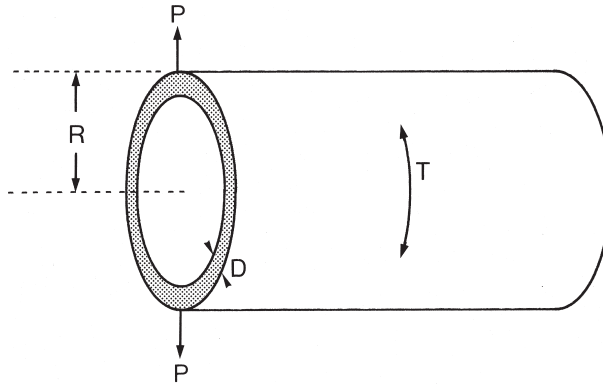


Fig. 1-12. Application of Laplace formula (Fig. 1-3) to airways. The situation differs from arteries in that, in the airways, the pressure  $P$  is exerted as a “recoil” pulling the wall outward. Reproduced from Ebina, Takahashi *et al.* (1990): *Am Rev Resp Dis* 141, pp.1326.

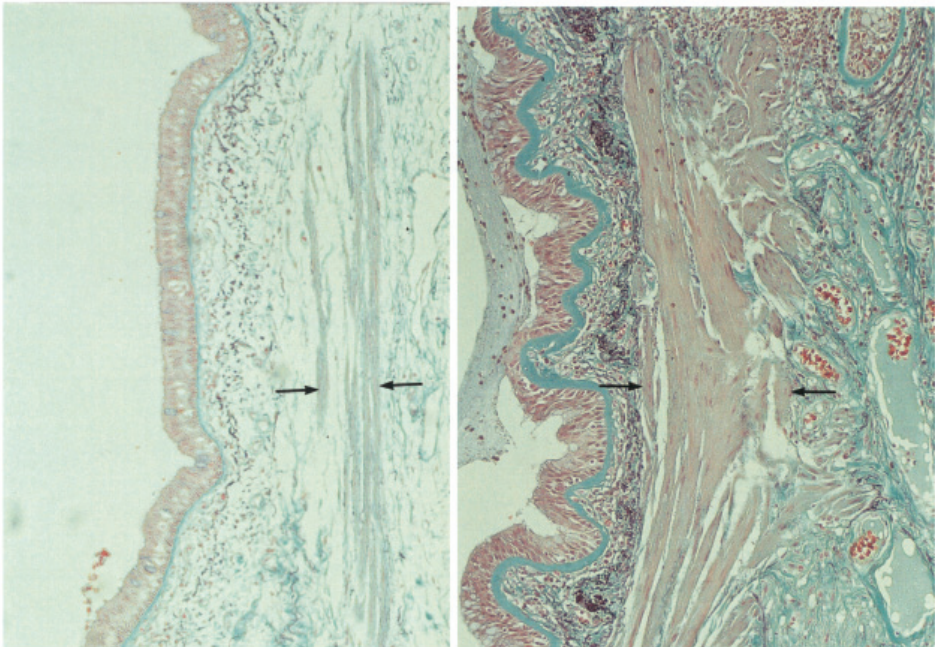


Fig. 1-13. Smooth muscle hypertrophy of bronchus in asthmatic patient. Though the muscular cells are not so densely packed (arrows) as in the medial layer of arteries, the bronchial wall of an asthmatic patient (right) appears equipped with a markedly thickened muscular layer compared with a non-asthmatic (left). Elastica-Goldner stain.

overstretched. In fact, a bronchus, when the mural smooth muscles were destroyed due to chronic inflammation, is liable to dilatation in the form of bronchiectasis, a state of bronchus which yielded to the recoil it was no longer able to resist. When an asthmatic attack occurs, the bronchial muscles constrict against this wall tension, and this implies an increased mechanical work for the smooth muscle cells. Asthmatic patients suffer from fits that occur more or less frequently and last for varying period, during which the patients endure severe respiratory distress.

### **Bronchial muscles in non-asthmatics and asthmatics (Fig. 1-13)**

Therefore, in lungs of asthmatic patients, it seems possible that we can find another example of adaptation: work hypertrophy of bronchial muscles that have been overworked, like the medial hypertrophy of arteries in hypertension. One can see in Fig. 1-13 that in the bronchial wall of an asthmatic (the right), the smooth muscle layer is remarkably thickened compared with the left figure which is from a non-asthmatic. In this situation, as in the arteries, the thickening of bronchial muscles may be interpreted as expressing the result of adaptation of bronchi to increased mechanical work. Accordingly, if the distribution of thickened smooth muscles is visualized over the entire range of airways from the large segmental bronchi to small bronchi to bronchioles, we will be able to see at what level the airways are most susceptible to paroxysmal constriction which generates asthmatic fits. What follows is a morphometric study performed by Ebina *et al.* (1990a, b) along this context.

### **Standardized measurement of airways (Figs. 1-14, 1-15)**

In determining the thickness of bronchial muscular layer, we face the same problem as in arteries. As in Fig. 1-14, the more dilated the bronchus, the thinner is its muscular layer, and vice versa. Therefore, the muscular thickness of a bronchial segment needs to be defined by reducing the segment to a state standardized with regard to its constriction or dilatation. There have been morphometric studies, although few in number, dealing with the thickness of bronchial muscles and its change in asthmatic patients (Takizawa *et al.*, 1971; Hossain, 1973). However, ambiguities remain, which seem at least partially attributable to bias inherent in the method of study.

In this study of bronchi, the standardization technique developed in the study of arteries was applied, where the perimeter length  $L$  of the elastic lamina and the sectional area  $S$  of smooth muscles were measured. However, there was in the airways a difference from arteries in the structure of muscular layer, which required a small modification: the muscular layer of bronchus does not form a compact layer like a united belt, but is separated into several muscular bundles. Therefore the area of each bundle was separately measured, and  $S$  was given by the total, as in Fig. 1-15. By the time this study was undertaken, a system for morphometry including a microcomputer and a digitizer had been put to practical use, which greatly facilitated the measurement.

### **Two types of asthma revealed by morphometry (Figs. 1-16, 1-17)**

Autopsy lungs from 16 patients, all dying of fatal asthmatic attack, were submitted to measurement of bronchial muscles. Figure 1-16 is the result obtained from an asthmatic patient, a male aged 71 years. As in the morphometry of arteries, the measurement data was presented on bilogarithmic coordinates, with the airway radius  $R$  in



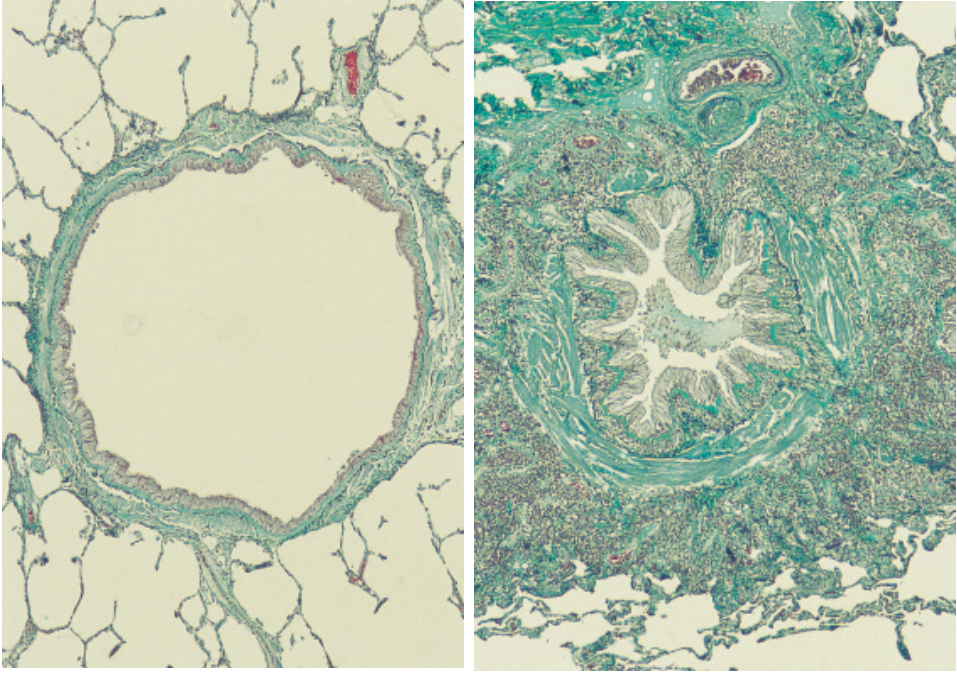


Fig. 1-14. A constricted bronchus (right) is compared with a dilated one (left). Apparently the muscular layer seems thicker in the former, making it necessary to define the muscular thickness and radius of an airway in a standardized state.

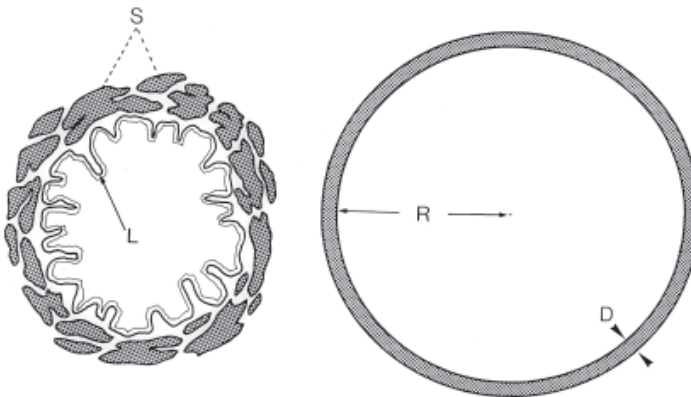


Fig. 1-15. Standardized measurement of airways. The method is basically the same as the one applied to arteries. In the bronchi however the muscular layer does not form a compact layer, requiring us to measure the area for each bundle separately.

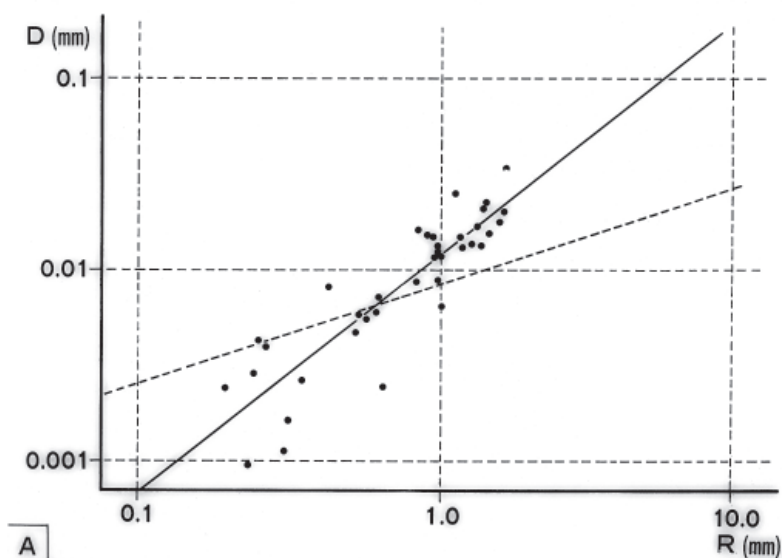


Fig. 1-16.  $D$ , the thickness of airway smooth muscle and  $R$ , the airway radius, in an asthmatic patient, Type I. Both  $D$  and  $R$  are plotted on bilogarithmic coordinates. The smooth muscle hypertrophy is found only in larger airways. Reproduced from Ebina, Takahashi *et al.* (1990): *Am Rev Resp Dis* 141, pp. 1330.

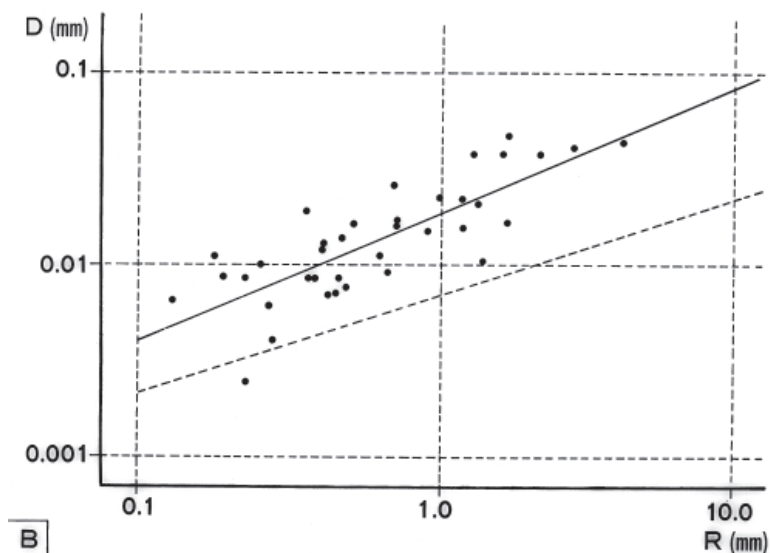


Fig. 1-17. The measurements of  $D$  and  $R$  in a patient of Type II asthma. The smooth muscle layer is significantly thickened over the entire range of  $R$ . Reproduced from Ebina, Takahashi *et al.* (1990): *Am Rev Resp Dis* 141, pp. 1330.

the abscissa, and the muscular thickness  $D$  in the ordinate. The solid line is the regression line for this patient, and the broken line is that of control lungs obtained from autopsies of 20 non-asthmatic subjects, where all the data were pooled to calculate a single regression. It is shown that in the present case of asthma, hypertrophy of muscular layer, though present, is confined to the proximal bronchi with  $R$  larger than 1 mm, while in the peripheral bronchioles the muscular layer remains as it was in a non-asthmatic state. Of the lungs from 16 cases of asthma, those from seven patients proved to have this type of distribution, and in these, airway constriction responsible for producing asthmatic attack was considered to take place in the larger range of bronchi, including the segmental and subsegmental levels. This is a result supporting what had generally been assumed (Nadel, 1980).

However, in the remaining 9 patients of asthma, the result of measurement was quite different. As shown in Fig. 1-17, which is from a male asthmatic 54-years-old, the muscular layer is significantly thickened over the entire range of airways from the segmental bronchi of 4 mm in radius to respiratory bronchioles of 0.2 mm. It is likely that in these nine patients, the asthmatic attack occurs as the result of airway constriction that involves not only the larger bronchi but the terminal and even the respiratory bronchioles. While comparing among the data, we noticed that in each of the 16 patients of asthma, the pattern of muscular hypertrophy belonged to either the former (Fig. 1-16) or the latter type (Fig. 1-17), and there was no patient showing an intermediate pattern. Therefore it was considered that according to what level of airways are involved in paroxysmal constriction, the patients of asthma are classifiable into two types; the patients with hypertrophy in the larger bronchi, and those with overall hypertrophy. The former was designated as Type I asthmatics and the latter, as Type II, respectively. Thus, there appears to be a significant number of patients in whom airway hyperreactivity is distributed over the whole bronchial tree, although so far, patients corresponding to Type I had been considered to be typical asthmatics. Some factors, in either pathological or clinical aspect, seemed likely to be underlying the difference between the two types. However, up to now, we have not managed to focus on a small number of factors to which the between-groups difference may be ascribed. Given the large number of factors potentially responsible for airway hyperreactivity, it may be necessary to study a larger population for clinical as well as pathologic abnormalities.

### c) Standardized morphometry of airways in normal and diseased lungs

Pulmonary emphysema and chronic bronchitis (or bronchiolitis) are diseases associated with chronic airflow obstruction, and are classified as chronic obstructive pulmonary disease (COPD). However, COPD is an entity mostly established upon studies of respiratory function, while the airway obstruction itself has not always been defined on a firm pathological basis. In emphysema, it is the loss of alveolar septa that has been considered responsible for producing impaired expiratory function (see Figs. 2-17 and 2-19).

On the other hand, in chronic bronchitis or bronchiolitis, obstruction is considered attributable to inflammatory processes that advance in the airway wall and produce various grades of irreversible luminal narrowing. However, in such cases, we are



still far from the state in which we can correlate the functional impairment (the reduced expiratory efficiency) with the morphological changes of airways. What level of airways in the bronchial tree are involved in obstruction? To what degree the whole airway bed is narrowed? Although these are questions to be answered only by morphology, the studies on the part of pathology are retarded, which seems attributable at least partially to the following difficulty.

In a microscopic section of lung, one can find a number of airways with different calibers. Imagine that in a biopsy specimen of lung we found an airway, 1mm in inner diameter. In this situation, can we determine whether the airway we are looking at has become narrower or wider than its previous state? Clearly, the answer is no. So long as information is lacking about the original dimension of the airway in question, we cannot say whether the airway at our hand is in a stenotic or dilated condition. Even if it seemed thinner than normal, one cannot deny that it had been a small segment in the first place. To overcome this, Yaegashi and Takahashi (1994ab) devised a method of standardized morphometry of airways.

### **Airways and their collateral pulmonary arteries (Figs. 1-18, 1-19)**

The method of standardization for airways was designed so as to make use of their close arrangement with pulmonary arteries, both running in parallel from the hilar large trunks down to the terminal branches. Figure 1-18 is a computer-assisted 3-D reconstruction of lung visualizing airways (green), small pulmonary arteries and arterioles (pink) and pulmonary veins (blue) where one can see segments of airways and pulmonary arteries running closely in parallel. On account of this arrangement, airway usually emerges in a microscopic section attended by an artery running in its close proximity, as in Fig. 1-19. In chronic bronchitis or bronchiolitis, the collateral

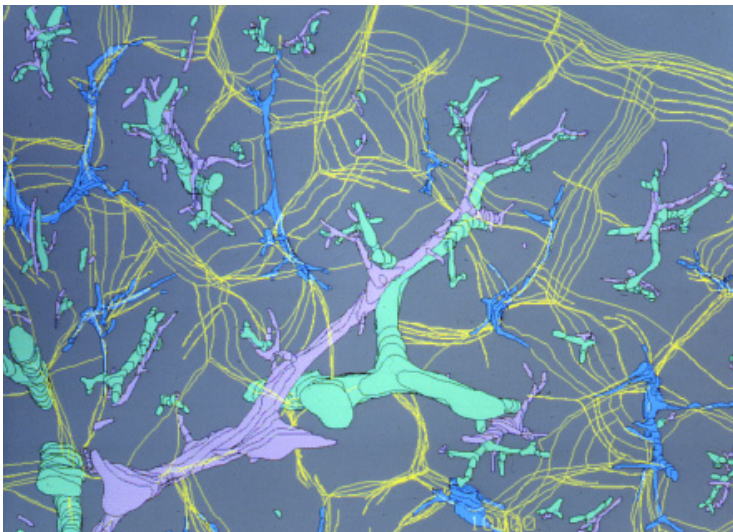


Fig. 1-18. Computer-assisted 3-D reconstruction of peripheral airways (green), pulmonary arteries (pink) and veins (blue). The yellow wireframes express the interlobular septa. Note that most of the airway segments are attended by a collateral pulmonary artery.

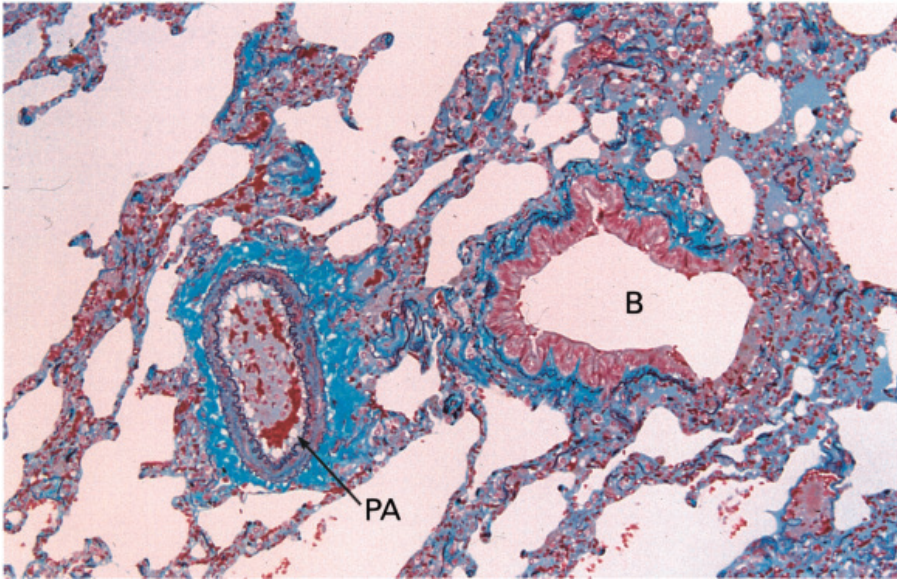


Fig. 1-19. Cross section of an airway (membranous bronchiole, denoted by B) and its collateral pulmonary artery (PA) in a microscopic section of lung. Elastica-Goldner stain.

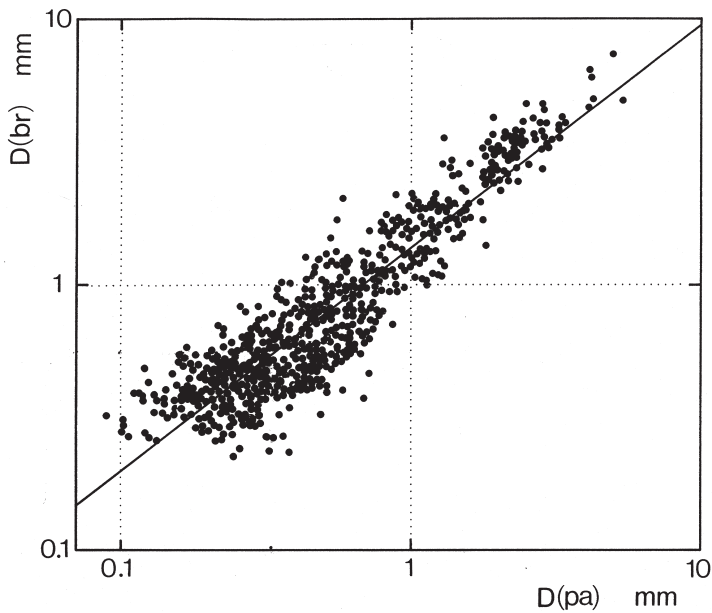


Fig. 1-20.  $D(\text{br})$ , the diameter of bronchi and bronchioles, and  $D(\text{pa})$ , that of pulmonary artery running parallel with the airway, measured on 695 pairs from 17 normal lungs. Note the close linear regression between  $D(\text{pa})$  and  $D(\text{br})$  on bilogarithmic coordinates. Reproduced from Yaegashi and Takahashi (1994): Arch Pathol Lab Med 118, pp.972.

pulmonary arteries, far more resistant to inflammation than the airways, retain their original structure and dimension until late in the course of disease. Hence, if there is a close correlation in the caliber between airways and their attending pulmonary arteries, we will be able to know from the dimension of collateral artery to what degree an airway is being narrowed or dilated. In view of this, autopsy lungs from 17 patients with neither clinical nor pathological finding suggesting lung disease were submitted to measurement of diameters for airways and attending pulmonary arteries. The age of the patients ranged from 10 to 78 years. A total of 695 pairs of airways and arteries were sampled. For the airways as well as the arteries, the diameter was defined in a standardized state in which both the epithelial basement membrane of airways and the inner elastic membrane of arteries were stretched into a circle. Airways were sampled including the whole ranges from the segmental bronchi down to the respiratory bronchioles.

### Regression in diameter between airways and their collateral arteries (Fig. 1-20)

Figure 1-20 demonstrates the result of measurement, where all the data from the 695 pairs were pooled, with  $D$  (pa), the diameter of pulmonary artery in the abscissa, and  $D$  (br), that of the airways in the ordinate, both expressed on logarithmic coordinates. There is a correlation close enough to allow to estimate the diameter of airway from that of the attending pulmonary artery, even in lungs with COPD in which airways can strongly be stenosed or dilated. Although there are practically no age changes in the regression equation, the ranges for bronchi, membranous bronchioles and respiratory bronchioles proved to move during the growth period.

### Peculiar disease of airways: small airways disease? (Figs. 1-21, 1-22, 1-23)

Here to be shown is an autopsy case where the standardized measurement of airways contributed to the elucidation of chronic airflow obstruction. The patient was

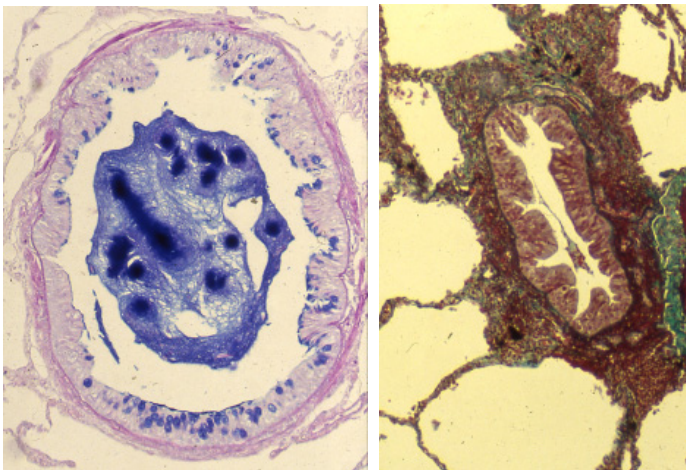


Fig. 1-21. The small airways in a peculiar case of chronic airway obstruction, perhaps corresponding to "small airways disease." Right: a membranous bronchiole with the lumen somewhat narrower than normal, and with mild fibrosis in the surroundings (elastica-Goldner stain). Left: luminal plugging with mucus, with goblet cell metaplasia of lining epithelia (alcian blue-PAS stain).

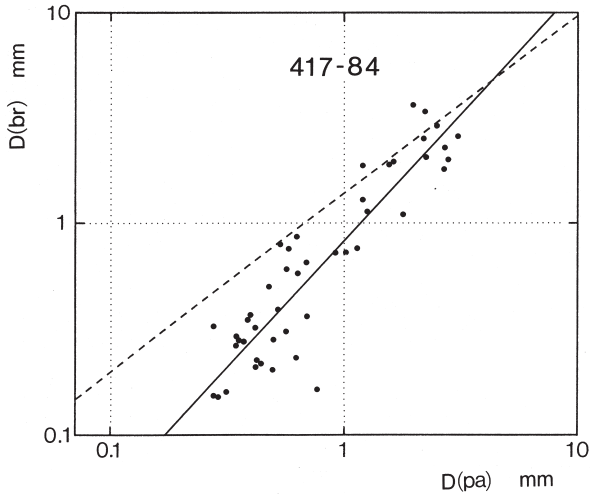


Fig. 1-22.  $D(pa) - D(br)$  regression in the case of “small airways disease” shown in Fig. 1-21. The airway diameter is significantly lower than the regression line of normal lungs (the broken line), particularly in the periphery. Reproduced from Yaegashi and Takahashi (1994): *Arch Pathol Lab Med* 118, pp. 981.

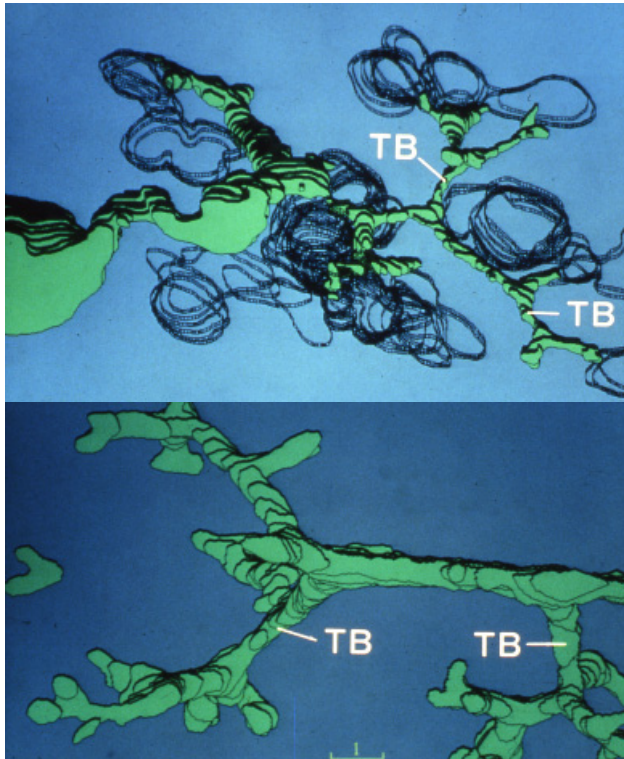


Fig. 1-23. Upper: computer-aided 3-D reconstruction of peripheral bronchioles in the lung with “small airways disease.” The small airways are apparently thinner than in a normal lung (lower). TB: terminal bronchiole. Reproduced from Yaegashi and Takahashi (1994): *Arch Pathol Lab Med* 118, pp. 981.



a male aged 68 years, who had been treated for 25 years under varying diagnoses including asthma, emphysema or chronic bronchitis, and died of respiratory insufficiency. Microscopically, emphysematous changes were minimum if any. The membranous bronchioles seemed to have lumina somewhat narrower than normal (Fig. 1-21 right). Signs of chronic inflammation were found in the wall of bronchioles with sparse infiltration of mononuclear cells and slight fibrosis, and there were goblet cell metaplasia of bronchiolar epithelia, sometimes with luminal plugging with mucus (Fig. 1-21 left). None of these, when acting alone, appeared to be serious enough to narrow the lumen by themselves. However, as in Fig. 1-22, the standardized morphometry revealed an overall airway narrowing that was distributed fairly uniform and tended to increase toward the periphery. The narrowing is of such a degree as to fully explain the development of airflow obstruction, independently of inflammatory changes. Without quantifying the luminal diameter with the standardized technique, this sort of bronchiolar obstruction would never be assessed for certain.

In the upper part of Fig. 1-23, the above lung was subjected to computer-aided 3-D reconstruction to visualize the peripheral airways. The figure, produced at an equal magnification as in the control lung shown below, discloses a marked luminal narrowing uniformly involving the whole range of membranous bronchioles, where TB denotes the terminal bronchioles. Thus, the case appears to be a sort of lung disease not definable within the scope of conventional categories of COPD, shedding light on the presence of bronchiolar disease that previously has not been defined in clear pathological terms. Besides the luminal narrowing, there were in the membranous bronchioles signs of mild chronic inflammation and hypersecretion of mucus as shown by goblet cell metaplasia and mucus plugging, suggesting that chronic irritation of bronchiolar mucosa had been lasting. The luminal narrowing seems to be the result of peribronchiolar fibrosis due to mild but recurring inflammation. This may be a state corresponding to the bronchiolar version of chronic bronchitis, the latter involving the larger bronchi and having been regarded as a response to chronic irritation rather than as an inflammation in the strict sense of the term. Thus, study of the case reminds us of the concept of small airways disease proposed by Hogg *et al.* (1968). However, there has been ambiguities about what pathological changes actually progress in the bronchioles in "small airways disease." We think that in the present morphometry and 3-D visualization, the pathological features corresponding to this condition has become a little clearer.

## **Stereology and Its Application to Pathology**

In the examples of morphometry shown in the foregoing chapter, we were able to reach a conclusion only through measurements on 2-D pictures. There was no need to take into consideration the 3-D structure of objects. However, often we are required to obtain information about the 3-D structure.

We pathologists always make diagnosis based on observation of pictures, including macroscopic, microscopic and electron microscopic pictures. However, available for us are almost always 2-dimensional (2-D) pictures, or sections. A microscopic picture is of course a sectional one, and so is an electron micrograph. Also, a cut surface of an organ is another example of 2-D picture. However, they are all sections of what in itself is a 3-D structure. It seems that while looking at a 2-D microscopic section, we are always trying to understand, even if not being aware, what 3-D structure such a section may have been generated from. Often this attempt fails and ends up in confusion, particularly when we are dealing with a complicated one. On such occasions, some of us may attempt at resorting to 3-D reconstruction from serial sections, a time-honored technique of morphology long used in pathology and microanatomy. However, this will not be undertaken very often even when it is necessary. Reconstruction is a demanding task which may cost a pathologist a great deal of time and labor.

On the other hand, efforts have been paid to establish theoretical methods to obtain information about the 3-D properties of objects, quantitative or qualitative, thereby avoiding the laborious reconstruction. As a famous and successful example one can introduce the method to estimate the surface area of the alveolar septa contained in the human lung. Weibel (1963) gave an estimate of 120 m<sup>2</sup> for the total alveolar surface area of both lungs combined together, and this has been considered a good one. Apparently this is a 3-D quantity which is a very important factor in correlating the structural changes of lung with its function. For example, one can expect the alveolar surface area to be much reduced in lungs with advanced emphysema, and this helps correlate the functional abnormalities of emphysematous lungs with their structural changes. Of course it is not practicable to separate the lung tissue to pieces and directly measure the surface area of fragments. In fact, the quantity was estimated indirectly from microscopic measurement on 2-D lung sections, relying on a mathematical principle. Here we find a “bright” technique allowing us to know about the three dimensions without making direct access with serial sections. There are also other principles and technique we can apply in estimating 3-D quantities from measurements on 2-D sections. To such methodology, a generic term has been given: stereol-

ogy, the science of 3-D (Bach, 1963).

Of the various methods of stereology developed, some basic principles are to be introduced here, together with examples of their application:

- the volume ratio of a structural component ( $V_V$ : volume density)
- the surface area in a unit volume ( $S_V$ : surface area density)
- the total length in a unit volume ( $L_V$ : length density in space)
- stereology of particles (granulometry).

### a) Evaluation of paraquat-induced atelectasis

#### Hamster lung in experimental paraquat toxicity (Figs. 2-1, 2-2)

Paraquat (1,1'-dimethyl-4, 4'-bipyridylum chloride), a herbicide widely used in Japan, has been the prime cause of fatal intoxication after ingestion, whether accidental or with suicidal intent. In fatal cases of intoxication, severe respiratory distress emerges on the fourth or fifth day and the condition of the subject rapidly deteriorates (Smith *et al.*, 1974). At autopsy, lungs are confirmed to be the main site of fatal changes, ranging from diffuse alveolar damage to dense fibrosis. In an experimental attempt at visualizing the earliest changes of lung, hamsters were given a small amount of paraquat intraperitoneally. Figure 2-1 is a microscopic section of lung 30 minutes after the administration where, as yet, no paraquat-related changes have emerged. The image contains a terminal bronchiole, respiratory bronchioles, alveolar ducts and many alveoli, with their air spaces fully open and with all the alveoli unfolded. Figure 2-2

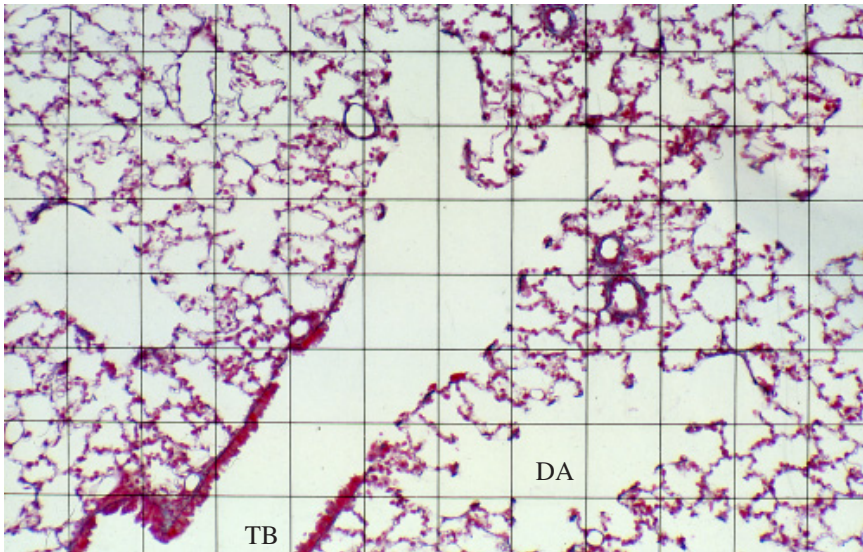


Fig. 2-1. Estimation of areal ratio for ductus alveolaris (DA) and terminal bronchiole (TB) by point counting, in a lung of hamster 30 minutes after paraquat was given, still retaining the normal structure. The cross points of the overlaid grid serve as sampling points. The areal ratio of DA combined with TB (20/77) can directly be interpreted as their volume ratio. Elastica-Goldner stain.

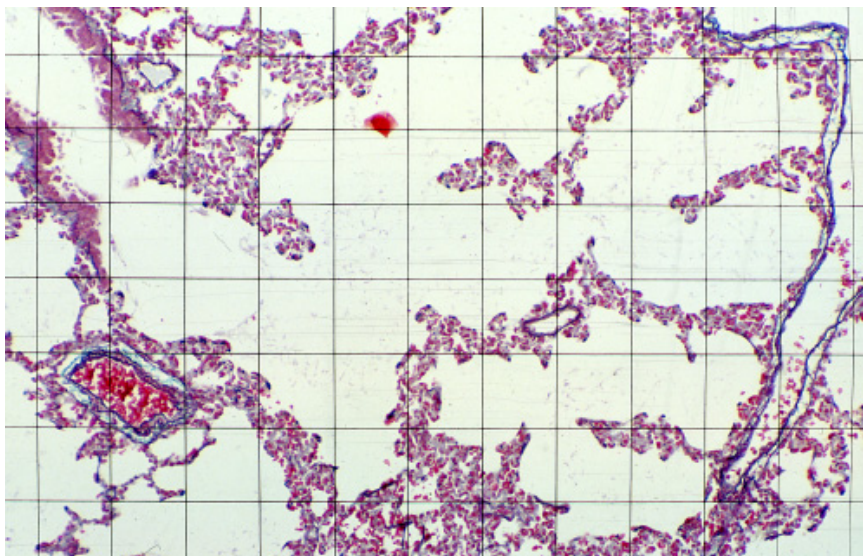


Fig. 2-2. Point counting in a hamster lung in early paraquat toxicity, 24 hours after administration. The alveolar ducts are strongly dilated, as demonstrated by the areal (volume) ratio that is elevated to  $44/84 = 0.524$ . The alveoli are all collapsed in a state of alveolar atelectasis. Elastica-Goldner stain.

demonstrates the state of lung 24 hours after the administration. Here the individual alveoli have lost aeration, with the septa closely adherent one to another, showing a change called alveolar atelectasis; instead, however, the alveolar ducts are all strongly dilated. Both of the lungs were carefully fixed so as to keep the *in vivo* state of aeration as faithfully as possible; they were kept in fixative and aspirated from exterior by connecting the air-tight container with a water-jet pump. The difference in the volume share of alveolar ducts and other parts of bronchiolo-alveolar system was compared between the two conditions with  $V_V(\text{ad})$ , the volume of alveolar ducts (including the terminal bronchioles) in a unit volume, or the volume density.

Look at the grid of “tessellated” type with vertically crossing parallel lines that is overlaid upon the microscopic pictures. In practice, we use an eyepiece bearing the grid pattern which is put in an ocular lens of microscope (Fig. 2-4 upper). Figure 2-1 contains 77 crossing points of lines and Fig. 2-2 contains 84, and we can find some of the points hitting, for example, air spaces in the alveolar ducts. In Fig. 2-1 we count the number of points hitting the alveolar ducts (and terminal bronchioles), and obtain a result of 20 points. Then, the fraction of area occupied by the air space of alveolar ducts  $A_A(\text{ad})$  on section is estimated to be approximately  $20/77 = 0.260$ . According to one of the basic principles of stereology,

$$V_V \doteq A_A \quad (2-1)$$

which means that the volume ratio of a component in a 3-D structure ( $V_V$ ) is approximated with its areal ratio ( $A_A$ ) on a random 2-D section of the structure. Therefore in



this case, we can regard the air space fraction of alveolar ducts  $V_V(\text{ad})$  also as about 26.0%. The measurement was extended to Fig. 2-2, and here we see 44 of 84 points hitting the spaces of alveolar ducts, showing that  $V_V(\text{ad})$  has been increased into  $44/84 = 0.524$ . Similarly, the air space fraction for alveoli  $V_V(\text{al})$  in Fig. 2-1 is shown to be about  $49/77 = 0.636$  while in Fig. 2-2, it is reduced to  $26/84 = 0.310$ . All these may be interpreted as suggesting that the alveolar septa are stuck one to another, causing a state of alveolar collapse, suggesting that the lung as a whole has lost its extensibility. This is a state of alveolar atelectasis which is attributable to surfactant deficiency caused by paraquat-induced injuries to Type II pneumocytes, the main producer of surface active agents. In fact, in the lungs of hamsters in the state of Fig. 2-2, clear signs of injury in Type II cells were confirmed electron microscopically.

There are several methods to measure the area of the structure of interest in a section. If a semi-automatic digital image processor is available, it may prove to be helpful. However, the "point counting" technique shown above is the easiest to practice and therefore used worldwide. If microphotographs are used as material, one can perform point counting by overlaying the photograph with a plastic sheet printed with tessellated grid, instead of using an eyepiece.

### Point counting vs. chord length measurement for $V_V$ (Figs. 2-3, 2-4)

There is another method of estimating  $V_V$  on section instead of point counting. Figure 2-3 is meant to show a sectional picture of carcinoma where the areal ratio  $A_A$  is to be determined for either the carcinoma cell nests, or the interstitium. Of course,

$$A_A (\text{cell nests}) + A_A (\text{interstitium}) = 1.0$$

In the upper figure, point counting is performed, with the nests occupying 20/63 points, or  $A_A(\text{nests}) = 0.32$ . An alternative is shown in the lower figure, and here we put parallel sampling lines drawn randomly on the sectional picture. If the area of the section (or the total length of the lines) is sufficiently large, the lines come to traverse the carcinoma cell nests many times, and at each transection, generate a linear intercept, or a chord, of various length  $\lambda$ . If we measure  $\lambda_i$  for hundreds of chords that arose,  $A_A$  is estimated by

$$(V_V =) A_A \cong \sum \lambda_i / L \quad (2-2)$$

where  $L$  is the total length of sampling line.

Figure 2-4 demonstrates two types of eyepiece, the upper one for point counting and the lower, for chord length measurement. The lower one may look like an ordinary eyepiece widely used for microscopy, but the difference is that it has a line transversely penetrating the scales, and this serves as sampling line. While observing a sectional picture under microscope, we can extend sampling as much as necessary by moving the picture in the direction parallel to the line.

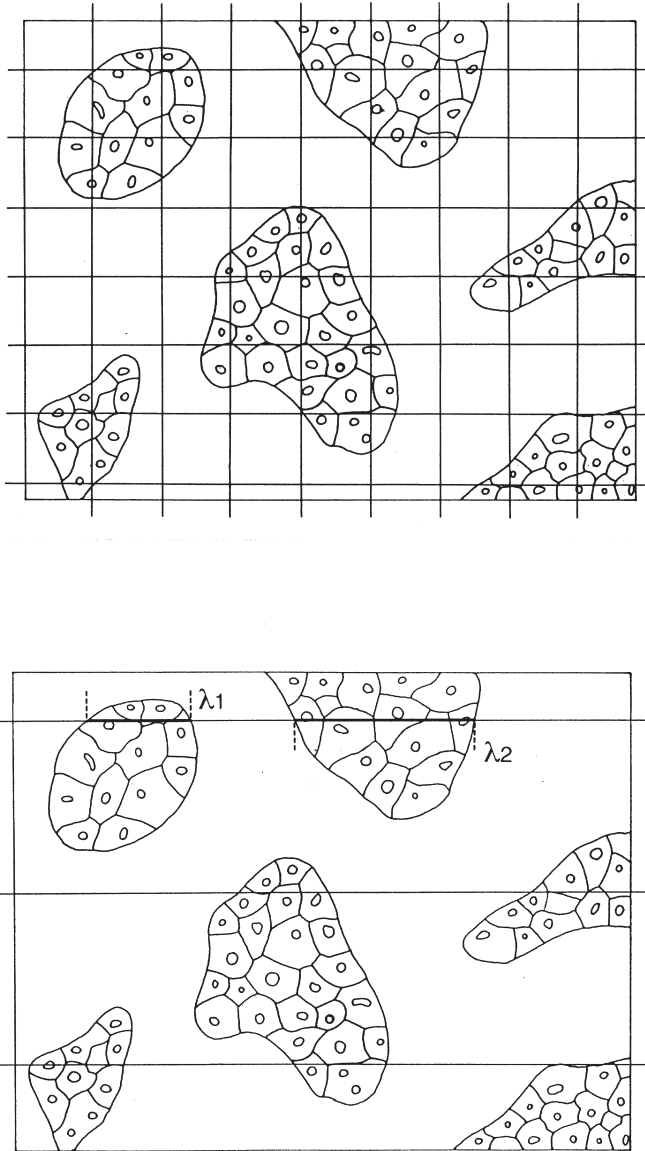


Fig. 2-3. Two methods for the estimation of  $V_V$  are schematized. Point counting (upper) vs. chord length measurement (lower) applied to carcinomatous tissue in order to determine the stromal (or parenchymal) volume ratio.

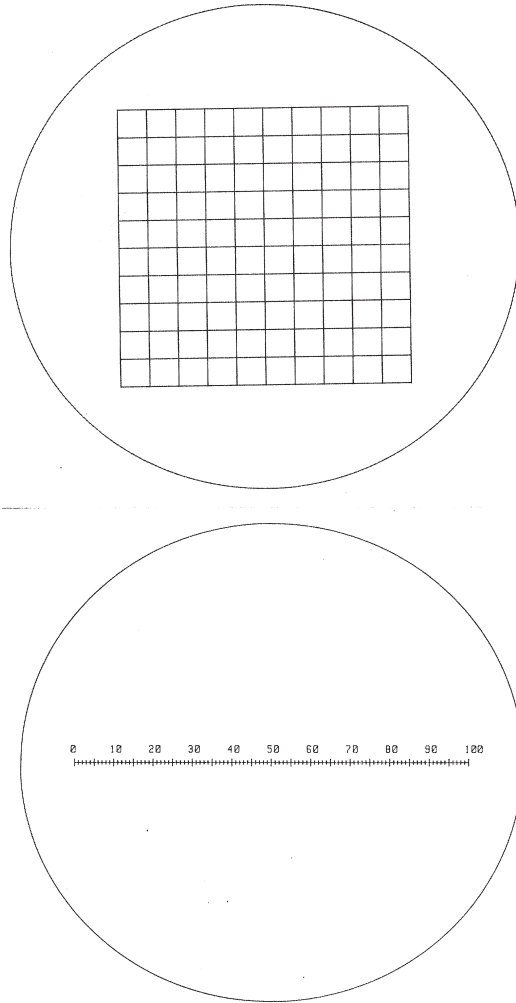


Fig. 2-4. Two types of eyepiece. Upper: “tessellated” grid which is useful in making point counting. Lower: an ocular micrometer with a line transversely penetrating the scales, convenient for chord length measurement.

## b) Langerhans islets of the pancreas in diabetics

### Langerhans islet of pancreas and diabetes mellitus (Fig. 2-5)

Figure 2-5 demonstrates an islet of Langerhans found in the pancreas of a non-diabetic subject. Millions of such micro-organs are dispersed in a normal pancreas of human. An islet comprises several sorts of cells, each assigned to secrete one of the islet hormones: insulin, glucagon, etc. Of the diseases associated with abnormal islet function, it is diabetes mellitus that in developed countries affects a significant and increasing part of population, raising a serious health problem.

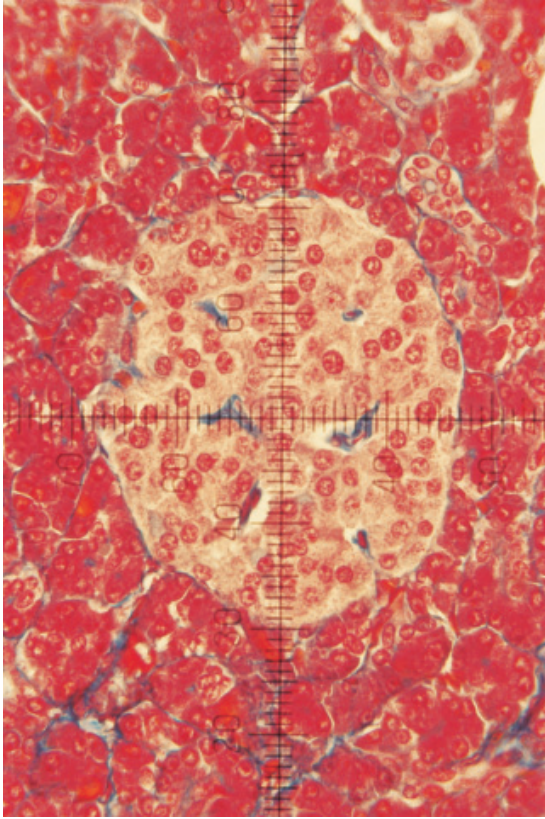


Fig. 2-5. The microscopic picture of a normal islet of pancreas. Azan-Mallory stain.

Diabetes mellitus is a metabolic disorder in which the function to metabolize carbohydrates is more or less impaired. This has been attributed to faulty activity of insulin that is secreted by what is called B cells of islets, resulting in hyperglycemia and glycosuria. There are several complications of diabetes which are often fatal and clinically more important than the metabolic disorder itself, including lowered resistance to pyogenic infection, ischemic heart disease due to advancement of atherosclerosis, and microangiopathy leading to devastating retinopathy and nephropathy. Since diabetes is primarily associated with malfunction of insulin, it would be of profound significance to make clear whether or not there are morphological changes of islets underlying the disease. Particularly, it may be crucially important to know whether diabetes is associated with quantitative changes of islets, such as their reduced volume or number. As yet, however, quantitative study of islets is retarded, and this may be attributable to the difficulties in establishing a useful geometric model for this microorgan.

The quantitative treatment of spherical bodies dispersed in the space, or granulometry, is a classic subject of stereology. Also in morphological pathology, these sorts of problems are encountered not infrequently. One may immediately be reminded

of several examples, such as regenerative nodules of cirrhotic livers or nuclei of some kind of cells, for example hepatocytes, besides, of course, pancreatic islets. However, distribution of radius of dispersed particles has not been accessible to easy morphometric technique, and the estimation of sphere number  $N_V$  in a unit volume still remains to be one of the hardest problems of biometry. In 1976, Suwa *et al.* developed a stereological method workable if one can assume that the radius  $r$  of spherical bodies follows some distribution function. This method has practical advantage as compared with the methods introduced by Scheil (1931), Schwartz (1934) or Saltykov (1958) where no such distribution function was assumed. To be outlined in the following is an application of this algorithm by Saito *et al.* (1978, 1978) to the pancreatic islets in diabetic and non-diabetic subjects.

### Chord length measurement on a model of dispersed spheres (Fig. 2-6)

The aim of this model-based quantification was to estimate the total number  $N_i$  and volume  $V_i$  of islets contained in the pancreas, and parameters of islet radius distribution, including the mean and variance of radius.

Figure 2-6 is a schema showing the geometric model we used. Here we assume that the pancreatic islets can be approximated to spheres which are of varying radius  $r$  and dispersed in the space as schematized in the figure. Suppose that the space containing spheres is sectioned with a plane. In the figure, the space is cut into a cube, and in its frontal face, a number of islets are shown emerging as circular sections of various size. This is a situation corresponding to the microscopic picture of pancreas in which circular islets are scattered. Now suppose that a sampling line is drawn randomly on section generates a number of chords. Microscopic measurement is performed of the length  $\lambda$  for a large number of chords. Based on a stereological theorem,  $N_V$ , the number of spheres in a unit volume, the mean and variance of  $r$  are estimated from the measurements of  $\lambda$ .

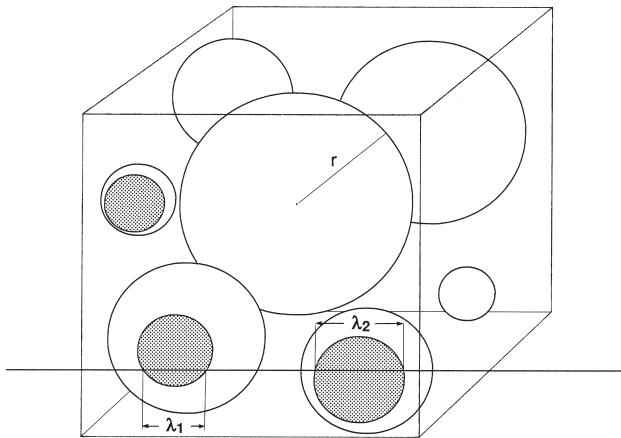


Fig. 2-6. A geometric model used for the morphometry of Langerhans islets. Islets are assimilated to spheres of different radius  $r$  and dispersed in the space. A sampling line drawn randomly on section generates a number of chords. Microscopic measurement is performed of the length  $\lambda$  for a large number of chords. Based on a stereological theorem,  $N_V$ , the number of spheres in a unit volume, the mean and variance of  $r$  are estimated from the measurements of  $\lambda$ .

the sectional plane. It intersects a series of circles and generates “chords” of various lengths  $\lambda$ . Under microscope, the length  $\lambda$  was measured for a number of chords, usually 200 or more, and the parameters of sample distribution for  $\lambda$  were obtained:  $N_L$ , the number of chords;  $\sum(\lambda)_L$ , the sum of  $\lambda$ ; and  $\sum(\lambda^2)_L$ , the sum of  $\lambda^2$ , each per unit length of sampling line. Here the task is to estimate the necessary quantities about the radius  $r$  of spheres from these measurement data.

### Weibull distribution assumed for sphere radius (Fig. 2-7)

As above, we assume that the sphere radius  $r$  follows a distribution function  $N(r)$ . Several different functions may be workable, including logarithmic normal distribution or gamma distribution, but in this study, Weibull distribution

$$N(r) = N_V m \alpha (\alpha r)^{m-1} \cdot \exp[-(\alpha r)^m] \quad (2-3)$$

was employed on account of its convenience in practical use (Fig. 2-7). The function contains three parameters.  $N_V$  is the number of spheres in a unit volume (the numerical density). The second parameter  $\alpha$  is called the scalar because it is responsible for transformation of coordinates along the  $r$ -axis. The third,  $m$ , is the shape parameter, allowing us to obtain widely divergent shapes of distribution as the value is shifted. What a variable pattern of  $N(r)$  is obtained by shifting the  $m$ -value is visualized in Fig. 2-7, where both the values of  $N_V$  and  $\alpha$  are fixed at 1.0. It is on account of this feature that Weibull distribution finds a wide application to biological forms.

The distribution of chord length,  $F(\lambda)$ , is related to the distribution of  $N(r)$  by the

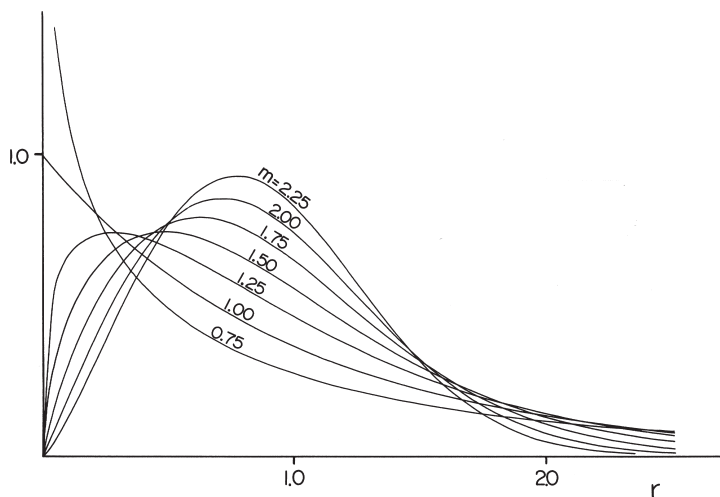


Fig. 2-7. Weibull distribution. The distribution curves with different  $m$  values.  $N_V$  and  $\alpha$  are fixed at 1.0.

equation:

$$F(\lambda) = \frac{\pi}{2} \int_{\frac{\lambda}{2}}^{\infty} \lambda N(r) dr \tag{2-4}$$

Based on this, the parameters characterizing the distribution of  $r$  were calculated, including  $N_v$  and the mean and variance of  $r$ . For the mathematical derivation of (2-4), and also for the treatment of measurement data, see Appendix which is found at the end of this book.

**Chord length  $\lambda$  : measurement data vs. theoretical distribution (Fig. 2-8)**

Chord length  $\lambda$  obtained by measurement in a non-diabetic pancreas was expressed in Fig. 2-8 as a histogram. The curves entered in the figure are the theoretical  $F(\lambda)$ s calculated by assuming Weibull distribution, gamma distribution and logarithmic normal distribution for  $N(r)$ , respectively. One can see that each of the curves sufficiently agrees with the histogram, justifying to assume that  $r$  follows each of these functions.

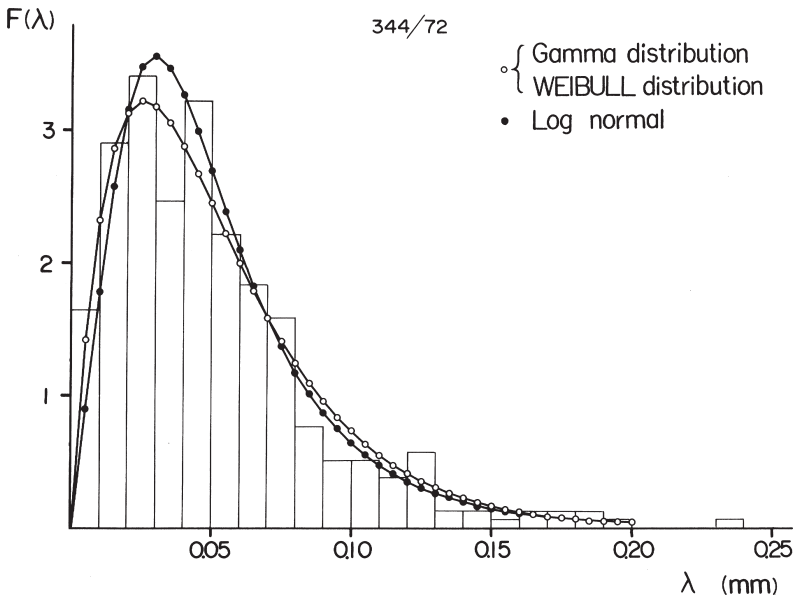


Fig. 2-8. The histogram of chord length  $\lambda$  generated by Langerhans islets, measured in a non-diabetic pancreas, is superimposed with the theoretical distribution assuming Weibull, gamma and logarithmic normal distributions. Each of the distributions is shown sufficiently agreeing with the histogram. Reproduced from Suwa, Takahashi *et al.* (1976): *Tohoku J Exp Med* 118: pp. 108.

### Mean radius, total number and total volume of islets (Figs. 2-9, 2-10)

Figure 2-9 demonstrates the results of islet morphometry based on the model of dispersed spheres. The data were obtained on morphometry of pancreases taken at autopsy, all performed within 2 hours post mortem. In the upper figure, the values of mean islet radius are compared among the four groups: control non-diabetics, hypertensive non-diabetics, maturity onset (Type II) diabetics and growth-onset (Type I) diabetics. Hypertensive subjects were discriminated, considering the possibility that the islets could undergo some ischemic changes because the pancreas is one of the organs where small arteries and arterioles are particularly susceptible to hypertensive lesions. Among the four groups, one can find no significant difference in the mean islet radius. Therefore the possibility is ruled out that diabetes is associated with atrophy of islets. Shown in the lower figure are values of  $N_i$ , the total number of islets contained in the pancreas, which was obtained by multiplying  $N_v$ , the islet number in a unit volume (the numerical density of islets), by the volume of pancreas. The mean  $N_i$  for non-diabetics amounts to 8 million, but there is a notable dispersion of the estimated  $N_i$  in non-diabetic as well as in diabetic groups. Although  $N_i$  appears to be slightly smaller in maturity-onset (Type II) diabetics, the difference from the non-diabetics is not significant. Only in growth-onset (Type I) diabetics,  $V_i$  proved to be significantly lower than the other groups.

The most significant difference between the diabetics and non-diabetics was found in the total volume  $V_i$  of islets contained in the pancreas. Though there is a large within-group variation in each of the groups, the mean  $V_i$  is the highest in the non-

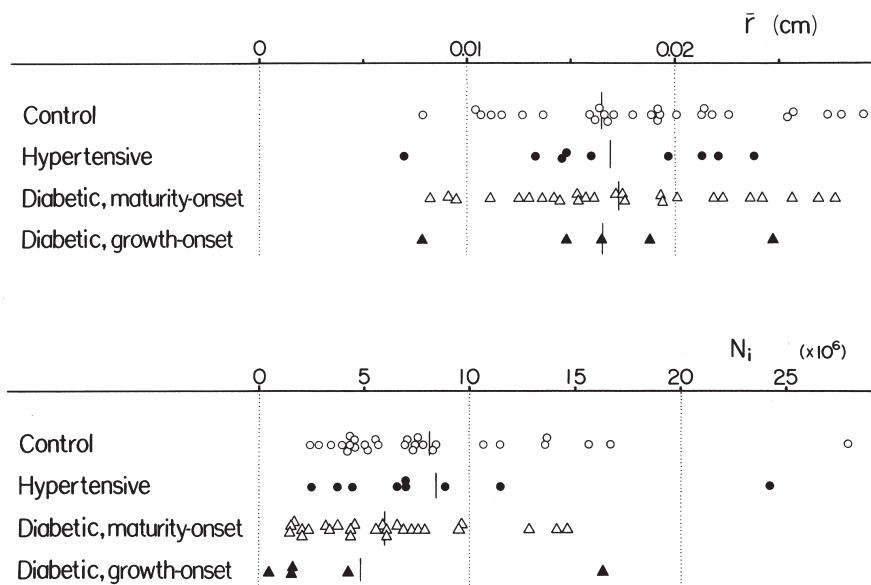


Fig. 2-9. The mean radius of islets (upper), and the total number of islets contained in the pancreas (lower), estimated stereologically. Measurement was performed on autopsy pancreases including non-diabetic non-hypertensives, non-diabetic hypertensives, maturity onset diabetics (Type II) and growth onset diabetics (Type I). Reproduced from Saito, Takahashi *et al.* (1978): *Tohoku J Exp Med* 125: pp.190.



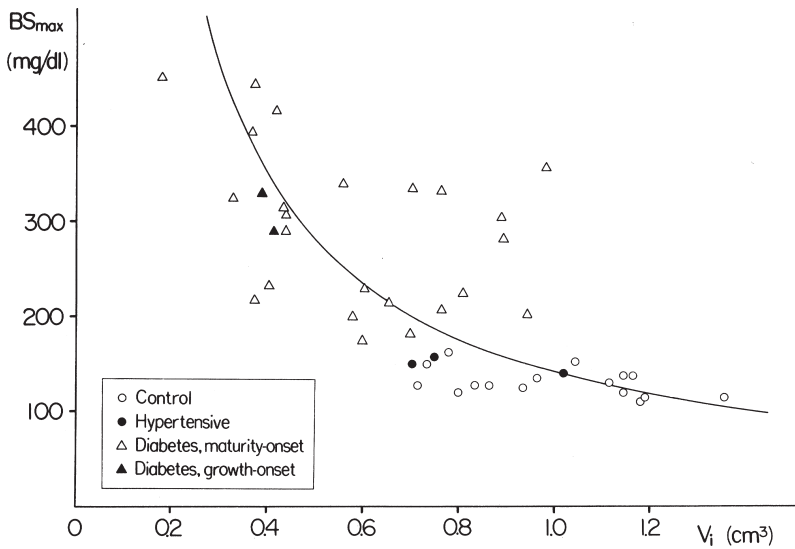


Fig. 2-10. The total islet volume  $V_i$  contained in the pancreas, correlated with the maximum blood sugar ( $BS_{max}$ ) during glucose tolerance test, which is elevated in diabetics. Reproduced from Saito, Takahashi *et al.* (1978): *Tohoku J Exp Med* 125: pp. 193.

hypertensive non-diabetics, while it becomes smaller in the order from the hypertensive non-diabetics to maturity-onset and to growth-onset diabetics. The difference in the mean between any pair of the groups proved significant on *t*-test. In Fig. 2-10,  $V_i$  is correlated with  $BS_{max}$ , the maximum blood sugar level during glucose tolerance test (GTT), where  $BS_{max}$  during GTT increases steadily with decreasing  $V_i$ . There is a significant correlation on semi-logarithmic coordinates, showing that, of the quantitative-morphological parameters of islets, the total islet volume may serve as the best marker of glucose tolerance.

### Extension to the extrainsular islet cells

An extension of this study was made by Kaiho *et al.* (1986). They extended the object of study so as to cover what had been called extrainsular islet cells, the endocrine cells dispersed in the pancreas as small clumps or even as a single cell. By this time, visualization of such minute endocrine organs had become easily practicable with the assist of immunohistochemistry. Normal pancreases obtained from three adults, taken surgically or at autopsy, were submitted to preparation of serial sections, which were immunostained for insulin. All the islets contained in a test volume (1.4 to 1.7 mm<sup>3</sup>) were sampled, including single cell islets, and the radius  $r$  was measured under microscope for each. It was found that the distribution of  $r$  was of a strongly skewed shape, with a majority of islets having an  $r$  near to the minimum. Based on the pattern of distribution curve that was monomodal in every examined case, it was concluded that the extra-insular islet cells, though discriminated from the typical (large) islets,

belong in reality to a population common to the latter. Also, the Weibull distribution was shown to sufficiently fit the histogram of islet radius, giving support for assuming this function which has a single peak. Small islets like single cells, while accounting for a majority in the number of islets, were demonstrated to account for only a very small percentage of islet volume. It was considered that the bulk of the endocrine functions of the pancreas is carried out by large islets, whereas the extra-islet cells are likely to be their precursors.

### c) Morphometry of metastatic tumor nodules in the liver

#### Livers with metastatic nodules: different appearance (Fig. 2-11)

Shown in the following is another example of granulometry: the quantitative treatment of metastatic tumor nodules dispersed in the liver.

Previously, it was thought that for a patient having carcinoma, for example in the large intestine, perfect cure by surgical means could hardly be expected if the patient was already confirmed to have metastasis in the liver. Recently, however, attempts are made with increasing frequency at surgical excision of the metastasis-containing part of the liver, if the part is considered removable and if a minimum life-sustaining volume of the liver can be left in a tumor-free state. In establishing a surgical strategy along this line, it would be of fundamental significance to know how many metastases a given liver can contain and at what density. Also this may be necessary in biological studies of cancer because it is often required to define, in strictly reproducible terms, to what degree a cancer is apt to generate hepatic metastasis. However, clinical imaging like CT allows to recognize only the presence of gross nodules, leaving the matter to

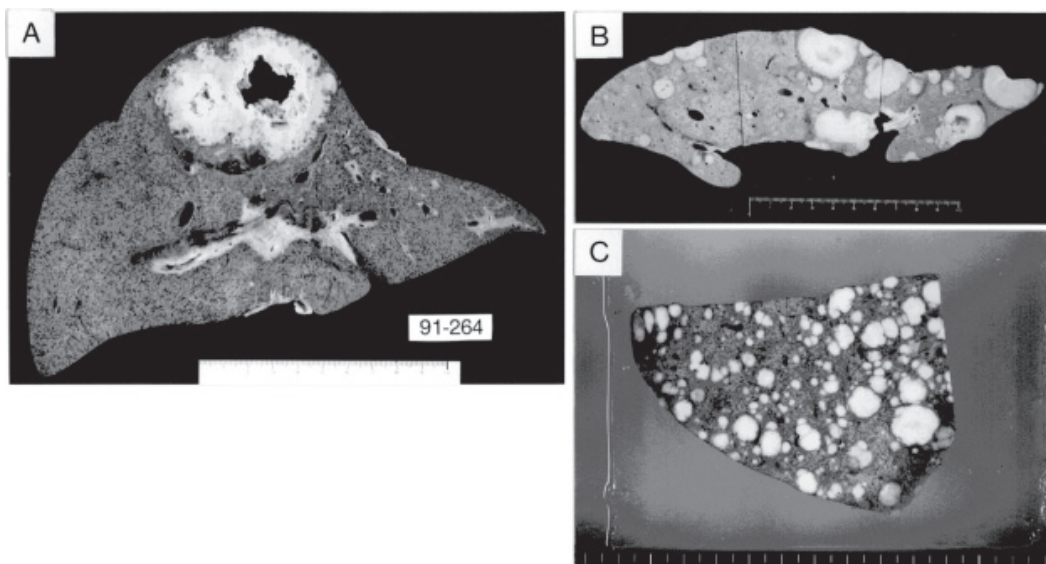


Fig. 2-11. Livers from three autopsy cases dying from carcinoma of the pancreas or large intestine. Metastatic nodules are dispersed in the livers but the size and dimension of nodules are various. Reproduced from Yamanami, Takahashi *et al.* (1999): *Anal Quant Cytol Histol* 21, pp. 220.

pathological studies. Yet, aside from a few attempts performed so far (Cameron *et al.*, 1988; Tabuchi *et al.*, 1991), we are still far from obtaining systematic knowledge about the quantitative-morphological aspect of hepatic metastasis. If one attempts to enumerate all the metastatic nodules contained in a liver, it will take him or her a great deal of time.

The metastases in this problem are hematogenous ones, presenting as nodular colonies of carcinoma cells delivered from the primary site to the liver via the portal blood flow. Usually they present as spherical nodules of varying dimension, dispersed in the liver uniformly but with varying density, as shown in Fig. 2-11. In the lower right (C), numerous small nodules are densely dispersed, whereas in the upper left (A), there seems to be only a large nodule having a central cavity. The upper right liver (B) presents an intermediate pattern. In geometric terms, the metastatic nodules appear more perfectly spherical than the pancreatic islets, making it seem much easier to apply the model of dispersed spheres. However, there is a problem: the dimension of nodules greatly varies, ranging from a fist-sized mass to clumps of small number of carcinoma cells not identifiable without using microscope.

### Circle diameter measurement (Fig. 2-12)

Recently an attempt was undertaken by Yamanami *et al.* (1999). This time, the study was designed to measure, instead of chord length, the diameter  $\delta$  of circular sections emerging in microscopic slides or macroscopic organ sections (Fig. 2-12). Gross nodules that were already identifiable with the naked eye were measured directly on liver slices, and small ones were subjected to micromorphometry.

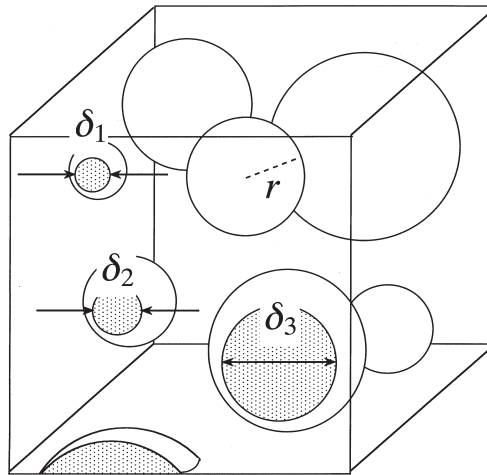


Fig. 2-12. Measurement of circle diameter  $\delta$  of metastatic nodules on liver section. Reproduced from Yamanami, Takahashi *et al.* (1999): *Anal Quant Cytol Histol* 21, pp. 218.

**Logarithmic normal distribution assumed for sphere radius (Figs. 2-13, 2-14)**

Here again, the radius  $r$  of spherical nodules was assumed to follow a distribution function, but in this study, logarithmic normal distribution was employed:

$$p(r) = \frac{1}{\sqrt{2\pi}mr} \cdot \exp\left[\frac{-(\ln r - \ln r_0)^2}{2m^2}\right]. \quad (2-5)$$

Figure 2-13 shows an example of logarithmic normal distribution having a skew pattern, with a peak positioned in a small range of  $r$ . The figure expresses the distribution in the form of  $p(r)$ , the probability function of  $r$ , which means

$$p(r) = N(r) / N_v.$$

For the detailed mathematical derivations, see the original article.

The assumption of logarithmic normal distribution for the radii of metastatic nodules was not based on a strict biological background but mainly on account of its mathematical relevance. As in Fig. 2-14, the conformity of this assumption was confirmed in a liver harboring a number of metastatic nodules by comparing the theoretically induced curve of  $p(r)$  with the result of actual measurement of nodular radii.

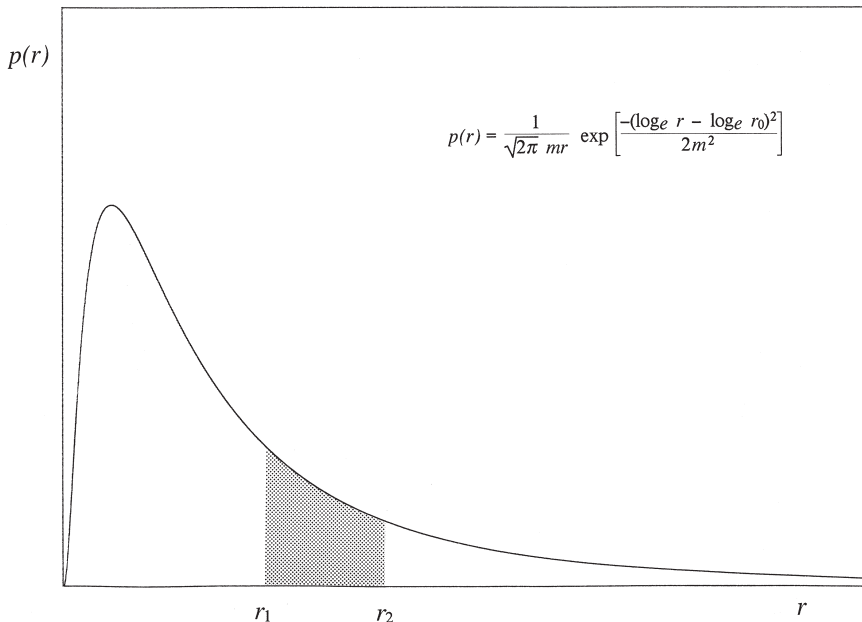


Fig. 2-13. Logarithmic normal distribution. The pattern of distribution resembles Weibull and gamma distributions.

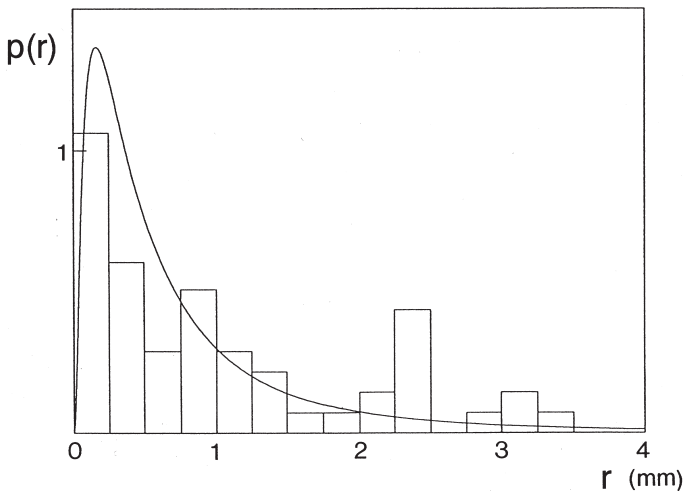


Fig. 2-14. The radial histogram of metastatic nodules directly determined on serial sections of an autopsy liver, shown together with the curve of  $p(r)$  theoretically induced. Sufficient agreement of  $p(r)$  with the histogram justifies to assume logarithmic normal distribution for  $p(r)$ . Reproduced from Yamanami, Takahashi *et al.* (1999): *Anal Quant Cytol Histol* 21, pp. 222.

Here, in sampling the nodules, we relied upon the disector method, a design-based technique of granulometry introduced by Gundersen *et al.* (1984). One can see the theoretical curve sufficiently approximating the result of measurement, justifying to assume logarithmic normal distribution for  $p(r)$ .

### Measurement data of hepatic metastases (Table 2-1)

The basic material of this study was autopsy livers from a total of 31 patients, in all of whom the liver had metastases of carcinoma. Apart from a patient in whom the tumor originated from the lung, in all the cases the primary carcinoma arose in organs drained by the portal system: the stomach, large intestine and pancreas. Listed in Table 2-1 is the result of estimation. The most remarkable finding in this table is that there is a great variance in  $N$ , the total number of metastatic nodules contained in the liver. Even in Case 1 in which the total number was estimated to be the minimum of the 31 cases,  $N$  was shown to be as large as 10. For surgical oncologists who are pushing forward aggressive treatments for hepatic metastasis, this may be a disappointing result. However, it should be kept in mind that what we obtained was from autopsies. The result would not be the same if investigation were made on patients who were alive and, from a general status point of view, eligible for partial hepatectomy. The largest estimate of  $N$  is found in Case 31 of pulmonary carcinoma where the number was shown exceeding 300,000. Between these extremes, there are a series of different estimates ranging almost continuously.

Table 2-1. The cases examined and the results of morphometry for the metastatic nodules in the liver.  $N_V$ : the number of nodules in a unit volume ( $/\text{cm}^3$ ).  $N$ : the estimate for the total number of nodules contained in the liver. Reproduced from Yamanami, Takahashi *et al.* (1999): *Anal Quant Cytol Histo* 21: pp. 220.

Case No.	Primary site	mean $r$ (mm)	$N_V$ ( $/\text{cm}^3$ )	Liver weight (g)	$N$
1	Colon	12.39	0.01	1,450	10
2	Stomach	9.54	0.02	780	13
3	Pancreas	4.56	0.08	980	80
4	Pancreas	5.51	0.08	1,600	136
5	Rectum	4.36	0.03	4,110	139
6	Pancreas	5.22	0.08	1,980	154
7	Pancreas	0.76	0.41	960	389
8	Stomach	2.12	0.19	2,500	470
9	Stomach	0.50	0.66	830	549
10	Stomach	2.36	0.51	1,600	820
11	Pancreas	2.24	0.26	3,230	834
12	Pancreas	1.91	1.22	1,120	1,369
13	Colon	1.61	1.08	1,390	1,502
14	Pancreas	0.73	2.38	1,230	2,921
15	Pancreas	0.62	4.72	760	3,586
16	Pancreas	0.84	2.26	1,900	4,285
17	Gallbladder	0.57	4.13	1,300	5,364
18	Pancreas	0.85	5.25	1,300	6,826
19	Pancreas	0.56	6.18	1,130	6,986
20	Stomach	0.55	3.48	2,160	7,512
21	Stomach	0.83	6.70	1,150	7,708
22	Biliary tract	0.83	8.24	1,300	10,713
23	Colon	0.62	4.16	4,450	18,494
24	Pancreas	0.52	13.9	1,690	23,423
25	Pancreas	0.52	16.3	1,950	31,824
26	Pancreas	0.51	18.1	2,042	37,006
27	Pancreas	0.21	32.0	1,220	39,089
28	Colon	0.32	36.5	3,490	127,490
29	Stomach	0.21	91.6	1,400	128,170
30	Stomach	0.49	61.8	2,810	173,546
31	Lung	0.36	156.0	2,100	326,970

### Correlation between $N$ and mean radius (Fig. 2-15)

In Fig. 2-15, the total number  $N$  of metastases in the liver is correlated with the mean radius of nodules. A negative correlation is apparent, showing that the larger the mean radius of nodules, the smaller their total number. This correlation seems worthy of special attention. It demonstrates that when in a patient, a metastatic nodule of

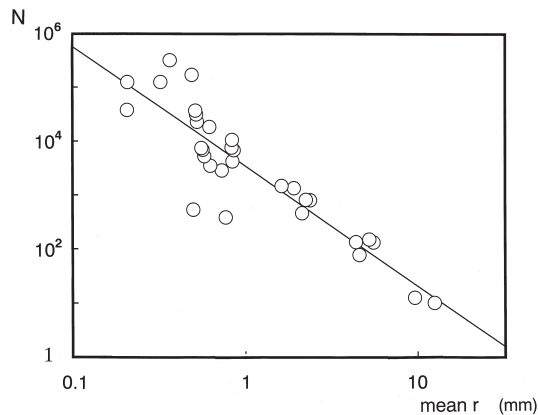


Fig. 2-15. The total number  $N$  of metastatic nodules in a liver is correlated with the mean nodular radius, plotted on bilogarithmic coordinates. Note quite a significant negative correlation. Reproduced from Yamanami, Takahashi *et al.* (1999): *Anal Quant Cytol Histol* 21, pp. 221.

extraordinary dimension was visualized in the liver, there is little need to worry about the possibility that in their surroundings, smaller nodules may abound and escape detection at computerized tomography (CT) or other clinical imaging. This will be a good news for those looking forward to seeing a successful treatment for metastatic liver tumors.

#### d) Alveolar surface area of normal and emphysematous lungs

##### Normal and emphysematous lungs (Figs. 2-16, 2-17, 2-18, 2-19)

Shown in Fig. 2-16 is a section of normal lung and in Fig. 2-17, that of another lung with advanced emphysema. In the former, the section looks finely spongy, reflecting its structure consisting of a huge number of alveolar air spaces that are separated by thin membranous septa. Instead, in the latter, the lung consists of cavernous spaces of varying size, while normal spongy tissue is left among the spaces only as rudimentary remains.

The difference in the structure between the normal and emphysematous lungs is more clearly visible in their microscopic pictures. As in Fig. 2-18, the normal lung consists of a large number of alveoli, minute air spaces of about 200  $\mu\text{m}$  in diameter, each opening into an alveolar duct. A pair of neighboring alveoli are separated with an interalveolar septum that is about 12  $\mu\text{m}$  thick and contains a dense network of capillaries. Figure 2-19 is from an emphysematous lung. Although the figure presents an early stage of emphysematous changes, the alveolar clusters found in the normal lung are lost and replaced by irregular air spaces that are much larger than the ordinary alveoli. The development of emphysema from a normal lung can be attributed to destruction of alveolar septa due to various noxious agents, particularly long-term smoking. After having been exposed to such agents, the alveolar septa are injured, torn and destroyed, giving rise to the creation of cavity-like common spaces.



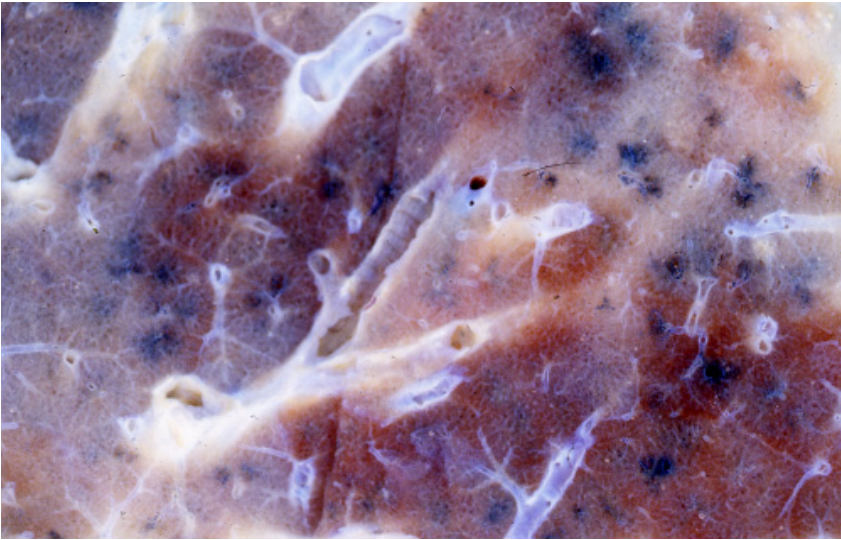


Fig. 2-16. A close-up sectional appearance of normal human lung. The alveolar tissue looks like a sponge, where the individual alveoli are beyond confirmation by naked eyes.

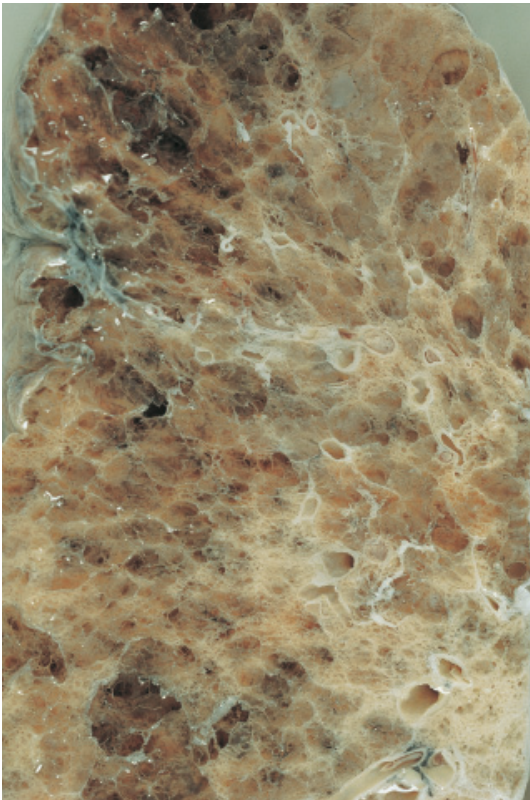


Fig. 2-17. A close-up sectional appearance of lung with advanced emphysema from a patient dying of respiratory failure. Compare with the normal lung of Fig. 2-16. The lung contains grossly cavernous spaces, with the finely spongy alveolar tissue of the normal lung remaining only rudimentarily between the cavities.



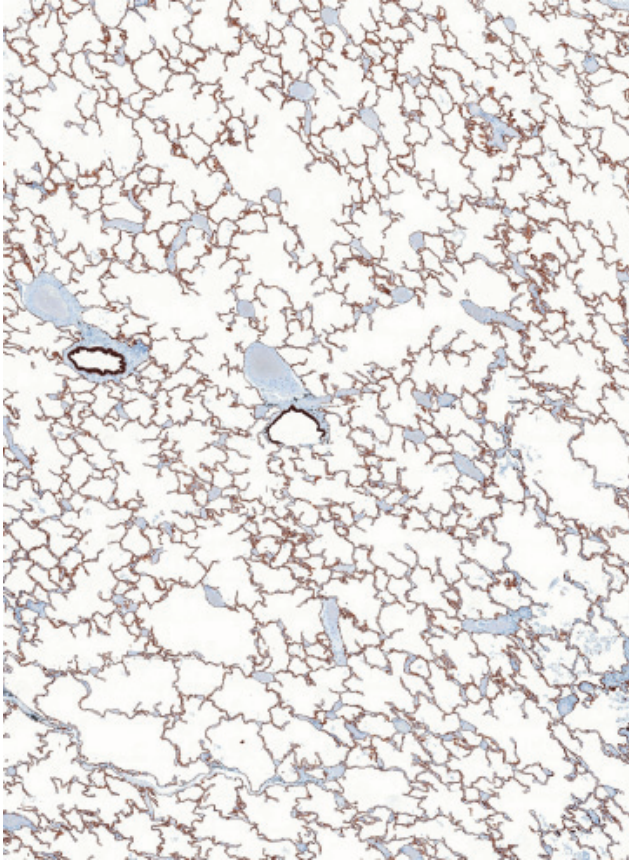


Fig. 2-18. A low power microphotograph of normal lung. The tissue comprises a vast number of alveoli, each about 0.2 mm in diameter. Immunostain for cytokeratin (pan).

A patient having emphysema more or less suffers from respiratory distress, and this primarily is due to the loss of significant part of alveolar septa contained in the lung. Since the septa contain a fine meshwork of elastic fibers, the advancement of emphysematous changes implies that the elasticity retained by the normal lung has been reduced, making it difficult for the lung to shrink during expiration. It also happens that in such lungs, airways more or less have difficulties in keeping themselves open during expiration. This is because of the reduced density and loss of alveolar septa. While in a normal lung, several septa are attached to the wall of an airway, pulling it outward with “recoil pressure,” in emphysema the decrease or loss of recoil makes an airway quite vulnerable to collapse and obstruction during expiration, when the pressure around the airway can exceed the internal pressure. On the other hand, the surface of the septa is the place where gas exchange takes place between the alveolar air and the blood flowing through the capillaries running in the septa. Thus, from a structure-function correlation point of view, it seems quite significant to estimate the

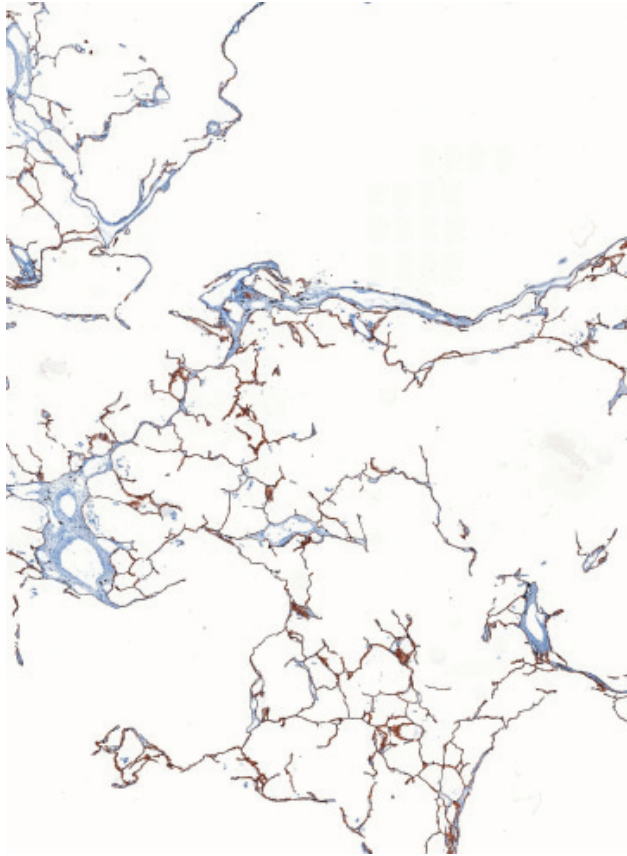


Fig. 2-19. A low power microphotograph of lung in an early stage of emphysema. Note the markedly reduced density of alveolar septa. Immunostain for cytokeratin (pan).

total surface area of septa in the normal lung and its changes in emphysema.

### Line sampling of alveolar septa (Fig. 2-20)

Figure 2-20 is a schema showing the stereological method to estimate the total surface area of membranous structure like the alveolar septa. The figure presents a microscopic picture of alveolar tissue, and here we suppose that a sampling line (S.L.) was randomly drawn. The line will come to intersect many alveolar septa, but here we define the intersection as the crossing of the line with the basement membrane of alveolar epithelia (confirm that there are eight intersections). This is because a patch of alveolar septum has two sides, each serving as a surface through which diffusion of gas takes place. Therefore, when the line comes to penetrate a septum, two intersections usually occur. Now, we assume that as a result of measurement,  $N$  intersections were generated along a line of sufficient length  $L$ . Then, we can calculate  $N_L = N/L$ , which gives the number of intersections arising over a unit length of the line; in terms

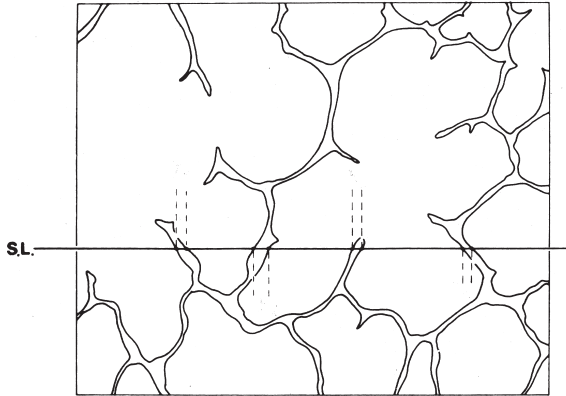


Fig. 2-20. A schema illustrating the line sampling of alveolar septa to estimate the surface area density ( $S_V$ ). A sampling line (S.L.) is randomly overlaid on a microscopic section of lung, and the number of intersections of the line with epithelial basement membrane is counted. In the figure, eight intersections are confirmable. The number of intersections per a unit length of line ( $N_L$ : the numerical density along a line) is calculated, and  $S_V$  is estimated by  $S_V = 2 N_L$ . Reproduced from Takahashi *et al.* (1994): Human Pathol 25, pp. 704.

of stereology,  $N_L$  is expressed as the numerical density of points along a line. Now, if the surface area of septa in a unit volume of lung tissue is  $S_V$ , we can obtain its estimate by the equation

$$S_V = 2 N_L . \quad (2-6)$$

This is one of the basic principles of stereology, and  $S_V$  is called the surface area density. Its mathematical derivation can be shown in various ways but one may be recommended to refer to the explanation given by Hennig (1956) or Weibel (1962, 1963). There is a restriction placed on the application of this formula. It can work only when the membranous structures one is going to measure are distributed sufficiently randomly in the space with regard to their orientation, a requirement that appears to be well satisfied for the alveolar septa of lung.

Note that  $S_V$  obtained as above is the surface area density and not the total area contained in the lungs. The total area  $S_{\text{total}}$  contained in the lungs is given by multiplying  $S_V$  by the volume of both lungs combined.

### **$S_V$ of alveolar septa: normal and emphysema (Fig. 2-21)**

Figure 2-21 exhibits  $S_V$  estimated by Suwa and associates in 1966 in lungs from 50 autopsy cases (the present author was not collaborating). The figure includes data from 35 non-emphysematous subjects, where one can see that apparently,  $S_V$  decreases with age. The fall of  $S_V$  during the postnatal growth may be understood as expressing the enlargement of the lung. However, the value keeps lowering even after the subjects have come of age, falling at 80 years to a level as low as half that of the young adult. In patients having emphysema,  $S_V$  is shown to have significantly been reduced

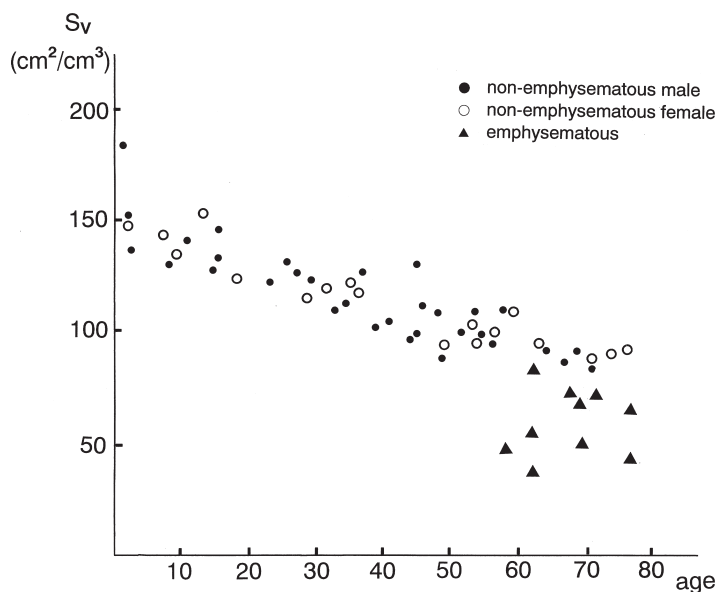


Fig. 2-21. The surface area density  $S_V$  of alveolar septa in autopsy lungs from 50 patients, including 15 with emphysema. Note that  $S_V$  linearly falls with age even in non-emphysematous subjects.  $S_V$  is significantly reduced in emphysematous lungs.

compared with the non-emphysematous subjects. It seems that even in the absence of emphysema, the lung undergoes slow but continuous loss of alveolar septa, coming to be in a slightly emphysematous state in advanced ages.

### e) Remodeling of alveolar structure in paraquat lung

#### Fibrosis in advanced paraquat lung (Figs. 2-22, 2-23)

To be presented next are examples of analysis where a simplified geometric model is introduced to assimilate the microstructure and describe its changes in quantitative terms. The first example deals with fibrosis of lung in patients intoxicated by paraquat, where estimation of  $S_V$  is combined with that of  $V_V$ . The earliest lesions, produced experimentally by giving paraquat to hamsters were shown above (Figs. 2-1 and 2-2). As described there, patients intoxicated with paraquat suffer from severe respiratory distress that emerges on Day 4 or 5 and deteriorates thereafter.

Figure 2-22 presents the macroscopic picture of lung from a patient of paraquat intoxication who died of respiratory failure, presenting lung fibrosis in the terminal stage. Figure 2-23 is from another case, and here, the spongy tissue of ordinary lung (shown in Figs. 2-16 and 2-18) is replaced with a dense mass of collagen (green), sparsely penetrated by alveolar ducts that remain and are more or less dilated. Usually, the lung lesions reach this stage about one month after ingestion, and by the time the

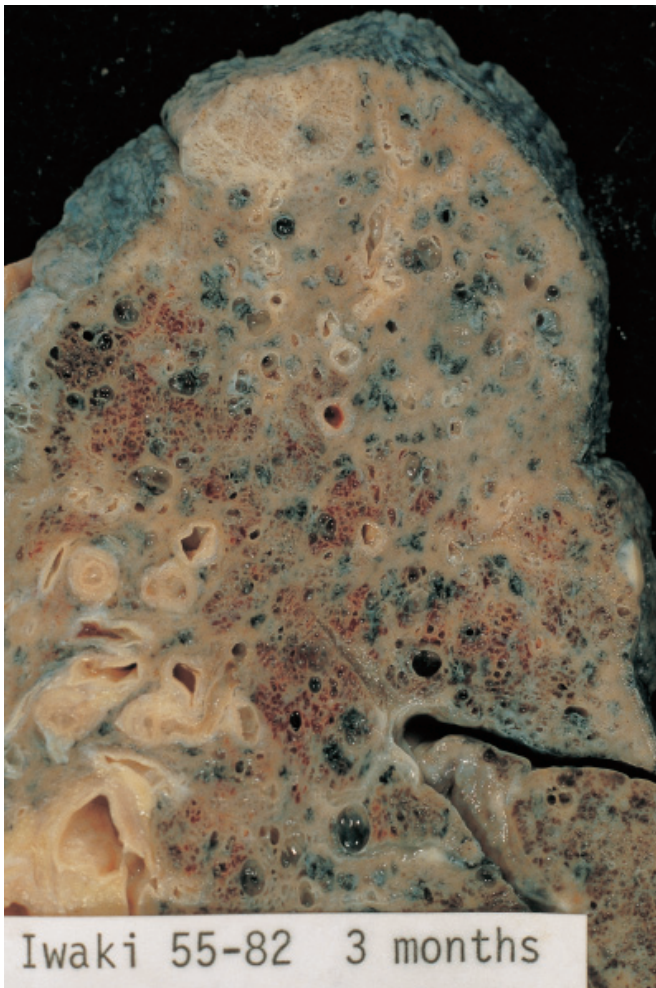


Fig. 2-22. The sectional appearance of lung from a patient of paraquat intoxication dying three months after ingestion. Diffuse induration of the organ resulting from advanced fibrosis.

intoxicated patient usually succumbs to respiratory failure. To study how the changes of lung begin, develop and culminate in this state, morphometric analysis was undertaken of autopsy lungs from 15 patients dying of paraquat intoxication (Takahashi *et al.*, 1994; Takahashi, 1994). The period from paraquat ingestion until death was varying, ranging from 12 hours to 40 days. The analysis helps understand how, from a microstructure point of view, paraquat-associated lung injuries begin and advance toward the terminal stage of pulmonary fibrosis, where the alveolar structure has been severely remodeled.



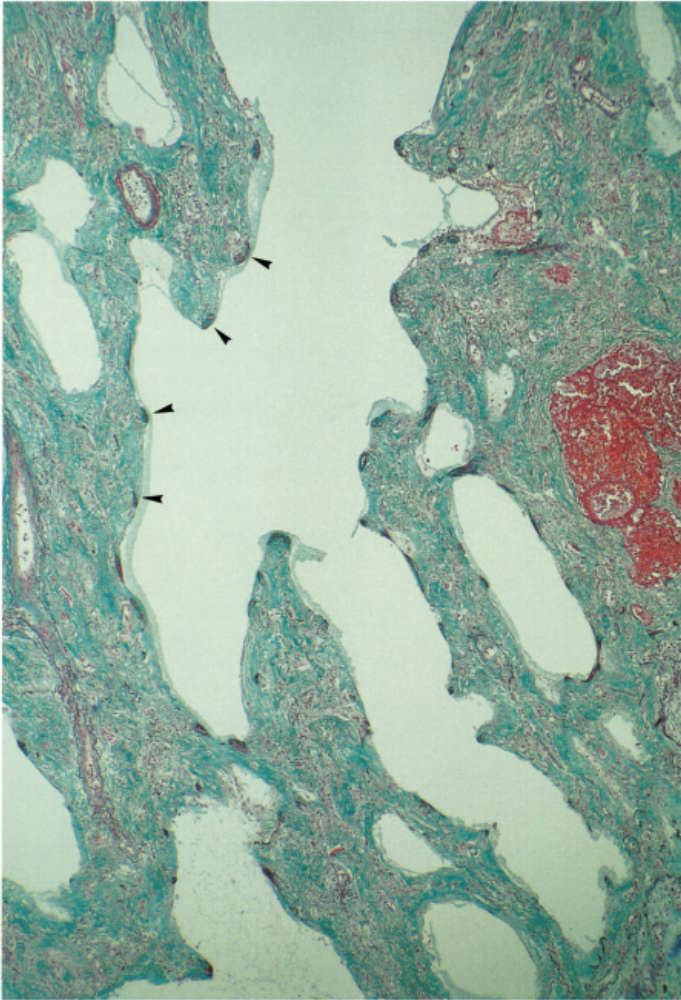


Fig. 2-23. Microscopic appearance of paraquat lung in an advanced stage. The normally spongy lung tissue (see Fig. 2-18) is replaced by dense masses of collagen (green). There are remains of branching air spaces that correspond to alveolar ducts. Visible along the spaces are black dots, and these are the entrance rings of alveoli (arrowheads). Elastica-Goldner stain.

#### **Deposition of matrix layer on alveolar septa in early paraquat lung (Figs. 2-24, 2-25)**

Shown in Figs. 2-24 and 2-25 is the lung of a patient dying on Day 13 of intoxication. In Fig. 2-24, although one can find alveoli still retaining their septa (blue), there are mesenchymal cells vigorously proliferating on the septal surface and beginning to produce collagen in the surroundings. Attention is to be paid to the finding that there is a jelly matrix layer, stained faintly in violet and possibly containing proteoglycans, extending on the surface of the septa.

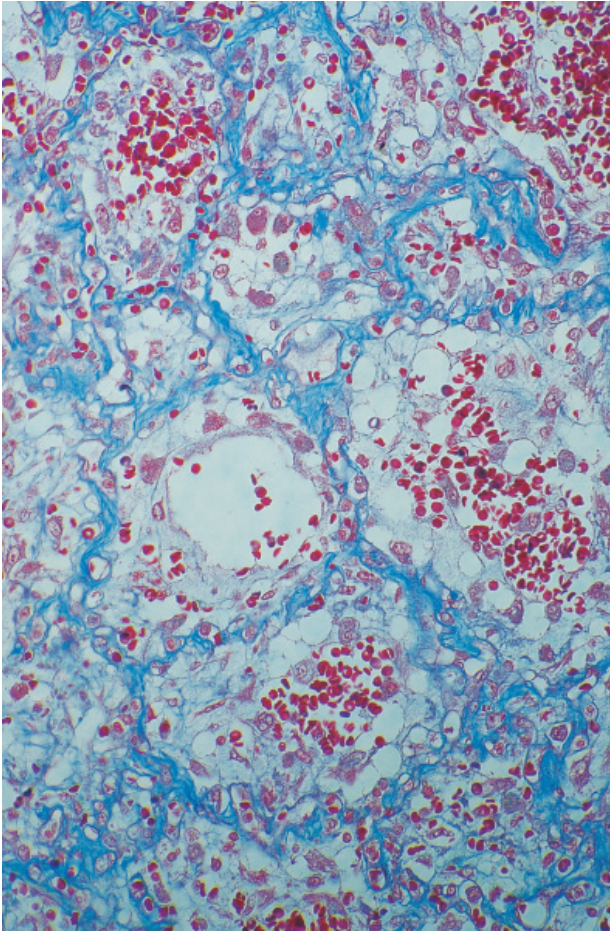


Fig. 2-24. Microscopic appearance of lung from a patient of paraquat intoxication dying on the 13th day. There are several alveoli in the picture, all containing matrix substance (stained homogeneously faint blue) in which mesenchymal cells are proliferating. Azan-Mallory stain.

In Fig. 2-25, where the contours of matrix layer are illustrated in a collateral sketch, it seems that the layer is deposited on the surface of alveolar septa at a certain thickness, narrowing the air spaces correspondingly. It is in this matrix that the mesenchymal cells are proliferating and beginning to secrete collagen. From a lung function viewpoint it may be conceivable that the matrix layer, interposed between the intra-alveolar air and the blood flowing in the capillaries embedded in the septa, acts as a barrier to diffusion of  $O_2$  as well as  $CO_2$ . Also the matrix, mucous in itself and diffusely stuck to the alveolar surface, may significantly impair the ventilation function of lung by restricting the elasticity of normally thin, membranous septa. Thus the septa, if the overlying matrix layer is included, are likely to increasingly thicken with the advancement of lung disease, and this mainly accounts for the progressive impedi



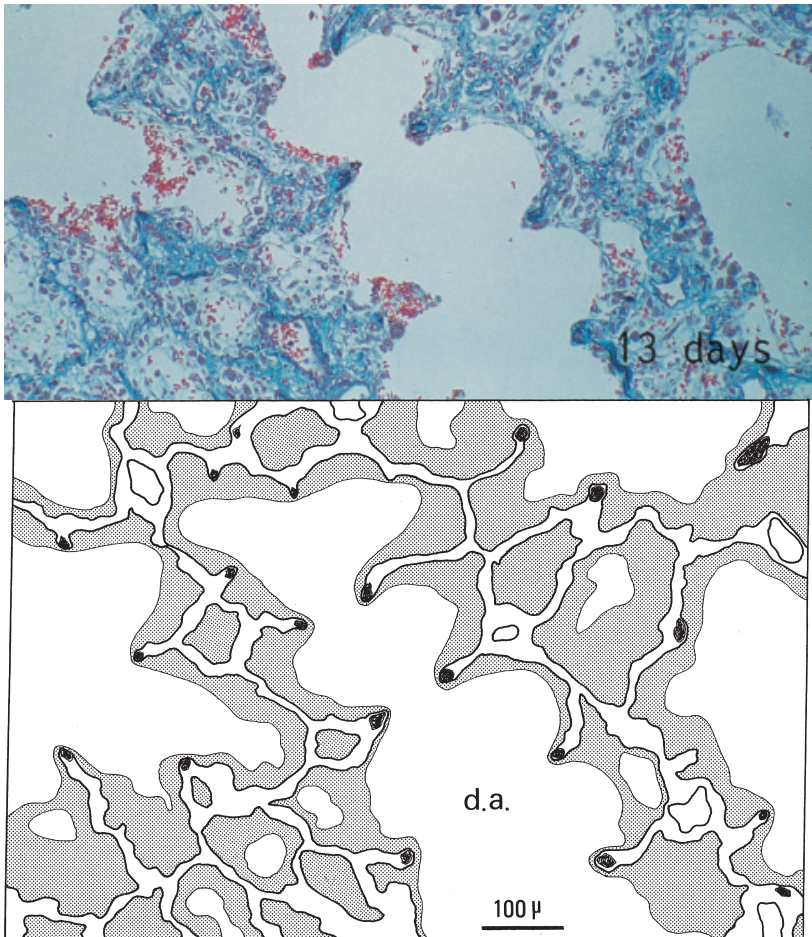


Fig. 2-25. The alveolar septa, the matrix layer deposited upon the septa and the remaining air spaces in the above lung, as illustrated below. Reproduced from Takahashi *et al.* (1994): *Human Pathol* 25, pp. 703.

ment of lung function. Finally, the lung reaches the state of Fig. 2-23, where all the alveolar air spaces have been lost and replaced with mass of collagen deposited in the gelatinous matrix. Thus, the mean thickness of septa including the matrix, if quantified, is considered to serve as an index for the advancement of paraquat-induced lung disease. Here, the problem is how to define the mean thickness of septa, which apparently is a 3-D quantity.

#### **The plate model for the determination of septal thickness (Fig. 2-26)**

Figure 2-26 schematizes a geometric model which was introduced to define the thickness of membranes or plates randomly dispersed in the space. Suppose, as in the figure, a cubic lung tissue contains a sufficiently large number of alveoli. For the sake

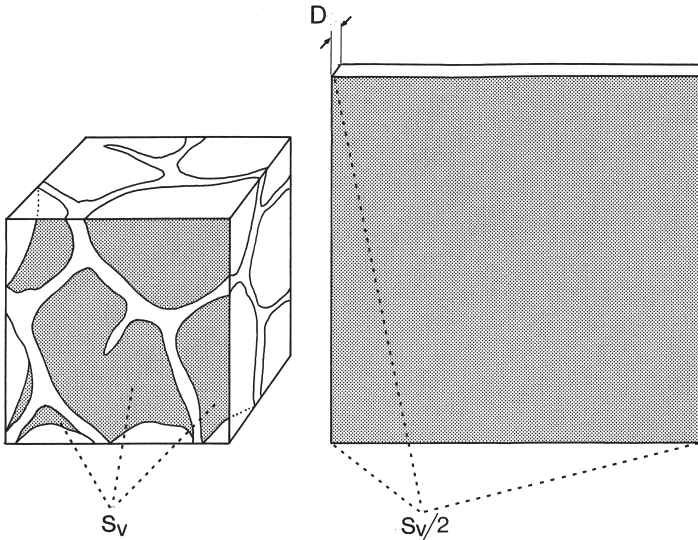


Fig. 2-26. The plate model for the determination of mean septal thickness. Suppose that we estimate stereologically, in a unit volume of cubic lung tissue, the volume  $V_V$  and the surface area  $S_V$  of alveolar septa contained. Next suppose that we transform the septa into a plate of uniform thickness, with  $V_V$  in volume and  $S_V$  in surface area. Then the thickness  $D$  of this plate gives the mean thickness of septa. Reproduced from Takahashi *et al.* (1994): *Human Pathol* 25, pp. 704.

of simplicity, we assume that the edges of the cube are of unit length. Then we perform measurement on one of its 2-D sections, in this figure on the frontal one. We make on this section line sampling and obtain  $S_V$ , the alveolar surface area contained in a unit volume. At the same time, “chord length measurement” of septa is performed, and we obtain  $V_V$ , the volume of alveolar septa in a unit volume. Now suppose that we transform the entire septa contained in the cube into a plate of uniform thickness as in the right half of the figure. Consider that this plate is made so as to be of uniform thickness  $D$ , with its volume equal to  $V_V$  and with its surface area, with the two faces put together, equal to  $S_V$ , namely,

$$D S_V/2 = V_V.$$

Then we find in the thickness  $D$  a quantity that exactly corresponds to the mean thickness of septa in a 3-dimensional sense. This is a method of analysis we express as the plate model.

### Increasing thickness of septa after paraquat ingestion (Fig. 2-27)

The result of morphometry is shown in Fig. 2-27. Here  $D$ , the mean thickness of septa, is plotted in the ordinate, and the days after paraquat ingestion in the abscissa. In the early stage of intoxication  $D$  remains about 12  $\mu\text{m}$ , a value not significantly different from the alveolar thickness in normal lungs. One can see that  $D$  begins to rise on about the 7th day. It accelerates to thicken thereafter, following a course which is

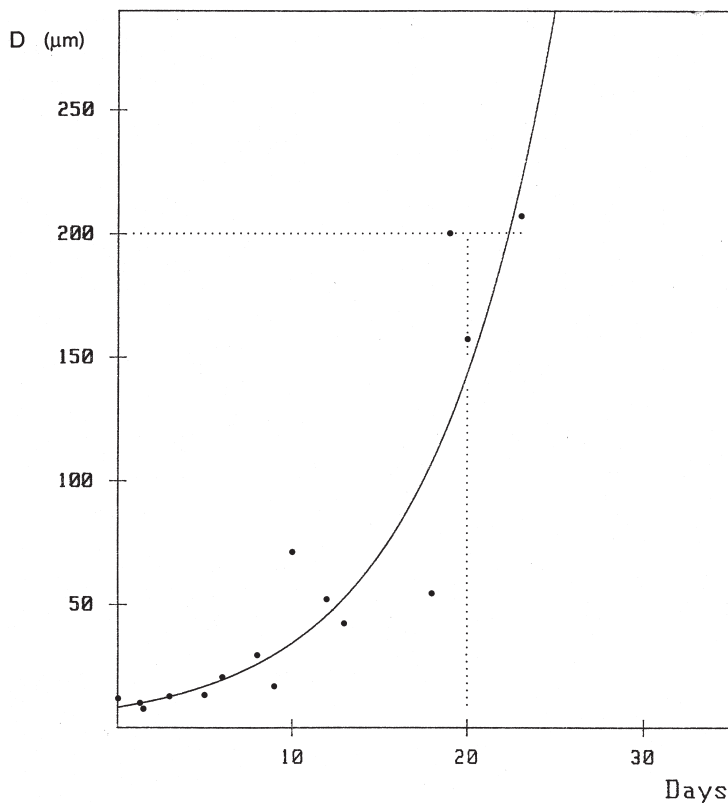


Fig. 2-27.  $D$ , the mean thickness of alveolar septa, is presented against the days after paraquat ingestion. The elevation of  $D$  with days is assimilated with an exponential function.  $D$  reaches 0.2 mm about three weeks after ingestion, showing that by this time, the alveoli have totally been obliterated. Reproduced from Takahashi *et al.* (1994): *Human Pathol* 25, pp. 705.

approximately exponential, as shown by the curve. Note that  $D$  attains a level of 200  $\mu\text{m}$  twenty days after taking paraquat.

Weibel (1963), in his extensive morphometric studies of lung, estimated the mean depth of a single alveolus at about 200  $\mu\text{m}$ ; he gave about the same estimate for the mean diameter of its opening to the alveolar duct. According to this, one may interpret the above result as suggesting that by about 3 weeks after ingestion of paraquat, the septa have become so thick as to completely obstruct the alveolar air spaces. That this really is the case is demonstrated in the lung changes in Fig. 2-23. The lung, from a subject dying on Day 23, presents the alveolar tissue in a state of advanced remodeling. What is found here is severe fibrosis of lung; the alveolar tissue has changed into a mass of dense collagen (stained in green) penetrated by branching duct-like spaces. That these spaces are remains of alveolar ducts is witnessed by the black dots delimiting the spaces: the entrance rings of alveoli (pointed by arrowheads). The rings are mass of elastic fibers encircling the opening of alveoli to the alveolar ducts, reinforc-

ing the alveolar structure. Tracing the rings in the picture, it may be understood that indeed by about 3 weeks of intoxication, the remodeling has finished, with the alveolar air spaces completely obliterated with collagen.

It may be pertinent to give a brief comment on the exponential character of disease advancement shown by the rising  $D$ . It reflects that with time, the lung disease progresses in a divergent fashion. This may be interpreted as meaning that we are dealing with a phenomenon, in which remission cannot be expected to occur, since there is no room for the curve to reach a plateau, or a state of equilibrium. This may be an essential difference from a phenomenon in which adaptation can be expected to take place, an example of which has been presented in the medial hypertrophy of arteries in hypertensive subjects.

#### **f) Changes of bone trabeculae in osteoporosis — a cylindrical model**

##### **Spongy bone: normal and with osteoporosis (Figs. 2-28, 2-29)**

Osteoporosis is a disease debilitating many senile persons who are liable to fracture due to age-related fragility of bones. Figure 2-28 demonstrates a microscopic

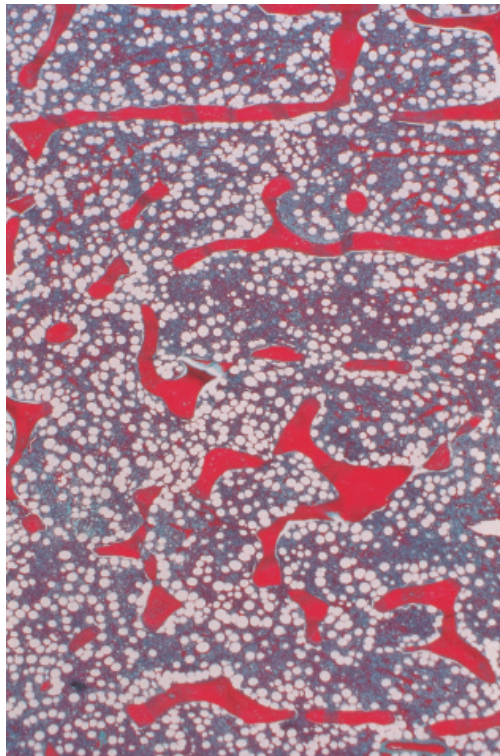


Fig. 2-28. Low power microphotograph of normal spongy bone taken from the body of lumbar vertebra. Bone trabeculae, the beam of framework, are shown retaining a certain thickness and arranged at a certain density. Extending around the trabeculae is bone marrow. Elastic-Goldner stain.



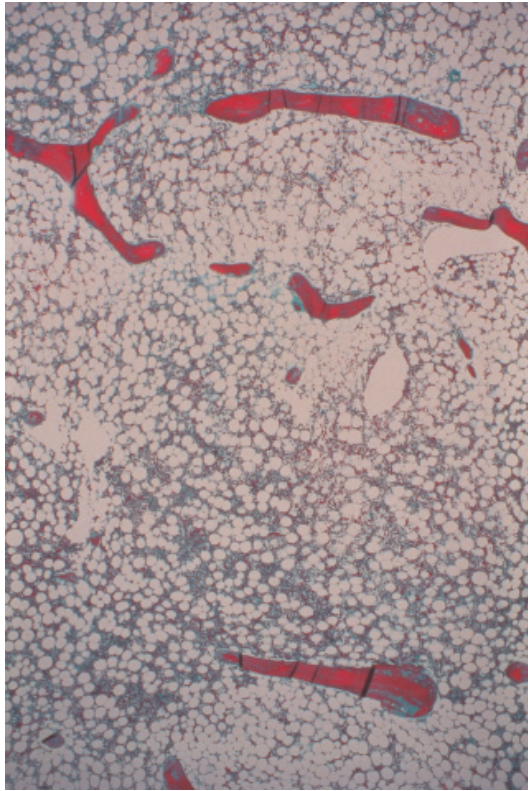


Fig. 2-29. Low power microphotograph of vertebral body with osteoporosis. Note that the density of trabeculae as well as their thickness appear significantly lower than the normal bone shown in Fig. 2-28.

picture of normal spongy bone, the body of lumbar vertebra taken from a young adult male, and Fig. 2-29 that from an aged female with osteoporosis. While the non-osteoporotic bone contains sturdy bony trabeculae forming a dense 3-D network, the trabeculae in the bone of the aged seem thinner and sparsely arranged. On this difference, it seems quite understandable that in the latter, fracture occurs frequently and at a slight mechanical load. However, ambiguities still remain about the morphogenesis along which the structural bone changes advance toward the state of severe osteoporosis. Is osteoporosis simply reflecting a symmetric thinning of trabeculae, or, do some topological changes occur in the trabecular network itself? At least in some aspects, this is a problem which may require studies by 3-D morphometry. The following is a summary of recent attempt made by Sugawara *et al.* (2003).

### **Trabecular bone mass: changes with aging (Fig. 2-30)**

The volume density  $V_V$  of bony trabeculae was estimated by point counting on silver-impregnated sections of spongy bone. The material was the bodies of lumbar vertebrae (L3 or L4) taken from a series of 56 autopsy patients, with the age ranging

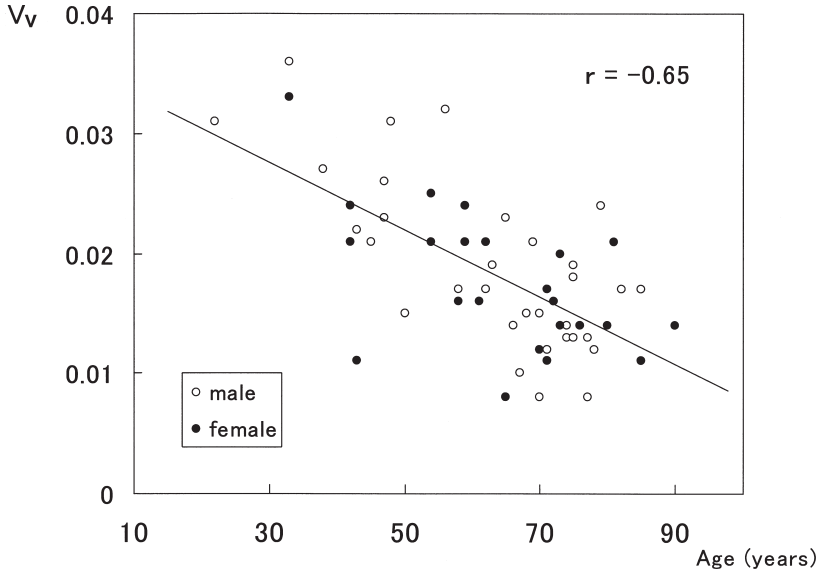


Fig. 2-30.  $V_V$ , the volume density of trabeculae estimated by point counting on microscopic sections of lumbar vertebral bodies from 55 autopsy cases. Apparently the density tends to fall with aging.

from 21 to 90 years. As shown in Fig. 2-30, the volume density of trabeculae decreases with age, clearly demonstrating the progress of osteoporosis. There are studies reporting data like this (Beck *et al.*, 1960; Hedlung *et al.*, 1988), but a problem still remains: whether symmetric thinning of individual trabeculae, or loss of trabecular segments, or both, is responsible for this age-dependent reduction of bone mass?

### The cylindrical model for the determination of trabecular radius and length (Fig. 2-31)

In order to obtain estimates on the mean thickness and the length of trabeculae in a unit volume, we introduced a geometric model, in which the structure of spongy bone was assimilated to a network made of cylindrical trabeculae, as in the schema of Fig. 2-31.  $S_V$ , the surface area of trabeculae in a unit volume, is easily obtained by the microscopic line sampling.  $V_V$ , measured by point counting, is already at hand. Here let us assume that the whole trabeculae in a unit volume of spongy bone were joined to form an elongated trabecula which is cylindrical in shape,  $L$  in the total length and with a uniform radius  $R$ . We assume that the volume of the cylinder is equal to  $V_V$  and its lateral surface area is  $S_V$ . In this setting,  $L$  corresponds to the total length of trabeculae contained in a unit volume, and therefore is to be renamed as the length density  $L_V$ , according to the systematized wording employed in stereology (Weibel, 1979). Then

$$\pi R^2 L_V = V_V \quad \text{and}$$

$$2\pi R L_V = S_V.$$

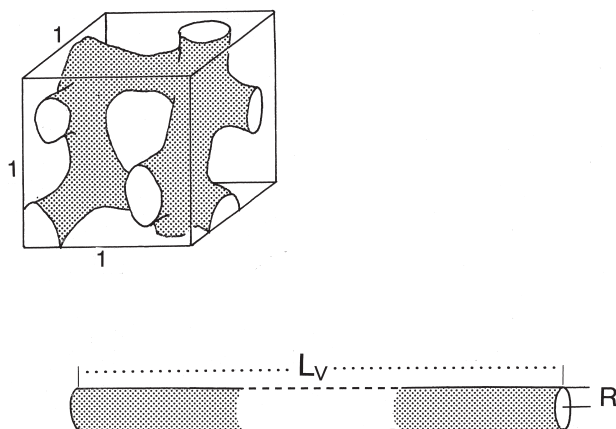


Fig. 2-31. The cylindrical model for geometric treatment of bone trabeculae. Suppose that the trabeculae in a unit volume of spongy bone are transformed into a cylinder of uniform radius  $R$ , during which process,  $V_V$  and  $S_V$  of trabeculae are kept unchanged.

By solving these, we obtain

$$R = 2V_V/S_V \quad \text{and}$$

$$L_V = S_V^2/4\pi V_V.$$

### The changes of trabecular radius and length density with age (Figs. 2-32, 2-33)

Microscopic sections of bone used above in the estimation of  $V_V$  by point counting were submitted to line sampling to estimate  $S_V$ , and the parameters  $L_V$  and  $R$  were calculated from  $V_V$  and  $S_V$ . In Fig. 2-32 the estimates of  $R$ , the mean trabecular radius, were plotted against the age of the patients on semilogarithmic coordinates. There seems to be a slight decreasing tendency with the age, but no significant correlation proved to exist. Thus, we were unable to demonstrate an age-related thinning of trabeculae in unambiguous quantitative terms.

On the other hand,  $L_V$ , the total length of trabeculae in a unit volume, clearly decreases with age as in Fig. 2-33. On semi-logarithmic coordinates, the correlation coefficient is  $-0.43$  which is significant at  $p = 0.01$ . With these results of morphometry, the age-related decrease of trabecular mass appears to be associated not so much with thinning of individual trabeculae as with loss of trabecular segments. The process creating this change may be understood as follows. Trabeculae keep bearing an excessive mechanical load, either tension or compression, for a long time. Finally microfracture occurs at some of the trabeculae. The trabeculae disconnected by microfracture, no longer bearing any mechanical load, get atrophied and disappear within a short time. Possibly, trabecular segments are involved in this process one after another, making the whole network of spongy bone increasingly rarefied, creat-



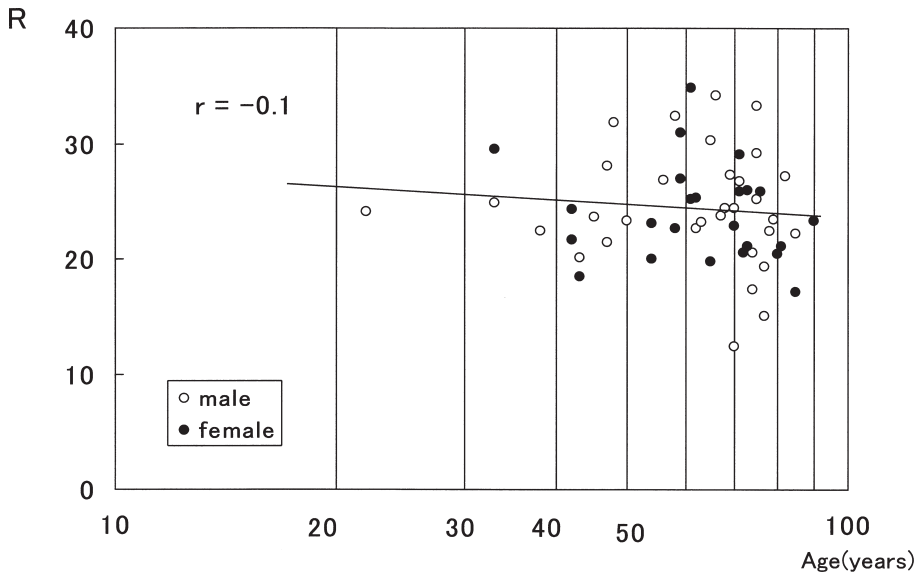


Fig. 2-32. The mean trabecular radius  $R$  estimated on 55 patients is shown against the age on hemi-logarithmic coordinates. No significant age-associated changes of  $R$ .

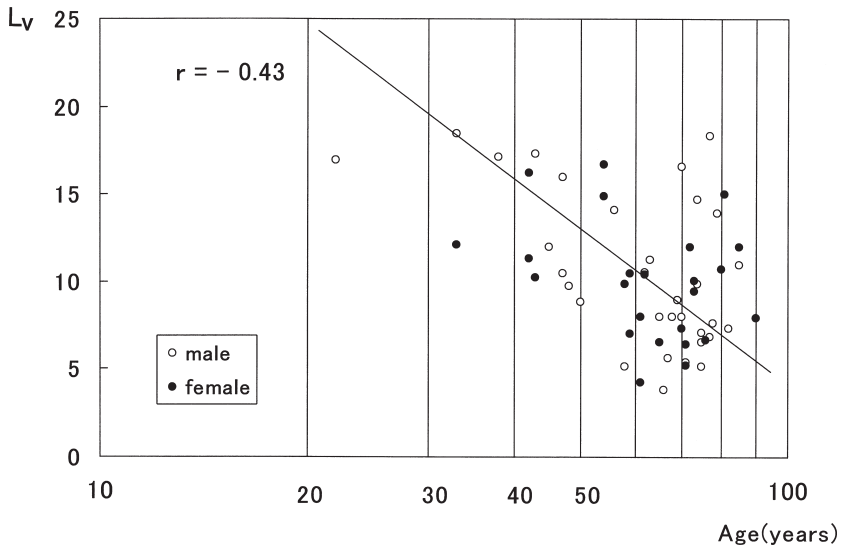


Fig. 2-33.  $L_V$ , the length density of trabeculae, against the age. There is a significant negative correlation of  $L_V$  with age, showing the progression of age-dependent loss of trabeculae.

ing the state of osteoporosis. Once this process is started, a bone with already rarefied trabeculae gets more susceptible to microfracture, thus putting a vicious cycle in motion.

### **Three-D structure of spongy bone: normal and with osteoporosis (Figs. 2-34, 2-35)**

To examine this possibility, we attempted 3-D visualization of trabeculae. Of the 56 cases studied, vertebral body of a young male aged 21 was selected as a normal control. After being decalcified, the spongy bone was embedded in celloidin-paraffin and was submitted to serial sectioning. From the sectional pictures, the contours of trabeculae were picked up and inputted into a reconstruction-assisting computer system. Figure 2-34 is a 3-D picture of trabeculae reproduced in a display. On the technical aspect of 3-D reconstruction, comments will be given in Chapter 4.

In the figure one can see that in a normal spongy bone, trabeculae are put together into a network, a state which reminds us of the frame of building made of steel beams. Here the individual beams, about equally thick, are shown forming a 3-D network; also the meshes of the network seem to be of about the same dimension and arranged with roughly uniform density.

Figure 2-35 exhibits the changes in 3-D structure of vertebral body in osteoporosis. This is from autopsy of a female aged 71 years. Although at some places the normal network of trabeculae as found in the foregoing picture remains, there are cavernous spaces or fissures, which apparently are produced by loss of trabecular segments. This is a state corresponding to the frame of building where several steel beams

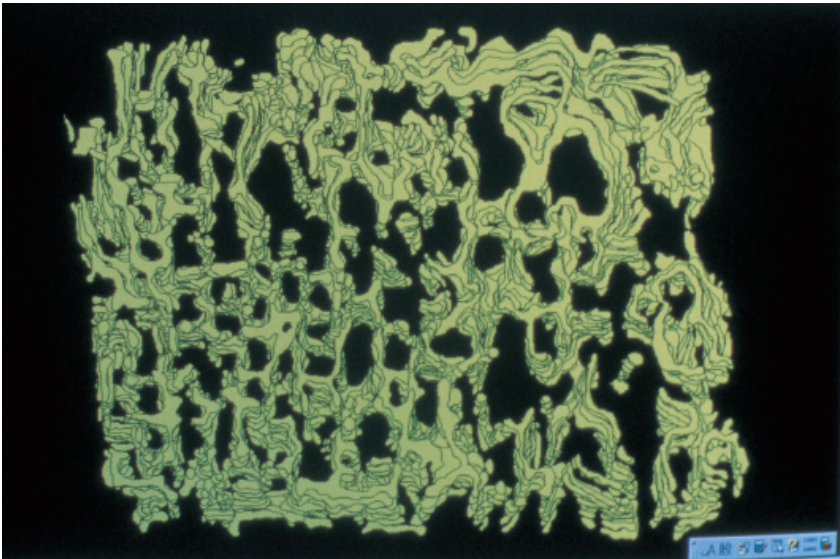


Fig. 2-34. Computer-assisted 3-D reconstruction of non-osteoporotic spongy bone from the body of lumbar vertebra. The trabeculae form a network like the frame of building.

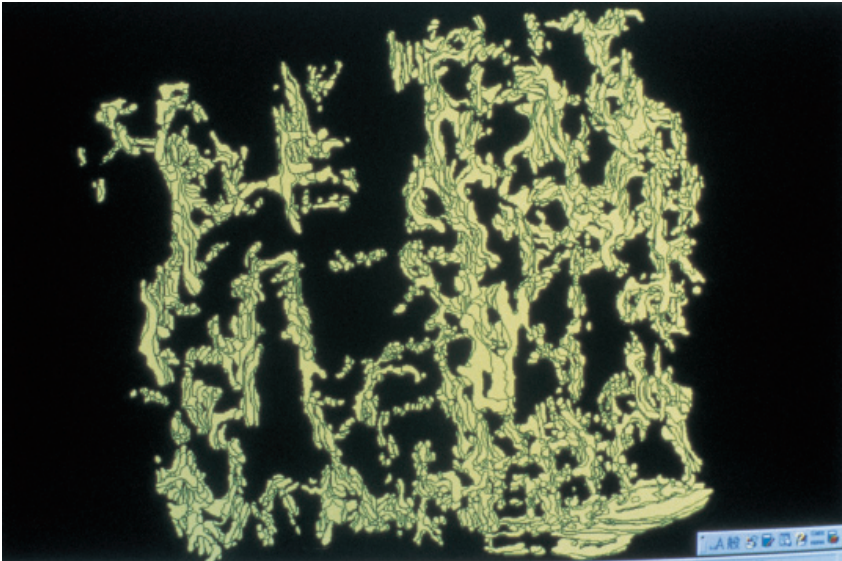


Fig. 2-35. Computer-assisted 3-D reconstruction of osteoporotic spongy bone. Lumbar vertebral body from a female, aged 71 years. Note the rarefied arrangement of trabeculae. There are cavernous spaces left after trabeculae were destroyed.

have been removed from the network. At the fissures, trabeculae seem disconnected by microfracture. It is clear and remarkable that in the spongy bone, fissures tend to extend in the vertical direction. This may be interpreted as suggesting that, of the network beams, mainly the transverse component was torn off by an excessive force pulling the network toward the lateral direction. Possibly, this may be the result of longstanding gravitational burden that continues to press the vertebral body in vertical direction.

Thus osteoporosis of the vertebral body is likely to be a process in which trabecular segments are lost one after another through microfractures, bringing about a typically rarefied, porous bone. Why in some subjects the trabeculae are particularly susceptible to microfracture, and are not in the others, may be accounted for perhaps from the difference in the rigidity and texture of bony trabeculae.

### g) The mean radius of hepatic lobules—another cylindrical model

#### The lobular contour: normal and hepatic-carcinoma-harboring livers (Figs. 2-36, 2-37)

There is a long history of controversies about the way the structural principle of the liver is to be understood. But here let us keep ourselves from being trapped in this debate because we will have to deal with this problem in Chapters 3 and 7. Now let us concentrate on how we can quantitatively measure the growth of liver tissue, either ordinary or pathological, on microscopic level.

For the sake of easier perspective, we assume that the liver is an assembly of the

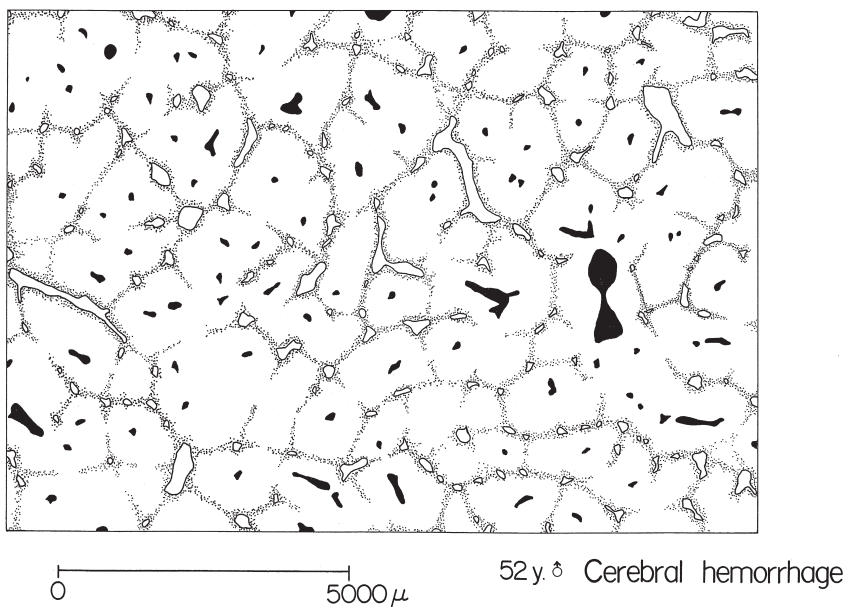


Fig. 2-36. Low power microscopic picture of normal liver of adult, produced by projecting the slide upon a sheet of paper and tracing along the contour of hepatic lobules. Note the approximate size of lobules. Reproduced from Takahashi *et al.* (1968): *Tohoku J exp Med* 94, pp. 207.

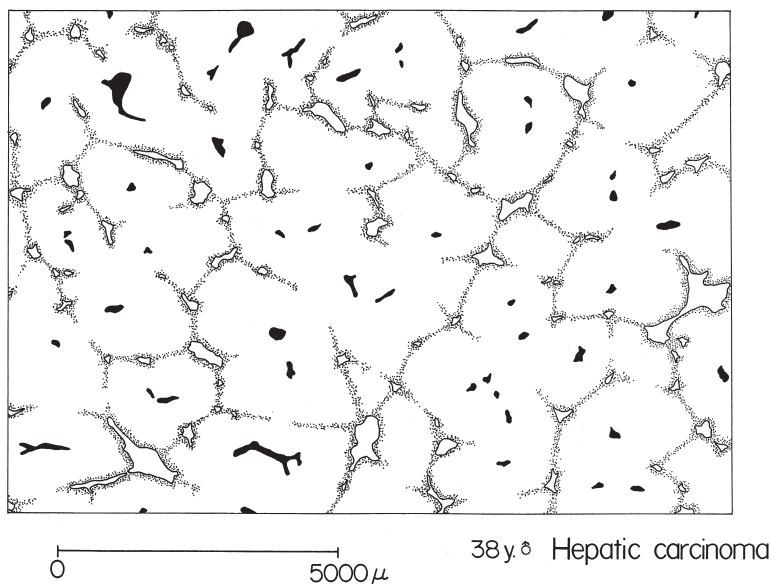


Fig. 2-37. Microscopic picture of a non-cirrhotic liver harboring hepatocellular carcinoma in other parts. The lobular architecture is retained. Compare with the foregoing picture (Fig. 2-36). Apparently the lobules look enlarged to a certain degree. But how can we describe the difference in quantitative terms? Reproduced from Takahashi *et al.* (1968): *Tohoku J exp Med* 94, pp. 207.

classical hepatic lobules (also variously called like Kiernan lobules, hepatic units or hexagonal lobules). In Fig. 2-36, one can see a sketch of normal liver tissue taken at autopsy. This was drawn by projecting a sheet of microscopic slide of an adult liver at a low magnification. It includes branches of portal (white) and hepatic veins (black), and the borders of hepatic lobules are expressed by shading. In this case, the lobular borders were visible microscopically to a certain degree because of a staining difference among the hepatocytes in the peripheral, intermediate and central zones. Note the approximate dimension of the lobules.

Figure 2-37 is from another autopsy liver, drawn at the same magnification as in the foregoing one. The patient died of hepatocellular carcinoma. However, in the part of the liver spared from tumor, there were no changes suggesting the presence of cirrhosis, chronic hepatitis or other parenchymal hepatic diseases. On account of this, the lobular structure was retained as clearly as the former case, as visualized in the figure.

Compare the two livers. It appears that in the latter liver, the individual lobules are uniformly enlarged. Here one cannot rule out the possibility that the lobular enlargement simply reflects a compensatory hypertrophy, seeing that a significant volume of the organ had been replaced by tumor. But it may also be possible that the enlargement reflects a hepatocellular growth *per se*, which is underlying the development of cancer. In any case, it may be desirable that one can define in quantitative terms whether there is a process of parenchymal growth advancing, and if there really is, to what degree. The growth of the liver as an organ can simply be defined with the increase in its volume, or more practically, in the weight. However, in the present example we have to define the growth not as an organ but on a tissue level. If the parenchymal tissue of the liver is an assembly of unitary structures such as lobules, we will be able to define and measure the parenchymal growth by comparing the size of the units. But it seems an uneasy task if one has to begin with defining the accurate geometric shape of individual lobules before quantification. How can we determine the mean size of lobules, without defining their 3-D shape?

### **A cylindrical model for the determination of lobular radius (Fig. 2-38)**

An attempt was made to define the size of the hepatic lobule with its mean radius  $R$  (Takahashi *et al.*, 1968). For this purpose, another cylindrical model was devised. Imagine a sufficiently large cubic liver tissue, with edges of unit length, as in the schema of Fig. 2-38. The cube is of unit volume and contains a sufficient number of hepatic vein branches that are dispersed in the cube. We assume that somehow, we have managed to obtain the total length of hepatic veins contained in this unit cube, or  $L_V$ , the length density in space. Next we suppose that the cube is transformed into a cylinder of uniform radius and  $L_V$  in length, without changing the volume. Then we see that if the radius of the cylinder is  $R$ , it corresponds to the mean breadth of parenchymal tissue surrounding a segment of hepatic vein. Apparently, what is expressed by  $R$  corresponds to nothing but the mean lobular radius defined in terms of 3-D geometry, and in this process we have managed to avoid being implicated in the issue of lobular shape.

The length density  $L_V$  of hepatic veins can be estimated by resorting to another basic principle of stereology. Suppose that the cubic space is sectioned, as in the figure, with a sheet of plane which is parallel to one of the sides of the cube. The

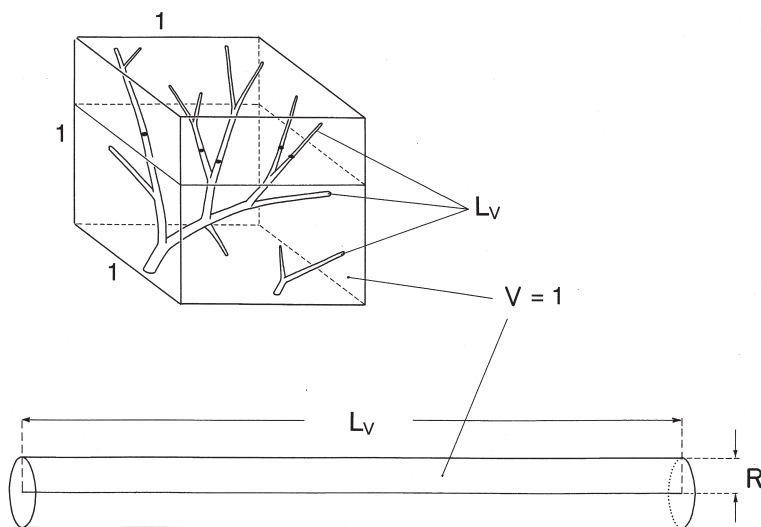


Fig. 2-38. A cylindrical model for the determination of mean radius for the hepatic lobules. The length  $L_V$  of hepatic veins in a unit volume of cubic liver tissue (the length density in space) is determined stereologically by  $L_V = 2 N_A$ , where  $N_A$  is the number of hepatic veins in a unit area of microscopic section (the numerical density in area). Next imagine that the liver tissue is transformed into a cylinder,  $L_V$  in length and of uniform radius  $R$ , without changing the volume. Then  $R$ , corresponding to the mean breadth of parenchyma around a segment of hepatic vein, corresponds to the average lobular radius. Reproduced from Takahashi *et al.* (1968): *Tohoku J exp Med* 94, pp. 210.

section is a square with edges of unit length, in which a large number of hepatic vein branches emerge as  $N_A$  points in the section.  $N_A$  denotes the number of points in a unit area, or the numerical density in area. Then, the total length  $L_V$  of the branches in the cube is related to the number of their cut points  $N_A$  in the section by

$$L_V = 2 N_A. \quad (2-7)$$

For the mathematical derivation of the formula, see the literature (Suwa *et al.*, 1966).

### The growth of lobules expressed by $R$ (Fig. 2-39)

In Fig. 2-39, the estimates of  $R$  from 36 normal livers obtained at autopsy are shown against the patients' age. As defined,  $R$  corresponds to the mean radius of lobules, and therefore, the figure expresses how the parenchymal growth of the liver proceeds; in other words, we find here a growth curve defined on a microstructural level.  $R$  is about 260  $\mu\text{m}$  in the newborn, rapidly rises until it reaches a plateau at about 18 years of age. It remains thereafter, though scattered, within a range between 350 and 400  $\mu\text{m}$ . The mean  $R$  was calculated at 376  $\mu\text{m}$  for the 26 patients older than 18 years. This sufficiently coincides with the lobular radius defined in another way, *i.e.*, as the mean length of the sinusoidal flow routes, which will be shown in the next

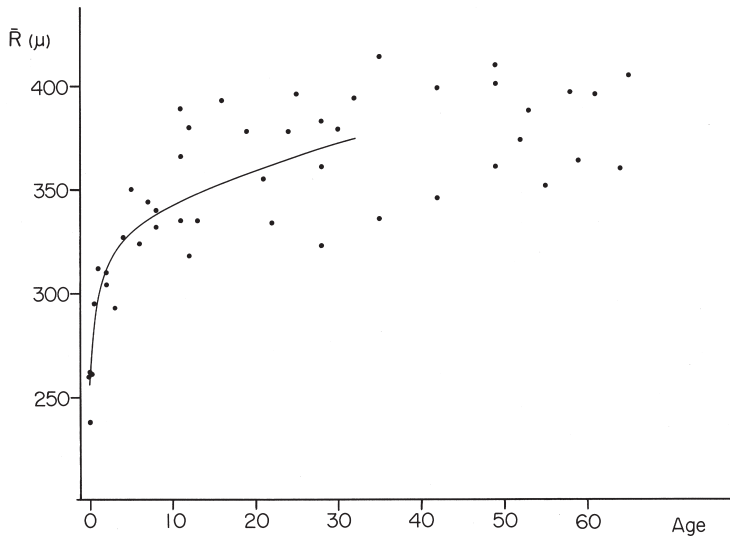


Fig. 2-39. The mean radius of hepatic lobule  $R$  estimated on 36 normal autopsy livers and plotted against the patients' age. This expresses the growth curve, not of the whole organ, but of hepatic parenchyma. Reproduced from Takahashi *et al.* (1968): *Tohoku J exp Med* 94, pp. 212.

chapter.

### Hypertrophic lobules in livers harboring hepatocellular carcinoma (Fig. 2-40)

The measurement of  $R$  was extended to autopsy livers from eight patients, in whom the liver was demonstrated harboring hepatocellular carcinoma but development of tumor was considered unusual in that there was no foregoing cirrhosis or chronic hepatitis which usually is associated. As in Fig. 2-40, the estimated  $R$  appears much larger in the eight cases of liver carcinoma arising in non-cirrhotic livers than in the normal control; the mean  $R$  in the tumor group was  $481.5 \mu\text{m}$  and the difference proved to be highly significant. It might seem possible that the enlarged  $R$  in the livers with hepatocellular carcinoma is an expression of compensatory hypertrophy, but this is untenable, seeing that in another series of livers harboring metastatic nodules of carcinoma originating from other organs, the mean  $R$  proved not to be significantly larger than the normal group. Thus it seems likely, as expected, that in the background of hepatocellular carcinogenesis, a sort of pathological growth of liver parenchyma is advancing.

### Another application of $L_V$ : proliferating bile ducts in livers with congenital bile duct atresia

Another application of the above relation (2-7) is found in the study of Oh-i *et al.* (1969) dealing with the changes of liver in infants with congenital biliary atresia. Infants having this disease are born with the extrahepatic bile ducts totally obstructed and replaced with scar-like cords. There had been little life-saving measure for this



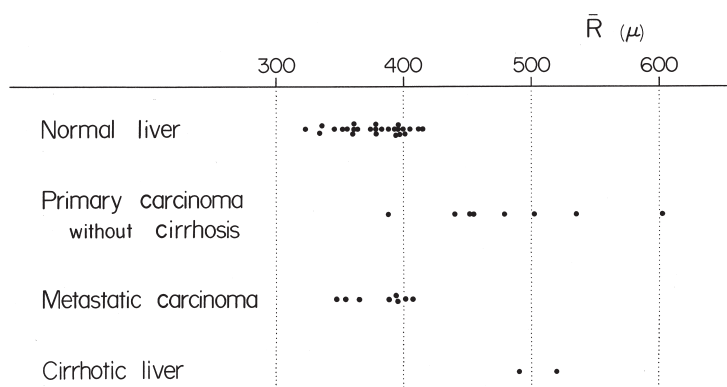


Fig. 2-40. The mean radius of hepatic lobule  $R$  is compared between normal adult livers and eight non-cirrhotic livers harboring hepatocellular carcinoma. The average  $R$  is significantly larger in the latter group, suggesting that a sort of pathological growth of liver parenchyma is progressing in the background of carcinoma development. Reproduced from Takahashi *et al.* (1968): Tohoku J exp Med 94, pp. 217.

disease until 1968, when Kasai *et al.* introduced a surgical treatment (hepatoenterostomy) which greatly extended surgical indication. However in the early days of trial, the result of operation was variable. It was known that the prognosis crucially depends upon the presurgical duration of jaundice, as shown by the fact that an operation, when performed on patients over four months of age, did not bring about any relief of jaundice. Microscopically, the livers of patients presented pictures consistent with biliary cirrhosis, but in those who were not relieved from jaundice, it was not known what changes were mainly to blame for bile-draining failure. In view of this, Oh-i *et al.* undertook a re-assessment of the changes, resorting to micromorphometry and 3-D reconstruction of small bile ducts. In thirty infants operated for congenital bile duct atresia, liver specimens were obtained at correction surgery or autopsy. The patients were divided into two groups: those in whom jaundice was reduced postoperatively (Group 1) and those in whom little change was confirmed (Group 2). The livers were submitted to measurement of two values:  $V_i$ , the volume density of interstitium, and  $L_V(\text{ducts})$ , the length density of bile ducts and ductules.  $V_i$  was obtained by chord length measurement to describe the grade of fibrosis.  $L_V(\text{ducts})$ , determined from the numerical density of ducts and ductules in a sample area ( $L_A$ ) and applying the formula (2-7), served as an expression of ductal proliferation that was more or less found in the livers. In Group 2, both the mean  $V_i$  and  $L_V(\text{ducts})$  proved to be significantly larger than in Group 1, showing that in Group 2 the livers had more advanced fibrosis, but there was also proliferation of bile ducts and ductules that was more vigorous than in Group 1. To examine whether the proliferating ducts form a continuous draining system, manual reconstruction of intrahepatic ducts was added from serial sections of selected livers. It was shown that the peripheral biliary system was replaced by an extremely complex network of proliferating ductules, which was interpreted as a reaction of biliary system to bile stagnation and leakage to the periportal

area. The restoration of patent intrahepatic bile system seemed to depend upon the preservation of pre-existing “main routes” of passage, and not on the grade of ductular proliferation. Thus the maintenance of anatomically recognizable routes of drainage was considered the crucial prerequisite for a successful correction operation.

## h) Problems that cannot be solved by stereology

### Classification of geometric properties of 3-D features (Table 2-2)

We have seen examples of studies to which principles of classic stereology were applied, but then, can we solve all problems of 3-D structures with stereology? So long as the biostructure is concerned, the applicability of stereology seems much more limited than it had been expected before. Table 2-2 is a classification of geometric properties given by DeHoff (1982) from such a viewpoint, and here, stereological estimation is shown workable in rather limited occasions. In addition, in the domain of pathologic anatomy where we have been working, quantitative analysis faces another difficulty. Application of stereology requires *uniform randomness* of the object in terms of distribution or orientation, while dealing with real organs one may often be hampered by the appearance of structure where the condition of randomness may scarcely be satisfied. Still, on such occasions, we are provided with two possibilities.

One is the extension of theoretical methods as have been proposed by European

Table 2-2. Classification of geometric properties according to whether stereology can effectively be applied. Reproduced from DeHoff (1983).

---

Class I:	Standard stereological properties, estimated without geometric assumptions.
	Volume fraction
	Area of surfaces or interfaces
	Length of lines, edges, or triple lines
	Integral mean curvature of surfaces
	Integral curvature of lines
	Integral torsion of lines
Class II:	Properties that require geometric assumptions for their estimation.
	Feature size distribution
	Number of features (simple shapes)
	Feature averages (volume, area, size)
	Degree of anisotropy
Class III:	Properties that cannot be estimated stereologically.
	Number of features (general)
	Connectivity of features (general)
	Size distributions (by volume, area, diameter)
	Spatial distribution information (covariograms)
	Real feature shape

---

researchers in various aspects of quantitative morphology, now generally called the new stereology. The fruit of their activity includes various new concepts which have been applied to granulometry (Gundersen, 1985; Gundersen *et al.*, 1988) or measurement of non-randomized structure (Baddeley *et al.*, 1985; Cruz-Orive *et al.*, 1990). Sometimes we also have been assisted by these new tools. For example, Ebina *et al.* (1993) resorted to disector technique of Gundersen in his study dealing with the problem about whether hypertrophy or hyperplasia causes thickening of bronchial smooth muscles in asthmatic patients; here the number of cell nuclei ( $N_V$ ) had to be determined.

The other approach is to attempt directly analyzing the 3-D space. Certainly, the 3-D structural analysis requires one to perform time and energy-consuming job like 3-D reconstruction from serial sections. However, it promises the performer to obtain fertile knowledge about the organ structure. Recently, we managed to bring into this field computer-assist, with which we have not only been aided to perform reconstruction at greatly improved speed and precision, but also managed to extend the scope of 3-D structural studies, for example into computational measurement of 3-D quantities. What we have done along this line will be the main theme of the chapters that follow.

## **The Basic Structure of the Human Liver from the Viewpoint of Vascular Architecture**

Let me begin analysis of organ structure with introducing some thoughts about the liver and its microvasculature (Takahashi, 1970; Takahashi and Chiba, 1990; Takahashi *et al.*, 1992). The liver is a voluminous organ comparable in size to the lung, with a microstructure appearing not only quite simple but randomized in terms of orientation with which the blood vessels are arranged. This makes us expect that we would be able to rely on stereological method in various facets of study. However, taking a step into asking what fundamental principle dominates this organ in its structure-function correlation, one may realize the study cannot be that easy. The following is an example showing how much had to be consumed to understand what the “organ structure” implies even in this simple organ.

### **a) The unitary structure—different concepts**

#### **The swine liver: 2-D and 3-D appearance of hepatic lobules (Figs. 3-1, 3-2)**

Shown in Fig. 3-1 is a microscopic picture of the liver, not of human but of swine. It seems to be an assembly of well demarcated chambers, each comprising parenchymal tissue. These chambers have been called the hepatic lobules. In the swine, the lobules are separated from the neighboring ones, though not always perfectly, with thin membranes made of connective tissue. At the places where three membranes meet, one can find a mass of collagen which contains a duct space and is usually called a portal tract because it conducts a triad of peripheral portal vein, hepatic artery and bile duct. Though various, the average shape of lobules on a 2-D section is said to be hexagonal, and one can find a portal tract at each of the vertices. Blood flows into the lobule from both the portal vein and hepatic artery, the former bearing more than 90% of the total blood flow. After irrigating the intralobular capillary network, the blood is drained by a small vein, which is found at the center of the lobule and therefore is called the central vein, a headspring of the hepatic vein.

As in the figure, the lobules appear in a 2-D microscopic section as polygons of various shape. This means that 3-dimensionally, lobules are polyhedra packed in the space. Figure 3-2 is a part of swine liver reconstructed with the aid of a computer system. Only an early stage of reconstruction is shown in the figure where a small thickness was reproduced, because with the advancement of reconstruction, the pic-

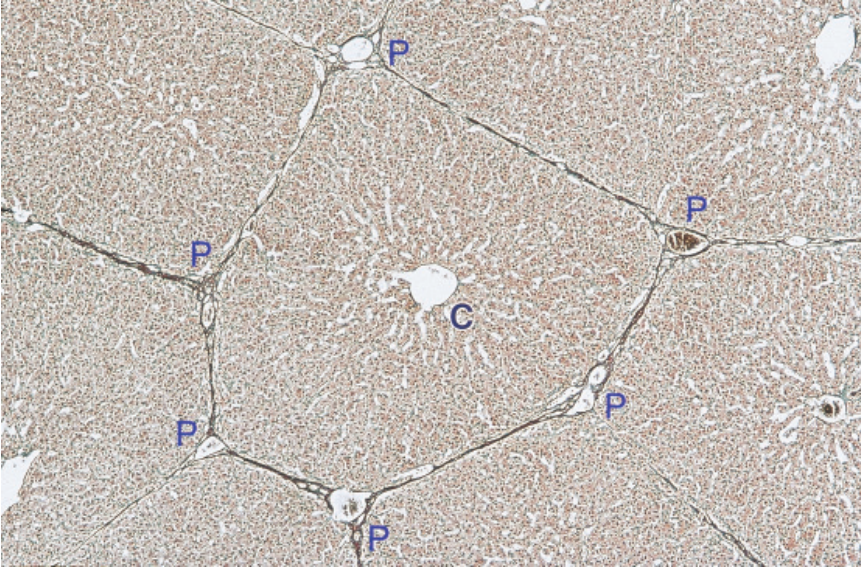


Fig. 3-1. Microscopic appearance of the liver of swine. Clearly, the parenchyma is divided with thin connective tissue septa into polygonal areas which are called the hepatic lobules. Terminal portal veins run through the portal tracts (P). At the center of each lobule, a central vein (C), the terminal segment of hepatic vein, originates and drains blood from the lobule. Gomori's silver stain.

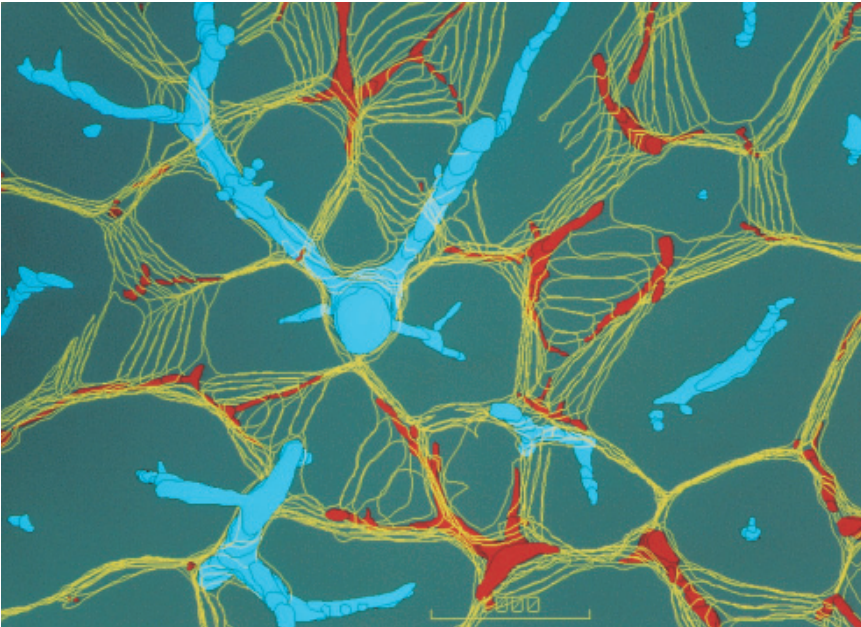


Fig. 3-2. Computer-assisted 3-D reconstruction of swine liver. The yellow wireframes are the interlobular septa, the vessels painted red are portal veins, and those painted blue are hepatic veins. Even in this early stage of reconstruction one can see that the parenchyma consists of polyhedral lobules.



ture becomes growingly complicated, making it hard to keep a clear perspective of the basic structural framework. Still, even at this stage of reconstruction where serial sectional pictures have just started to stack, it may be understood that the space is packed with polyhedral lobules with portal veins (red) running along the interlobular membranes and hepatic veins (blue) penetrating the lobules.

### Characterization of polyhedral lobules (Figs. 3-3, 3-4)

The geometry of lobular polyhedra was analyzed upon serial sections of swine liver. After the contours of lobules were checked in each of the serial sections as in Fig. 3-3, the sectional pictures were stacked and scanned through over a thickness of 1cm to define the shape of individual lobules. As the result, a total of 56 lobules were confirmed retaining integrity, without being truncated at the margin of the tissue block. Figure 3-4 is a histogram exhibiting the number of faces for the 56 lobular polyhedra. The polyhedra were shown to have varying number of faces, ranging from 8 to 22, but the mean was calculated at 13.7. This is a value close to fourteen, and reminds us that a face number of 14 was given for the average polyhedra, to which animal cells were assimilated (Lewis, 1923, 1933). Suwa (1981) also gave a mean number of 14 for the polyhedra produced by random packing of spheres. Discussing that this corresponds to the space division where the total surface area of polyhedra attains the minimum, he designated this as the equilibrium space division. Although we are far from understanding the physical significance of the lobular geometry, it seems to the author that mainly, the function of the connective tissue septa of the swine liver is a mechanical one. The septa are likely to be holding the lobules as they are, resisting excessive

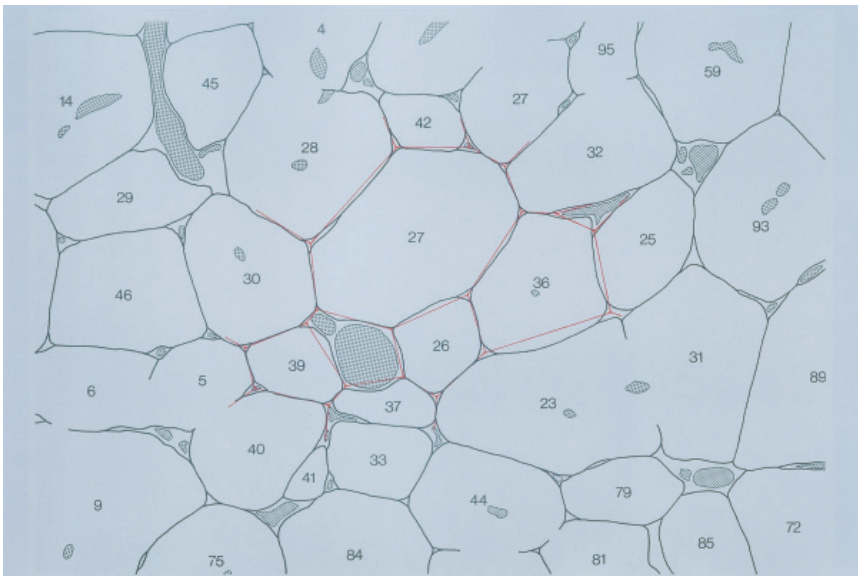


Fig. 3-3. In one of serial sections, the contours of lobules are picked up by tracing, a procedure necessary for the reconstruction of Fig. 3-2. Lobular contours are defined so as to construct a packing of polygons as partially shown by red lines.

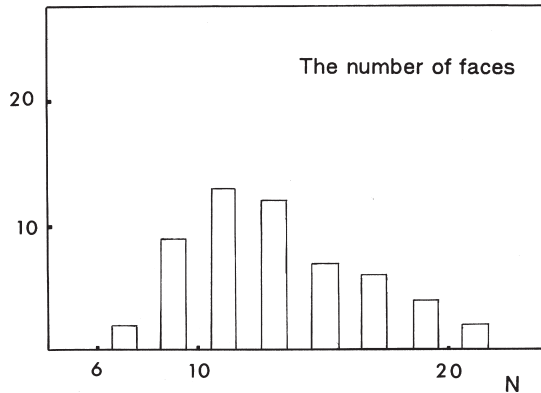


Fig. 3-4. The number of faces N counted for each of the 56 lobules reconstructed from serial sections of swine liver. A mean face number of 13.7 was obtained.

mechanical force exerted upon the liver which is a soft and voluminous organ, susceptible to rupture when too much deformed. From a microcirculation point of view, all the blood that has irrigated a lobule is drained by its central vein. Therefore one can say that functionally, the lobules may also be definable as a unit of venous drainage.

#### Normal human liver: microphotograph of lobule (Fig. 3-5)

Figure 3-5 is a microscopic picture of normal liver of human. Here one can no longer find such connective tissue septa that in the swine were enveloping the lobules.

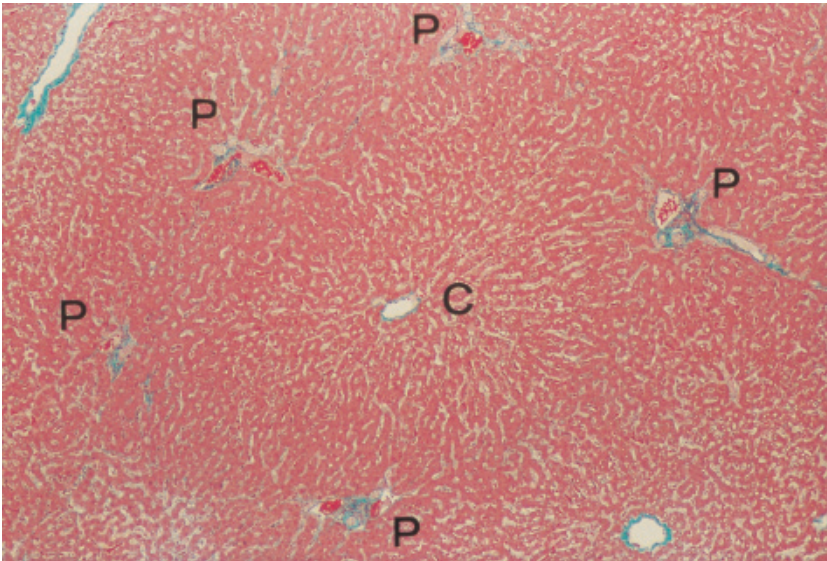


Fig. 3-5. The microscopic appearance of normal human liver. P: the portal tract. C: the central vein. Despite the lack of interlobular septa, arrangement of these vessels exactly reproduces that of the swine liver. Elastica-Goldner stain.



However, there is unmistakably a parenchymal area that may be definable with the portal veins (P) surrounding the area, and with a central vein (C) penetrating the area at the center. The area seems likely to be corresponding to the lobule of the swine liver from which only the septa were taken away, leaving the portal tracts and central veins at the places where they were. Also in the arrangement of lobules in the human liver shown in Fig. 2-36, little difference seems to exist compared with the swine.

### The acinar model (Fig. 3-6)

It would have been a matter of course that the lobular concept, as shown above, was widely accepted on account of its easy recognizability. In the early 1950s, however, Rappaport (1954) proposed another unit of the liver based on different concept. Displaying the schema of Fig. 3-6, he maintained that in the human as well as in the other mammals, the fundamental unit of the liver should be defined in the form of what he called an acinus. His unit was schematized as a small parenchymal clump having a terminal portal venule at the center and flanked by terminal hepatic venules, the latter corresponding to the draining vessels which were called the central veins in Figs. 3-1 and 3-5. According to Rappaport (1963), one of the reasons why he prefers this concept to the classic lobule is that in any organ, it should be the afferent vessel that determines the basic framework of the unitary structure. Moreover, he contends, the liver is a glandular organ that secretes bile, where the basic design of gland should be determined by the arrangement of secreting ducts. In fact, the intrahepatic bile ducts run and divide in parallel with the portal veins, and he concludes that in this respect too, the portal tracts have a much greater functional significance than do the hepatic veins.

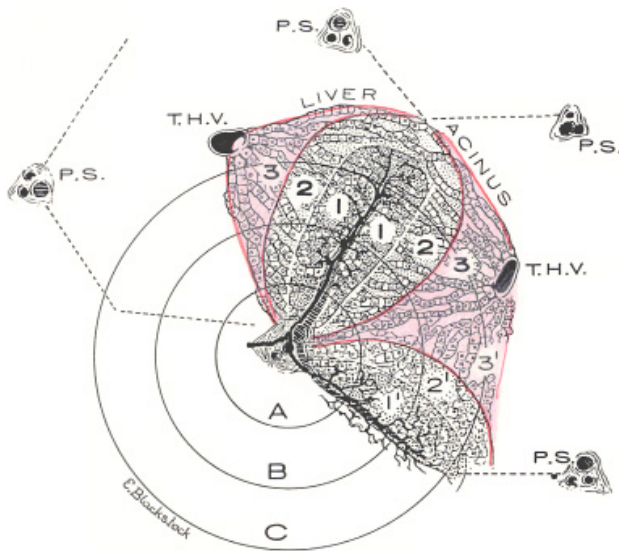


Fig. 3-6. The acinar model. With this schema, Rappaport maintains that the basic structural unit of the liver should be defined as an ellipsoidal mass having a terminal portal venule at the center, which he called the acinus. An acinus is said to comprise three zones, 1, 2 and 3, in which order, blood was assumed to irrigate through an acinus. Reproduced from Rappaport *et al.* (1954): *Anat Rec* 119, pp. 11.

However, the matter is not that simple. In the first place, one can hardly talk about something like the superiority of the afferent vessel over the efferent one, since microcirculation of an organ may not be sustainable under a malfunctioning efferent vessel, and in this respect the outlets of blood have to be considered equally indispensable with the inlets. In the second place, the liver is indeed an excretory gland producing bile. But structurally, the liver is classified into the type of netlike gland, quite a unique one. Here, bile is secreted into the bile canaliculi which form a vast network continuing over the whole organ, as shown later (Figs. 3-26 and 3-27). At many places, the network is tapped with a terminal bile ductule (the canal of Hering) which leads to an interlobular duct, the peripheral branch of biliary tree. Therefore, even if several terminal ductules came to be obstructed, bile can be drained through any of the other exits. In these circumstances, it may be clear that in the liver where bile can be secreted via any route of the biliary system, one cannot define a glandular lobule in such a way as in ordinary exocrine glands like the pancreas or salivary glands.

In the third place, if the acinar concept were tenable as a functionally significant circulatory unit of the liver, it must be able to explain the morphogenesis of various liver changes developing under impaired circulation, because it has been defined as a unit of tissue blood flow. In the practice of diagnostic pathology, hepatocellular necrosis due to ischemia or intoxication is often experienced. But in reality, the pattern of liver lesions actually found in such patients is far from what one might expect by assuming the acinar concept. This issue will be revisited in Chapter 7.

## **b) The microvasculature of human liver and its functional significance**

### **Three-D vascular architecture of human liver (Fig. 3-7)**

Let us consider the problem, watching the actual 3-D microvasculature of the normal liver. Figure 3-7 is the result of computer-assisted reconstruction of a human liver, and presents the architecture of small blood vessels, with the portal veins painted in pink and the hepatic veins in light blue. The terminal branches of the hepatic vein correspond to the central veins of lobules. One may find small areas surrounded by dots at two places. One of them, Area 1, has a hepatic venule (a central vein) at the center and is circumscribed by several terminal branches of portal vein. Apparently, this represents a single, swine-type lobule. With this in mind, let us trace the portal venules, and we can see that the whole space is separable into similar lobules. On the other hand, an acinus of Rappaport, though hardly recognizable from the arrangement of small vessels in the space, may correspond to something like Area 2, the other small space. Thus, from a microanatomical point of view, the classical lobules are far more clearly definable than Rappaport's acini.

However, let us re-examine the matter from another viewpoint, keeping ourselves from being too much absorbed in the issue of unitary structures. Now, pay attention to the spatial relation between the hepatic (central) venules and the portal venules surrounding them. Then one may see that over the whole area reconstructed, both of the vessels are positioned in the space so as to embrace between them a distance which is kept uniform to a certain degree. However, between a pair of neighboring portal and hepatic venules, any relationship can exist in terms of their mutual angle. Therefore

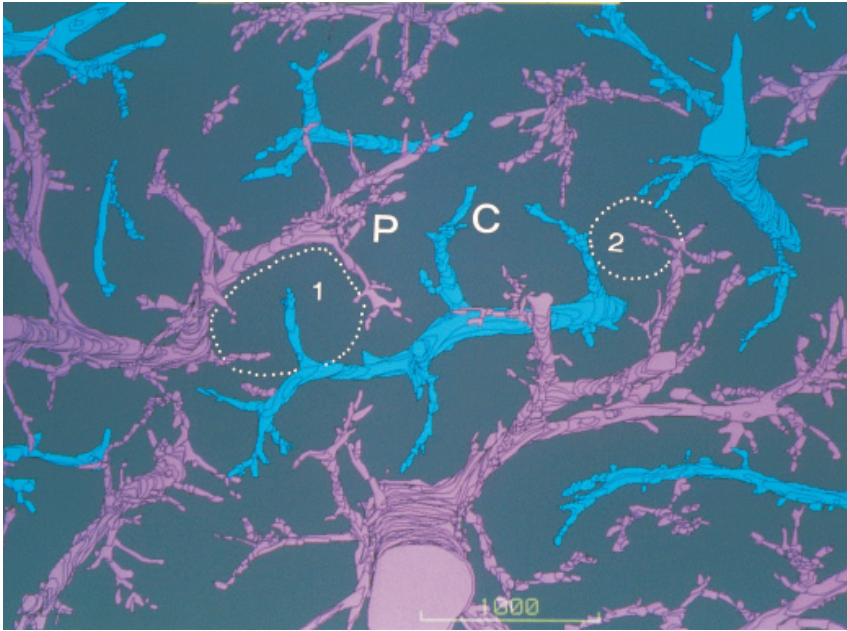


Fig. 3-7. Computer-assisted 3-D reconstruction of the hepatic microvasculature in a normal human liver. Portal veins (P) are painted in pink, and the hepatic veins (C: central vein) in light blue. Note that the terminal portal and hepatic venules are arranged in the space in an isodistant fashion, i.e., so as to embrace a similar distance between them. Two areas are encircled by dots: while Area 1, corresponding to a lobule, is well definable with the surrounding portal venules, an acinus (Area 2) is barely visible from the way the vessels are deployed in the space. Reproduced from Takahashi *et al.* (1990): *Science on Form II*, pp. 19.

the portal-central-venous distance has to be defined in clearer geometric terms. The definition will be introduced afterwards, and here let us only have an overview by comparing the picture with another organ where the isodistant relationship of vasculature seems to be retained much less than in the liver.

### **The vasculature of cerebral cortex: difference from the liver (Fig. 3-8)**

Shown in Fig. 3-8 for comparison is the microvasculature of human cerebral cortex. This is a reconstruction of small arteries and veins manually performed at a time when computer assist was not available. At a glance, the arrangement of small arteries (non-shaded) and veins (shaded) appears so much complicated and irregular as to suggest that in this organ, the afferent-efferent vascular distance may be less uniform than we saw in the liver.

### **The interdigitating relationship (Fig. 3-9)**

In the hepatic vasculature, the afferent portal and the efferent hepatic venules are arranged alternately in the space as schematized in Fig. 3-9. In anatomy, this relation is expressed as "interdigitation," with which to compare to the fingers of both hands locked together. Also in the cerebral cortex shown in the foregoing figure, one can

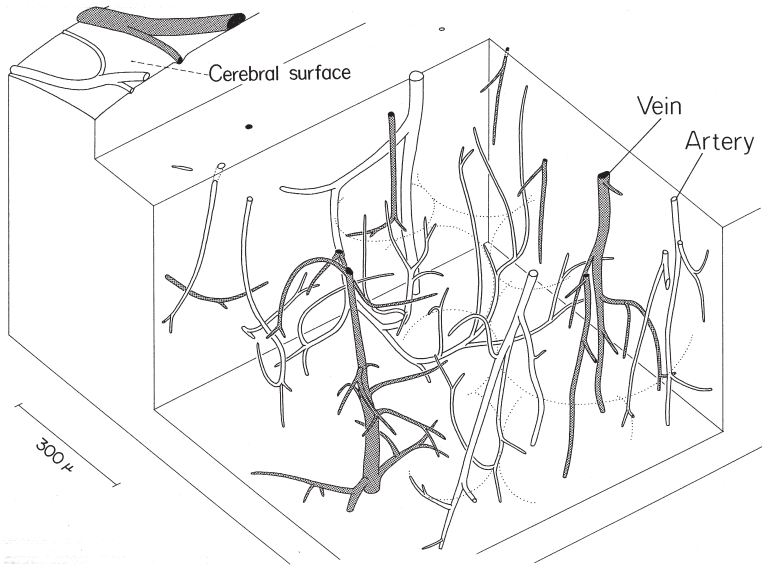


Fig. 3-8. Manually performed 3-D reconstruction of the microvasculature of cerebral cortex. Note the relation of small arteries (white) and veins (shaded). While an “interdigitating” relationship is retained, the pattern is more complicated and irregular than in the liver, with the arterio-venous isodistance not so clearly visible. Reproduced from Takahashi (1970): *Tohoku J exp Med* 101, pp. 123.

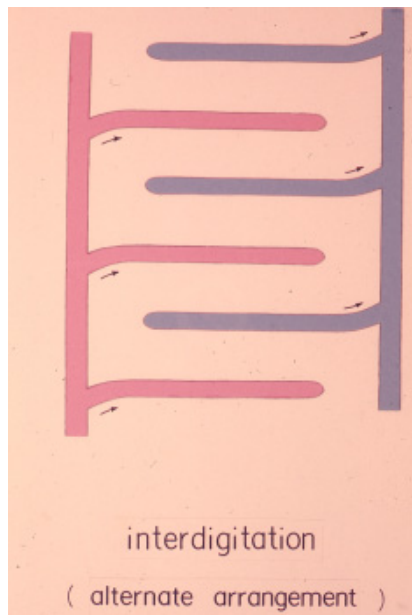


Fig. 3-9. A schema illustrating the “interdigitating” relation of afferent and efferent vessels. In other words, an alternating relation.

find, by closely watching, the interdigitating relation retained in the whole region, allowing to define circulatory "units" around small veins as roughly depicted with dotted circles along their putative borders. Thus, the difference between the liver and the cerebral cortex is that in the former, there exists quite an *isodistant* interdigitating vasculature, while in the latter the afferent-efferent vascular distance is much less uniform. As will be shown, the liver has a vasculature that retains the highest isodistance among the organs. If so, what significance does the isodistant vasculature of the liver have in the organ function? Because morphologically, it is the microvasculature that makes the liver a unique organ, it may be reasonable to assume that there may be some uniqueness in the hepatic circulation.

### The portal vein: its uniqueness (Figs. 3-10, 3-11)

With respect to circulation, the uniqueness of the liver lies, of course, in that it has the portal vein as its functional afferent vessel. The portal vein is a low pressure vessel, with the blood pressure at the trunk being as low as 8 mmHg, whereas the quantity of blood that flows through this vessel amounts to 1.5 L/min, or 25 to 30% of the cardiac output. This implies that the intrahepatic portal venous tree has to convey and distribute such an amount of blood to the periphery at such a low blood pressure. Figure 3-10 presents the fall of blood pressure theoretically estimated for the portal

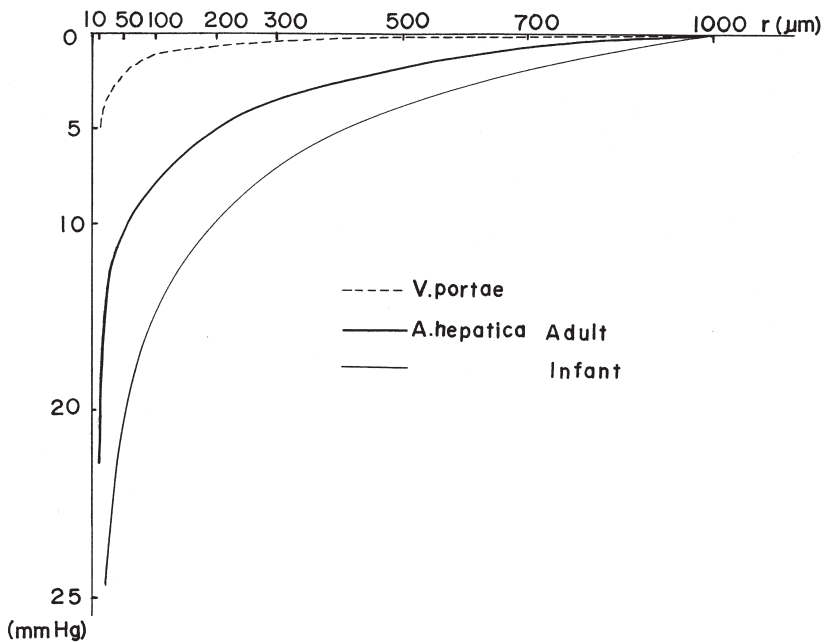


Fig. 3-10. The blood pressure drop is estimated for the intrahepatic portal vein and hepatic artery by measuring the length and radius of segments on a vascular cast and according to the model of Suwa *et al.* (1963). Over a range from a large vessel of 1,000  $\mu\text{m}$  in radius to a terminal branch of 10  $\mu\text{m}$ , the blood pressure of the portal vein was demonstrated to drop by only a few mmHg, a great difference from that of the hepatic artery.



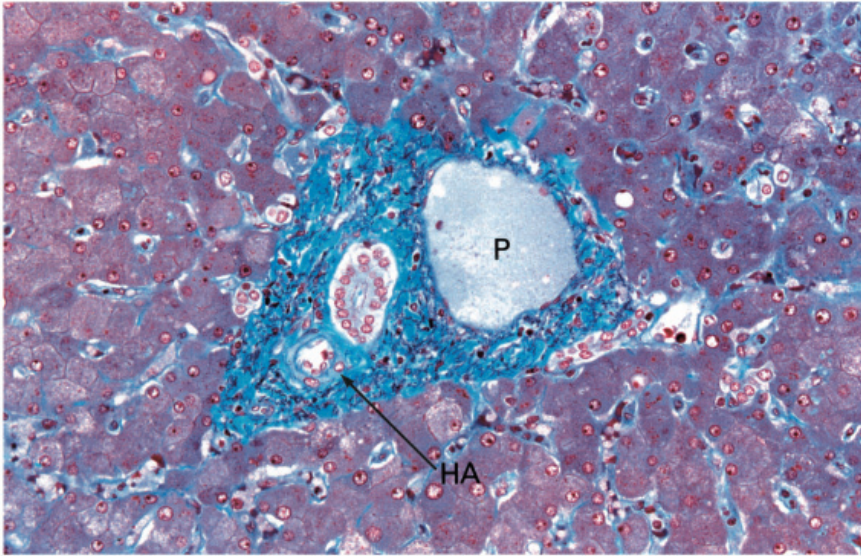


Fig. 3-11. Microscopic appearance of a portal tract of normal human liver. P: portal vein. HA: hepatic artery. The artery is equipped with thick layer of smooth muscles which however are not recognizable in the portal vein. Elastica-Goldner stain.

vein and hepatic artery by quantitative treatment of methacrylate casts of these vessels. The study, performed according to the mathematical theorem developed by Suwa *et al.* (1962), demonstrates that the pressure gradient of portal blood flow is incomparably smaller.

Moreover, the blood flowing into the liver has to be distributed to the peripheral lobules sufficiently uniformly over this large organ. This is a critical requirement to be satisfied so that the portal blood, after flowing into the liver, may make sufficient contact with the intralobular hepatocytes. Otherwise, the liver would be unable to function as the central organ of metabolism. Particularly, one has to keep in mind that the liver plays crucial role in detoxifying noxious substances absorbed in the GI tract and carried via the portal vein. If there were unevenness in the density at which portal blood irrigates the hepatic parenchyma, allowing a part of blood to pass through the organ without making sufficient contact with hepatocytes, the result would be a hepatic insufficiency, although various in its clinical seriousness.

In this connection, let us recall what was discussed in Chapter 1. It was shown that the systemic arteries have in the peripheral arterioles an enormously thickened medial coat, and that these hypertrophic smooth muscles are mainly assigned to regulate the peripheral flow of blood. However, the intrahepatic portal venous tree that is a low-pressure vessel has no such regulatory apparatus even at the periphery. Figure 3-11 presents a microphotograph of portal tract from a normal liver of human, and one can see that while the small hepatic artery (HA) is equipped with hypertrophic smooth muscles, no muscular component is recognizable in the wall of the small portal vein (P).



**The significance of isodistant vasculature: two vascular models (Figs. 3-12, 3-13, 3-14)**

The uniquely isodistant relation of the portal and hepatic venules shown above seems to be the structure that satisfies the requirement which the liver has in achieving its circulatory and metabolic functions. In other words, one can find in the hepatic

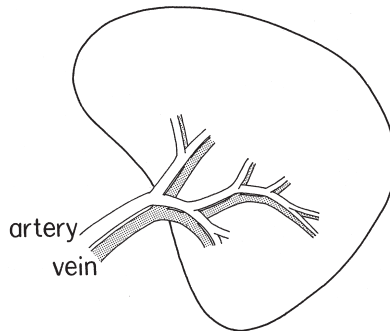


Fig. 3-12. A schema illustrating arteries and veins entering and going out of an organ, both running in parallel. In most organs, arteries and veins run and divide toward the periphery, retaining the contiguous relation.

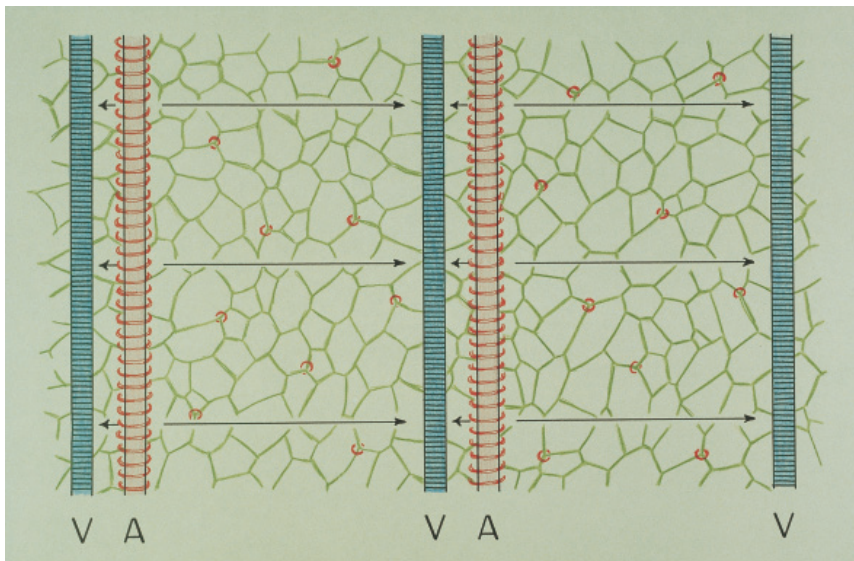


Fig. 3-13. Microcirculation Model 1, with contiguous arrangement of terminal arteries (A; or afferent vessels like portal vein), red, and terminal efferent veins (V), blue. Capillary network is shown in green. Under this vasculature, the distance of capillary flow routes greatly varies, and so does the flow resistance. This inequality has to be compensated by active flow regulation on the part of vascular smooth muscles which are illustrated with either red spirals surrounding the terminal arteries or red rings sporadically found around capillaries.

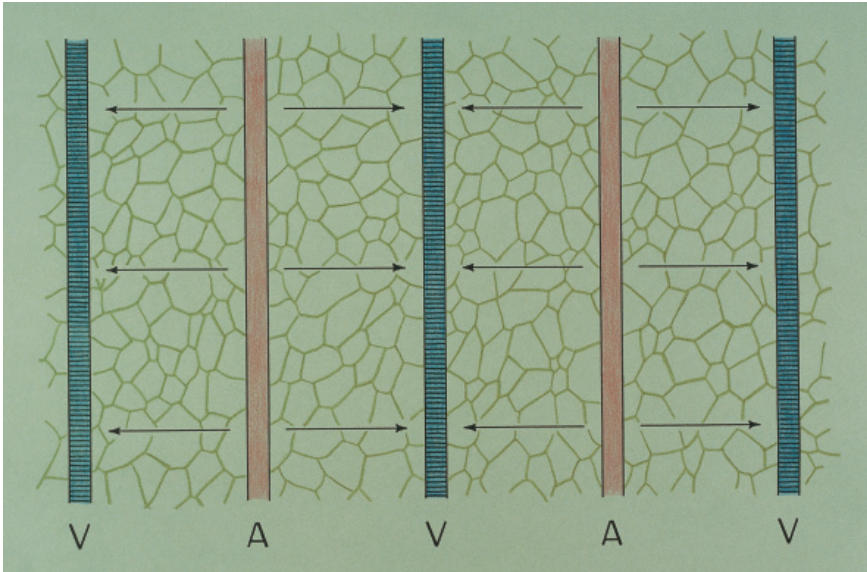


Fig. 3-14. Microcirculation Model 2, with isodistant arrangement of terminal afferent (A) and efferent (V) vessels. Here the distance of capillary flow routes, and also the flow resistance, is ensured to be fairly uniform.

microvasculature a sort of “adequate design,” the optimum structure-function correlation. This will be understood by making the following ideal experiment.

Usually, an organ has a hilus where an artery enters and a vein leaves the organ but they do so closely in parallel as in Fig. 3-12. This relation is brought into the organ, where arteries and veins run and divide, maintaining the close adjacency. What if, however, this contiguity should be kept down to their terminal region where they are joined with the capillary network? Here, one will have to expect a difficulty in the tissue microcirculation, for the following reason.

Figure 3-13 is a schema of contiguous vasculature. Here we assume that the space between the small arteries and veins (more generally, afferent and efferent vessels) is uniformly filled with capillary network (green). If arteries and veins are located in close adjacency like the figure, a great inequality occurs in the length of flow routes through capillaries, and produces shortcircuited flow at the places of contiguity. Therefore, under this vasculature, blood cannot be distributed uniformly over the tissue, unless there is a correcting mechanism which actively regulates and redistributes blood flow. As is well known, it is the sphincter action of vascular smooth muscles that is responsible for this regulation, i.e., the medial smooth muscles of small arteries and arterioles, and also the smooth muscle cells sporadically found in capillaries. The seemingly luxurious muscular coat of the arterioles as demonstrated by the elevated  $D/R$  ratio (Fig. 1-9) must have been expressing the extremely vigorous activities of these vessels assigned to regulate the tissue blood flow. Only with the combined activities of these regulatory apparatuses, will the tissue blood flow be equalized over the

whole region.

However, we have another extreme too, as in Fig. 3-14. Here, the terminal arteries and veins (or, afferent and efferent vessels) are keeping a uniform distance. Under this isodistant pattern, the length of capillary routes becomes uniform. It would ensure a uniform resistance to flow, and ensure a distribution of blood at a uniform density, even if the vessels are not equipped with any apparatus for regulation. Since in the liver, the peripheral portal veins are not equipped with smooth muscular coat and are considered to be devoid of regulatory function, it appears that this isodistant relation may be the very structure required by this organ.

**Organ difference in microvasculature: functional significance (Table 3-1)**

We now understand that in the organ circulation there is an aspect, in which the flow dynamics depends on the vascular architecture. This is an aspect of microcirculation that has nothing to do with the structure of capillary network itself. As summarized in Table 3-1, in organs having an isodistant vasculature, a uniform blood flow in the tissue is likely to be realized even in the absence of regulation. In contrast, in an organ with a contiguous architecture, an active regulation is indispensable. As we will see, the isodistant group includes the liver and the lung. Significantly, these are organs supplied by a low pressure vessel, namely, the liver by the portal vein and the lung by the pulmonary artery. The wall of intrahepatic portal venules has practically no smooth muscles. In the pulmonary arteries, where the mean blood pressure at the trunk does not exceed 15 mmHg, smooth muscular coat is only poorly developed in the peripheral branches (see Fig. 1-10). On the other hand, the contiguous group includes the myocardium and the renal cortex, and here, an active regulation is considered to prevail.

However, in gaining more insight into the structure-function correlation in this context, what we have to do first of all is to define accurately the degree to which the vascular architecture of an organ is isodistant or contiguous, instead of intuitively judging the pattern by inspection. Then, how can we describe in quantitative terms the difference in the vascular pattern? With what parameter can we measure the grade of isodistance or contiguity in 3-D? Here we face a problem of 3-D quantification.

Table 3-1. The pattern of microvasculature and the microcirculation considered to dominate under the vasculature. The organ difference.

Vasculature	Flow dynamics	Organ examples	Inflow vessel
Isodistant	Non-regulatory	Liver	Low pressure system
		Lung	
		.....	
		Brain	
Contiguous	Regulatory	Myocardium	High pressure system
		Renal cortex	
		.....	

### c) Quantitative expression of vasculature pattern

#### The concept of $L$ : 3-D distance distribution (Figs. 3-15, 3-16)

Figure 3-15 illustrates a geometric model the author proposed for the quantification of vascular patterns. Let us take a point  $P$  randomly in an organ. Suppose that we can determine  $L_a$ , the shortest distance from  $P$  to the nearest artery (or afferent vessel), and also  $L_v$ , that to the nearest vein (or efferent vessel). Then we define the distance  $L$ ,

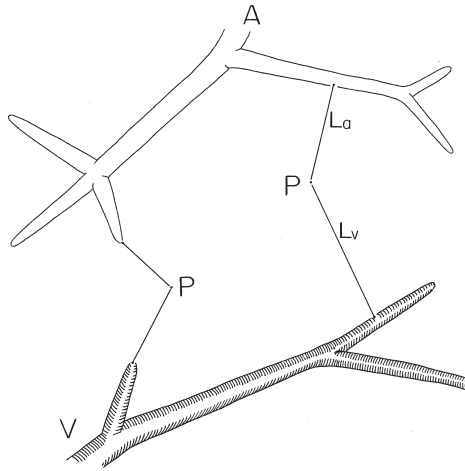


Fig. 3-15. The concept of  $L$ , the length of the shortest capillary flow route via a sampling point  $P$  randomly taken in the space. The length  $L$  changes if  $P$  is moved around in the space, for example to the other point in the left part of the figure. Reproduced from Takahashi (1970); *Tohoku J exp Med* 101, pp. 127.

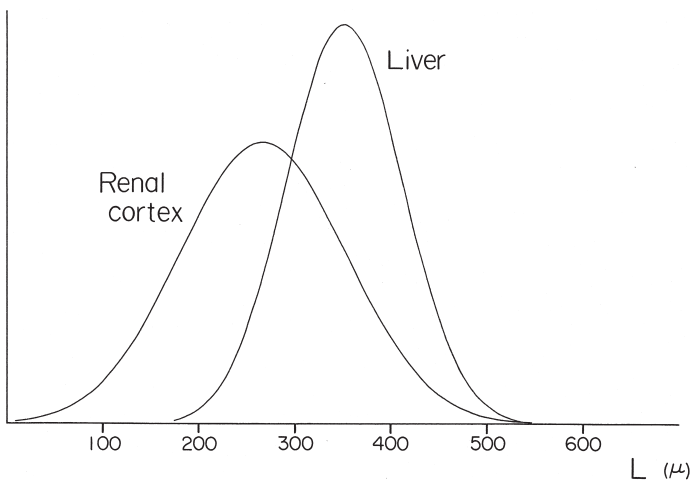


Fig. 3-16. The distribution of  $L$  obtained from measurement of a large number of points in normal liver and kidney. In the liver, the dispersion of  $L$  is smaller than the kidney, showing that the pattern of vasculature is more isodistant. Reproduced from Takahashi (1970); *Tohoku J exp Med* 101, pp. 127.

the sum of  $L_a$  and  $L_v$ , as the length of the shortest capillary route via P. This length changes when the point P is moved around in the organ, for example to the left-sided point in the figure. Accordingly, if we set a sufficiently large number of points randomly in the organ and measure  $L$ , then it will become a statistical quantity.

Consider that in an organ, the length  $L$  was measured for hundreds of points and the dispersion of  $L$  was calculated. In Fig. 3-16, results from two organs are shown for comparison. If the dispersion of  $L$  proved to be comparatively small as in the liver, the vasculature in the organ is likely to be more isodistant. In contrast, the larger the dispersion, the more contiguous vasculature is suggested to exist. Thus, in this context, what we have to obtain by morphometry is the mean and the dispersion of  $L$ .

### Three-D distance distribution: measurement (Figs. 3-17, 3-18, 3-19, 3-20)

In practice, measurement of  $L$  was designed to perform on serial microscopic sections. In an organ, 300 to 400 sampling points were set by “tessellation” on a level of serial sections as schematized in Fig. 3-17. In estimating the mean and variance of  $L$ , we cannot rely on stereology, as shown by DeHoff in the classification of geometric properties (Table 2-2), in which the present task belongs to “spatial distribution information.”

I thus undertook a manual measurement. While graphically reconstructing small vessels, the shortest distance from P to a nearest vessel was determined by calculating the distances sequentially on serial sections.  $L$ , which is a 3-D distance, was determined as in Fig. 3-18 by measuring the  $xy$ -distance on a stack of serial pictures and calculating the  $z$ -distance from the number of serial sections. As might be expected, this was quite a time-consuming work.

But now we have a computer-assist for this measurement thanks to the programming by T. Chiba (Takahashi and Chiba, 1990). From a set of serial sections, blood

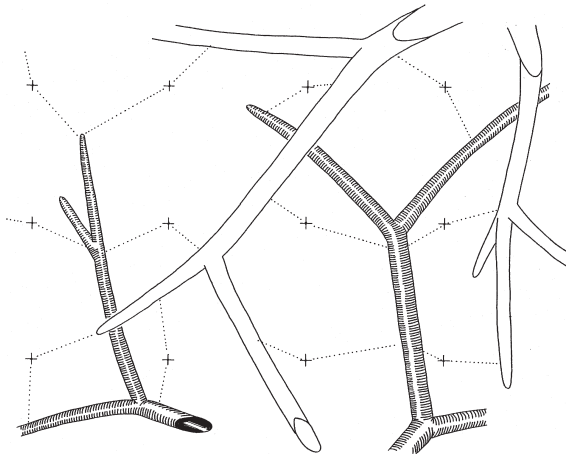


Fig. 3-17. Setting of sampling points for the measurement of  $L$ . In one of the serial sections, hundreds of points are set by “tessellation,” i.e., at the crossing points of orthogonal parallel lines. Reproduced from Takahashi (1970): *Tohoku J exp Med* 101, pp. 128.

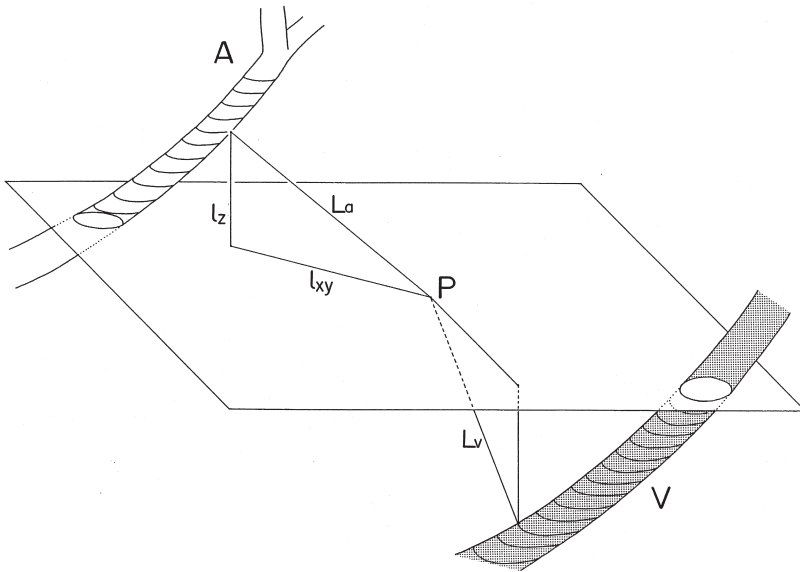


Fig. 3-18. A schema showing how  $L$  was obtained by manual measurement. The length of the shortest flow route  $L$  was obtained by comparing the values among several steps of serial sections. At each step of serial sections,  $L$  was calculated from  $L^2 = l_{xy}^2 + l_z^2$ , where  $l_{xy}$  is the distance from  $P$  to the nearest vessel projected on the  $xy$  plane.  $l_z$  is given by the number of serial sections. Reproduced from Takahashi (1970): *Tohoku J exp Med* 101, pp. 128.

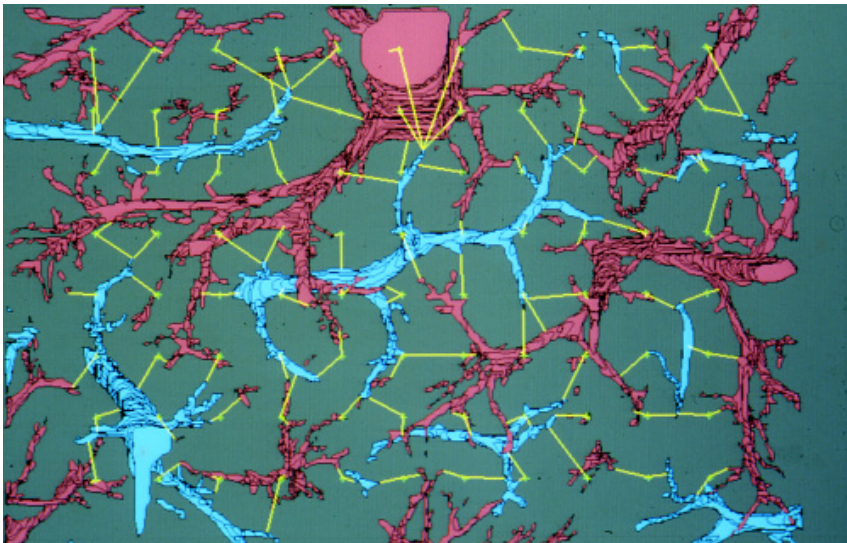


Fig. 3-19. Computer-aided measurement of  $L$ . The yellow lines are the shortest capillary routes selected by computational geometry. Reproduced from Takahashi and Chiba (1990): *Science on Form II*, pp. 24.



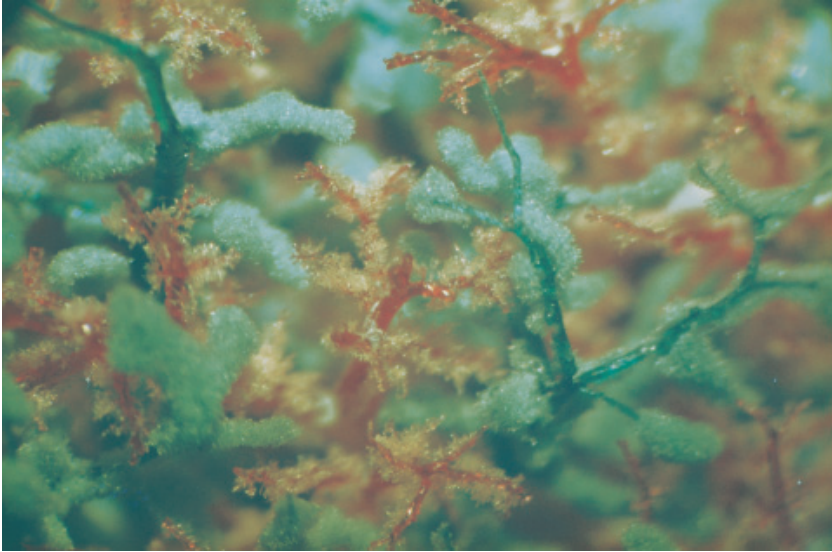


Fig. 3-20. A methacrylate cast of liver microvessels. Red are the portal, and blue are the hepatic veins. Here the arrangement of vessels may seem suggesting the presence of isodistant vasculature, but a cast does not allow to compare the 3-D vascular pattern in quantitative analytical terms.

vessels are digitized at every step, and we have a whole set of 3-D structural data in a hard disc. Figure 3-19 is an example in a normal liver (portal vein, red; hepatic vein, blue). Here one can see 88 test points, and the yellow lines are the shortest routes calculated.

The microvasculature of an organ may be visualized much more easily by preparing a corrosion cast than performing 3-D reconstruction of microvessels. Figure 3-20 presents an example where the portal veins were injected with red resin and the hepatic veins with blue one. Here too, one can see the isodistant spatial arrangement of the vessels as seen in Fig. 3-7. Despite its easy accessibility, however, a resin cast hardly serves if one attempts to quantitatively analyze the 3-D microvasculature of organs, for example by measuring the 3-D distance from a random point to the vessels. It is for this reason that the author preferred serial sections analysis to the use of vascular casts.

### Distribution of $L$ in normal liver (Fig. 3-21)

Figure 3-21 demonstrates the result of measurement in a normal liver, in this case on 325 points. Clearly, the spatial distance  $L$  follows a normal type distribution, and so does it in any organ examined. The mean  $L$  is calculated at 352  $\mu\text{m}$ , which corresponds to the mean length of sinusoidal routes because most of the sinusoids appear taking approximately the shortest linear course towards the central vein. It is noteworthy that the value is in good accordance with the mean lobular radius obtained in the foregoing chapter by applying stereology to a cylindrical model (Fig. 2-39).

As explained, the aim of this analysis has been to compare the dispersion of  $L$  among organs. But, the standard deviation of  $L$  was not an appropriate parameter,

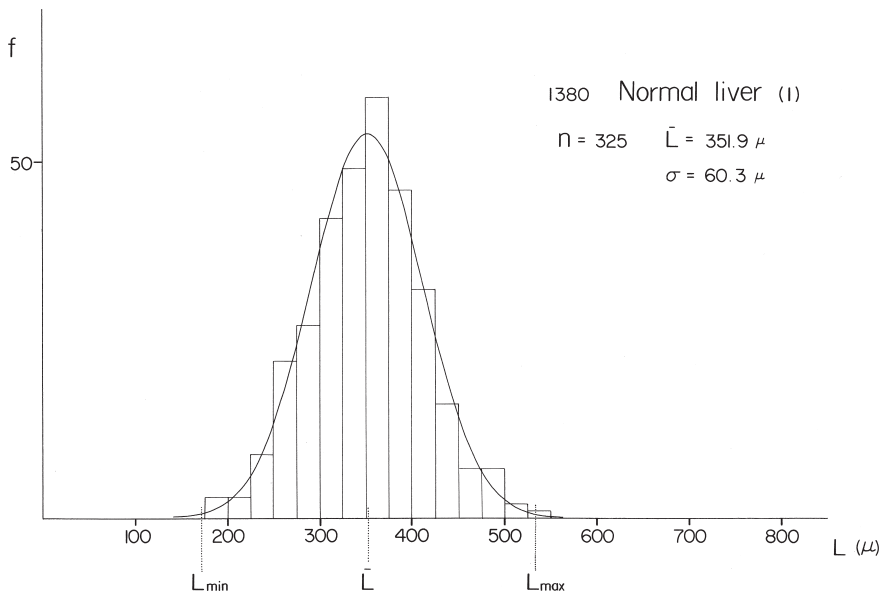


Fig. 3-21. Distribution of  $L$  in a normal liver based on a measurement with regard to 325 sampling points. Note quite a normal type distribution. The mean  $L$  is calculated at  $352 \mu\text{m}$ , a value exactly corresponding to the mean radius  $R$  of hepatic lobule obtained stereologically (Fig. 2-39). The dispersion of  $L$  is expressed by the "vasculature index," the ratio of  $L_{\text{max}}/L_{\text{min}}$ , with both  $L_{\text{max}}$  and  $L_{\text{min}}$  defined at  $3\sigma$  levels, i.e., the mean  $L \pm 3\sigma$ . In the liver, the index proved to be 3.0, the minimum of the organs examined, showing that indeed, the organ is equipped with a microvasculature that is the most isodistant. Reproduced from Takahashi (1970): *Tohoku J exp Med* 101, pp. 129.

because there was a certain between-organs difference in the mean  $L$ . Therefore another method was introduced. Since the distribution of  $L$  could be approximated by a normal distribution, its upper and lower limits were defined at  $3\sigma$  levels, the mean  $\pm 3\sigma$ . Here, if the ratio of the maximum  $L$  (mean  $L + 3\sigma$ ) to the minimum  $L$  (mean  $L - 3\sigma$ ) is calculated, it would serve as an index of vasculature, describing to what degree the afferent-efferent distance is uniform. The smaller the index, the more uniform the distance, and vice versa. In the normal liver of Fig. 3-21, we obtained an index value of 3.1. We examined a normal liver from another patient and obtained an index of 2.9. Thus, the quantity for the normal liver proved to be about 3.0.

### Organ difference in the distribution of $L$ (Table 3-2)

In Table 3-2, the index values are compared among five organs, the liver, lung, cerebral cortex, myocardium and kidney. It is shown that the value of 3.0 of the liver is by far the smallest, and demonstrates that certainly, this organ is equipped with a vasculature prominent in isodistance. It exceeds 50 in some organs of systemic circulation.

Table 3-2. Comparison of vasculature index  $L_{\max}/L_{\min}$  among the organs examined. Note that in the liver the index value is the smallest, showing the most isodistant vasculature among the organs.

Organ	mean $L$	$\sigma$	$L_{\max}$	$L_{\min}$	$L_{\max}/L_{\min}$
Normal liver(1)	352	60	533	171	3.1
(2)	419	69	625	214	2.9
Lung	218	50	368	69	5.4
Cerebral cortex	165	45	299	31	9.7
Myocardium	168	54	330	6	51.1
Renal cortex	267	86	525	10	54.7
Chronic hepatitis(1)	377	129	919	155	5.9
(2)	350	129	853	144	5.9
(3)	577	135	1466	227	6.5
Liver cirrhosis (1)	528	175	1770	158	11.2
(2)	572	181	1995	164	12.2

### Normal liver: a re-consideration upon microphotograph (Fig. 3-22)

The liver of man comprises a uniformly continuing parenchyma as in Fig. 3-22. Here the blood vessels seem to be enjoying the greatest freedom with which they spread in the space, realizing an ideal isodistant relation. Perhaps the structure of lobules as polyhedra packed in the space may have been another aspect of this extremely isodistant vascular arrangement. In the figure, a 2-D section of the liver, the contours of lobules as packed polygons are visualized on account of mild hydropic changes of hepatocytes in the central zone of lobules.

Still, we have a question. What is responsible for the variety of 3-D vasculature patterns? From a purely microcirculation point of view, the isodistant pattern must be the most advantageous, since it ensures the most stable and uniform distribution of blood. Nevertheless, it is allowed to exist only in the liver, and to lesser degree, in the lung. Why such an organ difference? Let us consider about the background of this variety by comparing the liver with the lung, as in the following.

### d) Why does the vascular pattern differ among organs?

#### Three-D vasculature of lung (Fig. 3-23)

Figure 3-23 is a manually performed reconstruction of small pulmonary arteries and veins in a normal human lung. At a glance, the vascular pattern seems to be isodistant to a similar degree as in the liver. However, there is a small difference. The terminal vessels tend to curve so as to wrap spaces about 500  $\mu\text{m}$  in diameter, as depicted by dots in the upper, middle left and lower left parts of the figure. By closer observation, one may realize that similar spaces are ubiquitous, and the whole lung tissue consists of an assembly of such spaces. In terms of microanatomy, each of these

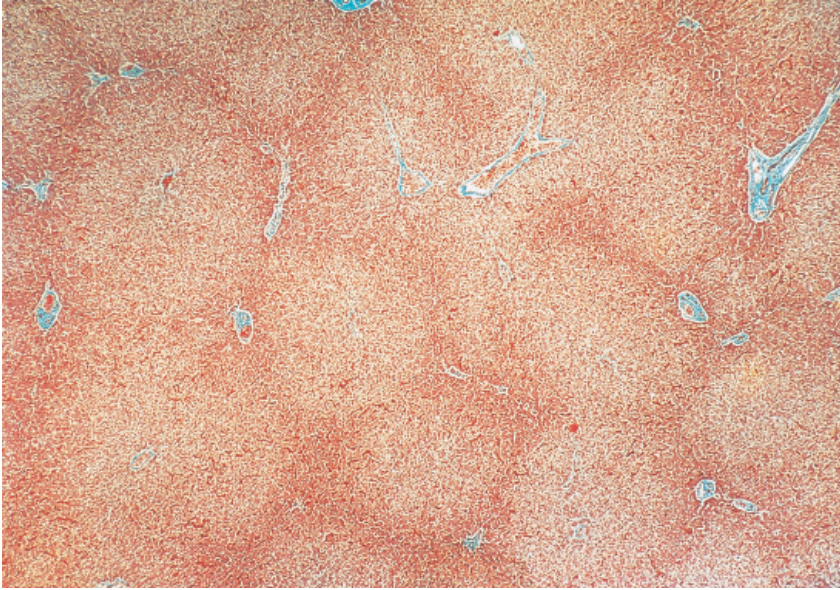


Fig. 3-22. A microphotograph of human liver. The polygonal lobules are visualized on account of mild hydropic changes of hepatocytes in the central zones of lobules. Elastica-Goldner stain.

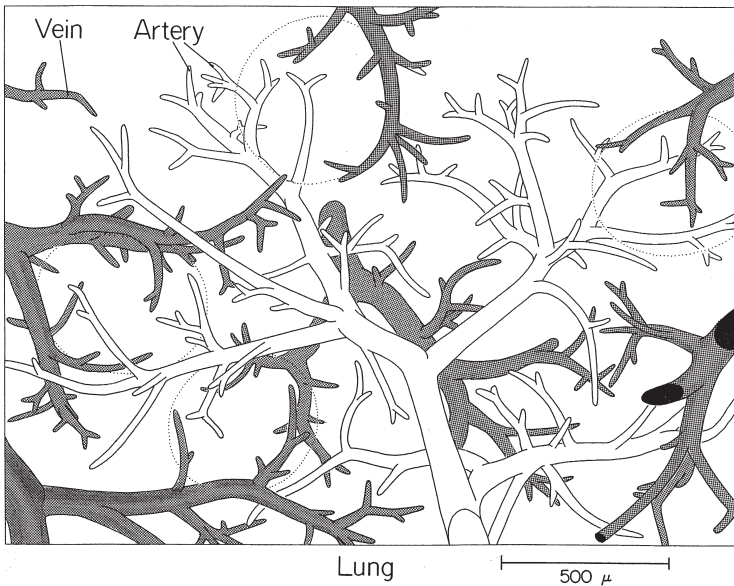


Fig. 3-23. The 3-D microvasculature of the human lung, visualized by manual reconstruction. The vessels shown white are pulmonary arteries and those shaded are pulmonary veins. The pattern of vasculature seems to be isodistant, but there is a difference from the liver. As denoted by dots, the small lung vessels tend to wrap a space 0.5 to 0.6 mm in diameter, which anatomically corresponds to either an alveolar sac, or a segment of alveolar duct. Reproduced from Takahashi (1970): *Tohoku J exp Med* 101, pp. 131.

spaces corresponds to either an alveolar sac or a segment of alveolar duct, including the alveoli opening there. In contrast to the liver where the afferent and efferent vessels penetrating the parenchyma can take any position, an alveolar sac as well as alveolar duct of normal lung is an air space which does not allow arteries or veins to enter its interior as a naked vessel not contained in alveolar septum. While in the 3-D picture of Fig. 3-23 the lung vessels seem to be arranged in an isodistant fashion, in reality, it is only among the vessels enclosed within the alveolar septa that the isodistance is realized.

### Three-D vasculature: difference between the lung and liver (Figs. 3-24, 3-25)

A slight deviation in the lung from the highest regularity is reflected in the distribution of  $L$  (Fig. 3-24). Here the index of vasculature is 5.4, a little larger than in the liver where it was 3.0. The background underlying this difference discloses itself in the microstructure of lung as shown in the next figure.

Figure 3-25 is a sketch of lung tissue and here, one thing is to be pointed out. The small pulmonary arteries (white), as well as veins (black), are all deployed in the wall of the airways. But the airways from bronchi to bronchioles to ductus alveolaris (d.a.) to alveoli are all organized into a tree, following a principle that is considered to give the lung a condition optimal for ventilation function (One may have a glimpse of what the principle looks like, in the studies published by Kitaoka *et al.*, 1999). In other words, in the lung, the degree of freedom assigned to the structure of blood vessels is correspondingly reduced.

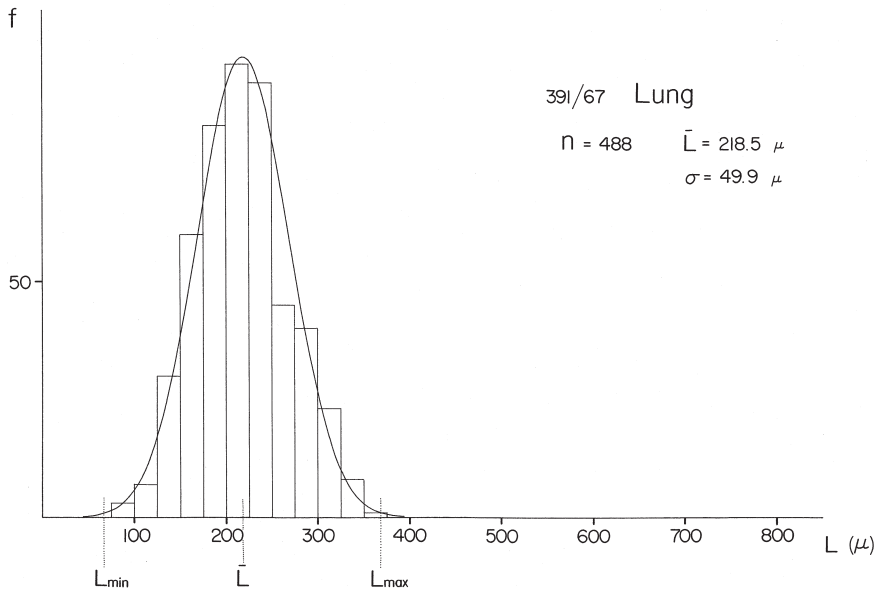


Fig. 3-24. The distribution of  $L$  in a normal human lung. A fairly isodistant pattern with comparatively small dispersion of  $L$ , but the vasculature index is 5.4, a little higher than in the liver. Reproduced from Takahashi (1970): *Tohoku J exp Med* 101, pp. 131.



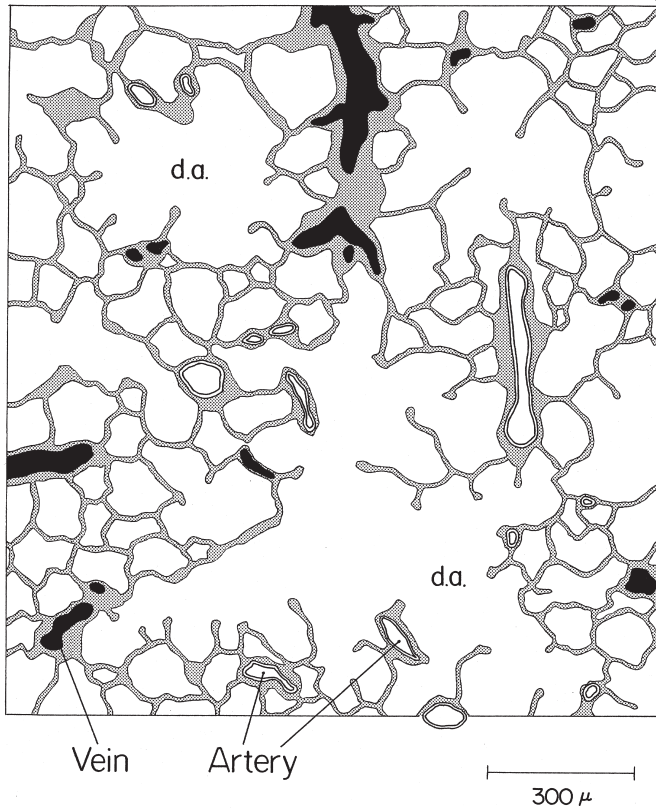


Fig. 3-25. On one of the serial sections of lung, the microscopic picture was projected on a sheet of paper, and the contours of airways, alveoli and blood vessels were drawn by tracing. d.a.: ductus alveolaris. Of the blood vessels, pulmonary arteries are shown white, pulmonary veins black. Reproduced from Takahashi (1970): *Tohoku J exp Med* 101, pp. 133.

### The isodistant vasculature and the structure of liver parenchyma (Figs. 3-26, 3-27)

Based on the above discussion, let us re-examine the parenchymal structure of the liver. The liver is the central organ of metabolism, but at the same time it works as an exocrine gland secreting bile as stressed by Rappaport. Figure 3-26 is a microphotograph of human liver impregnated with silver. There are capillaries densely connected to form a fine network. Flanked by capillaries are hepatocytes arranged in the form of one-cell thick plates, that are forming another network intertwined with the capillaries.

Figure 3-27 is a schema explaining the 3-D structure of liver parenchyma which is penetrated by a network of capillaries (s: sinusoids). The hepatocytes forming one-cell plates secrete bile into the bile canaliculi (bc), another fine network extending along the border between a pair of neighboring hepatocytes. This is a unique type of



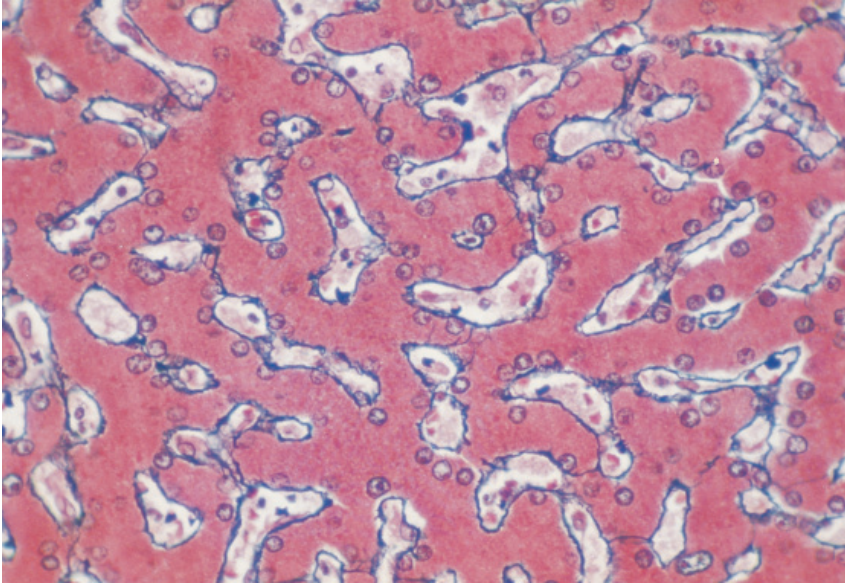


Fig. 3-26. High power microscopic appearance of normal hepatic parenchyma of man. Hepatocytes are arranged into forming thin, one-cell thick plates, the liver cell plates, which are organized into a fine 3-D network that are closely intertwined with the capillary network, the void spaces. Gomori's silver stain.

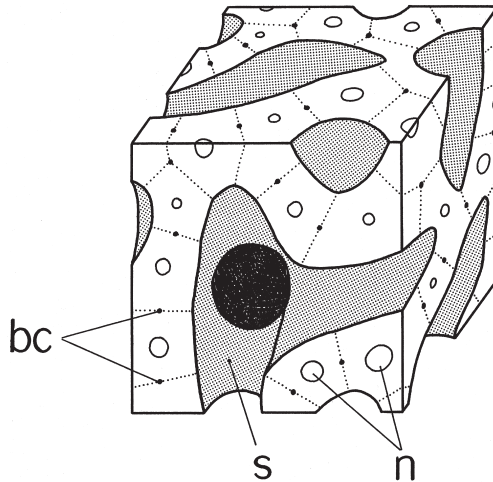


Fig. 3-27. A schema of 3-D parenchymal structure of the liver. The mass of liver cells is densely penetrated by capillaries, also called sinusoids (s), that leave the liver cells in the form of one-cell plates. Liver cells secrete bile into bile canaliculi (bc), another fine network extending along the border between a pair of neighboring liver cells.

exocrine gland called a netlike gland where no such hierarchic arborization exists as found in the ductal tree of usual gland. Thus, although the liver is a sort of exocrine gland, it presents quite a specialized one, requiring little if any structure of its own.

### An organ is composed of different functional systems (Fig. 3-28)

The regular isodistance may be the pattern of vasculature ideal for microcirculation, because it ensures uniform irrigation of blood even in organs where the peripheral vessels are not equipped with apparatuses for blood flow regulation. However, this ideal type of vasculature cannot always be realized, because every organ has functional systems other than the vascular system, each of which requires a structure most adequate for its function. For example, the lung has, besides the blood vessels, the airway system which requires a design adequate for its ventilation function. However, the different systems have to co-exist in a limited space somehow. The circumstances are the same in any organ. Besides the vascular system, the renal cortex has nephrons, the myocardium has a system of heart muscles, and they are all arranged in the space according to a rigorous rule. Thus, we find in actual organs a vascular pattern that is more or less contiguous, but this seems to be a result of compromise. Why in the liver the most ideal isodistant vasculature is realized may be understood if the other functional system of the liver, the bile-secreting gland system, is considered. As above, we find in the liver quite a specialized gland, requiring little if any structure of its own, thus allowing the vascular system to enjoy the highest degree of freedom to spread in the space and create a vasculature which is the most optimal for microcirculation. Figure 3-28 is a schema in which the transverse length for each of the rows is meant to express, in arbitrary fashion, the degree of freedom assigned to the functional system to form a structure adequate for its function.

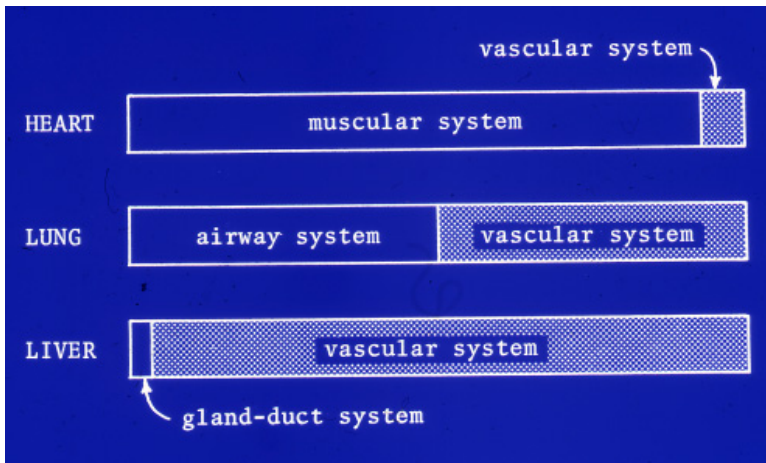


Fig. 3-28. A schematic presentation showing that an organ comprises several functional systems, and that to each of the systems, various degree of freedom is assigned with regard to the structure. For explanation see the text.

### e) Pathogenesis of hepatic failure in cirrhosis

#### The structure of cirrhosis: 2-D and 3-D (Figs. 3-29, 3-30)

Now let us see how the above discussion helps us understand why livers with cirrhosis are apt to develop hepatic failure, one of the major causes of death among cirrhotic patients. Figure 3-29 is a microphotograph of cirrhotic liver from a patient suffering from chronic hepatitis C for about 20 years. Here it is shown that a cirrhotic liver consists of two elements: the round nodules stained red-brown, and the interstitial zones stained green. The interstitium is the scar zone left after the hepatocytes were destroyed in an active phase of inflammation. The nodules are clumps of hepatocytes that were exempted from damage and are regenerating. In Japan, the prime cause of hepatocellular damage leading to cirrhosis is chronic hepatitis, either B or C, but in Western countries, it is said to be alcohol abuse.

Figure 3-30 is a computer-aided reconstruction of cirrhotic liver. The green wireframes denote the nodular profiles, painted in red are portal veins and those in blue are hepatic veins. One can see that almost all the vessels are running in the interstitium, and at many places they are making anastomoses in the form of P-C, the portal-central, bridging. Obviously, this implies a change from the isodistant vascular pattern of the normal liver into a contiguous pattern. Or in other words, what we find here is a breach of the basic structural principle of the liver. In this situation, the blood flowing in from the portal vein is apt to escape to the hepatic vein without making necessary contact with hepatocytes which are confined in the nodules. Thus the hepatocytes seem to be living upon a small part of portal blood not shunted away through

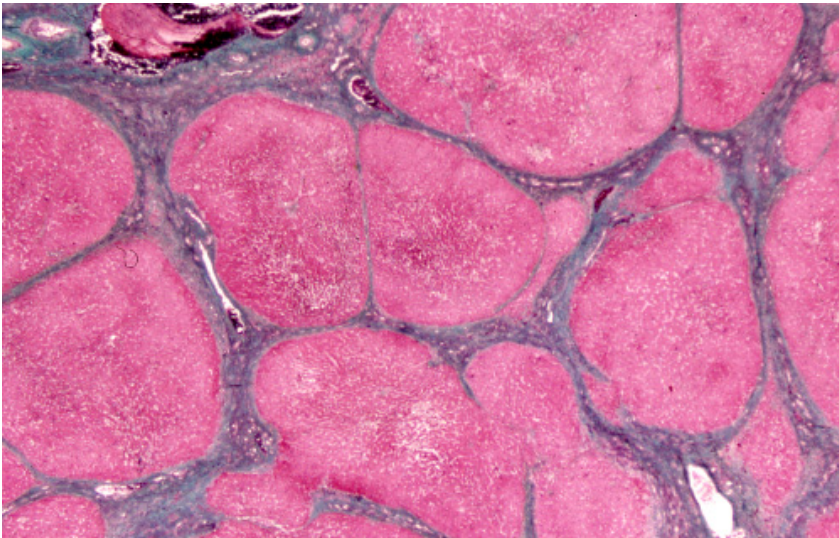


Fig. 3-29. Microscopic appearance of cirrhotic liver that consists of nodules (red-brown) and interstitial zones (green). The nodules are masses of regenerating hepatocytes, and the interstitium is the scar zone left after the hepatocytes were destroyed in the active phase of liver injury. Elastica-Goldner stain.

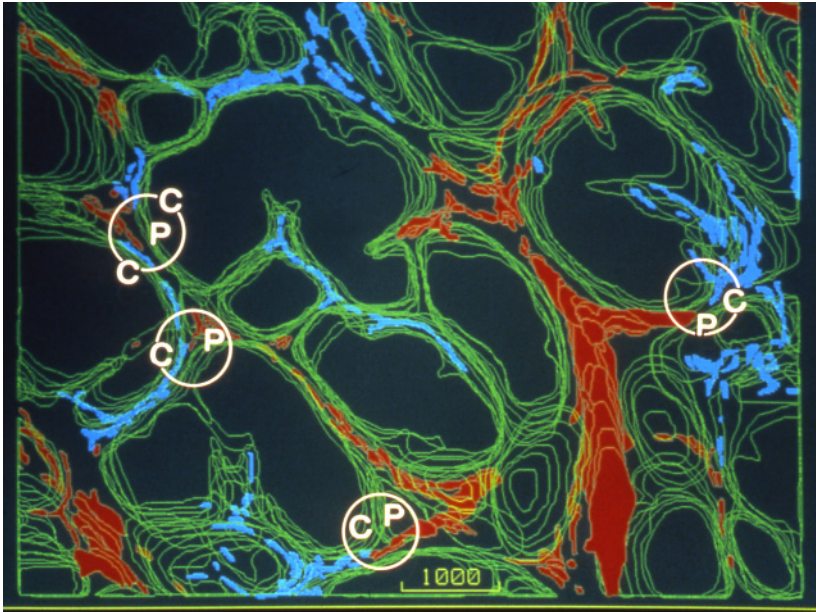


Fig. 3-30. Computer-aided 3-D reconstruction of cirrhosis. The green wireframes denote the contours of nodules. The vessels painted red are portal veins, and those blue are hepatic veins. Note that both of the vessels are mostly running in the interstitial zones. At several places one can find anastomosis between the terminal portal and central (hepatic) veins, forming a portal-central bridging as denoted by PC. This means that the isodistant vasculature of normal liver is lost and replaced by a contiguous arrangement.

the interstitium. In consequence, the liver cannot sufficiently detoxify the portal blood, and thus, hepatic failure ensues. And now we understand that all these are attributable to the deviation of vasculature from the normal isodistance.

### Vasculature change in cirrhosis described by the distribution of $L$ (Fig. 3-31)

Now that the development from normal livers over chronic hepatitis to cirrhosis is reduced to a change of vasculature from isodistance to contiguity, we can assess the progression with the index of vasculature. Figure 3-31 presents the result of measurement of  $L$  in three livers with chronic hepatitis and two cirrhotic livers, combined with the two normal livers shown above. One can see the distribution of  $L$ , while narrow-ranged in normal livers (green), become progressively flattened over chronic hepatitis (yellow) to cirrhosis (red). The index value which was normally 3.0, is elevated to 10 or more in cirrhosis (see Table 3-2, p. 87). Thus, the spatial distance distribution allows us to describe the degree to which the microvasculature is deviated from its normal state. How can the deviation occur? This is understood by studying livers with diseases preceding cirrhosis, which will be shown in Chapter 6.

In the present chapter it might appear that 3-D reconstruction was used only as a tool for obtaining the index of vasculature, but while performing reconstruction, a



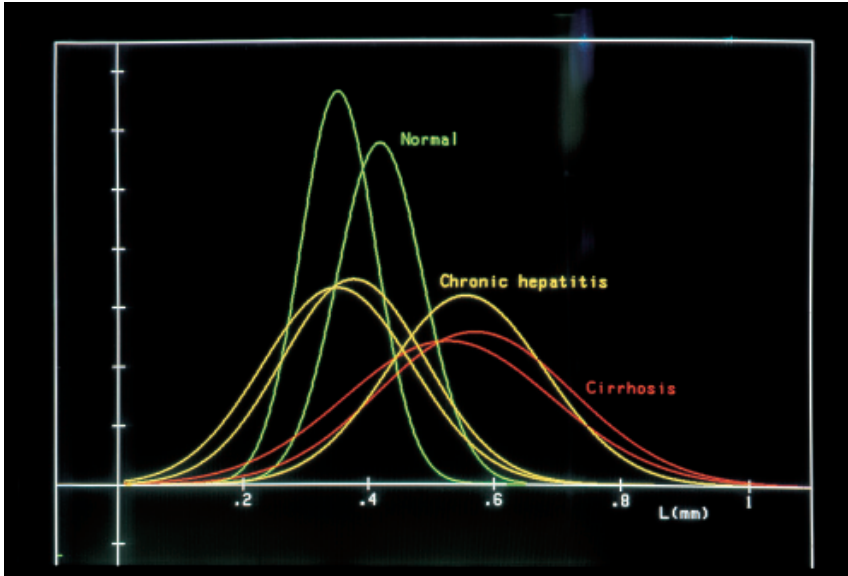


Fig. 3-31. The distribution of  $L$  was examined in two normal livers (green), three livers with chronic hepatitis (yellow) and two cirrhotic livers (red). Note that the dispersion of  $L$  becomes increasingly large with the progression of disease from chronic hepatitis, a pre-cirrhosis, to cirrhosis.

variety of knowledge and concepts on the structure of various organs have been obtained. In the next chapter, the technique of 3-D structural analysis will be introduced. Let us see how it can be applied to various problems of pathology.

## Three-D Structural Analysis: Method and Examples of Application

### 1) Preparation of serial sections

#### Serial microscopic sections (Fig. 4-1)

The first step of 3-D structural analysis is to prepare serial sectional (2-D) images of material one intends to study. Various 2-D images are available. The most familiar in the domain of pathology is of course microscopic serial sections (Fig. 4-1), but organ slices for macroscopic observation or ultrathin sections for electron microscopy, if sequentially prepared, can also be used.

In preparing serial microscopic sections using a conventional type of microtome, I suggest to select carefully the embedding medium for the tissue to study. A material, if embedded in ordinary paraffin, may be prone to tearing and distortion at sectioning, which can create serious flaws in 3-D reconstruction. It seems that paraffin is not durable enough to allow us to make a set of flawless sections. To minimize the artifact, I advise to use celloidin-paraffin instead of ordinary paraffin as embedding medium. However there is a disadvantage inherent in this method: celloidin-paraffin sections do not promise good results when immunostained or silver impregnated. Also they are apt to wrinkle in the process of extension in a water bath.

Sometimes we need to study macroscopic or submacroscopic structures. In this case, microscopic sections from a tissue block, usually smaller than  $3 \times 2$  cm, cannot always cover the area of interest. The same difficulties will be encountered when spatial distribution of lesions in a large organ has to be studied. In such cases, preparation of serial organ slices is indispensable. If either the whole, or a part, of a fixed organ is to be sectioned, a practicable method is to “embed” the material in gelatin and slice a gelatin block with a ham slicer (Suzuki *et al.*, 1988). This allows us to obtain good serial slices with suitable thickness, usually 1 to 1.5 mm. An example will be shown in Fig. 4-42, a set of “macroserials” of liver lobe surgically removed for carcinoma. Gelatin embedding is particularly desirable when a flabby material is to be serially sectioned. This would be understandable if you imagine that a material prone to transformation, like human pancreas or breast, has to be serially sliced, constantly at a thickness of 1 mm. The embedding procedure is quite simple: only to keep the fixed material in a container filled with 20% gelatin solution and cool it in a refrigerator. Gelatin solution can be replaced with 4 to 5% agar solution or 8% celloidin solution (in ether alcohol).

Sometimes, while performing 3-D mapping of lesions in an organ sliced into 1





Fig. 4-1. Serial microscopic sections prepared to study the 3-D structure of gastric adenocarcinoma. Stained by Azan-Mallory method.

mm-thick “macroserials,” we are required to confirm microscopically where the lesion in question exists and is extending. In this case, the slices have to be re-embedded in paraffin so as to obtain microscopic sections stained with some appropriate method. Here one had better devise a slice holder to prevent the slices from being bent through the process of dehydration and embedding. We use a thin box made of veneer sheets, with 1 mm interior thickness; the veneer sheets were made porous so as to permit free flow and diffusion of embedding medium.

## 2) Abstraction of 2-D images from serial sections

### Structure of interest: profile abstraction using a projector (Figs. 4-2, 4-3, 4-4)

First of all, we have to prepare serial 2-D drawings or pictures from a set of serial sections. These should contain the profiles of structures that are extracted from the microscopic pictures and are to be reconstructed. Suppose that you are going to reconstruct peripheral airways and arteries of lung from a set of serial sections. Besides airways and arteries, microscopic pictures of lung contain “noises,” the components that are not necessary and should be excluded: veins, connective tissue wrapping airways and blood vessels, interlobular and alveolar septa, and if there are inflammatory changes, exudates or granulation tissue. This is the very reality of microscopic pictures, and from these, one has to pick up only the profiles of airways and arteries. In most cases, recognition and extraction of necessary images have to be done with our



Fig. 4-2. A profile microprojector, Nikon model V-16C, useful for picking up necessary contours of structure from serial sections at various magnification.

own eyes and hands. As yet, we are not in the stage of technical development in which we can leave this laborious job to a computer-driven robot. An automatic extraction of profiles can be expected only when in a material, a certain microstructure is marked by fluorescent immunohistochemistry and submitted to image acquisition using a fluorescence microscope. A laser confocal microscope, if available, enables one to scan the tissue along the  $z$ -axis and obtain continuously changing, fluorescent sectional images (tissue tomograms) which can be conveyed to a computer for 3-D reconstruction in the display. However, this is essentially a sort of (transmission) light microscope, so that there is a limit in the tissue thickness (usually less than hundred  $\mu\text{m}$ ), beyond which, opacity of tissue would make it hard to penetrate even for laser beam.

The best way to abstract the necessary images from serial microscopic sections, I think, is to use a profile projector of the type shown in Fig. 4-2. This is an optical device with which one can project a microscopic image on a screen at a magnification from  $\times 5$  to  $\times 200$ . If a mercury bulb is available as the light source, one can obtain pictures of higher magnification, up to  $\times 1,000$ . Usually, images are projected onto a

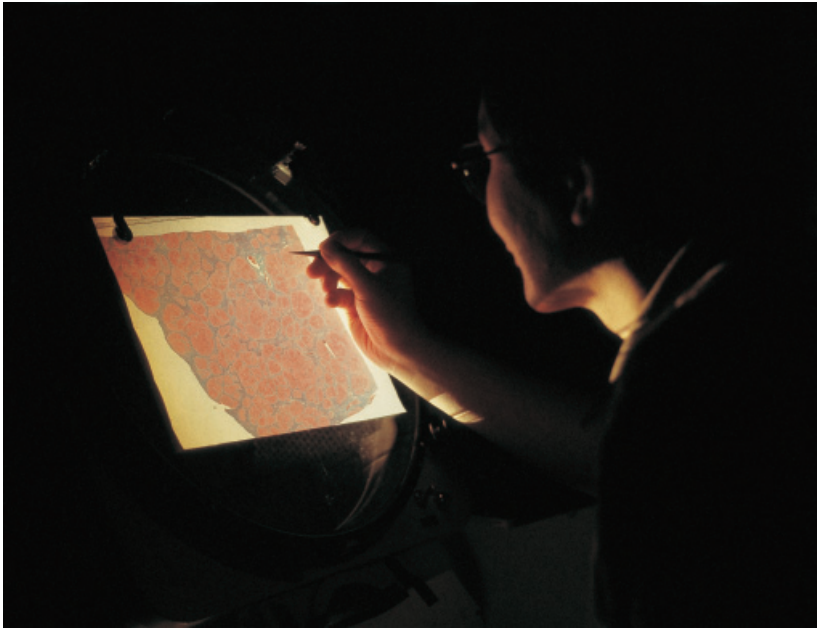


Fig. 4-3. Tracing of profiles to be reconstructed using the projector of Fig. 4-2. A sheet of tracing paper is placed on the screen, upon which the microscopic picture is projected at various magnification.

sheet of tracing paper placed on the screen, and the structures of interest are faithfully delineated along their profiles as in Fig. 4-3.

If a profile projector is not available, then try to project the optical field of microscope directly on a sheet of tracing paper using a simple, makeshift projector, an example of which is shown in Fig. 4-4. One only has to prepare a monocular microscope equipped with Köhler illumination. In a darkroom, a clearly focused projection of image is obtained at a distance 50 to 100 cm from the ocular lens. There is however a drawback in this method. The projected image is more or less distorted in the peripheral area of the round optical field due to spherical aberration inherent in the optical system, leaving only the central area adequate for analysis. Instead of delineating a projected image, you can of course use an enlarged microphotograph, but so long as relying on a microscope, aberration-free images are hard to obtain. In contrast, the profile projectors of the type shown in the foregoing figures are designed to keep the aberration below a minimum level so that they can serve specifically for the examination of precision products like semiconductors or microchips.

Sometimes, in performing reconstruction, accuracy is required to align sequential 2-D pictures rigorously with regard to the position and orientation. Several methods of alignment have been proposed. For example, one can rely on some guide marks such as the contour of the tissue block trimmed exactly vertically to the plane of section. Structures continuing in the tissue, such as the blood vessels, nerves etc., also serve as a guiding mark.



Fig. 4-4. A makeshift projector making use of a monocular microscope, equipped with Köhler illumination.

### 3) Manual reconstruction

#### Observation of 3-D by stacking serial images (Figs. 4-5, 4-6)

If a set of serial 2-D images have been completed, place the drawings sequentially on an X-ray film illuminator. Then the 3-D structure is visualized in a series of images gradually changing along the  $z$ -axis. In Fig. 4-5, serial pictures from an adenocarcinoma of stomach are stacked and looked through in order to see the 3-D form of cell nests. The result of observation can be expressed in the form of stereogram, *i.e.*, a manually drawn, graphic expression of spatial structure.

Figure 4-6 is another example of manual reconstruction aimed at visualizing the course and ending of the vasa efferentia of renal glomeruli (Takahashi, 1970). Normal renal cortex obtained at autopsy was serially sectioned, and reconstruction was per-



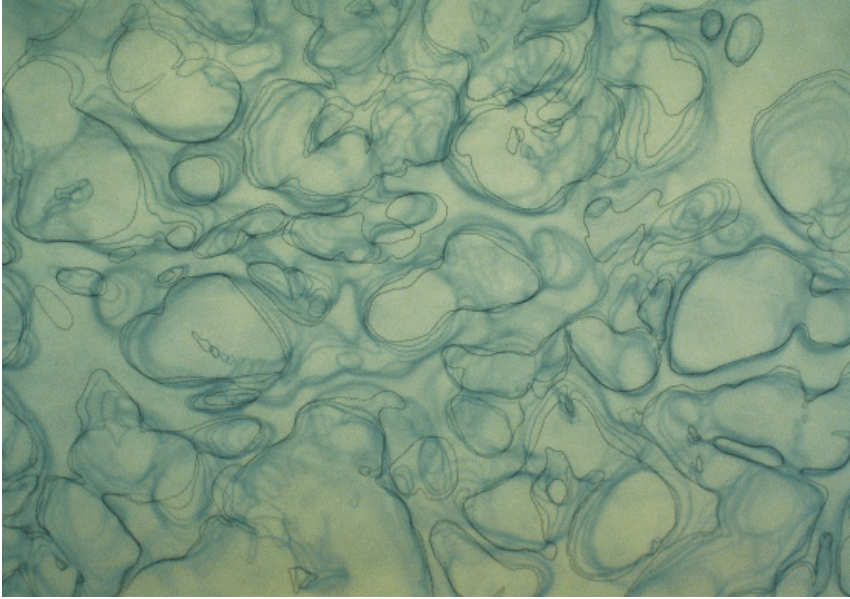


Fig. 4-5. A series of profile tracings are stacked and looked through upon an X-ray illuminator. From serial sections of moderately differentiated adenocarcinoma of the stomach. The 3-D structure of carcinomatous nests is clearly visualized.

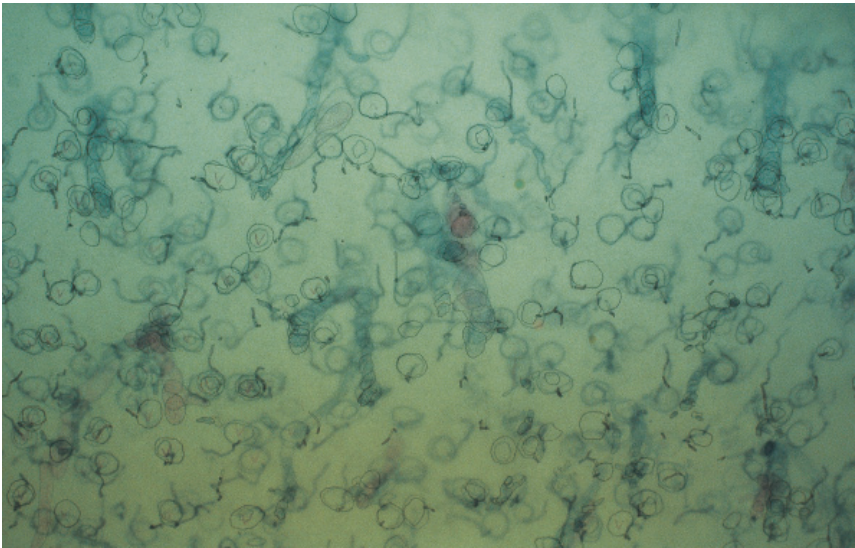


Fig. 4-6. A stack of serial tracings of normal kidney is looked through. The aim of this reconstruction was to see how vasa efferentia of glomeruli run in the cortical tissue and where they terminate. For this, hundreds of pairs of vasa efferentia and glomeruli were traced from serial sections of kidney.

formed over a thickness of 1.2 mm. All the glomeruli, vasa efferentia, veins and venules contained in the thickness were drawn. It was demonstrated that the vasa efferentia, 200 to 400  $\mu\text{m}$  in length, have only sparse ramification, run through the cortical labyrinth and, interestingly, end at the outer boundary of the medullary ray without exception. The physiological significance of this distribution remains to be elucidated. In this example, the serial drawings were prepared at a thickness interval of 32  $\mu\text{m}$ , i.e., every eight sections, with a single section 4  $\mu\text{m}$  thick. Thus, there is no rule in the coarseness or fineness of reconstruction with regard to the inter-sectional interval, but from an economical and time-sparing viewpoint I would like to suggest to design a reconstruction study so that, the necessary knowledge may be obtained with a least number of serial images, if possible within 50 steps.

#### 4) Computer-assisted reconstruction

##### Axial view of bronchus (Fig. 4-7)

Though simple and practicable with little expense, the manual method works only in studies dealing with an object which is relatively uncomplicated. If not, it sometimes happens that one is brought to confusion in a labyrinth of microstructure. When analyzing such a complicated structure as a 3-D network intertwined with blood vessels, one would be exhausted before completing a sufficiently accurate stereogram. Even if we manage to complete one, the stereogram only presents a picture viewed from a fixed angle, i.e., perpendicular to the plane of section. In reality, there are

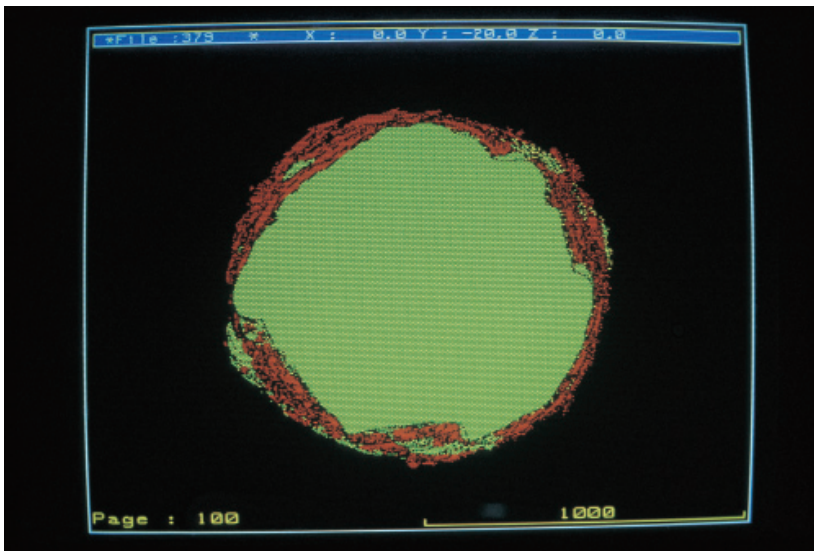


Fig. 4-7. Computer-aided reconstruction of a membranous bronchiole, presenting an axial view, in contrast to Fig. 1-11 where the same material is reproduced to show a lateral view. Reproduced from Yaegashi, Takahashi, *et al.* (1986): *J Microsc* 146, pp. 57.



instances in which we cannot attain a full understanding of 3-D structure unless views from different angles are combined. For example, figure 4-7 is a computer-assisted reconstruction of a bronchial segment which was serially cross sectioned. So long as relying on manual method, one would be unable to see, in its lateral view, how the smooth muscles (red) are arranged in the wall. This is however clearly visualized by resorting to a computer system which reproduces a lateral view of the segment as previously shown in Fig. 1-11. There the smooth muscles are shown following a spiral course with an inclination of about 25 degrees. This sort of image transformation cannot be attained without computer-assist.

#### **A system assisting 3-D structural analysis (Fig. 4-8)**

In 1986, our team designed a system for 3-D structural analysis for the study of pathology and microanatomy (Takahashi 1986; Yaegashi *et al.*, 1987), which was produced by what was a nascent team of engineers, that has since then developed into Rise Corporation, Sendai, Japan. Based on a desktop computer with a color display and a graphics tablet, this was probably the first reconstruction system designed for biomedical research and put to practical use (Fig. 4-8). The software, written in Hewlett-Packard BASIC at the first trial, has been updated several times, now working on WINDOWS. It covers basic functions of 3-D reconstruction including data input, data processing for visualization of 3-D structures at various magnification, style, color and angle, and basic 3-D measurement. A series of 2-D pictures are inputted from a graphics tablet where an image profile is digitized into a series of xy coordinate values. When a set of sequential 2-D pictures have been inputted, basic conditions for reconstruction are given, including the angle of viewpoint, the magnification of image, color for different structures or expression styles. Sometimes one need to repeat reconstruc-



Fig. 4-8. A system designed to assist the analysis of 3-D organ structure (OZ system, produced by Rise).

tion trial before obtaining an appropriate condition. Shown in the following are examples of reconstruction, some of which were performed by manual method before the advent of computer-assist.

## 5) Examples of 3-D reconstruction

### a) The vasa vasorum of aortic wall

#### Vasa vasorum of the aorta (Fig. 4-9)

Larger arteries of adults like the aorta or pulmonary arteries are thick-walled, with the smooth muscle layer, called the media, as thick as 2.0 mm at the ascending aorta of a normal adult. In general, the smooth muscle cells of media is sustained in two ways. On one hand, the cells are considered to rely on oxygen and nutrients carried by molecular diffusion either from the luminal blood or from small vessels of the adventitia. The other media-sustaining mechanism is a continuous flow of plasmal fluid which is filtered through the endothelial barrier, permeates through the wall and drained by venules or lymphatics of the adventitia (Linzbach, 1958). However, it seems that when the medial thickness surpasses a certain limit, the artery can no longer sustain its medial layer without the aid of vasa vasorum. The vasa vasorum are minute blood vessels that penetrate the wall from the exterior of an artery. Distributed within the outer medial layer, they are considered to help the smooth muscle cells subsist. Figure 4-9 is a microphotograph of the outer medial layer and adventitia of normal human aorta. The adventitia is the layer of connective tissue one can find in the upper



Fig. 4-9. Microscopic appearance of the human aortic wall to show the vasa vasorum (white arrowhead). The uppermost layer is the adventitia made of collagen (green). The vasa vasorum are minute vessels sporadically deployed in the outer layer of media. Elastica-Goldner stain.

1/4 of the figure where thick collagen fibers, stained in green, stack up. The lower 3/4 is the outer part of the media and here, a few vasa vasorum are deployed in the smooth muscle layer.

### Density of vasa vasorum in the aortic wall: morphometry (Fig. 4-10)

Okuyama *et al.* (1988a) made a morphometric study of aorta and its large elastic type subbranches to make clear the relation between the thickness of arterial media and the development of vasa vasorum, with the latter expressed by the density of the tiny vessels in the medial layer. The left part of Fig. 4-10 illustrates the geometric significance of the density. In a cross-section of arterial wall, the number of vasa vasorum was counted along a sampling line ( $L$ ), and the mean number  $N_L$  per a unit line length was calculated.  $N_L$  is a quantity proportionate to the mean total length  $L_A$  of vasa vasorum in a unit area  $A$  of wall (the length density in area). The result of measurement is shown in the right figure where the medial thickness  $D$  is shown in the abscissa, and  $L_A$  in the ordinate. The density of vasa vasorum rises as the arterial wall thickness  $D$  increases, and there is an intimate exponential correlation between  $L_A$  and  $D$ . Here one can see that the regression curve crosses the abscissa at  $D = 0.6$ , showing that in average, the vasa vasorum emerge when the medial thickness of an artery exceeds 0.6mm. In other words, the arterial media can be sustained in an avascular state only when it does not exceed this critical thickness.

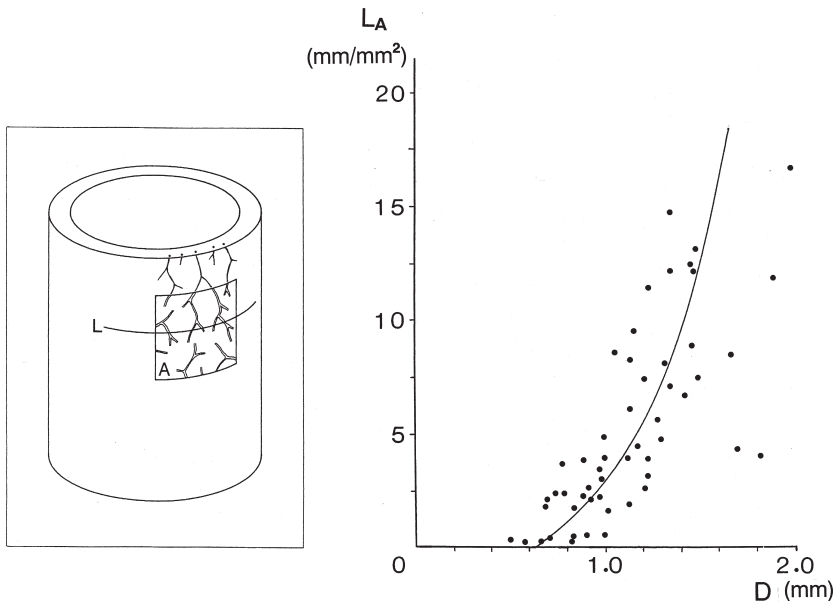


Fig. 4-10. The density of vasa vasorum in the aortic wall studied by morphometry. Left: the method of morphometry. Right: the density of vasa vasorum  $L_A$  plotted against the medial thickness  $D$  of the aortic wall. The density  $L_A$  is defined as the length density of the vessel per a unit area of aortic wall, as in the left. Note that the vasa vasorum develop exponentially along with the thickening of wall. Reproduced from Okuyama, Takahashi, *et al.* (1988): Arch Pathol Lab Med 112, pp. 723.

However, at the time the study of Okuyama *et al.* was performed, no information was available about the distribution of these minute vessels in the arterial wall, motivating the authors to undertake 3-D visualization (1988b).

### Three-D structure: vasa vasorum of normal aorta (Figs. 4-11, 4-12)

Figure 4-11 is a schema illustrating how serial sections were prepared from arterial wall. A patch of wall tissue, about  $1 \times 1$  cm, was taken from the wall of normal ascending aorta as in the figure. The material embedded flat in celloidin-paraffin was subjected to serial sectioning so as to produce the sections parallel to the wall surface.

The result of 3-D reconstruction is shown in Fig. 4-12 and presents what the vasa vasorum look like when observed from an angle vertical to the plane of aortic wall. The picture discloses quite a peculiar character of these vessels that perhaps one would be unable to find in any other part of the human body. First, it is shown that the media of the aorta is not provided with the usual network of capillaries. Instead, the vasa vasorum, while including terminal arterioles (shown red), venules (blue) and capillaries (beige), are distributed at a density that is strikingly low. They have been found to run in special tunnels that are penetrating the media as sparsely deployed tracts, with a pair of neighboring tunnels having a distance as large as 0.5 to 1.0 mm interposed between them, while in ordinary capillaries the mesh size does not exceed 0.15 mm. On account of this, we introduced a term “vascular cord” for these tracts. Second, it is clearly visualized that the vasa vasorum divide in the form of tree instead of network found in ordinary capillaries, and moreover, run in the tunnels as parallel double track. An inlet part of capillary forwards to and reaches the blind-ended terminal of tunnel,

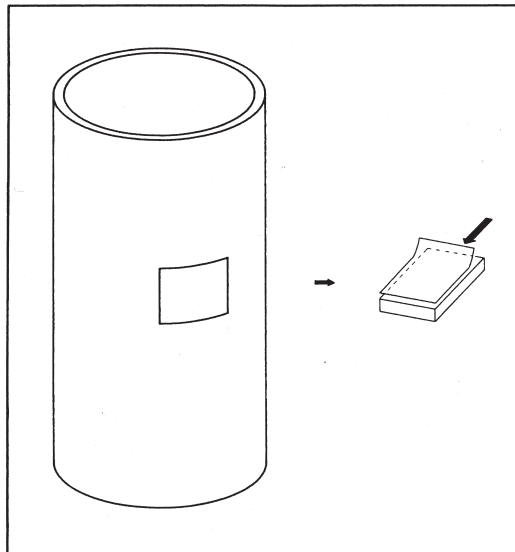


Fig. 4-11. A schema showing how and in what direction serial sections were prepared from the aortic wall. Reproduced from Okuyama, Takahashi, *et al.* (1988): Arch Pathol Lab Med 112, pp. 727.

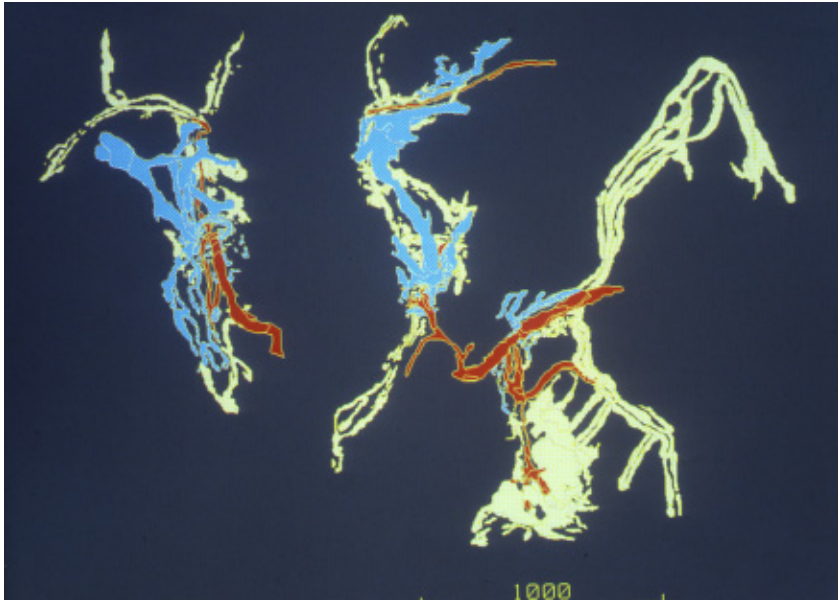


Fig. 4-12. Computer-assisted 3-D reconstruction of vasa vasorum in the wall (media) of normal aorta. A view vertical to the aortic wall from the outside. Painted red are inlet arterioles, blue are venules, and beige are capillaries. Reproduced from Okuyama, Takahashi, *et al.* (1988): *Arch Pathol Lab Med* 112, pp. 728.

where it takes a sharp U-turn and returns the way it had come. What is found here may be regarded as an extremely contiguous pattern of microvasculature (see Chapter 3), but we still have no idea on what type of microcirculation dominates in and around the vasa vasorum, or how the smooth muscle cells of media are assisted by these vessels.

### b) Three-D mapping of vascular lesions in lungs with pulmonary hypertension

#### **Pulmonary veno-occlusive disease: vascular changes (Figs. 4-13, 4-14)**

Pulmonary veno-occlusive disease (PVOD) is a rare disorder of lung vessels, classified as a special type of primary pulmonary hypertension. Its etiology remains unknown. Figure 4-13 demonstrates the lung of a patient who had this disease and died of severe right-sided heart failure. One can find in the microphotograph two peripheral branches of pulmonary vein, both severely obstructed. In the alveolar tissue in the surroundings, there is extensive edema resulting from elevated pressure of capillaries in the alveolar septa due to impaired draining of blood.

An affected pulmonary vein is shown in Fig. 4-14. One can see the lumen is severely obstructed with fibrous tissue probably resulting from organized thrombus. However, in a 2-D section of lung, such obstructed veins are found only sporadically, so that one cannot evaluate how far the total vascular bed of lung is obstructed, without observing the distribution of lesion in the three dimensions.



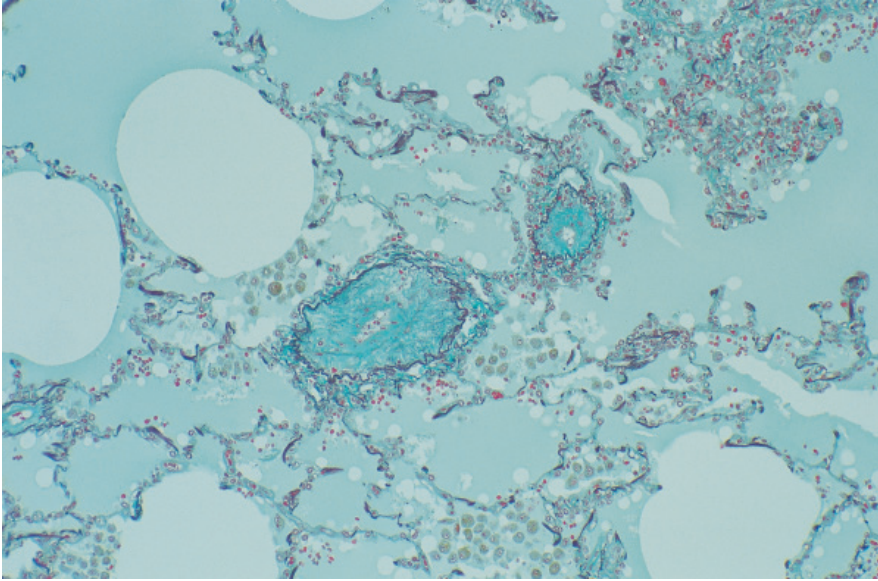


Fig. 4-13. A low power microphotograph of the lung of patient who died of cardiac (right ventricular) failure due to pulmonary veno-occlusive disease (PVOD). There are two small pulmonary veins, both severely obstructed. Extensive edema is visible in the alveolar tissue around the veins. Elastica-Goldner stain.

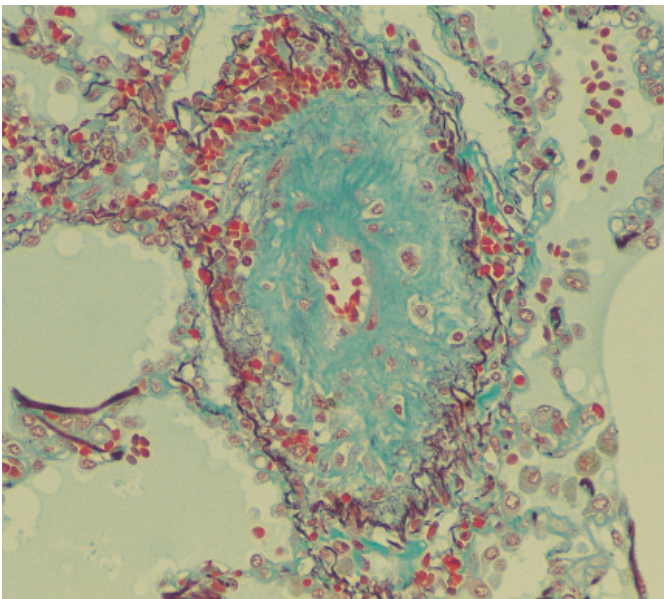


Fig. 4-14. A high power view of obstructed pulmonary vein. The lumen is obstructed with fibrous tissue resulting from organized thrombus. Elastica-Goldner stain.



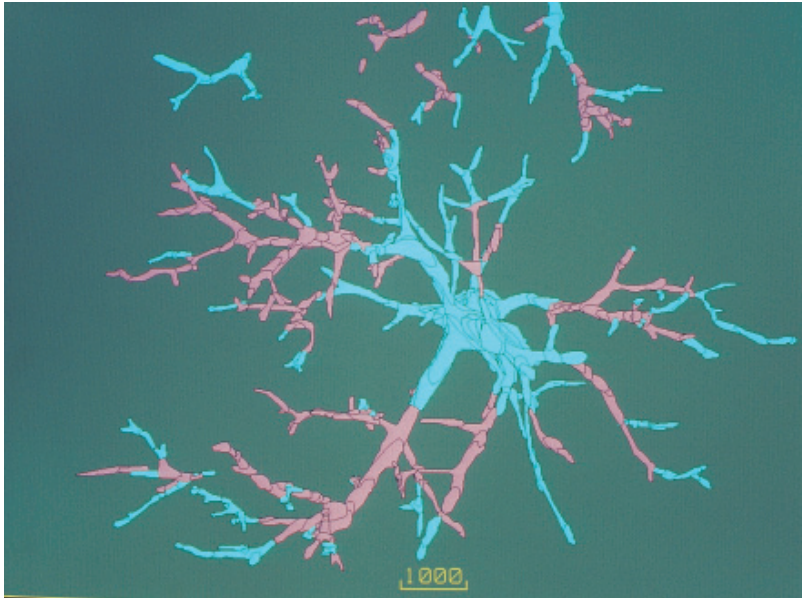


Fig. 4-15. Computer-aided 3-D reconstruction of pulmonary veins in the lung of PVOD patient shown in the previous figures. Obstructed segments are painted pink, non-obstructed segments light blue. The pulmonary venous bed is severely narrowed with few if any routes of drainage from the alveolar tissue toward the larger pulmonary veins.

### Three-D mapping of obstruction in the pulmonary venous bed (Fig. 4-15)

Figure 4-15 is the result of computer-aided 3-D mapping where obstructed segments are shown in pink and those non-obstructed in light blue. The picture, while containing only peripheral venous trees with the largest segment having a diameter of about  $350\ \mu\text{m}$ , clearly demonstrates that obstructions are distributed in much smaller segments. One can trace routes of venous drainage from the treetops, and it may be clear that there remain few if any routes that are kept open. Thus, already the whole vascular bed has severely been stenosed, which however is apt to be underestimated on a single microscopic section.

### Hypertensive pulmonary arteriopathy, Grade 1 (Fig. 4-16)

It is well known that some patients having congenital cardiac anomaly such as ventricular septal defect (VSD) are complicated by pulmonary hypertension (PH) which may be progressive, often bringing a fatal outcome. This is because if PH is sustained for a long time, obstructive lesions of small pulmonary arteries develop, gradually narrowing the vascular bed of lung in an irreversible way. The progression of this “hypertensive pulmonary arteriopathy” has been graded by the famous Heath-Edwards criteria (1958). In patients in whom arteriopathy has advanced too far, surgical correction of cardiac anomaly, for example closure of ventricular septal defect, has been considered equivalent to “opening the door of death,” because it results in squeezing

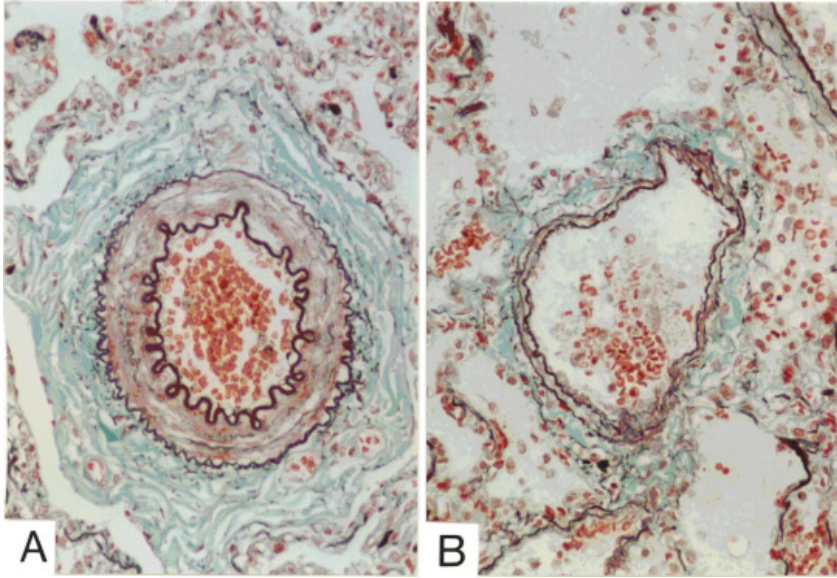


Fig. 4-16. Pulmonary artery with hypertensive pulmonary arteriopathy, Grade 1 (A), found in a patient of ventricular septal defect (VSD). The medial layer is strongly thickened as contrasted with an artery of about the same size, taken from a non-hypertensive (B). Elastica-Goldner stain.

an acutely increased blood volume into the already narrowed vascular bed. However, understanding has been and is still imperfect about to what degree the peripheral vascular bed of lung is obstructed by what type of lesion in what stage of hypertension. In view of this, Yaginuma *et al.* (1990) performed 3-D mapping of pulmonary arterial changes in surgical biopsy specimens of lung taken from several patients with congenital heart disease. Figure 4-16 left demonstrates the earliest change of pulmonary artery (Grade 1) where one can find only medial thickening due to hypertrophy of smooth muscles. This is from a patient of VSD, in whom the mean pulmonary arterial pressure was strongly elevated, reaching a level almost equal to the systemic blood pressure. Figure 4-16 right is a normal pulmonary artery of equivalent dimension. Note that the medial layer is markedly thinner.

#### **Hypertensive pulmonary arteriopathy: Grade 2 and 3 (Figs. 4-17, 4-18)**

Defined as Grade 2 are the arterial changes with the intima thickened due to proliferation of myointimal cells as in Fig. 4-17. Though moderately stenosing the lumen, this sort of change is considered to be reversible.

In the artery shown in Fig. 4-18, the intimal layer seems moderately thickened and consists of concentrically arranged deposit of hardened collagen. This lesion is defined as Grade 3 and for this, Wagenvoort and Wagenvoort (1977) coined an expression, the concentric laminar intimal fibrosis. The change has generally been considered to be a sign that the vascular disease has attained at an irreversible stage.

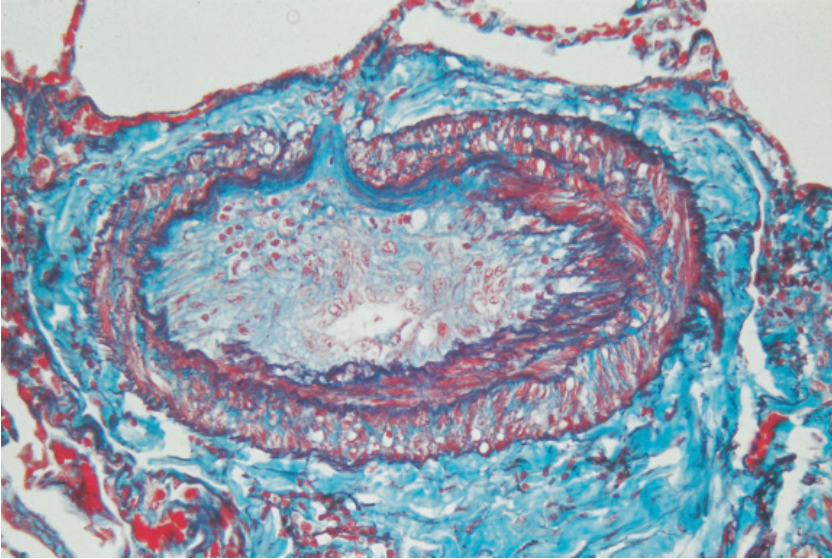


Fig. 4-17. Hypertensive pulmonary arteriopathy, Grade 2, with luminal stenosis brought about by cellular intimal proliferation. Elastica-Goldner stain.

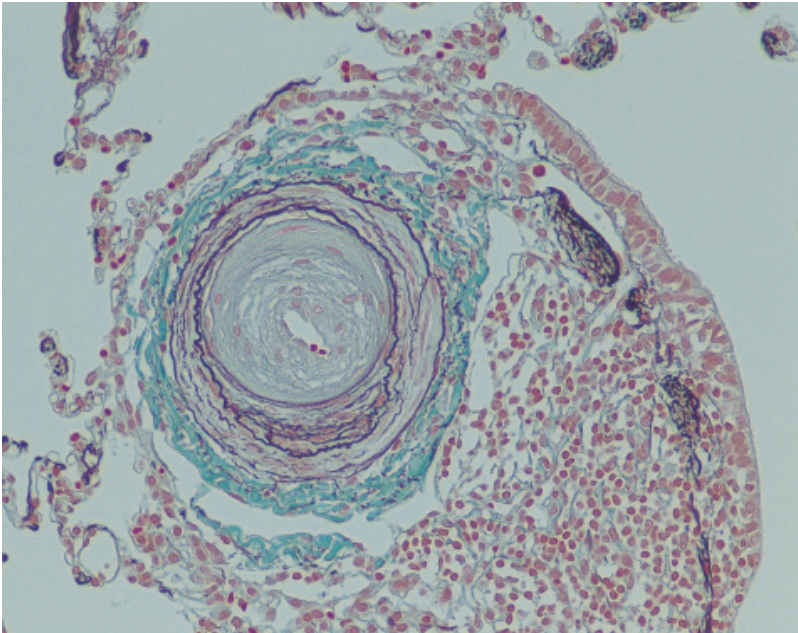


Fig. 4-18. Hypertensive pulmonary arteriopathy, Grade 3, a unique lesion called concentric lamellar intimal fibrosis. Development of this lesion is considered to mark the watershed for the patients of pulmonary hypertension in whom surgical correction of cardiac anomaly is contraindicated. Elastica-Goldner stain.



### Grade 4 and 5: plexiform lesion (Figs. 4-19, 4-20)

The severest form of arteriopathy is a unique change, generally called the plexiform lesion. Two examples of plexiform lesion are exhibited in Fig. 4-19. It involves a small pulmonary artery ranging from 100 to 150  $\mu\text{m}$  in diameter and develops at a place shortly after the segment is divided off its parent artery (denoted by 1). The lesion presents as what may be expressed as a microaneurysm filled with fibrous tissue (2) that apparently is left after a massive thrombus has been organized. The term “plexiform” originates from the finding that the fibrous part of the lesion contains a network of small vessels. Around the lesion, one can find several ectatic vessels (3) which seem to function as collaterals bypassing the plexiform lesion. (We call these vessels the dilatation lesions although, in the original article by Heath and Edwards,

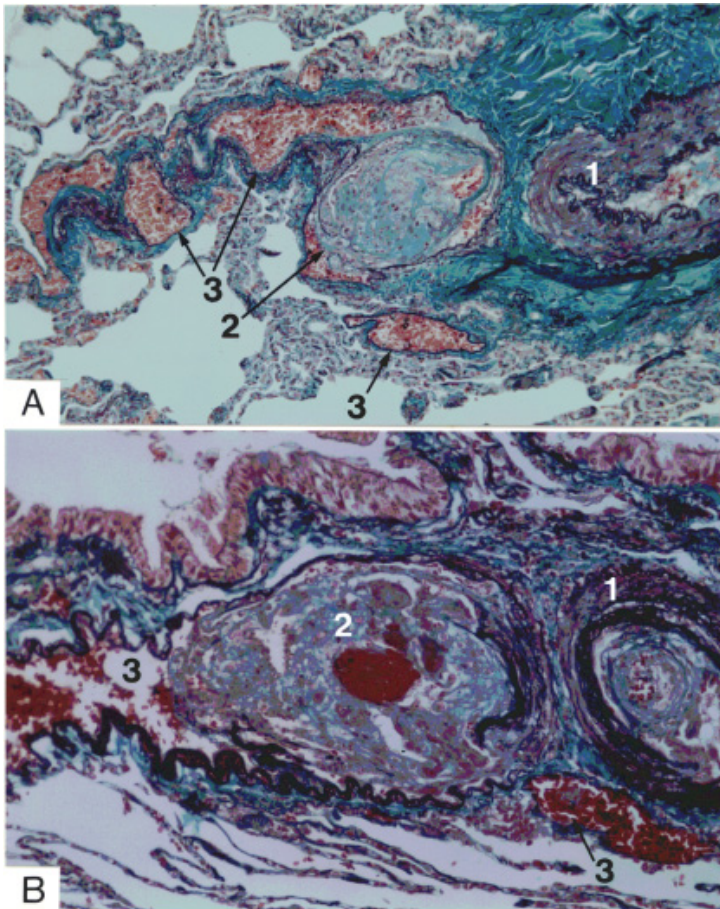


Fig. 4-19. Two examples of “plexiform lesion” defined as hypertensive pulmonary arteriopathy, Grade 4 to 5. The lesion develops in a small artery of 100 to 150  $\mu\text{m}$  in diameter at a place shortly after its division off its parent artery (1). The lesion presents as a complex, with a sort of microaneurysm filled with fibrous mass penetrated by plexus-like small vessels (2), and several ectatic vessels (3) that bypass the microaneurysm. Elastica-Goldner stain.

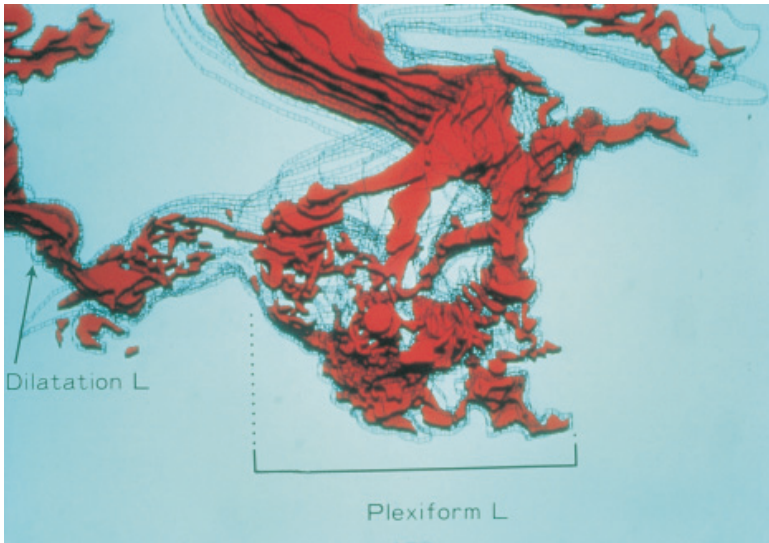


Fig. 4-20. Computer-aided 3-D reconstruction of the microaneurysmal portion of plexiform lesion, revealing plexus-like small vessels penetrating the fibrous mass filling the lumen. Reproduced from Yaginuma, Takahashi, *et al.* (1990): *Thorax* 45, pp. 589.

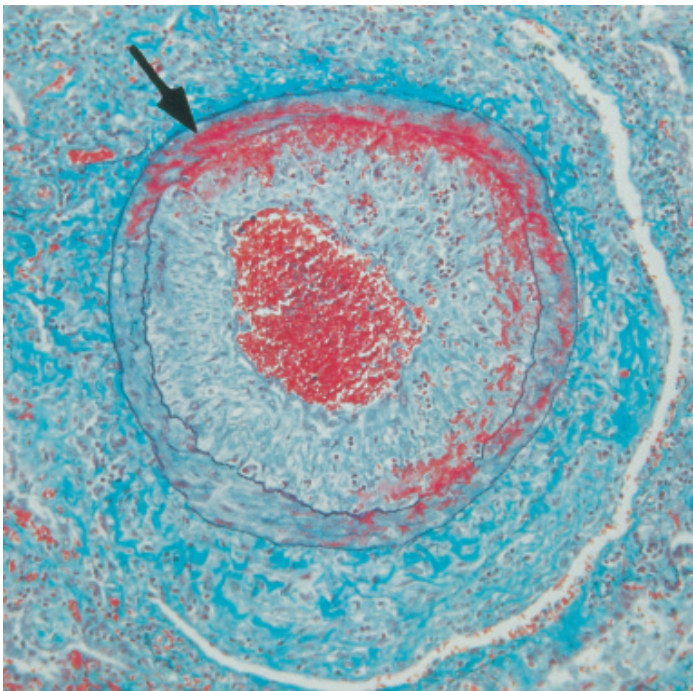


Fig. 4-21. Hypertensive pulmonary arteriopathy, Grade 6, that is marked by the development of pulmonary arteriitis. There is necrosis of medial smooth muscles infiltrated with fibrinoid material (arrow). Elastica-Goldner stain.

this term was given a wider connotation, including also the plexiform lesion) Usually, the presence of plexiform lesion is interpreted to be suggesting that in the patient, the disease is too far advanced to allow a radical cardiac surgery. It is said that a correction operation, if performed, can lead to a fatal outcome by acutely elevating the pulmonary arterial pressure that results in right-sided heart failure.

A plexiform lesion, when reconstructed, reveals that the inner mass of fibrous tissue is penetrated by a network of minute vascular channels, as in Fig. 4-20. It seems however that only less than 10% of normal blood flow is allowed to pass through the lesion.

#### **Grade 6 lesion: arteriitis (Fig. 4-21)**

In a terminal stage of PH, vasculitis of small pulmonary artery can develop and is designated as Grade 6 lesion. Figure 4-21 presents pulmonary arteriitis found in a patient of PH. The arrow denotes deposition of fibrinoid material (red). But this is only rarely encountered.

#### **Three-D mapping of Grade 2 and 3 lesions (Fig. 4-22)**

Figure 4-22 exhibits the result of 3-D mapping in a patient of VSD. Here the pulmonary arteries are shown to harbor Grade 2 (green) and Grade 3 (yellow) lesions, making the disease seem in a moderately advanced stage. One may recognize several

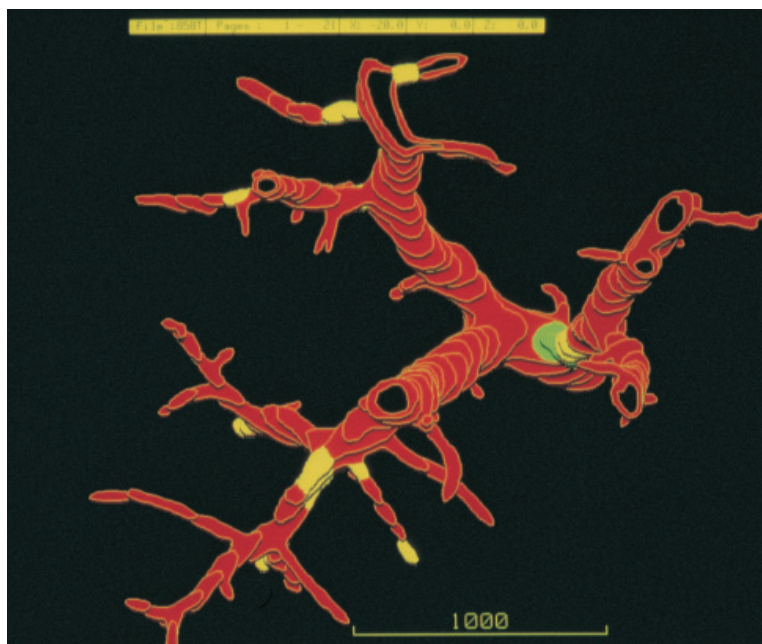


Fig. 4-22. Computer-assisted 3-D mapping of hypertensive arteriopathy in small pulmonary arteries. Moderately advanced case, with Grade 2 (green) and 3 (yellow) lesions. Note that as yet, more than half of the pathways are left open, allowing free flow to the alveolar area. Reproduced from Yaginuma, Takahashi, *et al.* (1990): *Thorax* 45, pp. 587.



flow routes that remain patent, where sufficient amount of blood can be led into the capillary region (the void space) without being blocked by obstructive changes.

### Three-D mapping in advanced cases (Figs. 4-23, 4-24)

Figure 4-23 is from a more advanced case of VSD and demonstrates that many if not all arteries of about  $150\ \mu\text{m}$  in outer diameter are involved in either Grade 3 (light green) or Grade 4 (white) lesions. Still, there are small number of arterial flow routes remaining patent. Besides, it is clearly shown that the plexiform lesions involve only a specific site of pulmonary arterial tree, namely, “supernumerary” arteries of  $150\ \mu\text{m}$  in diameter arising from disproportionately large parent vessels. Anatomically, pulmonary arteries of this dimension correspond to those running in parallel with a respiratory bronchiole, i.e., those found in a 2-D section of lung at the entrance of pulmonary acinus.

Even in patients having plexiform lesions, the degree of arterial bed obstruction seems to be varying. Figure 4-24 is from another patient having plexiform lesions, but here one can no longer find any flow route that leads blood to the periphery. In other words, the arterial bed seems to be obstructed by 100%. In this patient, a certain, but not sufficient amount of pulmonary blood flow seems barely maintained through collateral pathways. Thus, even among advanced cases, difference seems to exist in the

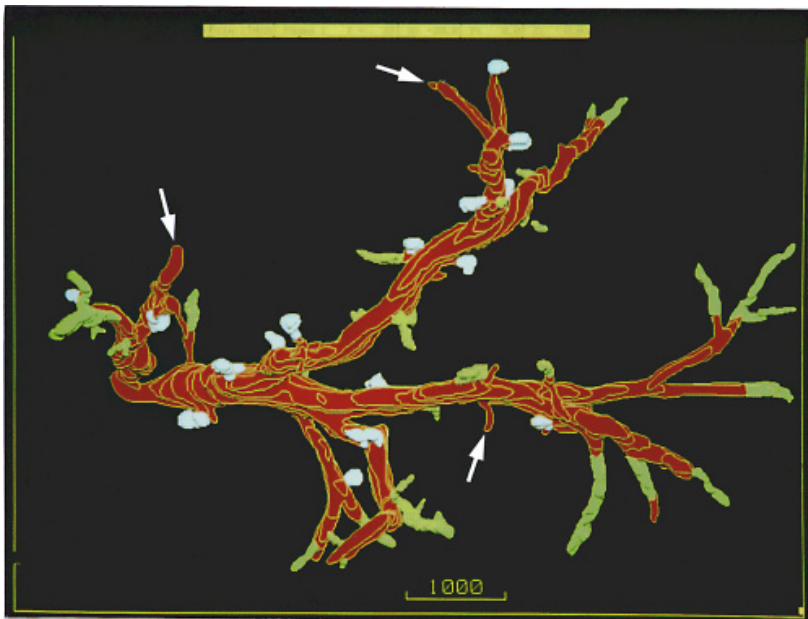


Fig. 4-23. Computer-assisted 3-D mapping of hypertensive arteriopathy in an advanced case. There are a number of plexiform lesions (white) and Grade 3 lesions (green), both involving a small pulmonary artery of 100 to  $150\ \mu\text{m}$  (the acinar arteries) shortly after their division from the parent artery. However the obstruction of vascular bed is not complete, with flow routes to the periphery remaining open at several places. Reproduced from Yaginuma, Takahashi, *et al.* (1990): *Thorax* 45, pp. 587.

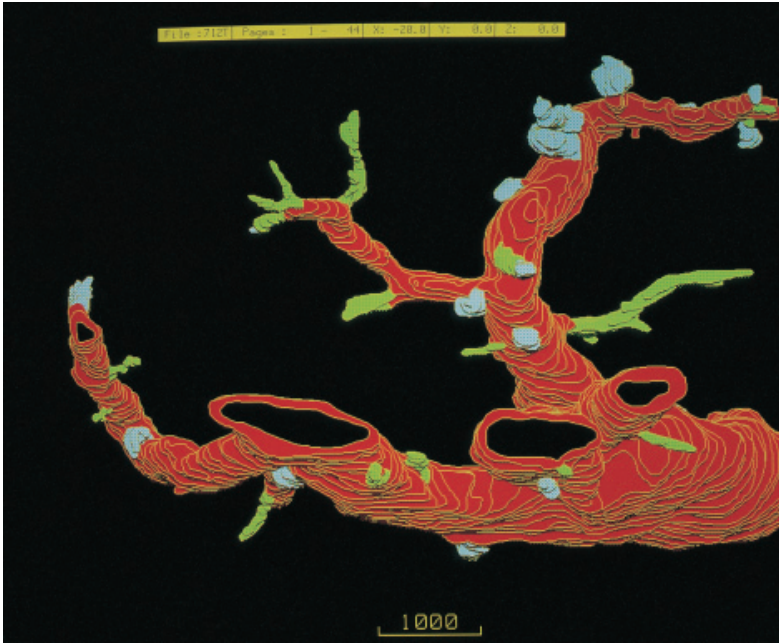


Fig. 4-24. Computer-assisted 3-D mapping of hypertensive arteriopathy in another advanced case. Here the flow routes to the periphery are entirely closed with plexiform (white) or Grade 3 (green) lesions.

degree to which the arterial bed is narrowed, and this makes us wonder whether a cardiac correction surgery should always and rigidly be contraindicated even when only a small number of Grade 4 lesions were detected on lung biopsy.

Studies were extended along this line by Matsuki *et al.* (1994). They attempted to estimate the grade to which the pulmonary vascular bed is narrowed in patients with congenital cardiac disease and pulmonary hypertension, by enumerating the Grade 3 and 4 lesions in a volume of lung. Sampling was done on serial sections and the numerical density of lesions  $N_V$  was calculated. The material included 17 autopsy lung specimens from different lobes of five patients dying of cardiac anomalies. All had advanced arteriopathies of pulmonary arteries. While performing computer-aided reconstruction, the number of lesions was enumerated on display. However, there was a problem: autopsy lungs are usually fixed in variously collapsed or overinflated state. With regard to this, standardization of lung volume was performed according to the method of Takahashi *et al.* (1983) who proposed to make use of the numerical density in lung section ( $N_A$ ) of muscularized pulmonary arteries larger than  $100 \mu\text{m}$  in external diameter, on the assumption that  $N_A$  may be constant, so long as the lungs are brought to a similar grade of inflation. The corrected  $N_V$  of vascular lesions thus obtained from patients with cardiac anomalies proved to be varying to an unexpected degree. Not only was there a marked difference between the individuals, but also among the site of lung within an individual. The degree of vascular bed narrowing, defined as the nu-

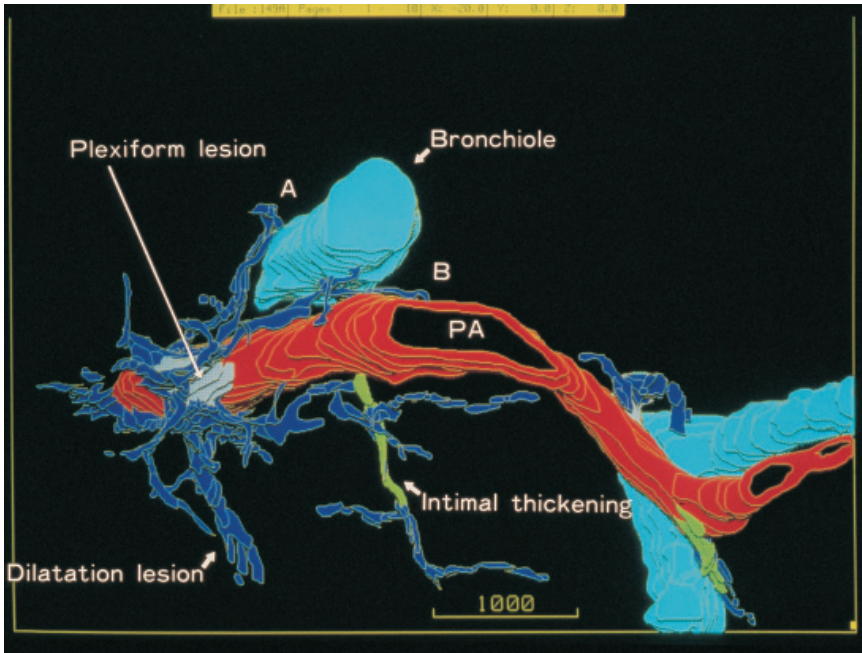


Fig. 4-25. Computer-assisted 3-D reconstruction performed to visualize the collateral pathways bypassing a plexiform lesion in an advanced case of pulmonary hypertension. A plexiform lesion (white) is bypassed by dilatation lesions (blue) developing in its surroundings. These varicose-vein-like ectatic vessels communicate on one hand with terminal bronchial arteries running along a bronchiole (A), and on the other, feed the wall of large pulmonary artery as its vasa vasorum (B). Thus, the dilatation lesions connect the bronchial and pulmonary arteries with peripheral capillaries. Reproduced from Yaginuma, Takahashi, *et al.*(1990): Thorax 45, pp. 588.

merical ratio of obstructed to the total of acinar arteries, was also various, suggesting that there can be operable patients who have a pulmonary vascular bed not so much narrowed even in the presence of Grade 4 lesions.

#### **Plexiform lesion and its collaterals (Fig. 4-25)**

Figure 4-25 is another reconstruction performed by Yaginuma *et al.* to visualize in an advanced case of pulmonary arteriopathy how collaterals develop and connect with what vessels. There is a plexiform lesion (white) developing in a small segment of pulmonary artery running along a respiratory bronchiole. Shown blue are “dilatation lesions” that in Fig. 4-19 presented as varicose-vein-like ectatic vessels meandering around the plexiform lesion and extending toward the alveolar capillaries. On the other hand, the dilatation lesions communicate with terminal bronchial arteries, either running along a bronchiole (A) or feeding the wall of pulmonary artery as its vasa vasorum (B). Thus, the dilatation lesions are so formed as to connect the bronchial arteries, pulmonary arteries and peripheral capillaries. This connecting relation suggests that the dilatation lesions are functioning as collaterals for the plexiform lesion.

### c) Hypoplastic zone of myenteric plexus in Hirschsprung's disease

#### The myenteric plexus and Hirschsprung's disease (Fig. 4-26)

The myenteric plexus (Auerbach's plexus) is autonomic nerve plexus of the intestinal wall, extending between the double-layered, longitudinal and circular, muscular coats. Normally it generates and controls the peristalsis of intestine by sending pulsatile stimuli.

One of the abnormalities involving the myenteric plexus is Hirschsprung's disease. This is a congenital disorder which brings about severe constipation of neonates emerging shortly after birth and lasting thereafter. The symptom has been attributed to lack of peristalsis in the distal part of the intestinal canal due to congenital agenesis of myenteric plexus in the wall of the paralytic segment (Whitehouse, 1948). The extension of aganglionic zone, the zone where the plexus has not formed, varies from one patient to another; in some cases it involves only a short segment of the anal canal but in others, the paralytic zone can extend from the anal region to variable height, sometimes involving the whole large intestine and even the distal part of the small intestine. The sole treatment of this disease is surgical resection of the aganglionic segment. In order to determine the range of intestine to be resected, surgeons resort to intrasurgical biopsy of the bowel wall, taking a specimen from the height suspected to be slightly proximal to the border between the normal and aganglionic zones; if ganglion cells are confirmed to exist, the intestine below the height is removed. However, there is a problem: it has been assumed that the aganglionic zone does not begin abruptly but there is an "intermediate zone" between the normal and aganglionic zones: the inter-

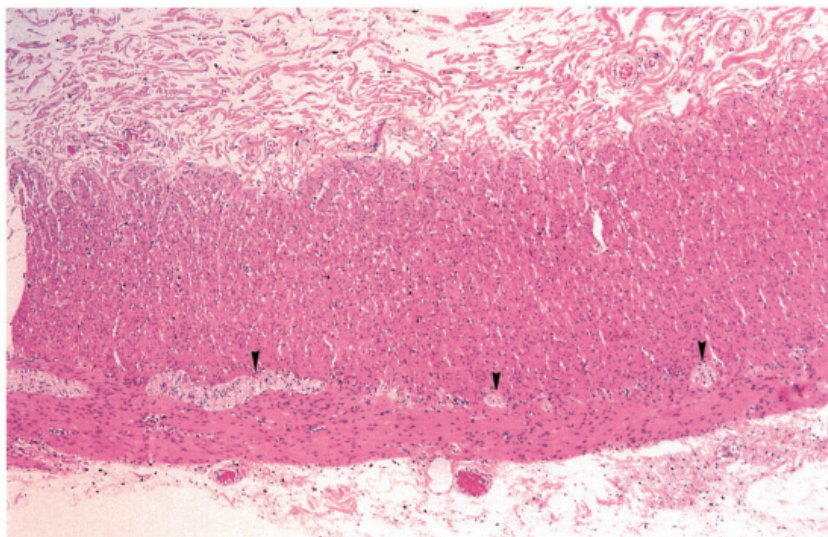


Fig. 4-26. Normal myenteric plexus. A microscopic picture of large intestine sectioned vertically to the wall. One can see sections of small ganglia and nerve bundles (arrowheads) deployed between the inner and outer layers of tunica muscularis propria. Hematoxylin-eosin stain.



mediate zone has seemed likely to be a segment of intestine where the plexus, though present, is so hypoplastic that when left unresected, the symptom may last after the operation. In fact, it has sometimes been experienced that various degree of constipation lingers even after surgery, and at least in a part of such cases, the transitional zone has been assumed to be remaining unremoved. Accordingly it seems desirable that, in performing an intrasurgical biopsy on frozen sections, the pathologist in charge could evaluate the grade of hypoplasia of the plexus. As yet, however, we are far from the state in which we can make a diagnosis of hypoplastic plexus with confidence, because the hypoplastic myenteric plexus has yet to be defined in clear morphological terms. To what degree does the thickness or density of nerve bundles are reduced in the hypoplastic zone? On what criteria can we rely in making diagnosis of hypoplasia when examining a 2-D section of bowel wall? Urged by these ambiguities, Miura *et al.* (1996) attempted to visualize the ordinary myenteric plexus and its changes in Hirschsprung's disease. No image of this sort has been presented so far. This will allow to compare the form of plexus between patients with Hirschsprung's disease and age-matched children on firm anatomical basis.

Figure 4-26 is a microphotograph showing the normal myenteric plexus in the wall of intestine. In a routine microscopic section which is cut vertical to the intestinal wall, the plexus appears as bundles of autonomic nerve, whose sections are scattered between the inner and outer muscular layers. Thus, to visualize the whole structure of the plexus, one needs to perform 3-D reconstruction so as to command the whole plexus in the form of network sandwiched between the two muscular layers.

### **Three-D structure of normal myenteric plexus (Fig. 4-27)**

Figure 4-27 presents a 3-D reconstruction of myenteric plexus in the terminal part of normal ileum from a male infant aged 6 months. The serial sections were cut at a slight angle of 3 to 5 degrees with the plane of plexus. Only ganglia (nerve cell clusters) and nerve bundles that connect a pair of them were visualized. The plexus (green) is shown forming a network with the size of meshes somewhat uneven. The upper portion of the plexus corresponds to the proximal (oral) side of the intestinal patch, and the lower part, to the distal (anal) side. Note the thickness of individual nerve segments so as to compare with the next figure. An extrinsic nerve (blue) is shown joining the plexus.

### **The transitional and aganglionic zones in Hirschsprung's disease (Figs. 4-28, 4-29)**

Figure 4-28 is a reconstruction of myenteric plexus in the transitional zone of intestine in Hirschsprung's disease. The patient was a male infant of 6 months, in whom the entire colon was involved in aganglionosis. Three-D reconstruction was performed at several places of intestine but the material for this figure was taken from the wall of the terminal ileum which is considered to be close to the transitional zone. Compared with the foregoing picture of normal control that was shown at the same magnification, the plexus is strikingly hypoplastic, with the individual bundles markedly thinner. Hypertrophic extrinsic nerves (blue) are also found joining the plexus.

Figure 4-29 is another reconstruction of the same bowel 1 cm distal to the area displayed in Fig. 4-28. Here one can see the last part of the transitional zone in the

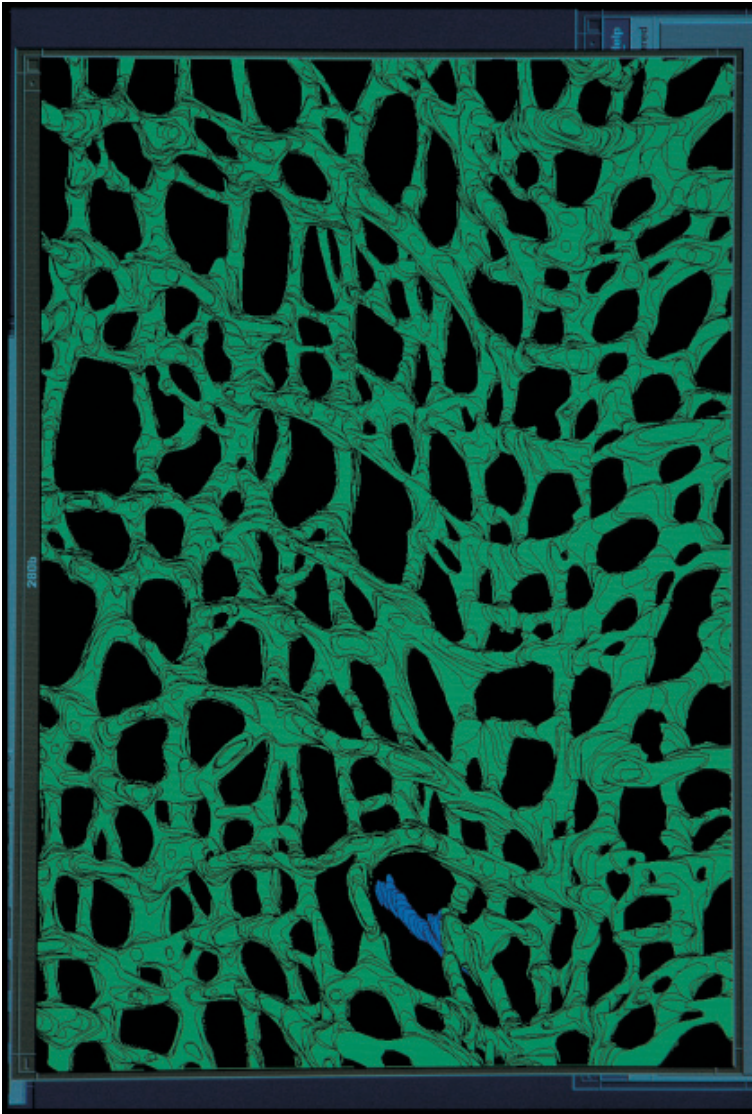


Fig. 4-27. Computer-assisted 3-D reconstruction of normal myenteric plexus, sandwiched between the inner and outer layers of tunica muscularis. Taken from the terminal part of ileum. The plexus presents as a dense, flat network where the connecting points of nerve bundles correspond to small ganglia. An extrinsic nerve (blue) joins the plexus. Reproduced from Miura, Takahashi, *et al.* (1996): *J Pediat Surg* 31, pp. 422.

upper, while at about the center of the figure, the aganglionic zone is beginning. In the latter zone extending toward the lower, one can find only small number of isolated ganglia.

Thus, the “transitional zone” of Hirschsprung's disease was clearly definable as an area extending over a certain length, where the density of network tapers toward the



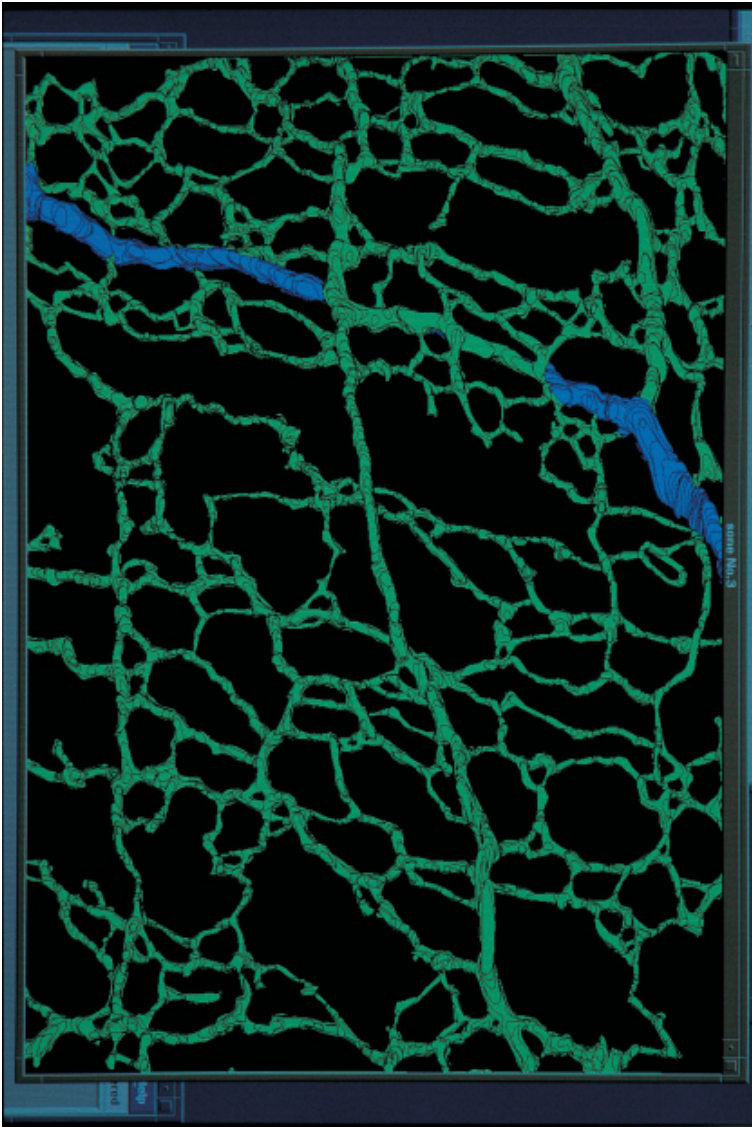


Fig. 4-28. Computer-assisted 3-D reconstruction of the transitional zone in the terminal ileum resected for Hirschsprung's disease, under the same magnification as in Fig. 4-27. Note the hypoplastic plexus, with the individual bundles markedly thinner as compared with the normal plexus. Reproduced from Miura, Takahashi, *et al.* (1996): *J Pediat Surg* 31, pp. 423.

aganglionic zone. This finding was considered to be of profound significance in designing a surgical strategy to prevent postoperative bowel dysfunction. A morphometric study was added to this by the same authors (Miura *et al.*, 1995). They have con-

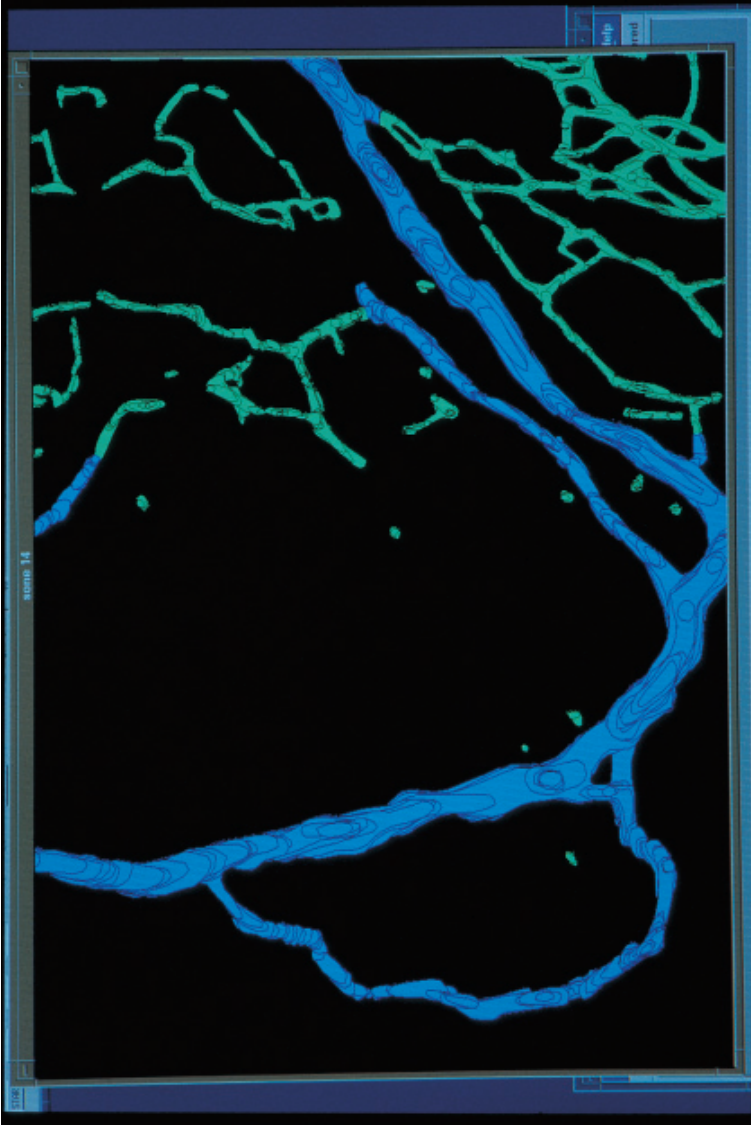


Fig. 4-29. Computer-assisted 3-D reconstruction of the myenteric plexus 1cm distal to the site reconstructed in Fig. 4-28. The terminal part of the transitional zone (upper) and the beginning part of the aganglionic zone (lower) are included. Reproduced from Miura, Takahashi, *et al.* (1996): *J Pediat Surg* 31, pp. 423.

firmed in intestines resected from four patients of Hirschsprung's disease that the extension of transitional zone in the longitudinal direction of intestine was various, ranging from 1cm to more than 5 cm.

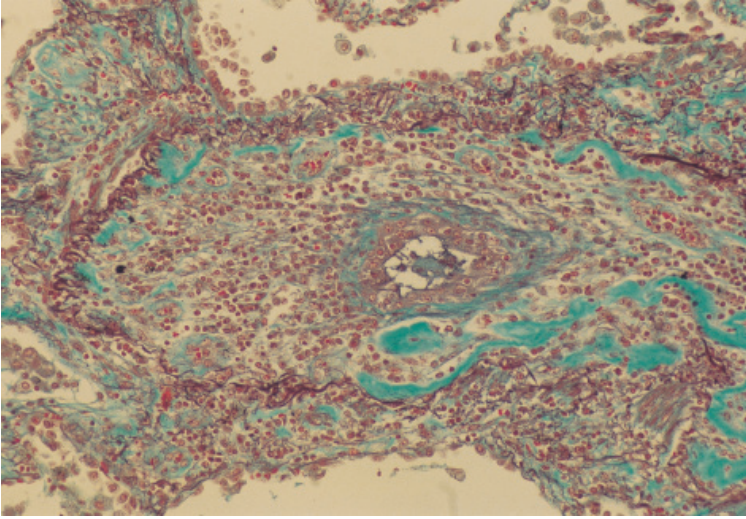


Fig. 4-30. Bronchiolitis obliterans in a florid state. A microphotograph of membranous bronchiole cross-sectioned, with the lumen strongly narrowed due to active inflammatory changes extending in the subepithelial layer. Elastica-Goldner stain.

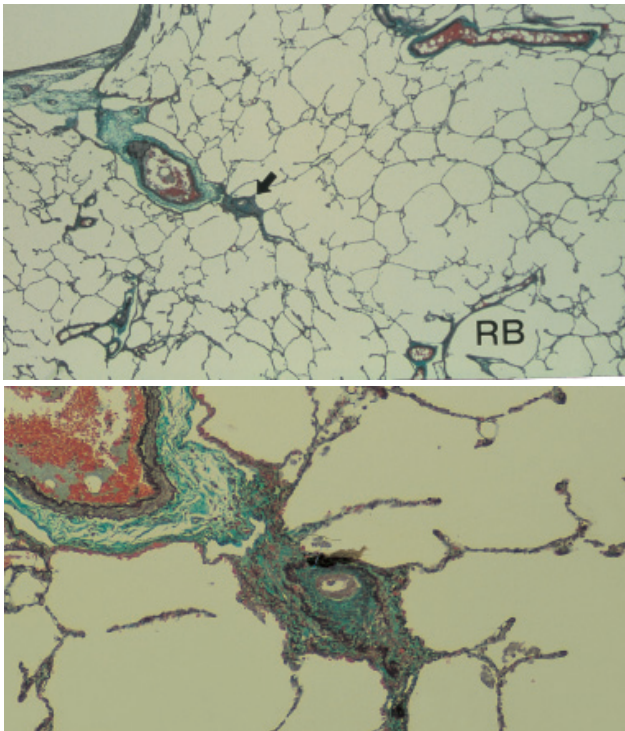


Fig. 4-31. Bronchiolitis obliterans in another case (scarring phase). Upper: a membranous bronchiole attenuated due to dense fibrosis, with the lumen left only as a pinhole (arrow). RB: respiratory bronchiole. Lower: the obstructed bronchiole magnified. Elastica-Goldner stain.

#### d) Three-D mapping of airway obstruction in bronchiolitis obliterans

##### The airway change in bronchiolitis obliterans (Figs. 4-30, 4-31)

Shown in Fig. 4-30 is the change of membranous bronchiole found in the lung of a patient having rheumatoid arthritis and dying of severe obstructive respiratory failure. The subepithelial layer is thickened with diffuse inflammatory changes, leaving only a pinhole lumen. This is a rare disorder called bronchiolitis obliterans (Seggev *et al.*, 1983) which is associated with either viral infection of affected bronchiole, rheumatoid arthritis or graft-vs. host disease, but there are many cases where etiology cannot be established.

Figure 4-31 is the lung from another patient dying of bronchiolitis obliterans, a female aged 64 years, in whom the etiology was not clear. Closely watching the lung sections, only a few, strongly obstructed bronchioles were found as in the figure. Without signs of active inflammation, they were considered to be in the state of postinflammatory scarring. Because such obstructed bronchioles were found only rarely in the sections, one may wonder whether the change can really have been responsible for developing respiratory distress that had been severe and apparently of obstructive nature. To obtain perspective about the state of the airway bed, a small scale reconstruction of the lung was undertaken by Yaegashi and Takahashi (1994).

##### Three-D mapping of bronchiolitis in the airway tree (Fig. 4-32)

Figure 4-32 exhibits a 3-D image of bronchioles in the lung shown in Fig. 4-31. The reproduced space measures  $89 \times 13$  mm in the area of section and with a thickness of 3.1 mm. Now, the narrowing of airway bed, though ambiguous in routine microscopic examination, is clearly visible in this 3-D mapping. Obstructions, shown in

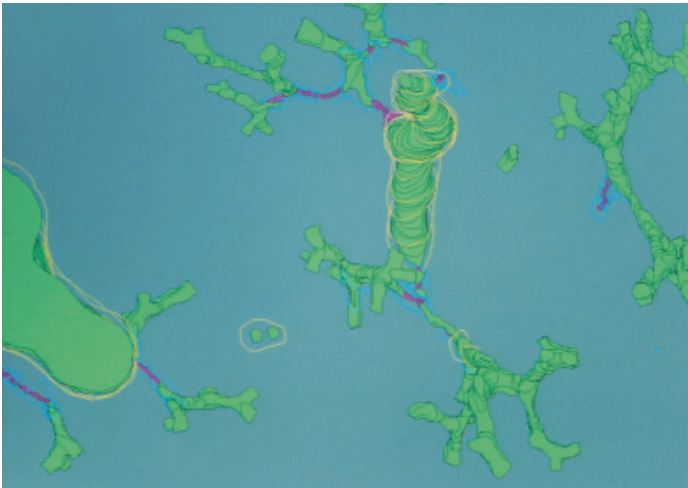


Fig. 4-32. Computer-assisted 3-D mapping of obstruction in a bronchiolar tree, in the lung shown in Fig. 4-31. Obstructions (purple) are exclusively involving the terminal bronchioles. More than 70% of the airway bed is obstructed. Reproduced from Yaegashi and Takahashi (1994): Arch Pathol Lab Med 118, pp. 979.





Fig. 4-33. Adenoma (A) and an early adenocarcinoma (C) of large intestine. The adenoma is connected with the intestinal mucosa with a slender stalk. Operation was performed to remove the carcinoma, with the adenoma coincidentally detected.

purple, are seen exclusively involving the terminal bronchioles; more than 70% of them are obstructed, but it is only a short segment of terminal bronchioles, 0.3 to 1 mm, that has been involved. One may understand in this situation why the lesions were not easily detectable in routine sections, causing the observers to underestimate the seriousness of disease. Thus, this may be a typical example showing that 3-D morphology works as an indispensable tool in revealing structure-function correlation.

#### e) Multistep carcinogenesis of the large intestine

##### Adenoma and adenocarcinoma of large intestine (Fig. 4-33)

It is now generally accepted that carcinoma of the large intestine arises, not directly from an ordinary mucosa, but usually from a sort of polyp that precedes. Polyp is a generic term expressing an elevated lesion arising in mucosa or skin. When examined endoscopically, subjects in the middle or advanced age are shown very often harboring polyps in their large intestine. Of the various sorts of intestinal polyps, those most common and prone to cancerous changes are the adenoma, which therefore is regarded as a precancer. Figure 4-33 demonstrates a segment of large intestine resected for an early carcinoma (C), but in the same material one can find another lesion, an adenoma having a slender stalk (A).

##### Vogelstein's hypothesis (Fig. 4-34)

In terms of microscopic features, carcinomas arising in the large intestine are mostly adenocarcinomas. This means that the carcinoma cells, having originated from

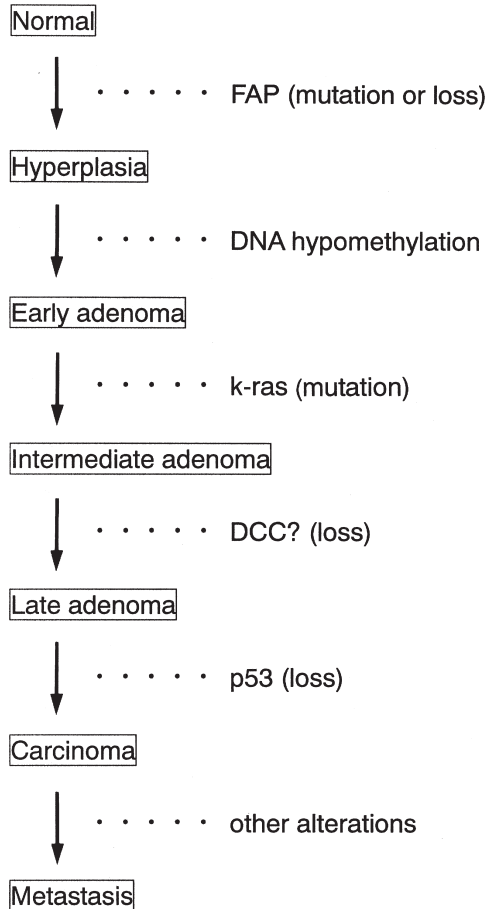


Fig. 4-34. Vogelstein's hypothesis proposed to explain the molecular background for multistep development of adenocarcinoma from adenoma of the large intestine.

the glandular epithelia of mucosa, continue to express more or less signs of differentiation as secreting cells. In the case of large intestine, carcinogenesis is considered to start with transformation of normal epithelia into hyperplastic cells. In the next place they are subjected to change into adenoma cells with mild cellular abnormalities, next into those with moderate and then into those with severe abnormalities, and then finally into overt carcinoma cells. Vogelstein *et al.* (1988) assume that each of these steps may be associated with a change of DNA (Fig. 4-34), meaning that the whole process of carcinoma development is a summation of molecular changes, or what is today spoken of as the multistep carcinogenesis. It seems likely therefore that each of the intermediate changes, such as adenoma with varying grades of cellular abnormalities, is a microscopic expression corresponding to a certain step in the assumed series of DNA changes.



**Various grades of atypia in colonic tumors (Fig. 4-35)**

Today, as growing number of adenomas are excised at endoscopic examination of large bowel, pathologists have come to experience tumors with various grades of cellular abnormalities. Such abnormalities are expressed as cellular atypia (see Chapter 8), and it is meant with this term that the higher the grade of atypia, the more does the malignant potential increase. Thus the disease ranges from adenoma with mild epithelial atypia to moderate to severe atypia and to overt carcinoma. Not infrequently, a single tumor is found consisting of zones with different grades of atypia, as observed in a 2-D microscopic section where zones of different atypia appear as patches that neighbor one upon another in mosaic fashion. Therefore if a tumor comprising areas with different atypia is submitted to 3-D mapping by reconstruction, the distribution of such areas may be visualized, allowing one to see their extension and mutual relation. Also, one can judge from the reconstructed image of the cut end whether or not a part of tumor is left unexcised.

In Japan, cellular atypia in these tumors is graded into five steps as in Fig. 4-35 (Japanese Society for Cancer of the Colon and Rectum, 1997). In this grading system, Group 1 means normal epithelial cells, Group 2 epithelial cells with mild atypia, Group 3 those with moderate and Group 4 with severe atypia. Group 5 denotes overt carcinoma. In Western countries, adenocarcinoma of large bowel is defined based on whether or not the tumor has started to grow invasively. This is different from the definition

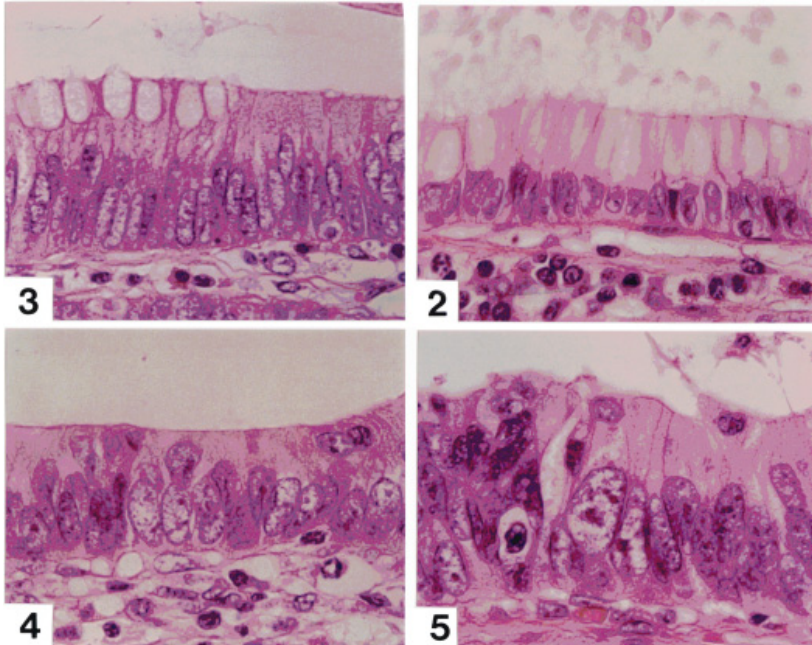


Fig. 4-35. Various grades of cellular atypia found in tumors of the large intestine ranging from adenoma with mild atypia (Group 2), that with moderate (Group 3) and severe atypia (Group 4), and overt adenocarcinoma (Group 5). Hematoxylin-eosin stain.

commonly used in Japan, where a carcinoma, even when remaining in the mucosa, is defined as such if the cells look sufficiently atypical and there are structural abnormalities such as the back-to-back pattern without intervening stroma. The latter feature and its significance will be discussed in the next chapter. In this study we conformed to these Japanese criteria.

### Three-D reconstruction of adenoma harboring carcinoma (Fig. 4-36)

As many as 50 adenomas taken endoscopically were submitted to computer-assisted 3-D mapping of atypical areas by Zhang *et al.* (1994). An example of mapping is shown in Fig. 4-36 which is from a large adenoma, about 1.4 cm in largest diameter. The mass was sequentially sectioned at a comparatively large interval of 200  $\mu\text{m}$ . This is because the study was designed so as to deal with such a large number of cases. It was preferred therefore to obtain an approximate knowledge about the distribution of atypia rather than to achieve the highest technical precision.

In this figure, there are patches of mild atypia (Group 2, yellowish green) which however are found as small fragmental remains after being replaced by moderate atypia (Group 3, faintly pink). The latter is shown to have extended almost over the whole surface, but within this, small areas with severe atypia have arisen (Group 4, dark pink), and in one of these, overt carcinoma is shown developing (Group 5, red).

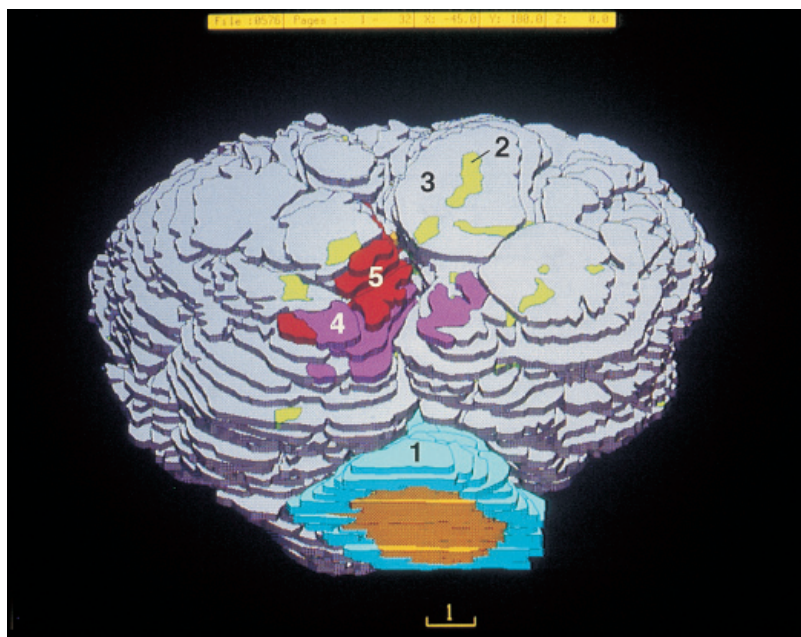


Fig. 4-36. Computer-assisted 3-D reconstruction of colonic polyp harboring lesions with various grades of atypia. Note that in adenoma with moderate atypia (Group 3, pink), adenoma with severe atypia (Group 4, dark pink) has developed, and in the latter, overt adenocarcinoma (Group 5, red) is arising, thus presenting a concentric zonation of increasingly malignant lesions. Reproduced from Zhang, Takahashi, *et al.* (1994): Pathology and Clinical Medicine 12, pp. 1397.

Thus, the distribution of atypia is clearly multizonal. Roughly speaking, different zones are arranged in a concentric fashion, with carcinoma at the center, which is surrounded by Group 4, which is then by Group 3 and so forth. Quite possibly, this distribution seems to be reflecting the multistep carcinogenesis as its morphological expression.

### Distribution of carcinoma in 17 adenomas (Fig. 4-37)

In the tumor reconstructed in Fig. 4-36, the stalk is shown having normal epithelia (Group 1, green), making us confirm that neither adenoma nor carcinoma has attained at the stump. Of the 50 adenomas examined, 17 proved to harbor carcinoma in the form of "cancer in adenoma," all of which are arranged in Fig. 4-37 to show the distribution of carcinoma. The values entered in the figure are the percentile share of carcinoma in the whole mucosal volume contained in the polyps. In five of these, carcinoma was shown infiltrating into the submucosal layer, as indicated by an arrow-head. In one of them, carcinoma was shown extending so far as to reach the stump, requiring an additional surgery. In this case (Case 40), carcinoma at the stump would have been hard to detect without performing serial sections analysis.

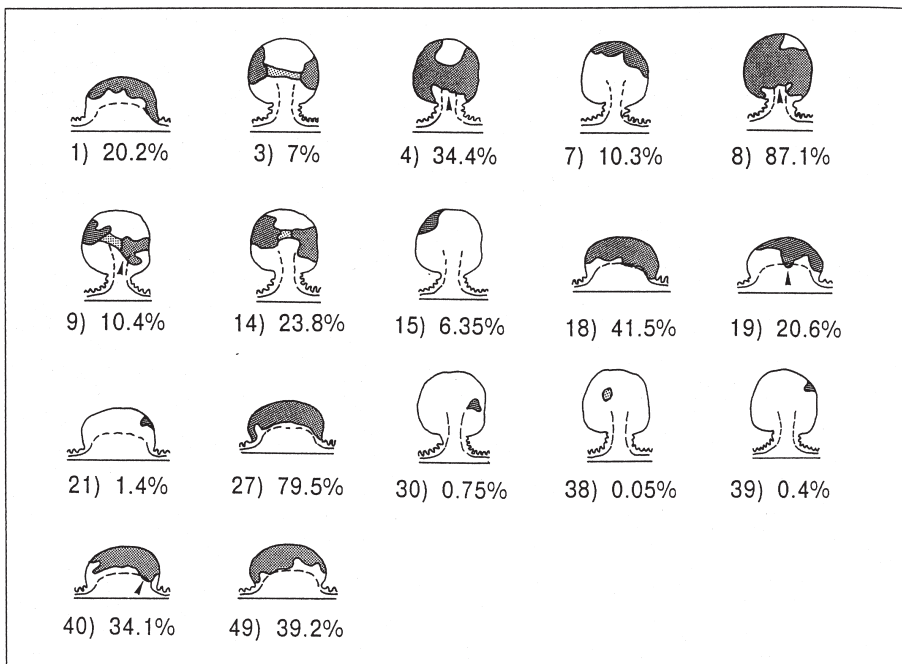


Fig. 4-37. Distribution of carcinoma schematically presented in 17 of the 50 adenomas reconstructed. The values entered are the percentile share of carcinoma in the whole mucosal volume contained in the polyps. In Case 40, carcinoma was shown reaching the stump. Reproduced from Zhang, Takahashi, *et al.* (1994): *Pathology and Clinical Medicine* 12, pp. 1399.

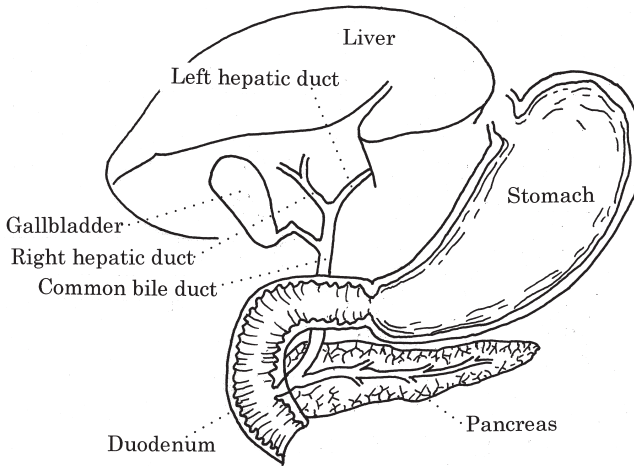


Fig. 4-38. A schema showing the anatomy of hepatohilar bile ducts.

#### f) The development and extension of hepatohilar bile duct carcinoma

##### Hepatohilar bile ducts (Fig. 4-38)

The extrahepatic part of bile ducts includes the right and left hepatic ducts, the cystic duct, the common bile duct and the duodenal papilla (see Fig. 4-38). Carcinoma often arises in this domain and is called hepatohilar bile duct carcinoma.

##### Cholangiogram of patient having hepatohilar bile duct carcinoma (Fig. 4-39)

Figure 4-39 is a cholangiogram of the patient having carcinoma developing from the common bile duct. In this patient, a catheter had been inserted through the abdominal wall into a dilated intrahepatic bile duct in order to drain away the accumulated bile, and the roentgenogram was taken after contrast medium was instilled through the catheter. Clearly, the intrahepatic ducts are strongly dilated due to bile stasis. This is the result of obstruction with carcinoma growing in the common bile duct, where the ductal lumen is shown abruptly coming to an end (arrow). In this situation, it is possible that carcinoma cells are not confined to the place of ductal obstruction; probably they have already extended along the ductal mucosa replacing the surface epithelial cells in the form of carcinoma in situ (CIS). However, about the extension of CIS-type carcinoma along the intra- and extrahepatic bile ducts, no reliable information is provided by any means available, including the X-ray imaging shown in the present figure. Thus, it still remains difficult for surgeons to establish an effective, pathology-based strategy against this tumor, and because of this, the tumor belongs to one of the most intractable cancers (Langer *et al.*, 1985). In an effort to provide knowledge about the way this tumor develops and extends in the biliary tree in strict histopathological terms, Suzuki *et al.* (1989, 1998) attempted at 3-D mapping of carcinoma and precarcinomatous lesions (dysplasia) in the hepatohilar and intrahepatic biliary tree.

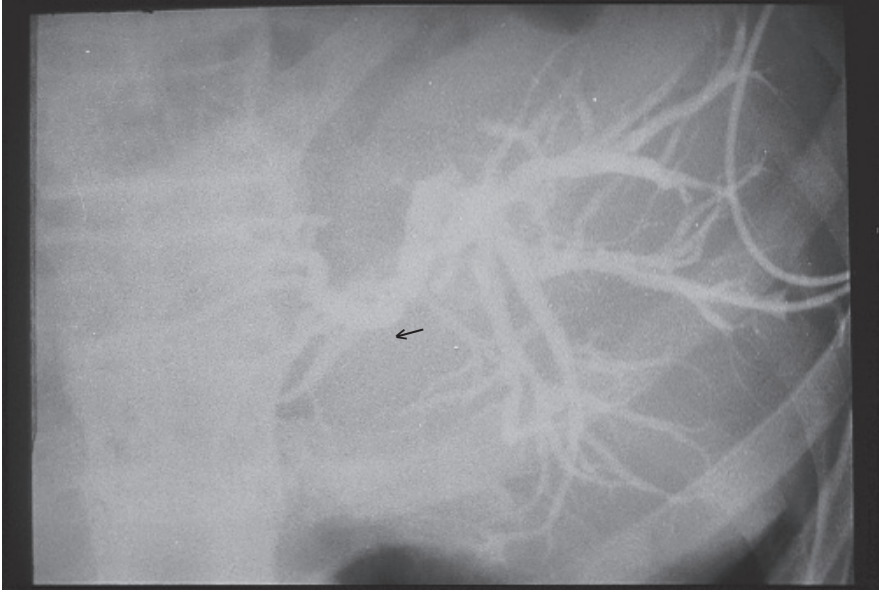


Fig. 4-39. A cholangiogram taken in a patient having hepatohilar bile duct carcinoma. Note the strongly dilated intrahepatic biliary tree. The tree is severed at the trunk, the common bile duct (arrow), showing a complete obstruction due to growth of carcinoma.

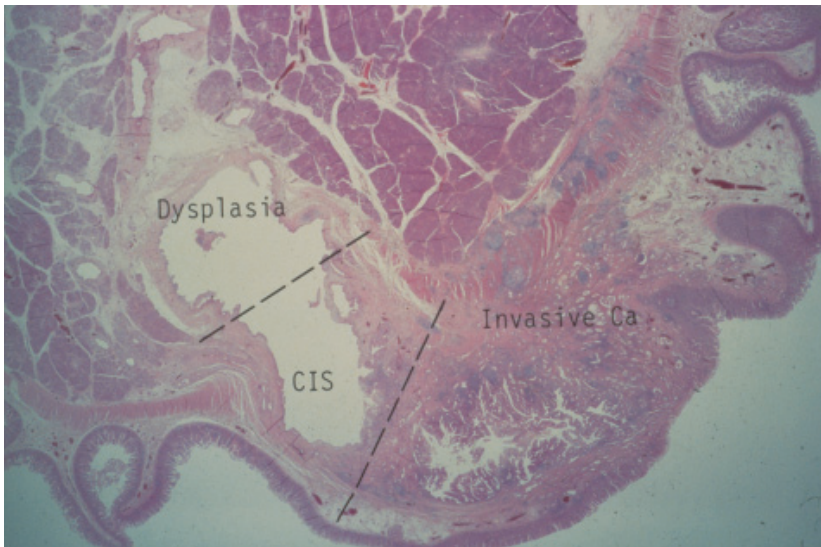


Fig. 4-40. Carcinoma of common bile duct developing at the lowermost portion (ampulla). A low power microphotograph. Carcinoma is invading around the duct and beneath the duodenal mucosa, but in the upper part, carcinoma extends non-invasively as CIS (carcinoma in situ) along the mucosal surface. In the more upper part, precarcinomatous cells (dysplasia) are extending, reaching the upper surgical margin. Hematoxylin-eosin stain.



### **Invasive carcinoma, CIS and dysplasia: distribution (Fig. 4-40)**

Figure 4-40 is a low-magnified microphotograph of carcinoma arising at the lowermost portion of the common bile duct. The tumor is infiltrating around the duct and beneath the duodenal mucosa, but in the neighboring upper part, CIS (carcinoma in situ) is extending along the mucosal surface replacing the epithelia but without invading the subepithelial tissues. In the more upper part, there is an area of dysplasia where the surface epithelia of mucosa is replaced by atypical cells which however are not abnormal enough for giving a diagnosis of carcinoma. The term dysplasia is used to express the latter sort of change, and generally connotes that the atypical cells are in a precarcinomatous state. Thus, an invasive carcinoma is likely to be surrounded by a zone of CIS, which then is surrounded by another zone of dysplasia, and here again, we may expect a multistep carcinogenesis expressed in the form of concentric zonation.

### **Various grades of dysplasia in superficial mucosal cells (Fig. 4-41)**

While microscopically examining bile ducts in materials taken from patients of hepatohilar bile duct carcinoma, one may find various grades of atypia distributed in a

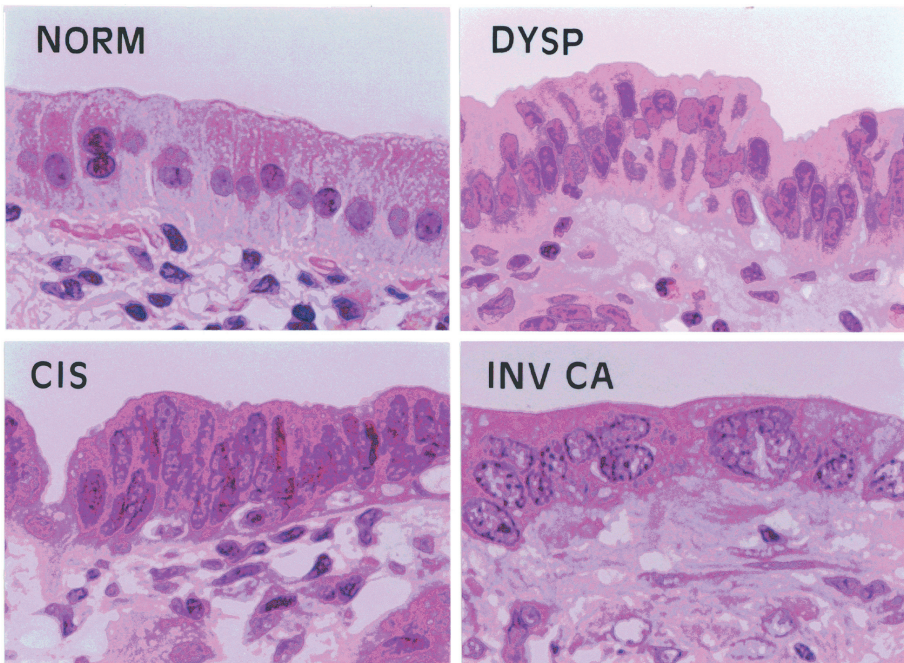


Fig. 4-41. Various grades of atypical cells found in bile duct. Normal (NORM), dysplasia (DYSP), carcinoma in situ (CIS) and invasive carcinoma (INV CA).

mosaic. Some examples are shown in Fig. 4-41 which includes normal bile duct epithelia, dysplastic cells, carcinoma in situ (CIS) and invasive carcinoma. One can confirm the cellular atypia advancing in this order.

### Whole liver reconstruction from “macroserials” (Figs. 4-42, 4-43)

In many cases, surgical treatment of hepatohilar bile duct carcinoma includes resection of hepatohilar bile ducts involved in carcinoma, together with the part of the liver into which CIS-type carcinoma is assumed to be extending along the intrahepatic bile ducts. Therefore in performing 3-D reconstruction of biliary tree, a partially excised liver has to be subjected to serial slicing, where the thickness of a single section is required to be as thin as 1 mm. Serial slicing of this voluminous and flabby organ at a uniform thickness of 1 mm, if manually attempted, is next to impossible. After several trials, we found it workable to use a ham slicer, a simple device widely used in processing edible meat (Suzuki *et al.*, 1988). The method ensures to obtain a serial 1-mm slices from a formalin-fixed liver lobe. The slices were “embedded” in gelatin to “fix” the flabby hepatoduodenal ligament containing the common bile duct. Figure 4-42 displays an example of liver thus sliced sequentially into what we call “macroserials.”

Figure 4-43 exhibits a 3-D reconstruction of the intrahepatic biliary tree in a whole liver which was obtained at autopsy and had carcinoma in the gallbladder. The organ was sliced into as many as 223 serial slices to visualize the distribution of carcinoma. The figure however was designed so as to show only the anatomy of normal bile ducts, not distinguishing among the normal, dysplastic and carcinomatous segments.

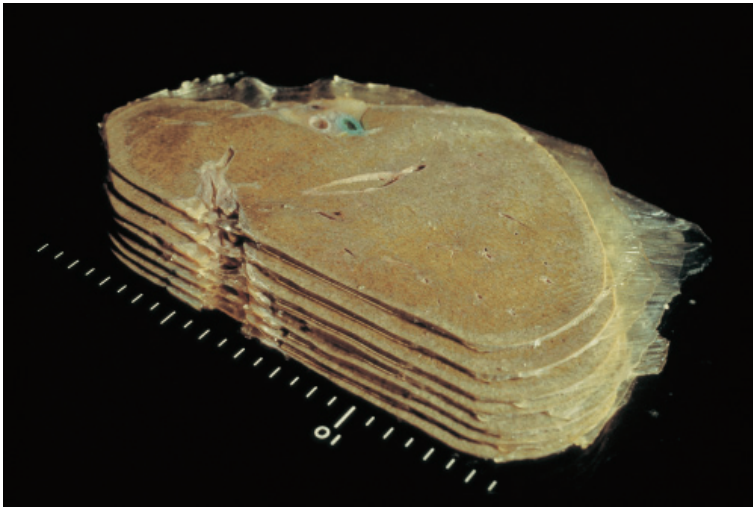


Fig. 4-42. Preparation of “macroserials,” serial slicing of surgically excised liver lobe, gelatin embedded, into 1mm-thick slices using a ham slicer. Also see page 97-98. Reproduced from Suzuki, Takahashi *et al.* (1989): *Cancer* 64, pp. 660.

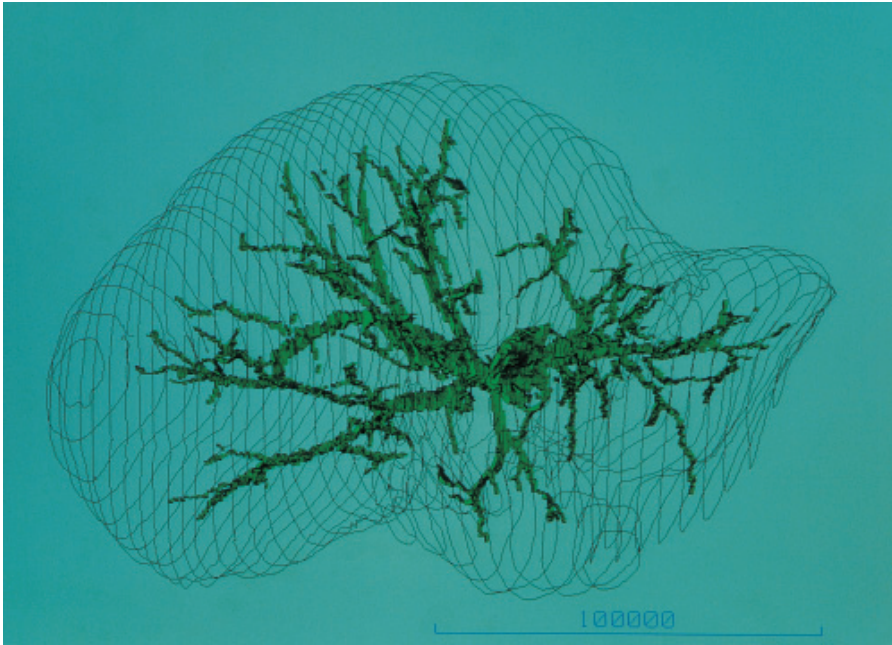


Fig. 4-43. Computer-assisted 3-D reconstruction of a whole liver taken at autopsy to show the intrahepatic biliary tree. The liver was sliced into 236 “macroserials.” A case of gallbladder carcinoma.

### Three-D mapping of carcinoma in the biliary tree (Fig. 4-44)

An example of 3-D mapping is shown in Fig. 4-44. This is from a patient in whom the left liver lobe was resected for carcinoma arising from the left hepatic duct. Painted green are ducts lined with normal epithelia. Carcinoma is shown growing in the left hepatic duct that is painted in red, where partially the tumor is infiltrating periductally, as indicated by yellow wireframes. There are segments painted blue, and these indicate ducts lined by dysplastic epithelia. It is clearly visualized that 3-dimensionally, the ducts with epithelial dysplasia are so arranged as to surround the duct having carcinoma. Thus the pattern of distribution seems to be suggesting that a zone of dysplasia had been extending before carcinoma developed within the zone, and once again we find an expression of multizonal advancement of malignant transformation. Carcinoma, not reaching the stump at either the right hepatic or common bile duct, seems to have totally been removed. However, dysplasia has already extended down to these stumps, leaving the possibility that ducts having this precancerous lesion remain unexcised in the patient, awaiting future malignant changes.

The 3-D mapping was extended so as to include as many as 26 patients operated for hepatohilar bile duct carcinoma (Suzuki *et al.*, 1999). Out of the 26 livers, as many as 21 (81%) proved to have a dysplastic zone around carcinoma. Thus, hepatohilar bile duct carcinoma arising from dysplasia seems to be quite common.

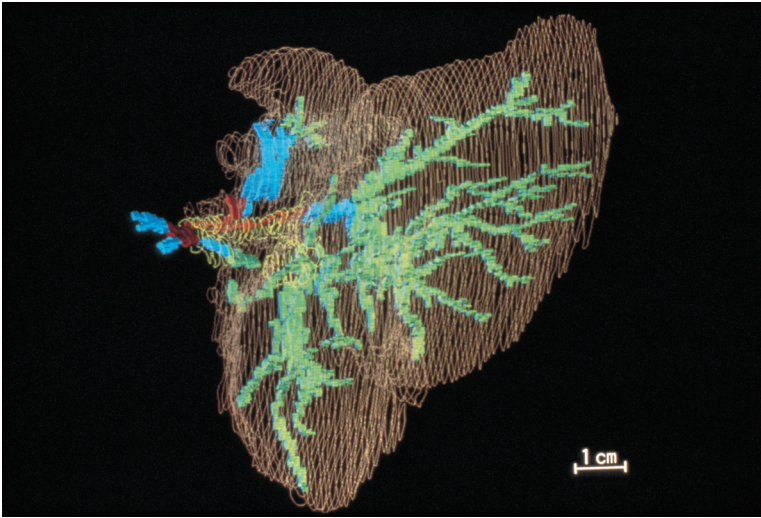


Fig. 4-44. Computer-assisted 3-D mapping of tumors in the biliary tree of the left liver lobe resected for carcinoma arising in the left hepatic duct. Bile duct segments having carcinoma are painted in red, those with dysplasia in blue and normal ducts in green. Note that carcinoma is surrounded by segments having dysplasia, demonstrating a sort of concentric zonal arrangement and suggesting that the carcinoma has arisen in a pre-existing zone of dysplasia. Reproduced from Suzuki, Takahashi, *et al.* (1989): *Cancer* 64, pp. 662.

### g) Intraductal papilloma of breast: extension and cancer development

#### A breast comprises several lobes (Fig. 4-45)

A unilateral human breast contains 15 to 20 glandular lobes, each drained by a segmental (lactiferous) duct which opens at the lactiferous sinus just below the nipple. Toward the periphery, the duct divides many times, forming a tree of mammary ducts. In the schema of Fig. 4-45, a breast is illustrated so as to contain four lobes.

#### Intraductal papilloma: microscopic appearance (Fig. 4-46)

Sometimes, papillary tumor arises from the epithelia lining the mammary ducts and extends intraductally forming a ductal cast as schematically shown in the foregoing figure. This tumor is called intraductal papilloma and appears on microscopic section as multiple tumors (Fig. 4-46). Not infrequently, carcinoma arises in intraductal papilloma, but the accurate site of ductal tree where carcinoma develops had not been known. Also, we cannot determine on a 2-D section whether there is a single dividing tumor or there are multiple tumors, since the tumor extends in the finely arborizing ductal tunnels. In Fig. 4-45, the right schema illustrates an intraductal tumor which is single and united, while in the left, there are multiple tumors. However, we cannot determine which of the two possibilities is the case, so long as our observation is confined to a sectional picture, for example, that of the plane along the broken line. In this situation, it requires 3-D visualization of ductal tree to obtain information about the development and extension of intraductal papilloma and its relation to carcinoma. This was performed by Ohuchi *et al.* (1984a) who studied breast lobes excised from 15 patients with intraductal papilloma.



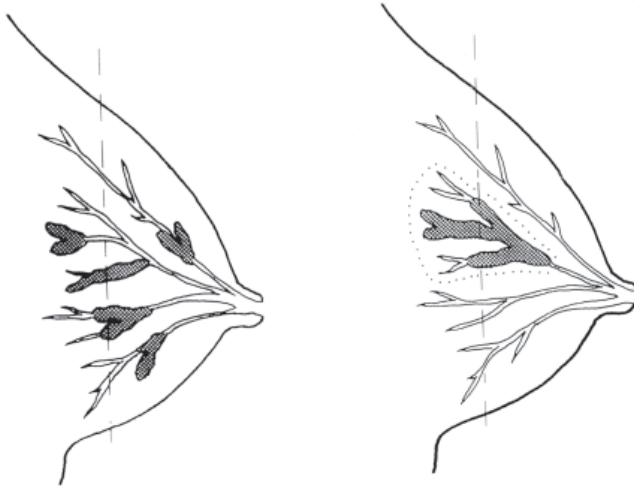


Fig. 4-45. Ducts and lobules of breast: a schema. Carcinomas as well as pre-carcinomatous lesions of the breast develop in the tree of mammary duct, but whether the ductal system harbors a single tumor or multiple tumors cannot be determined by observing a section shown by the broken line. In both the left and right pictures, three sections of tumor appear in the cutting plane.

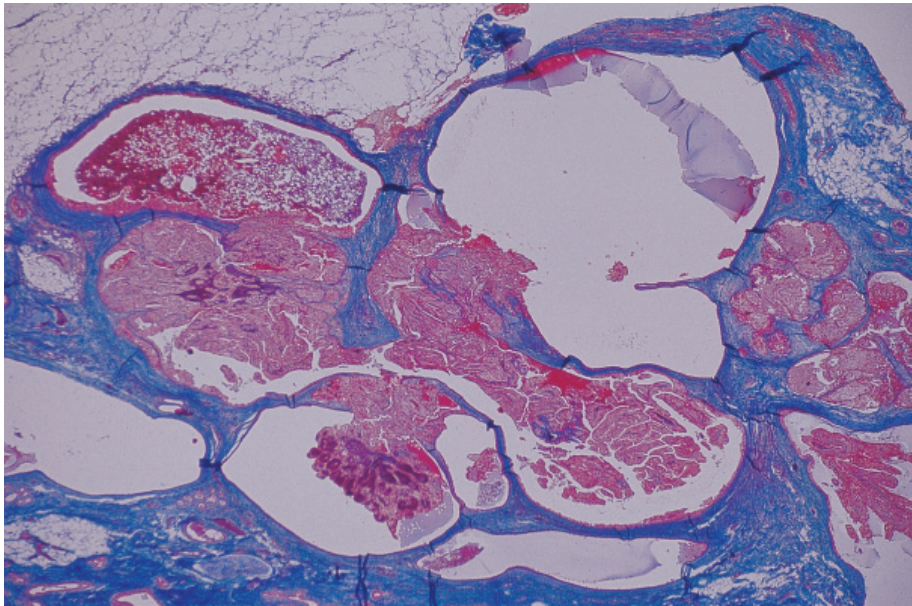


Fig. 4-46. Intraductal papilloma of the breast: a low power microphotograph. There are tumors growing in several ducts, but their connecting relation in the ducts is not visible on a single 2-D section. Azan-Mallory stain.



### Three-D mapping of intraductal papilloma (Figs. 4-47, 4-48)

Figure 4-47 is a semi-schematic presentation of reconstructed ducts in a patient with papilloma. The material was a single mammary lobe taken by segmentectomy. Smaller subbranches having no tumor are omitted from the figure for the sake of better perspective. In the figure, one can find a total of nine papillomas, each extending in

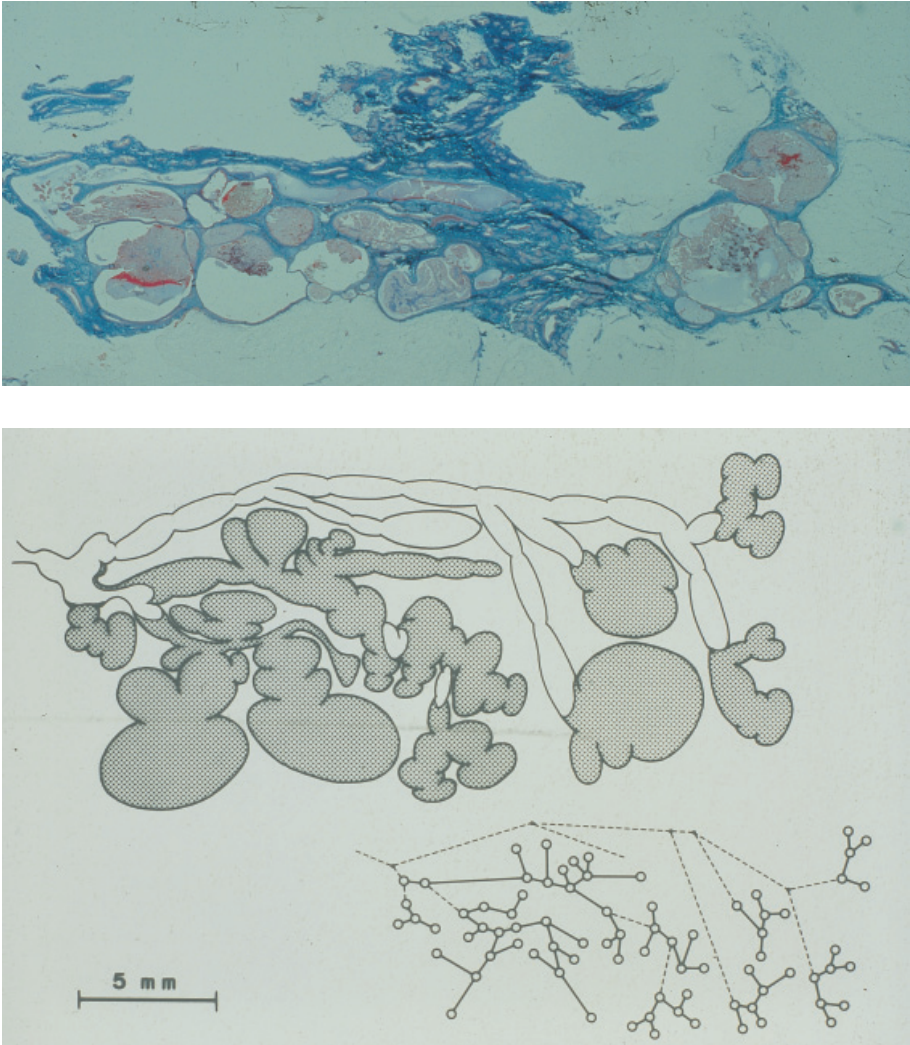


Fig. 4-47. Manually performed 3-D mapping of intraductal papillomas in the ductal tree of one mammary lobe. A half-schematized presentation. As a whole there are nine tumors, each rooted at a terminal segment of the ductal tree, suggesting that all the tumors have developed from the terminal segments. Reproduced from Ohuchi, Takahashi *et al.* (1984): *Breast Cancer Res Treat* 4, pp. 122.

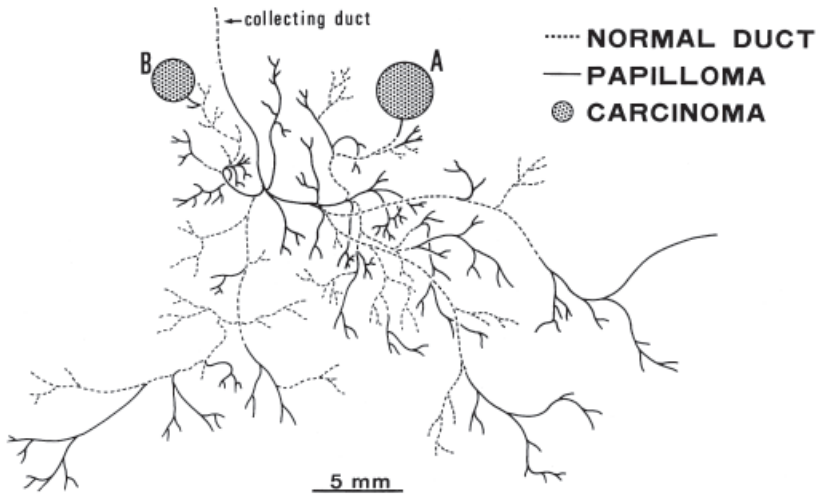


Fig. 4-48. Manual 3-D mapping of intraductal papillomas, another case. Here, a mammary lobe proved to contain a total of 18 papillomas (solid line), all of which are rooted at the treetop. The broken lines are ducts having no tumor. At two places, denoted with A and B, minute carcinoma was detected to be arising in papilloma. Reproduced from Ohuchi *et al.*(1984): Cancer 54, pp. 610.

the branching ducts but independent of the others. It is worthy of attention that without exception, all the nine papillomas are rooted somewhere at the terminal ending of the ductal tree. This seems quite likely to be suggesting that this type of papilloma arises in the terminal segment of mammary ducts, usually as multiple tumors and growing intraductally toward the nipple.

Figure 4-48 is another 3-D mapping of ducts from another patient of intraductal papilloma performed by Ohuchi *et al.* (1984b), again in the form of schematic presentation. Here too, the arborizing ducts contained in a lobe are reproduced, where the broken lines denote the segments having normal epithelia and the solid lines, those harboring papilloma. One can confirm that the ductal tree contains a total of 18 independent papillomas, and here again, all of the tumors have a root at the ductal terminal. In this case, however, minute carcinoma was found developing at two places, as denoted with A and B.

### Three-D mapping study of intraductal papilloma: summary (Fig. 4-49)

The results of 3-D mapping performed in a total of 15 cases of intraductal papilloma are summarized in Fig. 4-49. In all patients the material was a single mammary lobe surgically excised by segmentectomy. Comparison of the results led to the conclusion that from a 3-D distribution point of view, intraductal papillomas are classifiable into two types. In one, the tumor develops in a larger segment usually as a single mass. This type was found in five of the 15 cases, and in none of them carcinoma

	Solitary Papilloma		Multiple Papilloma	
No of cases	2	3	2	8
Anatomical sites				
Segmental duct				
Subsegmental duct				
TDLU				

Fig. 4-49. A summary of 3-D mapping of papilloma in 15 patients. It turned out that the intraductal papillomas were classifiable into two types: multiple and solitary. The former arises in the terminal segments and can secondarily develop carcinoma, whereas the latter grows in the larger part of the ductal tree as a single mass, where no cancer development was demonstrated. Reproduced from Ohuchi, Takahashi *et al.* (1984): *Breast Cancer Res Treat* 4, pp. 126.

proved to be arising. The pattern of distribution was different in the remaining 10 patients; here the tumor presents as multiple masses developing from the treetop of the ductal system. Carcinoma, when found in papilloma, never failed to arise in the latter type.

**h) Three-D microanatomy and pathology of human pancreas**

**Two types of ischemic necrosis: central and peripheral (Figs. 4-50, 4-51)**

While microscopically examining autopsy material, ischemic necrosis of the pancreas is found, not infrequently. Such necroses occur when the blood flow of pancreas is severely impaired, for example in patients who have been in the state of cardiac insufficiency or shock. We noticed from a microstructural viewpoint that two types of necroses were discernible. In one, as in the microphotograph of Fig. 4-50, necrosis involves the islet of Langerhans. This type of necrosis involves the central area of “primary lobule,” a unitary structure of the pancreas, which we defined as below. Therefore we designated this type as “central necrosis.” Entered in the lower part of the figure is a manual 3-D reconstruction from this pancreas. There are two necrotic foci (hatched), each containing a large islet supplied by an afferent arteriole.

The other type is “peripheral necrosis.” Here, as in Fig. 4-51, necrosis develops so as to surround an islet at a distance, while the islet itself remains exempted from ischemic injury. This type of necrosis is considered to extend along the peripheral zone of the “primary lobule.” In the lower part of the figure, portions of two large (secondary) lobules are reconstructed. Shaded are the necrotic foci, mostly sitting on the interlobular septa. Note that the islets are uninvolved, kept apart from the lesions.

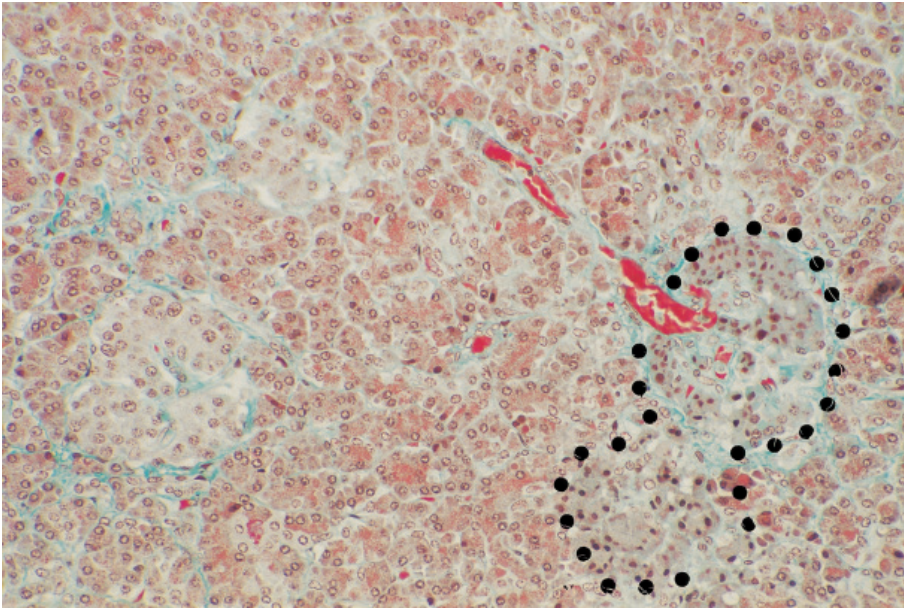


Fig. 4-50. The central type of ischemic pancreatic necrosis. (Upper) Necrosis involves two islets and surrounding excretory tissue (encircled by dots). Elastica-Goldner stain. (Lower) Manual reconstruction from a part of the pancreas containing five primary lobules. There are two necrotic foci (hatched), each having an islet. The lower figure reproduced from Takahashi, Yaginuma *et al.* (1985): *Path Res Pract* 179, pp. 647.



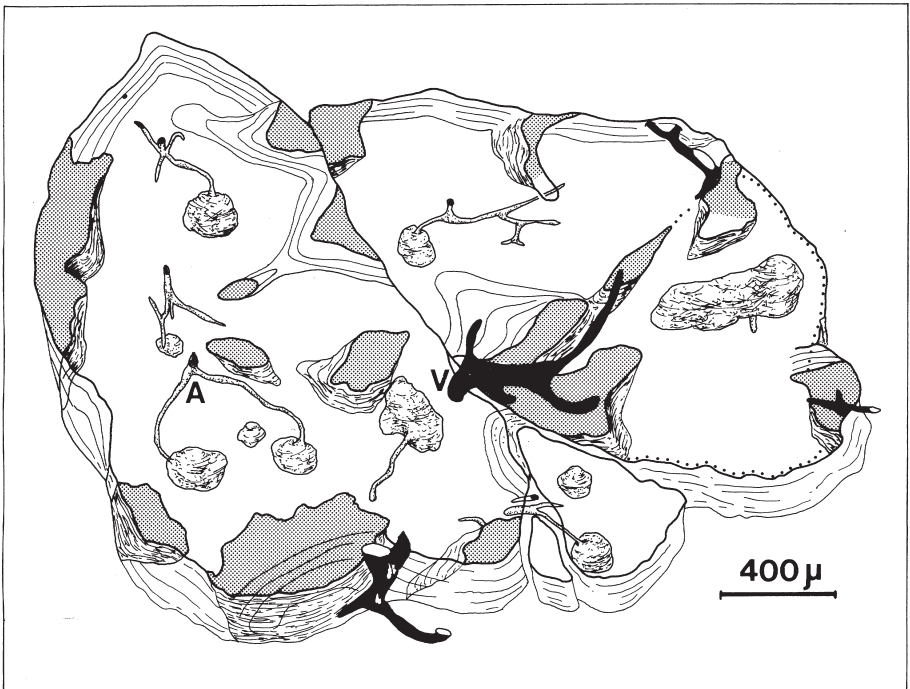
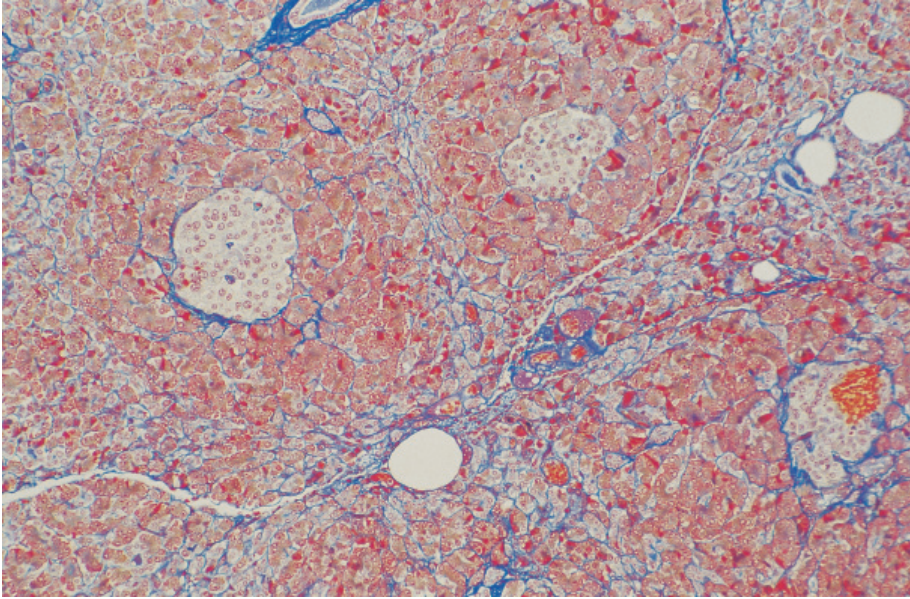


Fig. 4-51. The peripheral type of ischemic necrosis. (Upper) Necrotic belts are surrounding well-sustained areas, each having an islet at the center. Azan-Mallory stain. (Lower) Manual reconstruction showing the necrotic foci (hatched) distributed along venules (V) and surrounding the islets at a distance. A: arteriole. The lower figure reproduced from Takahashi, Yaginuma *et al.* (1985): *Path Res Pract* 179, pp. 649.



### Three-D vasculature of the pancreas (Fig. 4-52)

Since the lesions are ischemic in origin, the difference in morphogenesis of the two types of necrosis may become clear if the basic microvasculature pattern of the human pancreas is established. However, what had been known of the pancreatic vasculature was limited to the intimate anatomical association of islets with arterioles, a finding described in the early 1930s by Beck and Berg (1931). In this view, Yaginuma *et al.* (1986) and Takahashi *et al.* (1985) performed manual 3-D reconstruction of pancreases taken at autopsy to see what pattern of vasculature exists, underlying the development of such ischemic lesions. Shown in Fig. 4-52 is the microvasculature of a normal pancreas reproduced from serial sections by manual method. Two lobules are included in the figure, each containing Langerhans' islets of various dimension. Pairs of interlobular artery (white) and vein (black) are shown running within the interlobular septum, entering the lobules and dividing in the lobular parenchyma.

Four different types of relationship proved to exist between the terminal arterioles and islets:

- Type 1: Arteriole that terminates at a large islet and serves as its vas afferens
- Type 2: Long arteriole that ends in the peripheral zone of lobule
- Type 3: Arteriole having one or more small islets dispersed around its ending
- Type 4: Arteriole stemming from interlobular artery, directly entering a lobule and ending at an islet

Despite the variety in the pattern of arterial ending, larger islets are supplied without exception by an afferent arteriole.

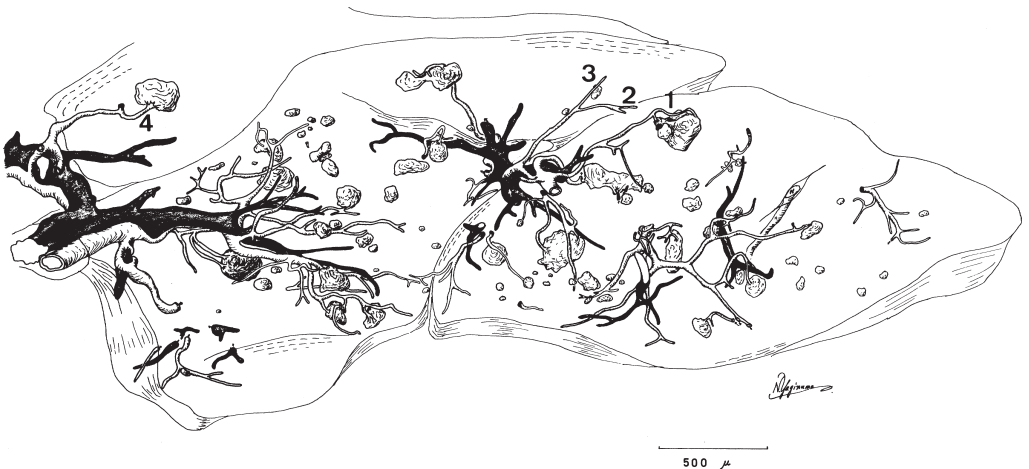


Fig. 4-52. Manually performed 3-D reconstruction of the pancreatic microvasculature. Two lobules are included. White: interlobular artery. Black: interlobular vein. Many islets are dispersed in the lobules. The relation of islets with terminal arteries is various, allowing to classify into four types, as denoted in the figure by 1, 2, 3 and 4. Reproduced from Yaginuma, Takahashi *et al.* (1986): *Pathol Res Pract* 181, pp. 80.

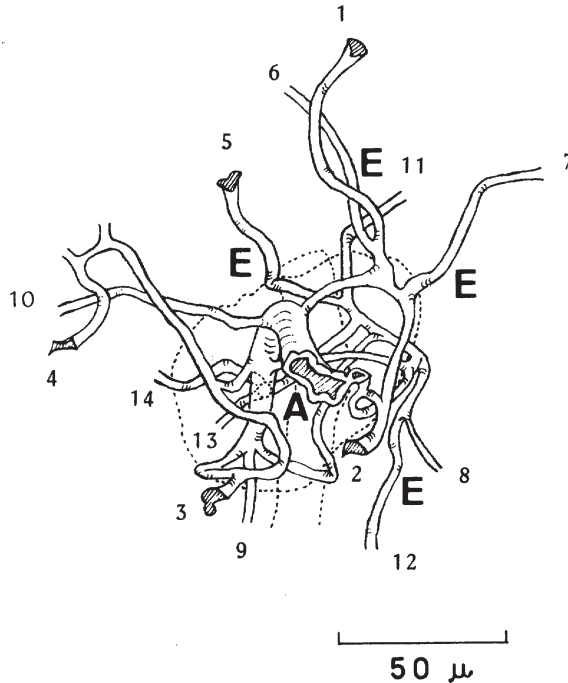


Fig. 4-53. Manual 3-D reconstruction of minute vessels in and around a medium-sized islet. An afferent arteriole (A) enters the islet and divides into a glomoid network of capillaries. A total of 14 efferent vessels (E) leave the islet and connect with the capillary network of the surrounding exocrine tissue. Reproduced from Yaginuma, Takahashi *et al.* (1986): *Pathol Res Pract* 181, pp. 81.

### Vasculature of a Langerhans' islet (Fig. 4-53)

In Fig. 4-53, 3-D vasculature in and around an islet of Langerhans is visualized. An afferent arteriole (A) is shown entering the islet. It divides into a glomoid network of capillaries. Blood leaves the islet, in this figure through 14 efferent vessels (E), and irrigate the capillary network of the surrounding exocrine tissue so that the hormones secreted by the islet cells may be carried directly to the exocrine region.

### Summary of pancreatic vasculature: the primary lobule (Fig. 4-54)

The basic pattern of pancreatic microvasculature was abstracted from Fig. 4-52 and summarised in Fig. 4-54. The schema illustrates that the lobule of the pancreas is an assembly of smaller structural units, each having a terminal arteriole at the center and flanked by venules. We designated these units as the primary lobules of pancreas with a connotation that the conventional lobules wrapped by connective tissue septa are to be called the secondary lobules. Sometimes the central arteriole does not supply an Langerhans' islet directly, but the islets never fail to find themselves at the center of the primary lobule so that the exocrine tissue, surrounding an islet or islets, may always be irrigated by blood containing islet hormones just secreted. Between the arte-

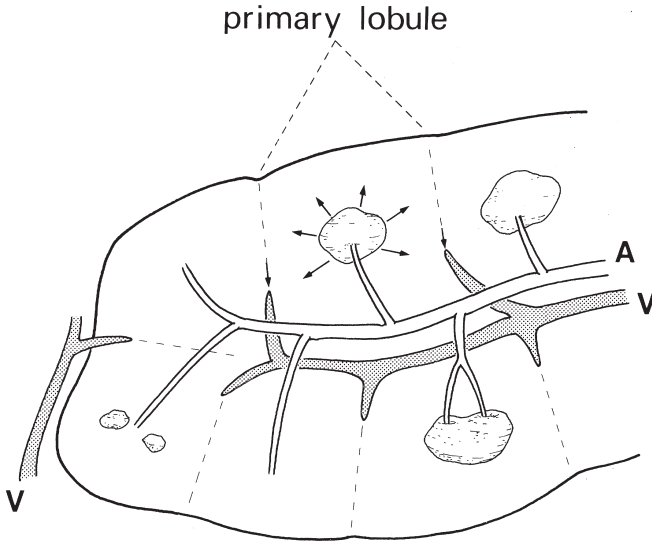


Fig. 4-54. The basic pattern of pancreatic microvasculature. A branch of terminal arteriole (A) is assigned to irrigate a small unitary area, which we call a primary lobule. A primary lobule has a terminal arteriole at the center and flanked by venules (V). Islets, whether or not directly supplied by an afferent arteriole, are always positioned at or near the central portion of primary lobule. The conventional lobule surrounded by connective tissue septa (the secondary lobule) is an assembly of primary lobules. Reproduced from Takahashi, Yaginuma, *et al.* (1985): *Pathol Res Pract* 179, pp. 646.

rioles (A) and venules (V) one can find an alternating (interdigitating) relation, where a certain degree of isodistance seems to exist.

### Two types of ischemic necrosis related with the microvasculature (Fig. 4-55)

Based upon the structural principle induced above, we are now able to explain the difference in pathogenesis of the two types of ischemic necrosis (Fig. 4-55). The development of “central necrosis,” i. e., ischemic necrosis involving the central zone of primary lobule, may be understood if we assume that arterial blood flow is blocked at the most peripheral segment. Such a segment corresponds to the arteriole supplying a primary lobule; when the primary lobule has a larger islet, the arteriolar segment functions as its afferent arteriole. Upon this type of ischemia, the peripheral zone of primary lobule may be exempted from ischemia because collateral blood can flow in from the neighboring primary lobules. In contrast, “peripheral necrosis” is considered to occur when a more proximal arterial segment is severely but imperfectly obstructed. In this case, the obstructed arterial segment may be responsible for supplying an area of pancreas containing, for example, tens or hundreds of primary lobules. Then, for individual primary lobules, no collateral flow from the adjacent ones can be expected. Thus, it may be the periphery of primary lobules that is most vulnerable to deficient bloody supply, since the zone corresponds to the part remotest from the afferent arteriole through which blood flows in.

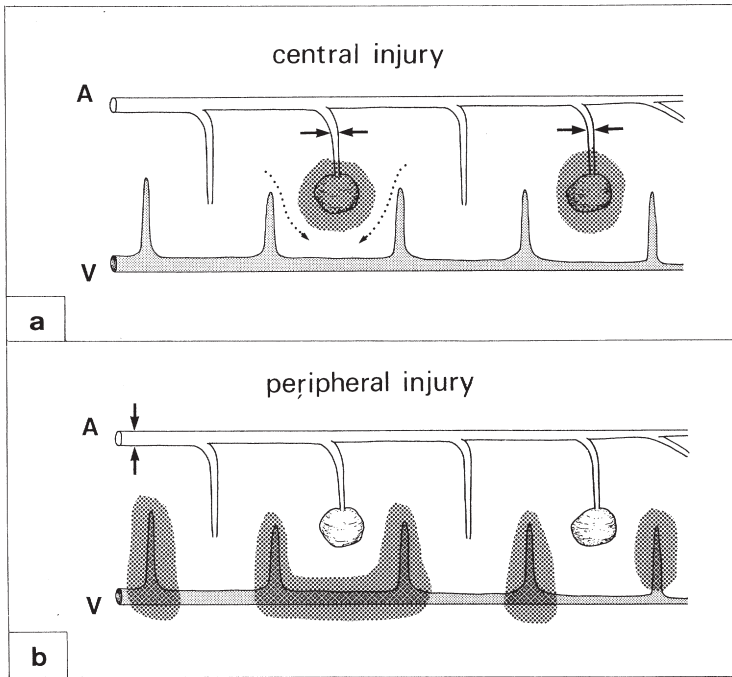


Fig. 4-55. The two types of ischemic necrosis is correlated with the microvasculature shown in Fig. 4-54. The central necrosis (a), involving the central portion of primary lobules, is explained by assuming that the blood flow is blocked at the terminal arteriole. Collateral blood flow, from the neighboring primary lobules, relieves the peripheral zone of primary lobules. In contrast, the peripheral necrosis (b) is understood by assuming an obstruction at a more proximal arterial segment. In this case, the periphery of primary lobules is the site most susceptible to ischemia. Reproduced from Takahashi, Yaginuma, *et al.* (1985): *Pathol Res Pract* 179, pp. 650.

### The lobule of the pancreas and its anatomical significance (Fig. 4-56)

Also to be introduced are another series of pancreatic studies by Watanabe *et al.* (1997, 1999) who performed 3-D reconstructions of pancreas with computer assist. Figure 4-56 demonstrates an adult human pancreas which was analyzed to examine whether the “lobules,” not primary but the secondary ones defined by the connective tissue septa, are a vascular or a ductal unit. Reconstruction disclosed that the demarcation of lobules by the membranes (black wireframes) was quite imperfect with many holes gaping in the septa, through which the parenchymal tissue proved to be continuing. Most lobules, however, were found to receive a single duct (yellow), justifying to define them as “glandular lobules.” Exceptions to this rule were not rare because sometimes, lobules were found receiving not only a lobular duct of their own but a small accessory duct from the neighboring lobule. There was no finding giving support for assuming that the lobules are a vascular unit, because from any viewpoint, they were not corresponding to any territories of arterial supply or venous drainage.

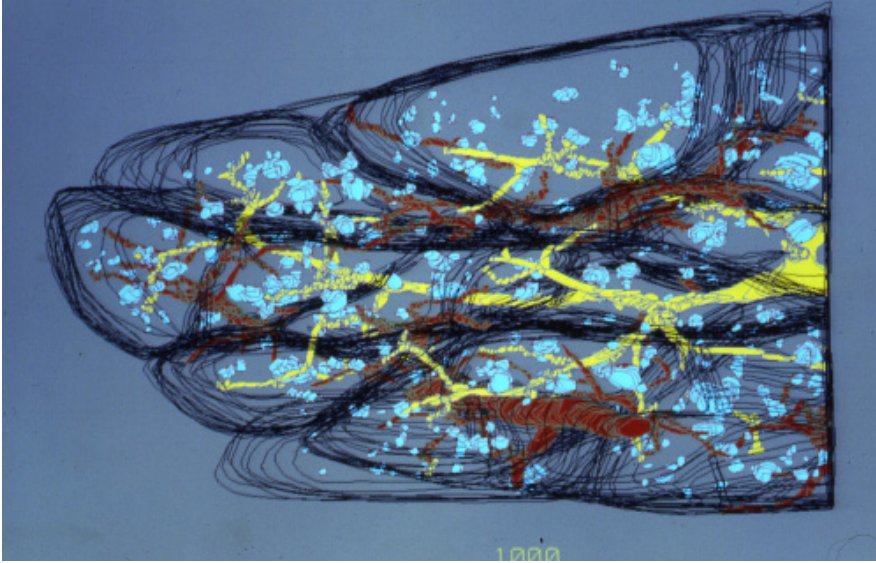


Fig. 4-56. Computer-assisted 3-D reconstruction of normal pancreas to understand the anatomical significance of the (secondary) lobules. Note that the demarcation with the septa (black wireframes) is imperfect and penetrated by large holes, through which the parenchymal tissue and ducts (yellow) continue. However, most lobules are shown receiving a single duct, justifying to define them as glandular units. Reproduced from Watanabe, Takahashi, *et al.* (1997): *Pancreas* 15, pp. 50.

#### **Islet-duct relation: changes with the development (Figs. 4-57, 4-58, 4-59)**

It is well known that in the human, pancreatic islets arise in an early period of gestation from the primitive pancreatic ducts as insular buds (Like *et al.*, 1972). Thereafter the islets are supposed to separate from the ducts and disperse throughout the lobules, but little has been known about how they migrate to take the ultimate spatial distribution in the lobule. To visualize the developmental process of pancreas in this context, its microstructure was studied by computer-assisted 3-D reconstruction.

Specimens of fresh autopsy pancreases from three fetuses, three neonates and three adults were submitted to serial sectioning and 3-D reconstruction of one secondary lobule. Representative pictures from each of the three age groups are exhibited in Figs. 4-57, 58 and 59, respectively. In the pancreas of a fetus, 24 gestational weeks (Fig. 4-57), small number of islets (light blue) were found, all of them still remaining in direct contact with the ducts (yellow). In a neonate on the first postnatal day (Fig. 4-58), 31 islets were contained in the lobule; 23 of these were still retaining contact with ducts, whereas the other eight (violet) were separated from the ducts and going to disperse in the exocrine tissue. In the pancreas of an adult, 47-year-old male (Fig. 4-59), 52 of the 101 islets in the reconstructed lobule were still having contact with ducts, while the others had migrated far into the peripheral lobular zone. This transition of islets from the periductal to more peripheral zone seemed to ensure direct effects of islet hormones on the exocrine part of the pancreas. However, even in adults,



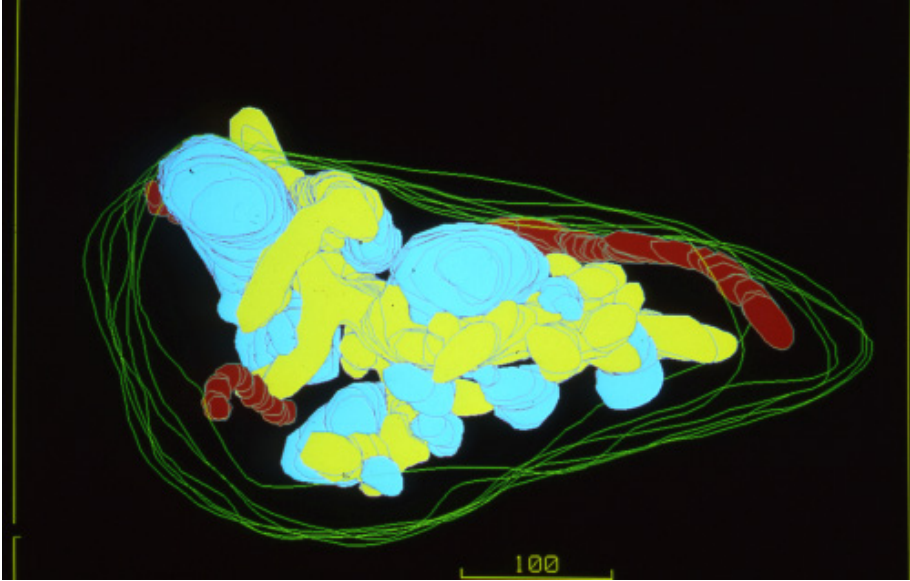


Fig. 4-57. Computer-assisted 3-D reconstruction of a fetal pancreas, 24 gestational weeks. In this stage of development, all the islets (light blue) remain as buds sprouting from the ducts (yellow). Arteries are painted in red. Reproduced from Watanabe, Takahashi, *et al.* (1999): *Pancreas* 18, pp. 351.

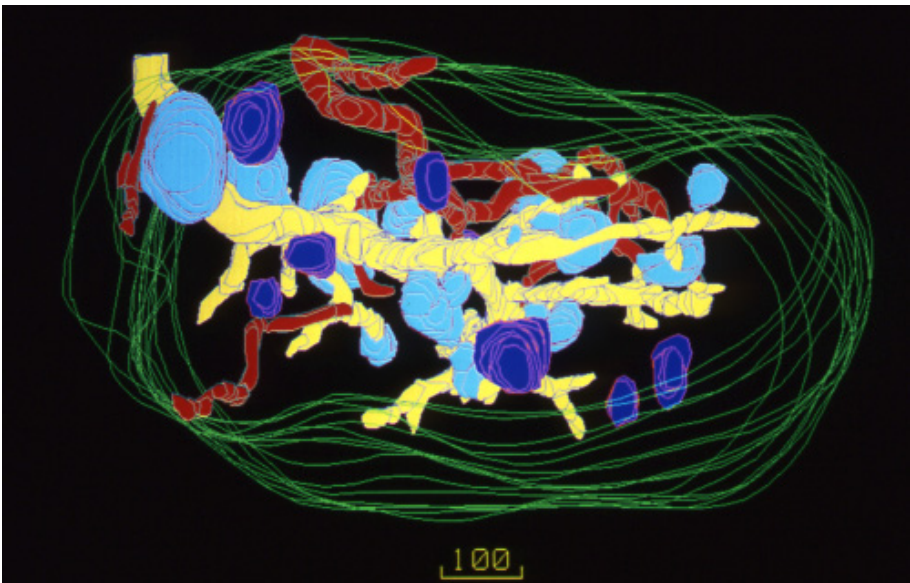


Fig. 4-58. Computer-assisted 3-D reconstruction of a neonatal pancreas. Most of the islets (light blue) are still retaining connectivity with the ducts, but there are small number of islets (violet) that have left the ducts and dispersed into the exocrine region. Reproduced from Watanabe, Takahashi, *et al.* (1999): *Pancreas* 18, pp. 351.

as many as half of the islets in a lobule were shown remaining next to the ducts. It seems possible that the latter group of islets are spare parts that will be mobilized in case of need, for example when a majority of peripheral islets have been destroyed. About this possibility, however, further studies have yet to be done.

**i) The microanatomy of terminal liver vessels and bile ducts (Figs. 4-60, 4-61)**

One of the serious complication of liver transplantation is the so-called vanishing bile duct syndrome, a progressive loss of intrahepatic bile ducts observed in chronically rejected allografts. Though much remains unknown about the causative factors of duct loss, the development of vascular lesions, particularly of hepatic arteries, seems playing an important role (Oguma *et al.*, 1989). However, little is known in the first place about the normal vascular supply of small intrahepatic bile ducts *of man*. In view of this, Takemura *et al.* (1991) undertook 3-D reconstruction of small bile ducts, peripheral hepatic arteries and portal veins in small portal tracts of normal livers and failed allografts, in order to visualize the basic pattern of vascular supply and to correlate the level of arterial obstruction with ischemic changes of ducts. As in Figs. 4-60 and 4-61, it was shown that in normal livers, interlobular bile ducts were wrapped by a dense peribiliary capillary network. Of the peripheral branches of hepatic arteries, some were confirmed running parallel with ducts, from which, branches were divided and sent to the network. We designated the former as the “accompanying arteries,” and the latter as “communicating arteries.” There were also arteries running indepen-

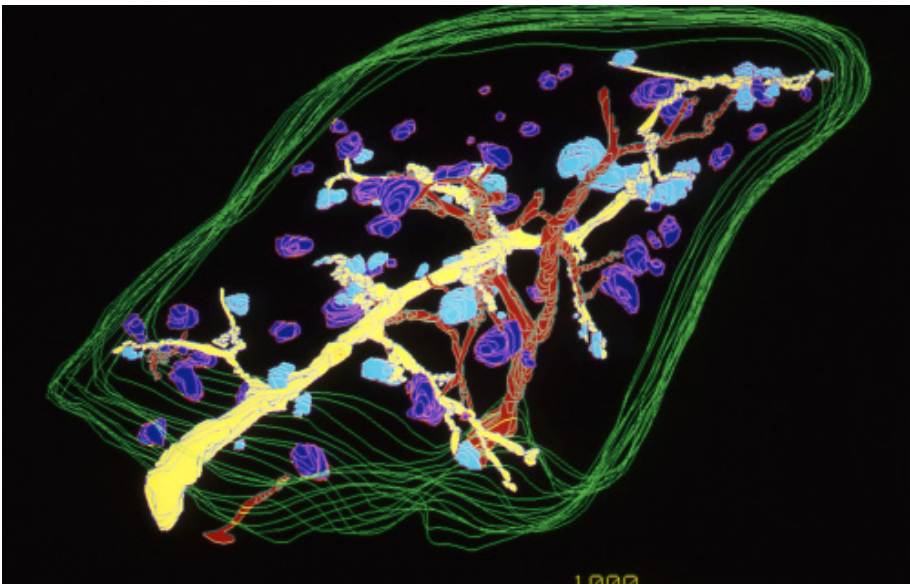


Fig. 4-59. Computer-assisted 3-D reconstruction of an adult pancreas. About half the islets have left the ducts and migrated far into the peripheral zone of lobule. Reproduced from Watanabe, Takahashi, *et al.* (1999): *Pancreas* 18, pp. 351.

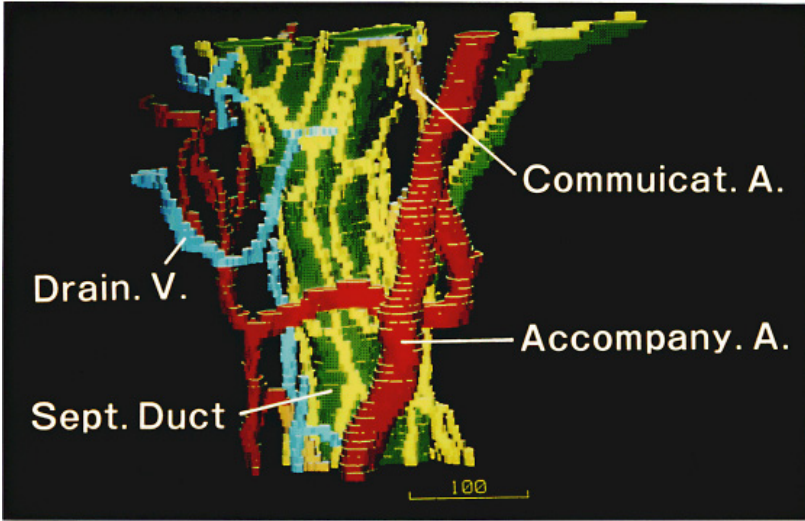


Fig. 4-60. Computer-assisted 3-D reconstruction of a peripheral bile duct and blood vessels in its surroundings, in a normal human liver. An interlobular duct (green) is wrapped by a dense peribiliary capillary network (yellow). There is a small artery running in parallel with the duct (the accompanying artery), from which small branches (communicating arteries) are divided and sent to the peribiliary network. Also, there is an artery running independently of the duct and directly pouring blood to the sinusoid. The peribiliary network is drained by a small portal vein (light blue). Reproduced from Takemura, Takahashi *et al.* (1991): *Transplant Proc* 23: 1410.

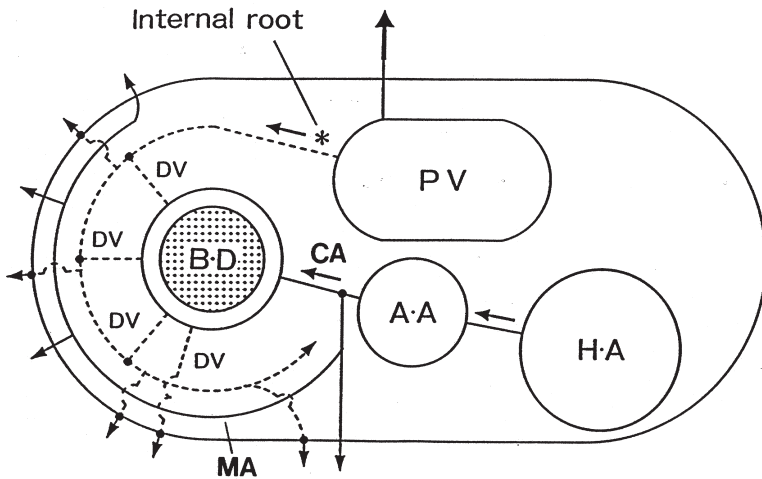


Fig. 4-61. A schema illustrating the microanatomy of peripheral bile duct (BD), its blood supply and drainage. HA: large hepatic artery, AA: accompanying artery, CA: communicating arteriole, PV: portal vein, DV: draining venule. Reproduced from Takemura, Takahashi, *et al.* (1991): *Transplant Proc* 23, 1409 – 1412.

dently of ducts and leading directly to the intralobular sinusoids. The network is drained by a small portal vein running at a distance, which is connected with the peribiliary network with “internal roots.” This is the basic pattern of peribiliary vasculature, which probably was the first demonstration for the liver of *man*, since previous knowledge had been either more or less fragmental or obtained from the liver of rodents. In the failed allografts severe arteriopathy proved to exist, where arteries were obstructed with proliferating intimal cells containing foam cells. Such changes were shown involving various levels of small arteries, including the accompanying and communicating arteries. Areas of network corresponding to obstruction were severely destroyed with significantly reduced density of capillaries.

## **The Structure of Adenocarcinoma and the Structural Differentiation**

While making microscopic diagnosis of tumor, pathologists encounter a wide variety of pictures. There are malignant and benign tumors, carcinomas and sarcomas, tumor cells showing various features, functions, grades of differentiation or ways to aggregate into different patterns. The variety reminds us of the structure of organs, where different pictures are presented from one organ to another. In fact, microscopically, the tumor is an organ. It comprises parenchymal cells (tumor cells), interstitial tissue and the vessels running in the latter, all arranged according to a certain principle. A tumor only differs from usual organs in that it keeps changing its structure incessantly and at a speed because of the continuous proliferation of tumor cells. Thus, what structure a tumor presents, and in what aspect the structure is proper to the tumor, is a subject to be studied from an organ structure point of view. And this viewpoint provides us with a clue to strengthen our microscopic diagnosis of tumor by refining the concept of “structural atypia.” This has long been considered to be of profound significance in diagnosis but so far, no clear definition has been given. In the following, we attempt to visually analyze the microstructure of gastric adenocarcinoma as an organ. It will make us realize that the concept of differentiation applies, not only to cellular constituents of tumor, but to the structure of adenocarcinoma which is more or less deviated from the glandular tree of ordinary stomach.

### **The structural pattern of normal gastric glands (Fig. 5-1)**

In Japan, carcinoma of the stomach has been and still is the malignancy that claims the largest number of lives. In histopathological terms, most of the gastric carcinoma belongs to adenocarcinoma. This type of carcinoma is so called because it is considered to originate from glandular epithelia of the stomach and more or less retains features of glandular cells even after they are transformed into carcinoma cells. Figure 5-1 is a schema illustrating normal gastric glands which open at the mucosal surface. They belong to the tubular type gland, dividing a few times downward within the mucosa and forming a small tree, with the secretory cells situated at the bottom. Gastric juice secreted by these cells is led upward to the gastric cavity through the duct. On account of this structure, the gastric gland, when sectioned in longitudinal direction, emerges in a section as a gland of “reversed Y” shape.



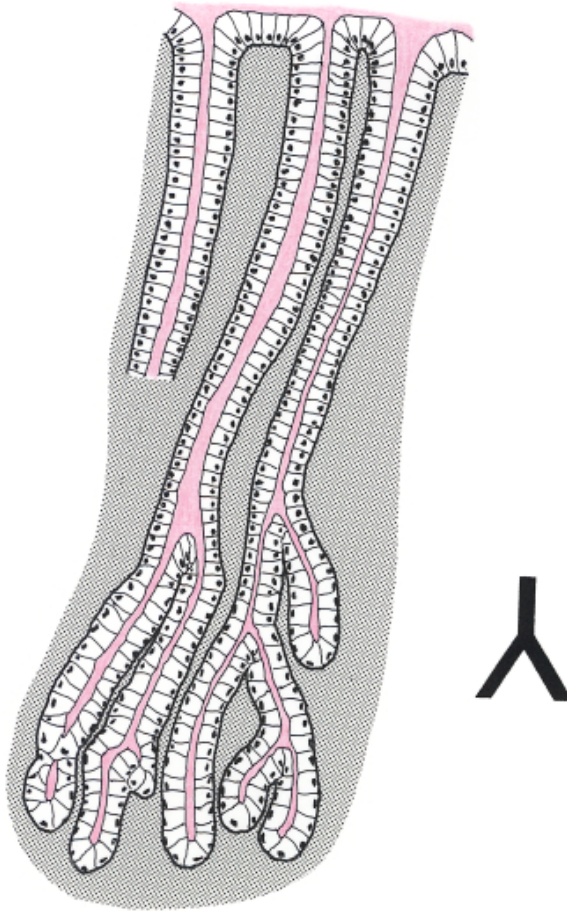


Fig. 5-1. A schema illustrating the normal gastric gland. The upper margin corresponds to the mucosal surface where the glandular duct opens and secretes the glandular product. The duct is tubular, runs vertically in the mucosa and divides a few times toward the mucosal bottom, creating on section a reversed Y-pattern. The ductal lumen (red) is continuous and its inner surface is lined with a monolayer of epithelial cells that are sitting on basal membrane.

### Cellular atypia of adenocarcinoma (Fig. 5-2)

As well known, pathologists make a diagnosis of carcinoma recognizing the feature of carcinoma cells that is expressed generally as cellular “atypia.” In the microphotograph in the left half of Fig. 5-2, one can see cross-sectioned glandular tubes (gastric pits) of normal gastric mucosa, and in the right half, an adenocarcinoma growing in gastric mucosa. The difference may be clear: the carcinoma is presenting as tubular glands lined with cells that are markedly “atypical” compared with the normal glands. The atypia is a concept comprising a series of morphological features of form, including enlarged nuclei and nucleoli, nuclear pleomorphism, coarse texture of nuclear chromatin, elevated nucleo-cytoplasmic (N/C) ratio and thickened nuclear membrane,

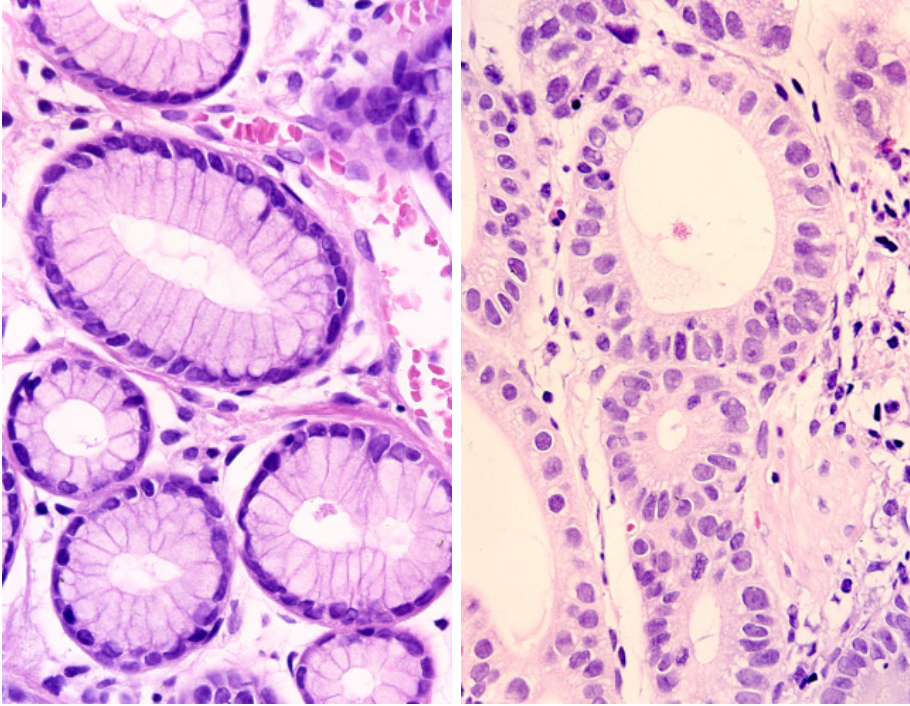


Fig. 5-2. Microscopic appearance of adenocarcinoma of the stomach (right). In the left, normal ducts of gastric gland (the foveolae), cross-sectioned, are exhibited for comparison. In carcinoma, the cells retain the basic feature of glandular epithelia by lining along the inner surface of tubes, but differ from the non-carcinoma cells in the presence of what is generally called “cellular atypia,” a feature most characteristically expressed in the form of nuclei. Hematoxylin-eosin stain.

all confirmable in the carcinoma cells exhibited in the figure. These features will be visited again in Chapter 8 dealing with the computer-assisted morphological classification of carcinoma and carcinoma-related cells.

### **Structural atypia in adenocarcinoma: Y-pattern (Fig. 5-3)**

However, there does exist another morphological aspect of carcinoma which is of equally basic diagnostic significance as the cellular atypia. That is, an abnormality in the structure of cellular assembly forming either a gland or something like gland. Look at Fig. 5-3, an early adenocarcinoma of stomach which has just begun growing in the mucosa. The tumor belongs to the well differentiated (tubular) type, and there is slight if any atypia of individual cells lining the tubular glands. However one can find here that even in the absence of severe cellular abnormalities, the glandular structure appears strikingly deviated from the norm. There are glands of non-reversed Y, in addition to X or H-pattern. If, in a mucosal biopsy, a pathologist fails to take notice of this, carcinoma may escape detection and remain in the patient where it will keep growing.

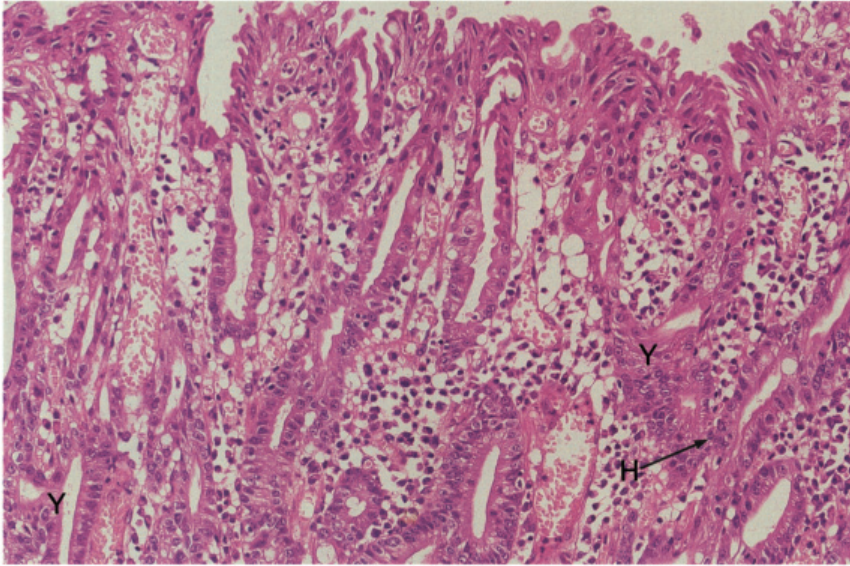


Fig. 5-3. Abnormality in the glandular pattern in a well differentiated adenocarcinoma of stomach. Several glandular tubes are arranged in the mucosa, but their structural pattern is markedly abnormal, with Y-pattern, not reversed but upright, at the places denoted by Y. Since in this case the cellular atypia is minimum, microscopic diagnosis of carcinoma solely depends on the recognition of abnormal gland pattern. Hematoxylin-eosin stain.

This structural feature of adenocarcinoma has been pointed out by some Western pathologists (Grundmann, 1975; Morson *et al.*, 1980). However, its importance in diagnosing early gastric carcinoma had been emphasized in the pioneer studies of Japanese pathologists (Ota, 1964; Nagayo, 1966) who established diagnostic basis for distinguishing carcinoma from various non-carcinomatous changes of mucosal gland. Japanese Research Society for Gastric Cancer (1974) expressed this feature as “structural atypia” (SAT) of adenocarcinoma, contrasting with “cellular atypia” (CAT), the abnormalities of individual cells. Of these, CAT has been the subject of a large number of studies with the information now accumulated and systematized in the form of exfoliative cytology. However, SAT still remains a matter of ambiguity, leaving us uninformed about how to establish a criterion for diagnosing adenocarcinoma on an architectural basis. Retardation in this aspect of study is understandable if we notice that SAT belongs to a feature that can only be definable in terms of 3-D structure of carcinoma.

Apart from its diagnostic significance, SAT poses another question: how, from a biological viewpoint, one can explain the morphogenesis of carcinoma that can assume such a variety of structures as will be shown. In view of this, 3-D structural analysis of adenocarcinoma and adenoma was undertaken, using surgical material of gastric tumors (Takahashi and Iwama, 1984a,b,c, 1985).

### Three-D structure of well differentiated adenocarcinoma (Figs. 5-4, 5-5)

Exhibited in Fig. 5-4 is a manually performed 3-D reconstruction of well differ-



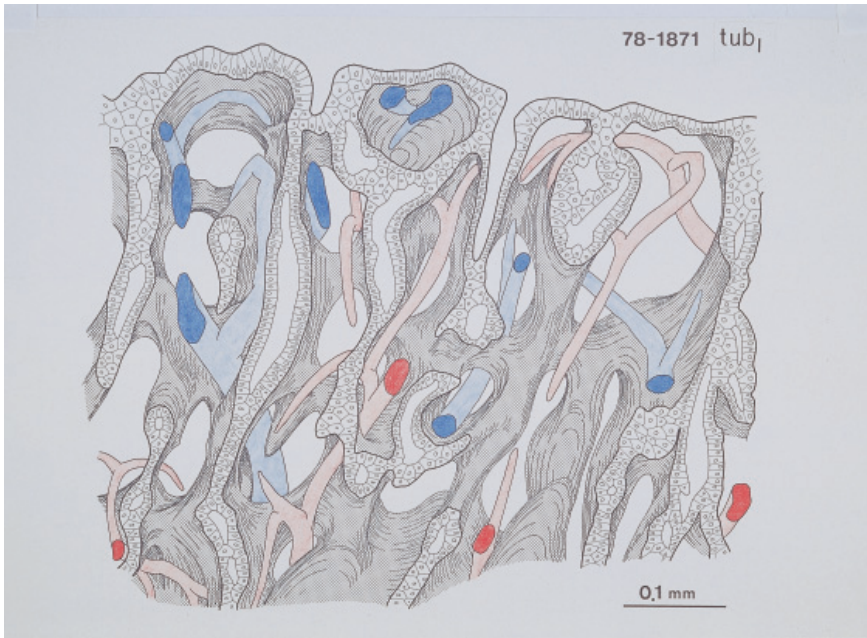


Fig. 5-4. Manually performed 3-D reconstruction of carcinomatous glands in the well differentiated adenocarcinoma shown in Fig. 5-3. This presents an exterior view of carcinomatous glands, a picture to be called a reconstruction of "nests," in order to discriminate from that of the glandular lumina. Note that the carcinomatous tubes are forming a 3-D network with loops, a structure different from the branching tree of normal gastric glands. Reproduced from Takahashi and Iwama (1984): *Virchows Arch A Path Anat Histol* 403, pp. 129.



Fig. 5-5. Manually performed 3-D reconstruction reproducing the tubular lumina (red) in the well differentiated adenocarcinoma shown in Fig. 5-4. Note that the lumina are continuous over the whole reconstructed region, nowhere leaving a separate part of lumen. Reproduced from Takahashi and Iwama (1984): *Virchows Arch A Path Anat Histol* 403, pp. 129.

entiated tubular adenocarcinoma shown in the foregoing picture (Fig. 5-3). What one can find here is a network of glandular tubes connected with the neighboring ones, instead of the trees of normal glands branching downward. Clearly this explains how in this carcinoma, glands of non-reversed Y, X or H pattern appear in a 2-D section instead of reversed Y. The network, having a number of meshes (or loops), is intertwining with small arteries (red) and veins (blue). However, the picture presents only an external appearance of the tubular tumor. Whether and to what degree the luminal tunnels are open and continuous cannot be visualized with this sort of expression.

The foregoing 3-D picture is reproduced in Fig. 5-5 to show the glandular lumina in red. This is necessary because in adenocarcinoma, usually the connectivity of lumina does not coincide with that of the cell masses, or cell nests, the latter reconstructed in Fig. 5-4. In fact, by closely comparing the two figures, one may detect discrepancy between the lumina and cell nests at several places. However in this tumor, one can say at least, the larger part of the luminal tunnels retain continuity. Since this is an early mucosal carcinoma, where the tumor is confined to the upper 2/3 of the mucosa, the proper gastric glands (fundic glands) in the lower 1/3 are left uninvolved by growth of carcinoma. They are continuous with the carcinomatous glands, and this brings about a situation where gastric juice secreted by the fundic glands is led through the carcinomatous canals to the mucosal surface.

### **Moderately differentiated adenocarcinoma: 2-D and 3-D (Figs. 5-6, 5-7, 5-8)**

The second type is the moderately differentiated (tubular) adenocarcinoma. An example is shown in Fig. 5-6, an area from a deep layer of gastric wall where carcinoma is infiltrating. Apparently, the cells look sufficiently atypical to make a pathologist instantly give a diagnosis of carcinoma. However, there are also structural abnormalities. At several places, one can find carcinoma cell masses (or cell nests) containing not a single lumen but several round lumina, a pattern widely expressed as either cribriform pattern or "back to back pattern without intervening stroma." Also, most of the glandular lumina appear rounded, suggesting that they are all spread due to accumulation of mucus that is secreted by carcinoma cells.

Often one can find carcinoma cell nest appearing in section as a gland ruptured and gaping, as in Fig. 5-7. This too may be the result of overextended carcinomatous gland and contributes to giving an impression of structural atypia.

Three-dimensionally, the moderately differentiated tumor of Fig. 5-6 is again forming a network with fine meshes (Fig. 5-8). However, there is a difference from the well differentiated tumor of Figs. 5-4 and 5-5. As painted in red, the lumina are no longer continuous, but are split into many small vesicles that are dispersed in the cell nests. Therefore 3-dimensionally, the cell nests containing separate lumina is not a tube but is a structure that may properly be expressed as porosity. Although microscopically classified as *tubular* adenocarcinoma, this may be a misnomer. Thus, strictly speaking, one cannot determine until 3-D reconstruction has been performed whether a pattern resembling a tube in a microscopic section is really a continuous tube. At the same time, reconstruction makes us understand that the cribriform pattern, which has been regarded as a typical SAT of adenocarcinoma, corresponds to nothing but a sectional picture of porous nests. Also in the intraductal tumors of the breast, Ohuchi *et al.* (1985) demonstrated by 3-D reconstruction that porous nests are the clearest mor-



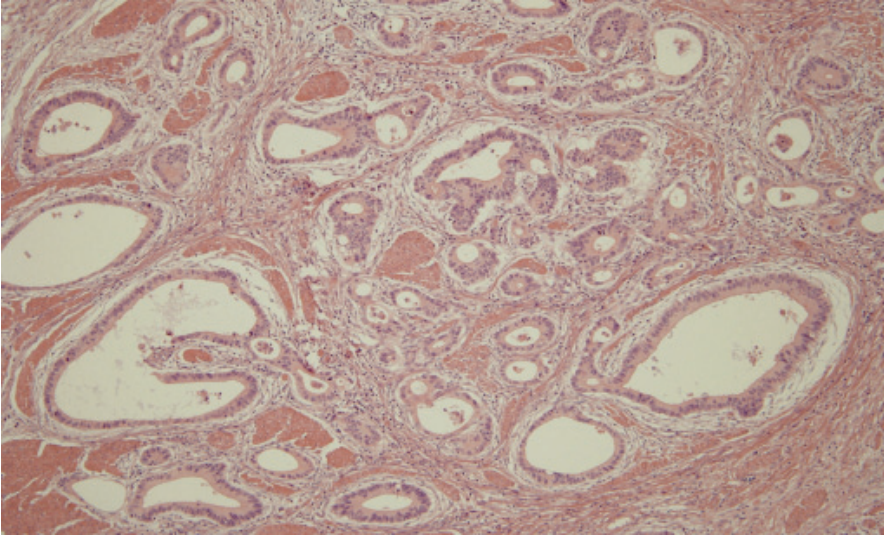


Fig. 5-6. Moderately differentiated adenocarcinoma of the stomach. From the portion of stomach where carcinoma is invading in the wall. Not only are the cells markedly atypical, but the glandular structure is also abnormal, with masses of carcinoma cells having multiple round lumina, a pattern expressed as "back-to-back without intervening stroma." Hematoxylin-eosin stain.

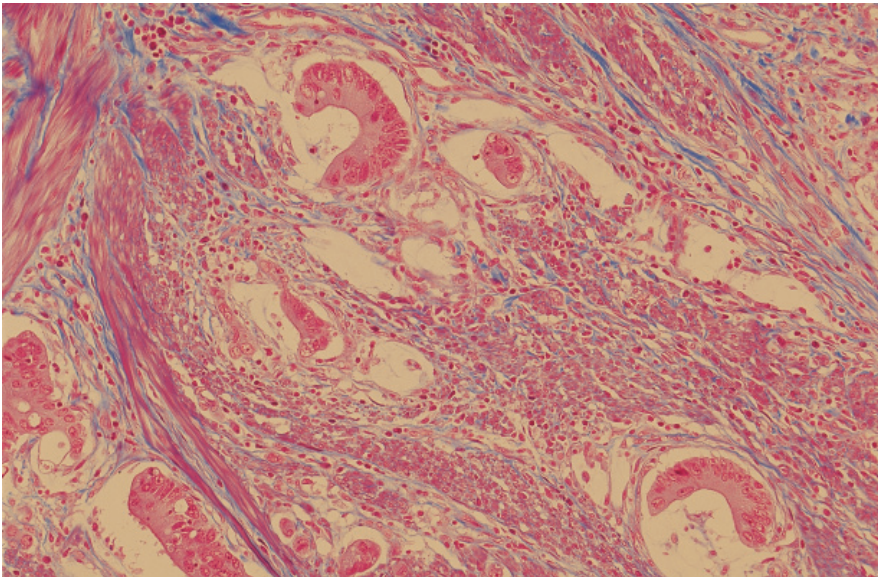


Fig. 5-7. Ruptured glands found in the moderately differentiated adenocarcinoma of Fig. 5-6. The glandular structure was broken because the lumina are separate, having no draining route for the products secreted by the carcinoma cells. Azan-Mallory stain.

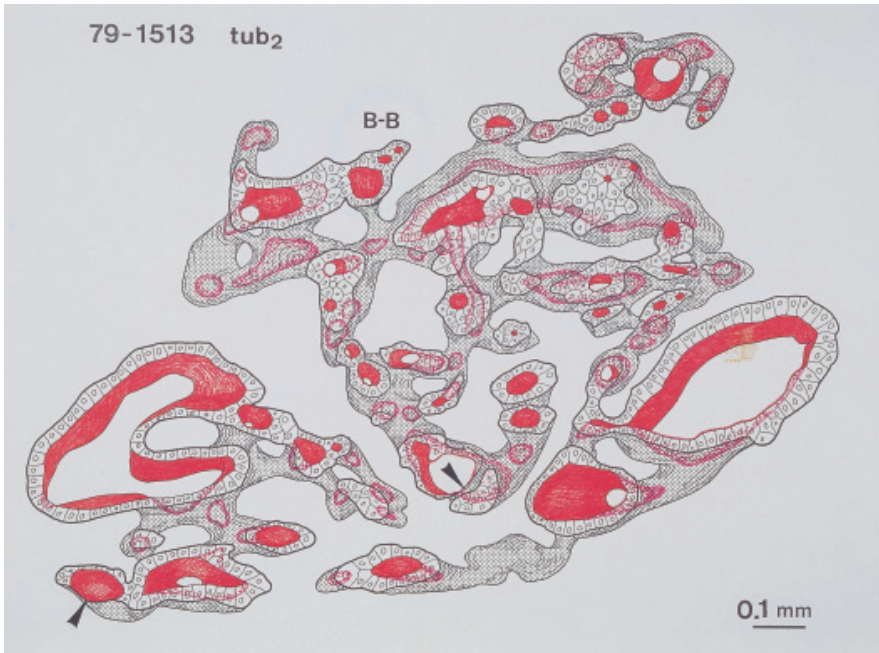


Fig. 5-8. Manually performed reconstruction of moderately differentiated adenocarcinoma of the stomach shown in Fig. 5-6. The glandular lumina are shown in red. Note that the carcinoma cell nests are forming a continuous 3-D network with loops, whereas the lumina are entirely split into solitary vesicles, a state of “porous nests” presenting on a 2-D section as “back-to-back” (B-B) pattern. Ruptured glands are also seen (arrowheads). Reproduced from Takahashi and Iwama (1984): *Virchows Arch A Path Anat Histol* 403, pp. 131.

phological sign of malignancy. Since cells of gastric adenocarcinoma secrete mucus more or less, the produced mucus comes to accumulate in the minute spaces. They are separate vesicles that continue to nowhere, creating in section the round-shaped, spread lumina that are often ruptured.

### Poorly differentiated adenocarcinoma: 2-D and 3-D (Figs. 5-9, 5-10)

The third type of the present series is the poorly differentiated adenocarcinoma. In a 2-D section, as in Fig. 5-9, this type of tumor presents as separate small clusters of carcinoma cells diffusely infiltrating in the connective tissue stroma (arrows). Glandular structure is retained in some of the clusters, but only rudimentarily.

In 2-D section, most of the cell nests seemed separated one from another. But three-dimensionally, there still remain carcinoma cells assembled in the form of continuous 3-D network with porosity (Fig. 5-10). It is shown however that from the network, clumps of a few carcinoma cells have begun separating, with some of them having a tiny, porous lumen. Thus, this type corresponds to the stage of dedifferentiation in which not only the lumina but the cell nests are losing connectivity.



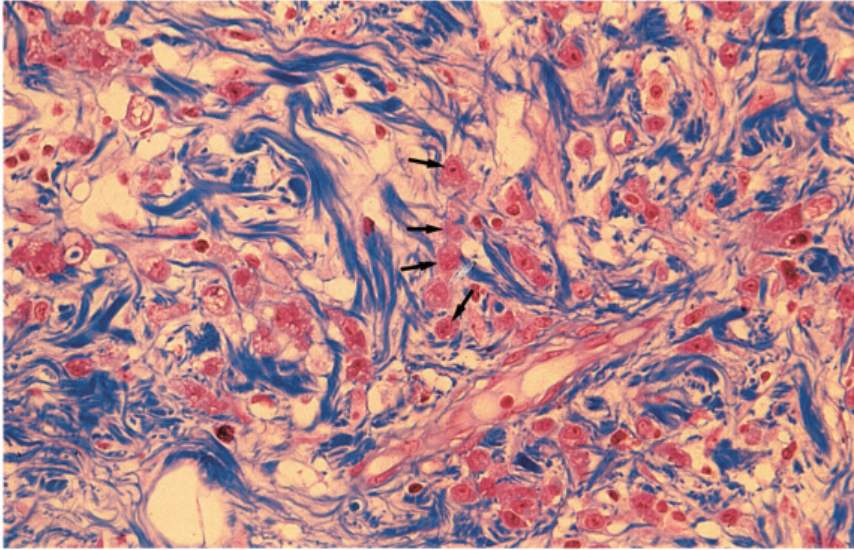


Fig. 5-9. Poorly differentiated adenocarcinoma of stomach: Carcinoma cells (arrows), solitary or forming small clumps, are dispersed in the stromal connective tissue. Tubular structure is not obvious. Azan-Mallory stain.

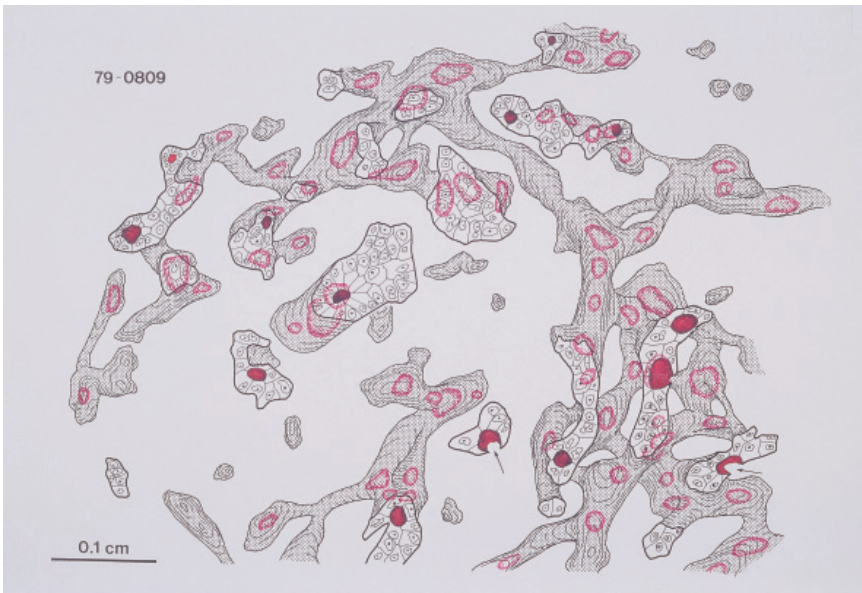


Fig. 5-10. Manual 3-D reconstruction of poorly differentiated adenocarcinoma. Although network made of porous nests remains in the right half of the figure, fragmental nests have begun leaving the network. This may be a state of disintegrating glandular structure. Reproduced from Takahashi and Iwama (1984): *Virchows Arch A Path Anat Histol* 403, pp. 132.

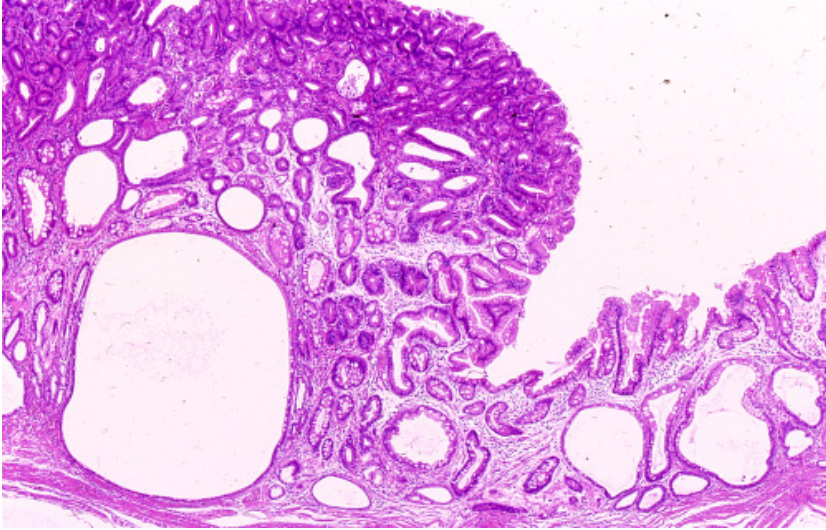
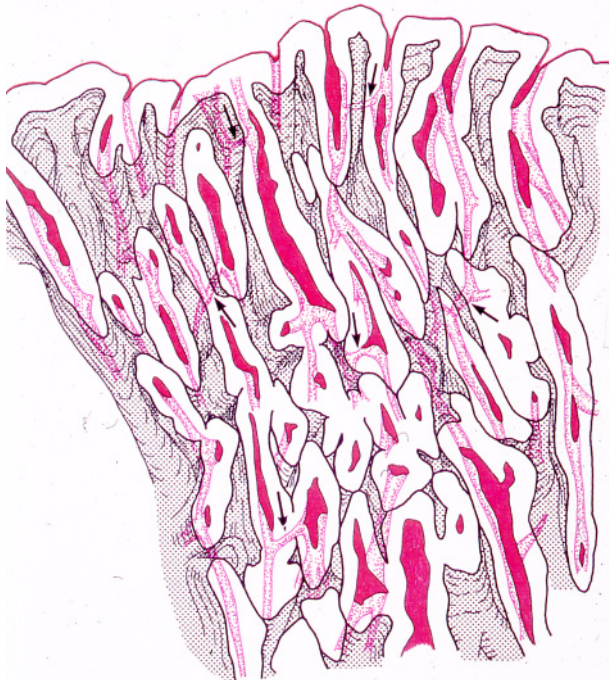


Fig. 5-11. Adenoma of the stomach, presenting a flat mucosal elevation comprising glandular tubules with moderately atypical cells, a picture reminiscent of an adenoma of the large bowel. Hematoxylin-eosin stain.



-3776 ATP

0,1 mm

Fig. 5-12. Manual 3-D reconstruction of gastric adenoma. Tubular glands, all penetrated with a continuous lumen, are packed in the elevated mucosa. At several places one can find connection, of both nests and lumina, between a pair of neighboring tubules (arrows), showing that network formation has already begun. Reproduced from Takahashi and Iwama (1984): *Virchows Arch A Path Anat Histol* 403, pp. 139.

### Gastric adenoma: 2-D and 3-D (Figs. 5-11, 5-12)

In the large intestine, adenomas are found very often. Though less common, it also arises in the stomach and sometimes carcinoma develops within adenoma. Fig. 5-11 is an example of gastric adenoma where one can find atypical glands bearing some resemblance to adenoma of large intestine. They gather in the superficial layer of mucosa, but the degree of cellular atypia is milder than overt adenocarcinoma.

Figure 5-12 presents a 3-D reconstruction of gastric adenoma. Atypical glands are closely packed in the mucosa, and though infrequently, there are places where a pair of neighboring glands are connected, as denoted by arrows. There, the lumen too is continuous as in the well differentiated adenocarcinoma. Thus, as a whole, the basic skeleton of adenoma is already a coarse 3-D network. In other words, the gastric adenoma can be expressed as a miniature of adenocarcinoma.

### Tree and network: what is connectivity? (Fig. 5-13)

As above, among the various types of adenocarcinoma and adenoma, there is a difference in the skeleton. This can be translated as difference in *connectivity*, or in other words, difference in the topological properties of structure, either among the cell nests, or among the lumina. We will have to recur several times to topological way of thinking in the problems that follow, and therefore it seems pertinent to give a small comment about the concept.

Figure 5-13 is a schema explaining the meaning of connectivity. In the left, one can see a pattern consisting of several nodes and branches. It includes a loop,

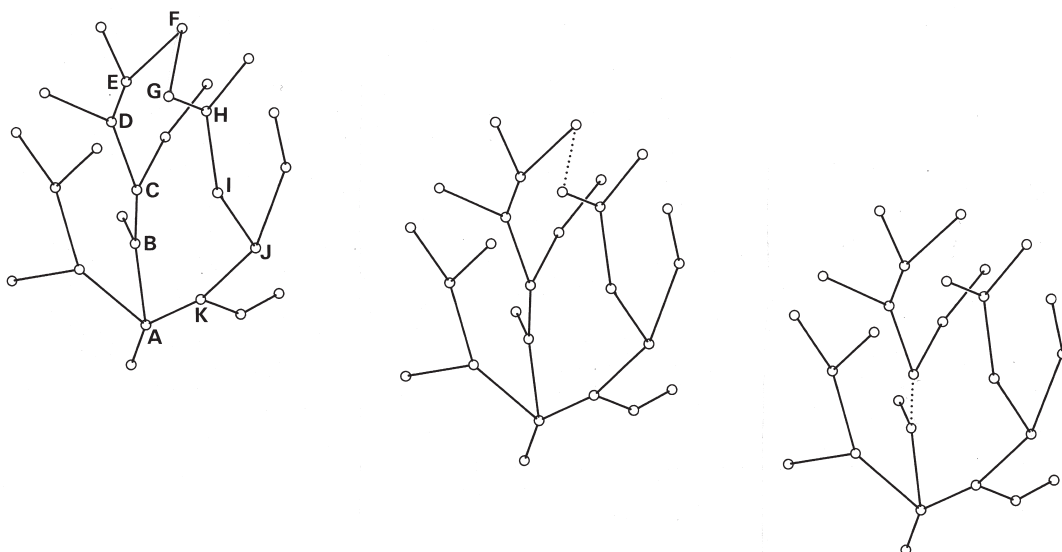


Fig. 5-13. A schema of small tree and network, explaining the meaning of connectivity. Presented in the left is a figure made of nodes and branches, all united in the form of small network with a hole (in other words, a cycle). In the figure in the center, one of the branches forming the loop has been taken away. The figure, still united as a whole but having no hole, corresponds to the state of tree. If, from this tree, any branch is taken away as in the right figure, the tree is inevitably split into two parts. This implies that the tree is definable as a pattern having no inner redundant connection.



ABCDEFGHIJKA, which can also be expressed as a hole, or a cycle. In the central figure, one of the branches forming the loop (FG) has been removed, and this causes the loop to disappear and the whole pattern is reduced to a simple tree having no hole. This means that if there is a loop, the node-branch system contains redundant connectivity, because even after one of the loop-forming branches is removed, the system still retains unity without breaking up into separate parts. If, from this tree, any branch is taken away as in the right figure (BC), then inevitably the tree is separated into two parts. This occurs because the tree is a pattern that is definable as having no inner redundant connection.

As shown, the structure of adenocarcinoma can be reduced to a skeleton that varies according to the degree of differentiation and dedifferentiation. There, the basic pattern of skeleton can be either a tree, or a united network having several loops, or a network that is partially disconnected. Then, how can we describe in quantitative terms the skeleton difference in this sense?

**Topological expression for the skeleton of carcinomatous glands (Fig. 5-14)**

For adenocarcinoma of stomach, we talk about “cell nest,” or simply “nest,” with which to express the whole cell mass wrapped in basement membrane. This is to distinguish the connecting relation of cell mass from that of luminal tunnel. For example, a normal gastric gland forms a miniature tree that is united as a whole, with regard to either the whole gland (the cell mass) or the lumen. However, in the well differentiated adenocarcinoma, both the cell masses (nests) and the lumina are forming a network with multiple holes (loops), meaning that they both are redundantly

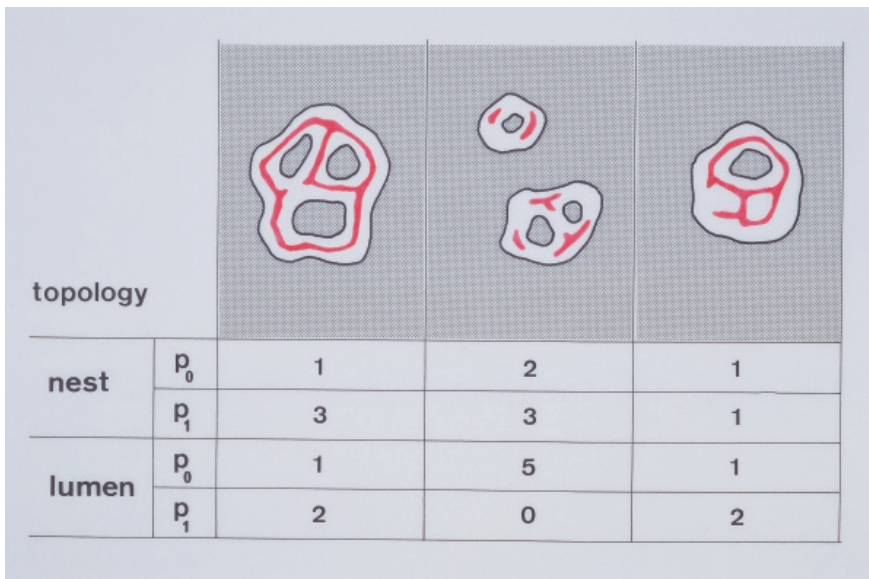


Fig. 5-14. Quantification of various structural skeleton for adenocarcinoma and adenoma with topological parameters. Illustrated using simple forms having nests and lumina (red).  $p_0$ : the number of separate parts.  $p_1$ : the number of holes.

connected. In the moderately differentiated tumor, the nests remain as a network with loops, whereas the lumina are split into many separate parts, showing loss of luminal connectivity. Thus, what we are dealing with is a difference in the connectivity of skeletons, which can pertinently be described if we use topological parameters.

Figure 5-14 illustrates the principle, taking as examples three simplified patterns. The lumina contained in the nests are shown red. In adenocarcinomas, usually the network of nests and that of lumina have different number of loops. Moreover, nests and lumina are often split into different number of separate parts. Therefore, each of them has to be quantified as an independent network. To quantify the connectivity, we introduce two parameters,  $p_1$  and  $p_0$ . Of these,  $p_1$  denotes the number of holes contained in a network.  $p_0$  is the number of separate parts of network. Here it should be taken for granted that there can be a network having no holes, since we make it a rule that even if the object is a small part consisting only of a segment of nest, this should be considered a network, so long as it remains as an independent pattern; in this case  $p_1 = 0$ , but  $p_0 = 1$ . In topology, the quantity denoted by  $p_1$  is called the genus.

Let us see the examples. In the left pattern, the nest is entirely connected and therefore  $p_0$  is 1 for the nest, while it contains three holes and therefore  $p_1$  is 3. On the other hand, the lumen (red) is united and forming two holes. Therefore for the lumen  $p_0$  is 1 and  $p_1$  is 2. In the middle pattern, the nests are separated into two parts and have three holes, and therefore  $p_0$  for the nest is 2 and  $p_1$  is 3, whereas the lumina are separated into five parts and there are no holes, and therefore  $p_0 = 5$  and  $p_1 = 0$ . In the right pattern the nest is united and has one hole, so  $p_0 = 1$  and  $p_1 = 1$ . The lumen is united and has two holes, so  $p_0 = 1$ , and  $p_1 = 2$ .

Both  $p_0$  and  $p_1$  are 3-D quantities that have to be counted directly on serial sections. This is because stereology does not work in estimating the topological parameter values (the connectivity of features: See Table 2-2). As one may see in the above discussion, if a pattern has a hole, the value of  $p_1$  is 1, no matter how the pattern is transformed. For example, from a topological viewpoint, the alphabetical letter B is equal to the Arabic numeral of 8 since  $p_1 = 2$  in both. Stereology is a methodology to estimate length, area, volume or angle, all in the scope of metric analysis. The connectivity of network as we have seen in the skeleton of adenocarcinoma belongs not to geometry but to topology. In this sort of problem, we can rely only on direct analysis of the space by scanning with serial sections.

### **Structural skeleton of carcinoma with various differentiation (Fig. 5-15)**

The above rule of quantification was applied to six gastric tumors. In Fig. 5-15, the pattern of glandular skeleton is compared among different tumor types with the topological parameter values. Values of  $p_0$  as well as  $p_1$  are expressed as the number contained in 1 mm<sup>3</sup> of tissue. The normal gastric gland is a tree with small number of ramifications. Since there is no hole,  $p_1 = 0$ . Three adenomas of the stomach were studied, in each of which small number of connections proved to exist between neighboring glands, thus showing that the network skeleton was beginning to form. Still, the number of holes remains small, with the  $p_1$  value for the lumina remaining only 24, 29 and 48 per 1mm<sup>3</sup>. In the well differentiated adenocarcinoma, the tree pattern is completely lost and replaced with a dense network. The  $p_1$  value for lumina is as large as 384/mm<sup>3</sup>. Here, the lumina are all connected with no separated cavity as shown by

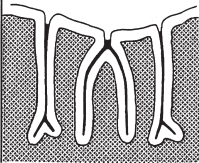

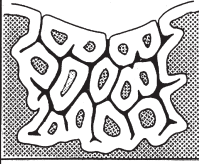
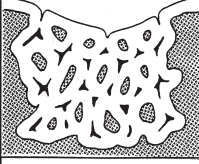

		$p_0$ (separate parts / mm <sup>3</sup> )		$p_1$ (loops / mm <sup>3</sup> )	
		Nests	Lumen	Nests	Lumen
	Normal	-	-	0	0
	Adenoma				
	Case 1	1	1	103	24
	Case 2	1	1	129	29
	Case 3	1	1	192	48
	Adeno-carcinoma Well diff	1	1	1640	384
	Adeno-carcinoma Mod diff	1	439	287	0
	Adeno-carcinoma Poorly diff	871	1133	653	0

Fig. 5-15. The skeleton difference among variously differentiated tumors of the stomach. All the parameter values were counted on serial sections. From the uppermost row downward: normal gastric gland, gastric adenoma, well, moderately and poorly differentiated adenocarcinomas.  $p_0$ : the number of separate parts in mm<sup>3</sup>.  $p_1$ : the number of holes in mm<sup>3</sup>. How the structure changes from fully differentiated normal glands to poorly differentiated tumor is described by the combination of  $p_0$  and  $p_1$ . From the top downward: tree pattern, formation of coarse network, fine network with continuous lumina, fine network with porosity, and network beginning to disintegrate. Reproduced from Takahashi and Iwama (1985): Science on Form I, pp. 548.

the  $p_0$  value of 1. In this combination of parameter values, one can see that although the tree pattern of ordinary gland is lost, the tumor still retains its glandular character. In the moderately differentiated tumor, the luminal connectivity is entirely lost as shown by the  $p_0$  value of 439, and this expresses that the tumor is now entirely porous. But the nests themselves, with a  $p_0$  value of 1, are still entirely united and remain forming a dense network, with a  $p_1$  value of 287. In the poorly differentiated tumor, not only the lumina but also the cell nests have begun separating into parts, as reflected by the

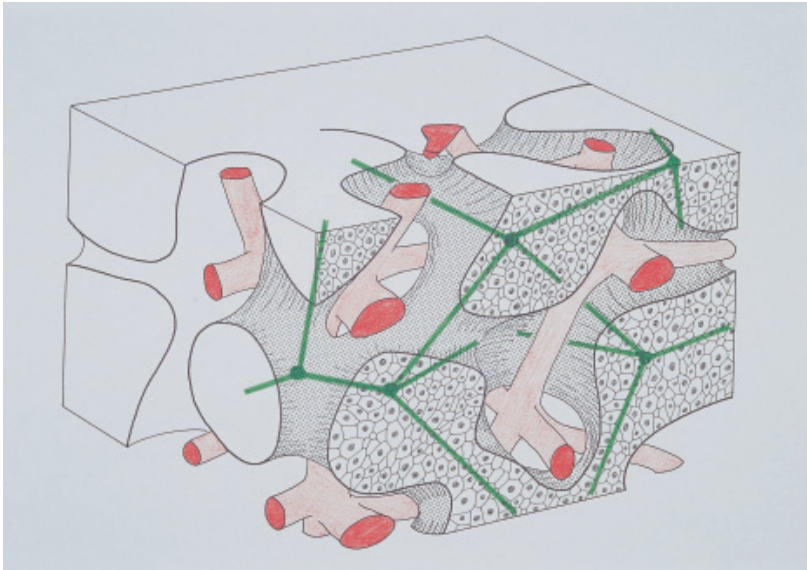


Fig. 5-16. A schema showing why gastric carcinoma has a network skeleton (green). The mass of carcinoma cells is intertwined in the space with capillaries (red) which form another network. Reproduced from Takahashi and Iwama (1984): *Tohoku J Exp Med* 143, pp. 463.

$p_0$  value that is as large as 871 per  $1 \text{ mm}^3$  tissue.

Thus, we find a transition of glandular skeleton from the normal to adenoma to well, moderately and to poorly differentiated adenocarcinoma. In the first step of changes, the tree pattern is lost and replaced with a network, still retaining the whole connectivity. Then the lumina lose unity, suggesting that the cells have begun stopping to form a canal and forming instead a simple trabecular mass containing vesicles filled with mucus. Finally, the cell nests begin to lose unity, and this means that the whole structure has started to disintegrate. Here one can see a chain of events where, the lower the differentiation of cells, the further does the glandular structure deviate from the normal tree.

In pathology, the usage of the term “differentiation” is usually confined to that of cells. However, based on what has been found, it seems that we can also define differentiation and dedifferentiation for the structure of cell assembly; in the case of stomach, the most differentiated structure is the tree of normal gastric gland. As dedifferentiation advances, the skeleton goes further and further away from the tree. Besides, visualization of the 3-D structure of carcinoma has been a lesson showing us what features in a microscopic 2-D picture should be counted as important signs of structural atypia (SAT) in making diagnosis. About this, however, the details are to be referred to the original papers (Takahashi and Iwama, 1984c, 1985).

### How does the network skeleton form? (Fig. 5-16)

Why do carcinomas form a network? We think that this may be explainable from the relation of carcinoma cell nests with the stromal tissue, as schematized in Fig 5-16.

In the stroma, capillaries form another network. Carcinoma cells will grow so as to fill the space as a continuous mass, but there is a limitation to this. As carcinoma continues spreading, at least it has to spare capillaries on which it depends for blood supply. Otherwise, the subsistence of carcinoma itself will be endangered. Since capillaries form a network in the space, carcinoma that has to co-exist with them must automatically be molded into another network which is topologically “conjugate” with capillaries.

In addition, it is to be pointed out that the capillaries, forming a 3-D network in various organs, are another object of topological research. An example will be found in the studies of Shimizu *et al.* (1993, 1996), who analyzed 3-dimensionally the topological difference in the structure of hepatic sinusoids in normal and cirrhotic livers and in hepatocellular carcinoma, relating the results with possible hemodynamical changes.

### The origin of various tumor skeleton (Fig. 5-17)

Finally, we propose a model of morphogenesis for different types of adenocarcinoma as in Fig. 5-17. The cells of adenocarcinoma express various degrees of differentiation into secretory cells. A normal glandular cell sits on a sheet of basement membrane and secretes its product upward from its top, or apex. Thus a secreting cell, when normally differentiated, is polarized into the basal and apical poles, and morphologically, the polarization is the very expression of differentiation for glandular cells. When a tumor arises, it comprises cells in which, in this sense, differentiation is more or less reduced. There can emerge cells half polarized or non-polarized, and these

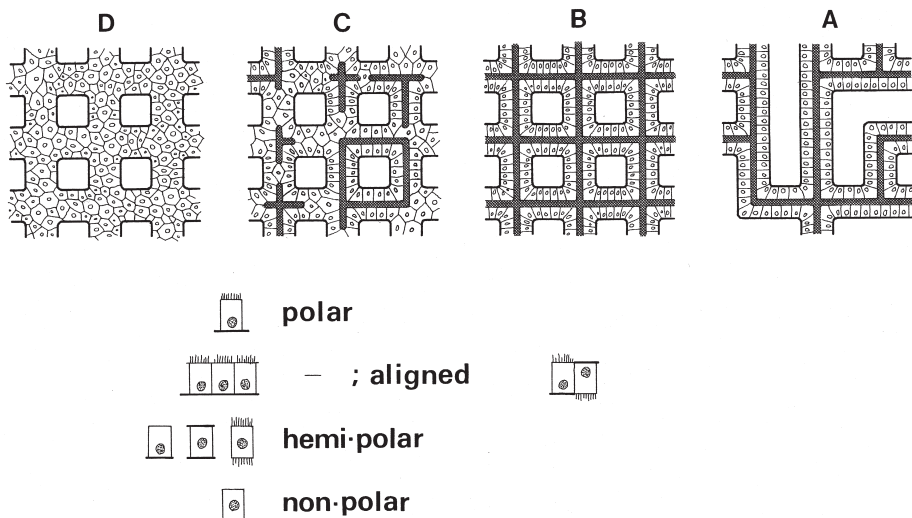


Fig. 5-17. The development of various skeleton in variously differentiated gastric tumors is schematized. A well differentiated tumor (B) has a network skeleton where the lumen is continuous throughout because the tumor comprises well differentiated cells that are sufficiently polarized into apical and basal direction. As less differentiated or undifferentiated cells come to join and have a larger share of cellular population (C), the lumina lose continuity, creating porous nests. Reproduced from Takahashi and Iwama (1984): *Tohoku J Exp Med* 143, pp. 464.



come to participate in forming the nests, taking various share of cell population. Assume, for example, that a certain percentage of non-polarized cells are mixed in the nests, as in Fig. 5-17-C. Then it would be conceivable that the non-polarized cells come to block the lumina here and there, resulting in the formation of porosity. When the nests consist exclusively of non-polarized cells as in Fig. 5-17-D, luminal canal no longer forms, and this is a state equivalent to the undifferentiated carcinoma. In this way, we can correlate various stages of structural differentiation with the differentiation of the individual cells that constitute the nests.

## Morphogenesis of Cirrhosis from Chronic Hepatitis

There are other examples of morphogenesis into which we can gain insight at least partially by taking a topological viewpoint. To be introduced in this chapter is the developmental process of cirrhotic livers from pre-cirrhotic lesions like chronic hepatitis. Here too, the liver lesion has a clear skeleton that spreads in the 3-D space, and morphogenesis of cirrhosis involves a progressive reformation of skeleton. Let us begin with visualizing what the skeleton of these diseases looks like.

Cirrhosis is the terminal state common to various chronic diseases of the liver. To put it more strictly, while pre-cirrhotic diseases like chronic hepatitis keep advancing toward cirrhosis, we also find in cirrhosis itself a disease continuously advancing to its terminal stage. This may be understood by the fact that there are a number of patients who have cirrhosis and yet are leading a life that is not very much disabled. Why can the condition of such patients deteriorate with time, and why, some day, do fatal events happen, like hepatic insufficiency? All these cannot be understood without assuming that in the entire course from chronic hepatitis to the terminal stage of cirrhosis, we have a slowly but incessantly advancing disease. Then, how do the liver lesions develop and progress? This is what we are going to examine in this chapter.

### **The cirrhotic liver: microscopic appearance (Figs. 6-1, 6-2)**

Shown as an example in Fig. 6-1 is a microscopic appearance of cirrhosis. It contains spherical structures that are called nodules. Their dimension is various, ranging in some cases up to 1 cm in maximum diameter. Stretching between neighboring nodules are narrow belts stained green. They are called the interstitium and consist of fibrous tissue, which may be regarded as a scar that is left after the hepatocytes were destroyed due to, for example, viral hepatitis. The nodules are spherical because in their inside the hepatocytes continue regenerating, and in this sense, nodules are also called the regenerative nodules.

Cirrhosis can also develop from livers with chronic alcoholic injury. Figure 6-2 presents an example and here the intranodular hepatocytes are shown containing vacuoles; these are fat droplets accumulating in the hepatocytes due to impaired metabolism. The basic pattern of hepatic lesion is similar as in the foregoing case. Why can cirrhosis, while developing from diverse pre-cirrhotic diseases, present quite a similar pattern? Despite many assumptions proposed so far (Popper and Elias, 1955; Thaler, 1952), problems still remain about the morphogenesis of cirrhosis, awaiting further studies. To be introduced in the following are some of our studies and attempts (Takahashi, 1978a,b; Takahashi and Suwa, 1978; Endoh and Takahashi, 1997; Takahashi and Endoh 2000).

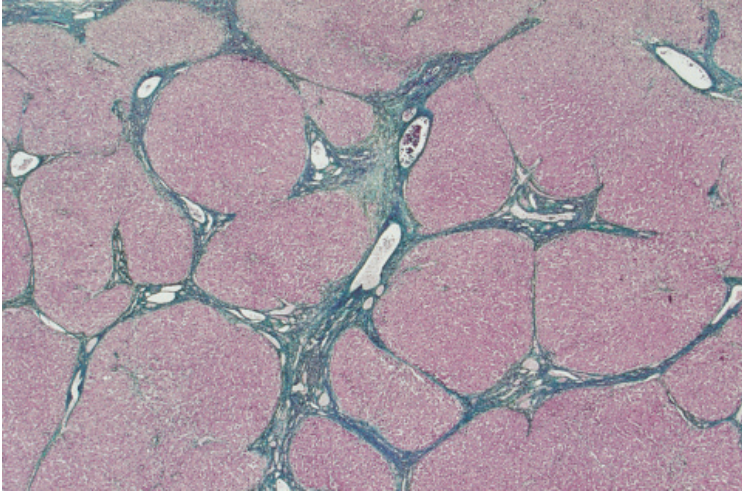


Fig. 6-1. Microscopic appearance of liver cirrhosis presumably resulting from chronic hepatitis. The round masses stained brown are called nodules consisting of hepatocytes that survived injury and are regenerating. The green belts are the interstitium, the scar zones left after hepatocytes were destroyed in the active phase of viral hepatitis. Elastica-Goldner stain.

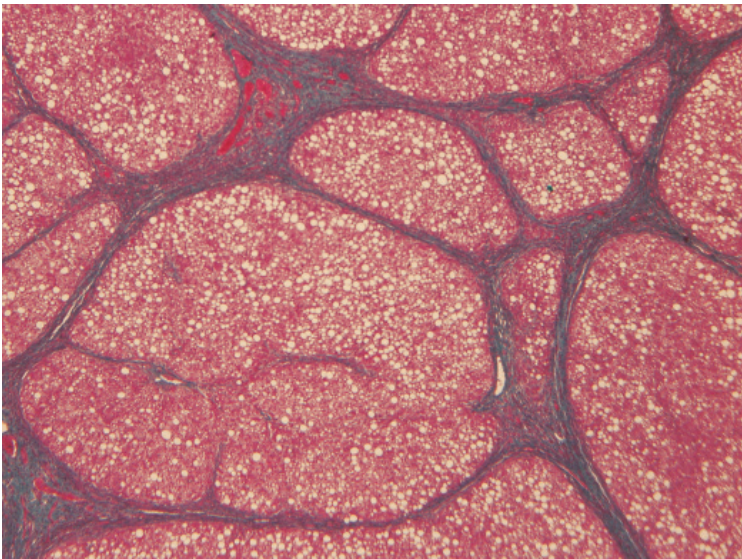


Fig. 6-2. Another cirrhosis, from a patient of chronic liver injury due to alcohol abuse. The microscopic pattern of lesion is basically the same as in the case of Fig. 6-1, except that the hepatocytes in the nodules contain droplets of lipid. Elastica-Goldner stain.

**Three-D structure of cirrhotic liver: the skeleton (Figs. 6-3, 6-4, 6-5, 6-6)**

Figure 6-3 is a 3-D reconstruction of the cirrhosis shown in Fig. 6-1. Expressed in green wireframes in this figure are the interphasic borders between nodules and interstitium. Both the portal (red) and hepatic veins (blue) are found mostly running within the interstitium, hardly entering the nodules. Indicated by PC are the places of P-C bridging where terminal portal veins communicate with terminal hepatic (or central) veins. All these are quite the same as exhibited in Fig. 3-30 (Chapter 3). As explained there, this vasculature implies that a significant part of portal blood flowing into the liver is shunted away via PC anastomoses without entering the nodules and therefore without being detoxified by hepatocytes. This explains the mechanism of hepatic insufficiency to which cirrhotic livers are particularly susceptible.

However, there is another aspect in the 3-D structure of cirrhosis. Figure 6-4 presents another cirrhosis and in this case it is the interstitium that is reproduced, while the nodules were left as void spaces. Here one may notice that the nodules are not perfectly wrapped by interstitium. There are defects at many places of interstitial septa, through which the regenerating parenchyma continues from a nodule to the neighboring ones. The skeleton of structure may clearly be visualized by registering nodules with consecutive numbers, and expressing the internodular connectivity in the form of linear diagram. Thus, as shown, one can confirm that all the nodules are connected with the adjacent ones, forming a fine 3-D network with many loops (holes). Solitary nodules having no connection with others are few, if any. This skeleton proved to be common to several cirrhotic livers studied, which were seemingly of various microscopic patterns. How can we explain the development of this network skeleton?

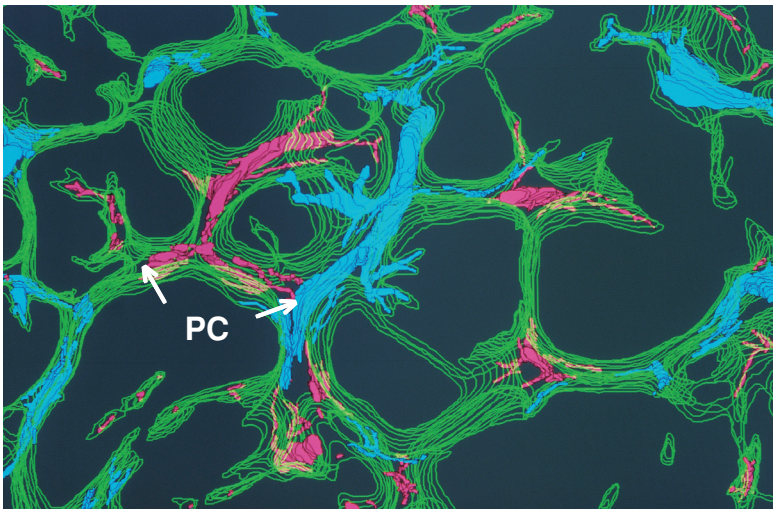


Fig. 6-3. Computer-assisted 3-D reconstruction of cirrhosis shown in Fig. 6-1 to visualize the relation of nodules (green wireframes) with portal (red) and hepatic venules (blue). At several places, anastomoses between portal venules and hepatic (central) venules are found in the form of P-C bridgings.



Fig. 6-4. Manually performed 3-D reconstruction of interstitial septa in a cirrhotic liver, visualizing the skeleton of cirrhosis. Regenerative nodules are not independent, but are continuing with the neighboring ones through the holes opening at many places in the septa. Thus nodules are united one with another into a vast 3-D network, as shown by a node-branch system where the individual nodules are identified with consecutive numbers and internodular connections with lines. Reproduced from Takahashi (1978): *Virchows Arch A Path Anat Hist* 377, pp. 190.

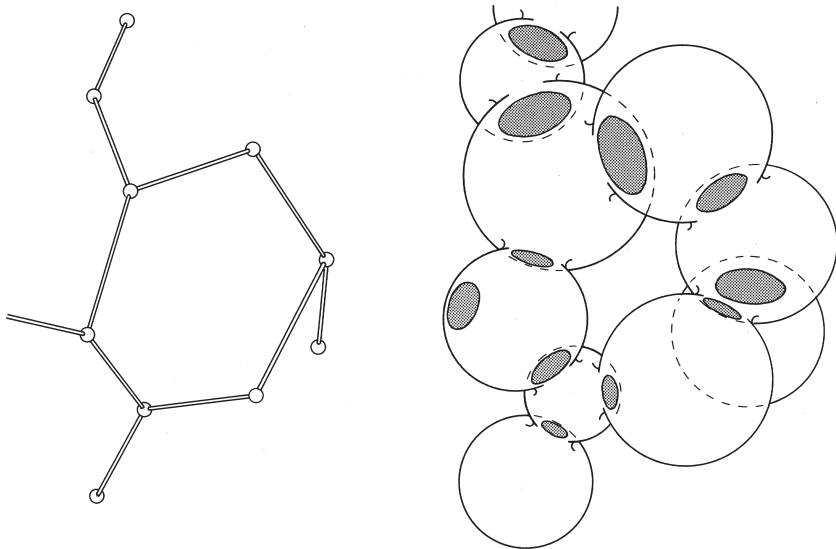


Fig. 6-5. A schema of nodular network. Nodules are adhered into a chain that forms a 3-D network with loops (holes).



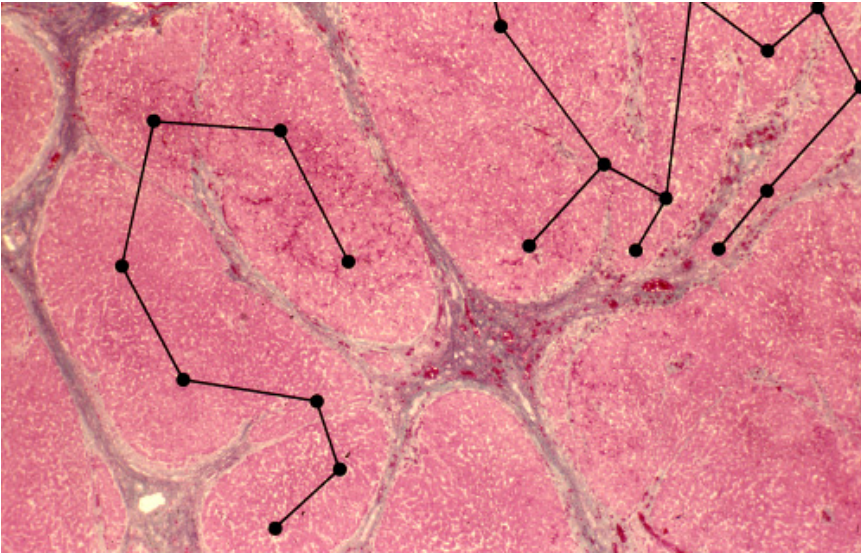


Fig. 6-6. Microphotograph of cirrhosis with a pattern produced by sectioning a nodular network. Note the complex indentation of mutually adhered nodules, as shown by the nodes and branches. Elastica-Goldner stain. Reproduced from Takahashi (1978): *Virchows Arch A Path Anat Hist* 377, pp. 98.

It seems to be improbable that in the creation of this skeleton, the intranodular parenchyma had a leading role. Instead, it is quite likely to be the interstitium that laid the basic mold. The parenchymal tissue forms a network, but it does so only passively, being cast by the interstitium that has already spread a frame in the space.

The nodular network as the skeleton of cirrhotic liver is schematized in Fig. 6-5. Nodules are connected into chains, and the chains are forming a network having many loops. The network character of internodular connection is often visible even in a 2-D microscopic picture. In Fig. 6-6 which is from a cirrhosis, complicated flexions of nodular chains are produced by deeply indented connective tissue septa. Obviously this corresponds to a 2-D section of nodular chains.

### **Skeleton formation in precirrhosis (Figs. 6-7, 6-8)**

The network skeleton shown here is not only common to various cirrhosis. It is found in various precirrhotic diseases and in various stages of development during which they smolder, recur, progress and finally end up in cirrhosis (Takahashi, 1978a). Therefore the basic requirement for a liver with chronic disease to advance to cirrhosis seems likely that somehow, it comes to harbor this network skeleton. Thus, the most essential question in the morphogenesis of cirrhosis is how, in precirrhotic diseases, interstitium emerges so as to form itself into a 3-D network.

Figure 6-7 is microscopic appearance of the liver from a patient dying of fulminant hepatitis on the 28th day. One can find broad areas of necrosis extending in a belt-like fashion, with the branches of hepatic vein dispersed along the axis of necrotic

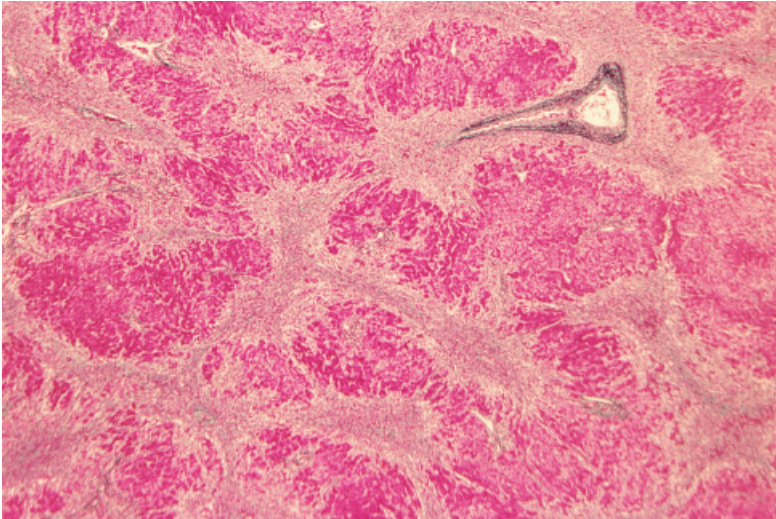


Fig. 6-7. Microscopic appearance of fulminant hepatitis, a potentially cirrhotic lesion. From a patient who died of hepatic insufficiency about one month after the onset of disease. The masses stained reddish are the zone of hepatocytes surviving injury and vigorously regenerating. The belts extending between the regenerating masses are the necrotic areas. Elastica-Goldner stain.

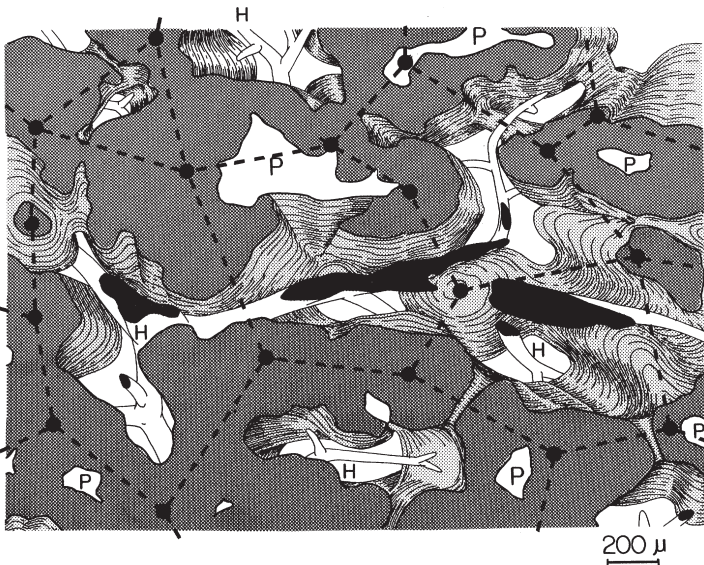


Fig. 6-8. Manual 3-D reconstruction of the liver with fulminant hepatitis shown in Fig. 6-7. The regenerating parenchymal zones form a network as shown by the node-branch diagram. One can see that the necrosis involved the parenchymal zone around the hepatic veins (H). P: portal tract. Reproduced from Takahashi (1978): *Virchows Arch A Path Anat Hist* 377, pp. 105.

belts, suggesting that this is a sort of “zonal necrosis” mainly involving the central zone of lobules (see the next chapter).

Figure 6-8 is a 3-D reconstruction of the liver with fulminant hepatitis shown in the foregoing figure. Here the zones of massive hepatocellular necrosis are shown as void spaces, leaving only the parenchymal zones consisting of hepatocytes that survived necrosis and are regenerating. P indicates the portal tracts and H, the hepatic veins. The result confirms that the necrosis took place in the parenchymal zone around the hepatic (central) veins. A linear diagram is entered in the figure so as to illustrate the connecting relation of the viable parenchymal zones, and it may be clear that here, a parenchymal network has already been created. Here we understand that it is the zonal necrosis that occurred first, and it is the 3-D pattern of necrotic zones that cast the parenchyma into a network. It seems likely that if this patient survived the acute stage, the liver would have started a process toward cirrhotic changes.

### The basic structural framework: cirrhosis and precirrhosis (Fig. 6-9)

From the above, the 3-D structure of cirrhosis may be schematized as in Fig. 6-9. The nodules are connected in the space in the form of network with loops (holes). This network of nodules is intertwined with another one, the interstitial network, which also has loops and is geometrically “conjugate” with the nodular network. The portal

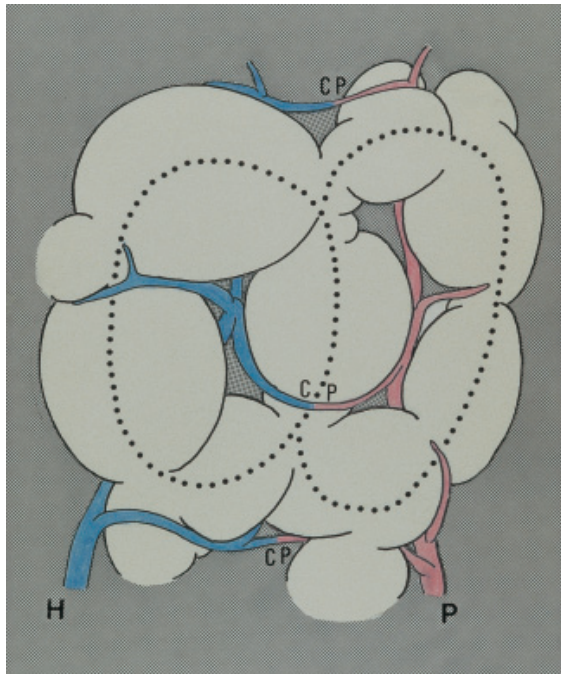


Fig. 6-9. A schema illustrating the basic 3-D structure of cirrhotic liver. The interstitium, the scar zone containing portal and hepatic veins, constitutes the skeleton which presents as a 3-D network. In this network, portal and hepatic venules anastomose at many places in the form of P-C bridgings. Also the nodules are continuous and form another network that is molded by, and intertwined with, the interstitial network.



(P) and hepatic (central: C) veins are running in the interstitium and as the result, they form a vascular network with PC bridgings. This is the basic structural plan of cirrhotic liver, and the problem of cirrhogenesis may be summarized in how, the skeleton of interstitial network develops so that at least partially, formation of its loops may result in PC bridging. Let us consider about this, taking as an example livers with chronic viral hepatitis.

### **Chronic hepatitis: focal necrosis and its 3-D distribution (Figs. 6-10, 6-11)**

Figure 6-10 is a microscopic picture of liver with chronic hepatitis B. There are focal interstitial areas that are stained green (arrows) and dispersed in the section. One can find in such foci various stages of inflammatory changes. Some present as collapsed areas relatively fresh from hepatocellular necrosis, while others are old scarrings leaving little inflammatory signs. Thus the interstitial areas represent foci of hepatocellular necrosis combined with variously advanced fibrotic changes. Often the areas assume star-like shape due to compression by the nearby parenchymal tissue where

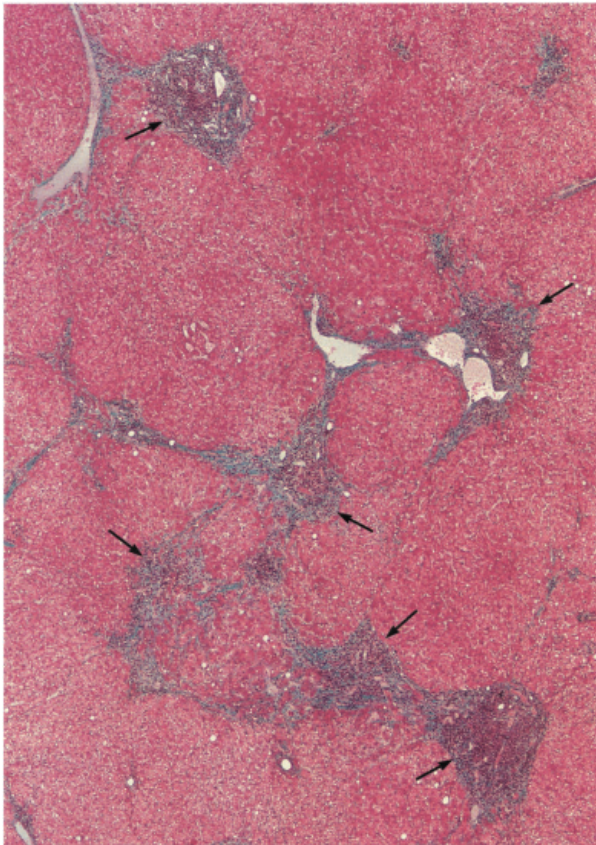


Fig. 6-10. Microphotograph of chronic hepatitis B with the lobular structure moderately reorganized. There are focal necroses dispersed in the hepatic parenchyma (arrows). Elastica-Goldner stain.

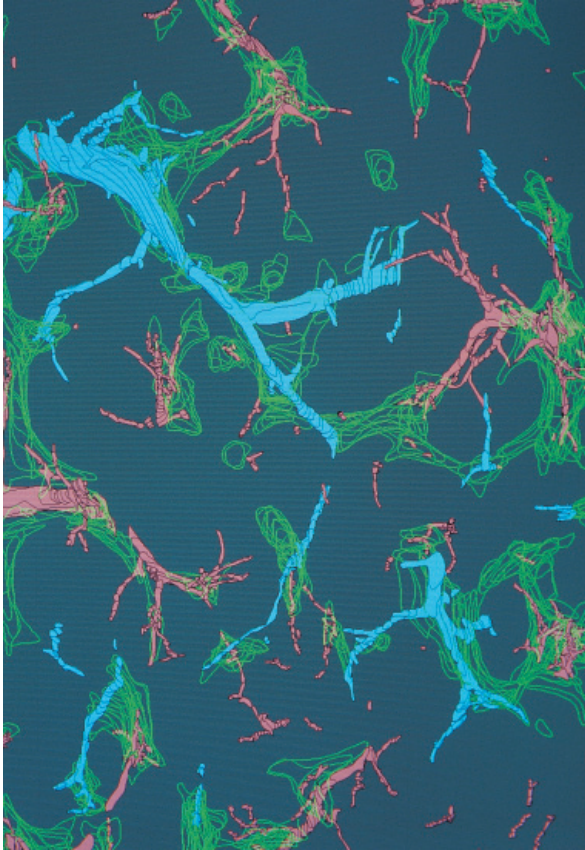


Fig. 6-11. Computer-assisted 3-D reconstruction of chronic hepatitis shown in Fig. 6-10. The green wireframes denote the profiles of focal necroses. Note that the necrotic foci, including both fresh and fibrotic lesions, are distributed randomly: some around the hepatic veins (blue) and some bridging the portal (red) and hepatic veins, although in general, there seems to be some predilection for the periportal zone.

regeneration of hepatocytes has already started. Yet, regeneration has not advanced so far as to transform the entire parenchymal zones into nodules, and the liver has yet to reach the state of cirrhosis.

The liver of Fig. 6-10 with chronic hepatitis is reconstructed in Fig. 6-11. The green wireframes denote the surface contours of the interstitial (or necrotic) areas, shown red are portal veins and blue are hepatic veins. A number of necrotic areas are found dispersed in the parenchyma. Their dimension is various but most are showing sublobular extension occupying a space ranging in volume from a quarter to 1/20 of lobule, though not accessible to precise evaluation because many of them look more or less flattened, which means that parenchymal regeneration in the surroundings has advanced to some degree, compressing the foci of necrosis. The distribution of these foci appears random, with some of them positioned close to the portal vein, with some of the others around the hepatic vein and also with some situated at a place distant from both portal and hepatic veins. As a whole, however, there seems to be a slight



tendency for the focal necroses to occur in periportal zone of lobule. It seems possible that the sort of necrosis described here may correspond at least partially to some types of necrosis which Baggenstoss *et al.* (1972) reported to occur in what they called “chronic active liver diseases.” However, at least from a 3-D distribution point of view, the necrosis is essentially focal and distributed randomly, and from this viewpoint, they do not appear fitting the term “subacute necrosis with bridging” or “subacute hepatitis with multilobular necrosis,” wordings proposed by them. We performed 3-D reconstruction of six livers with chronic hepatitis, using surgical biopsy or autopsy specimens, and obtained results that were essentially the same. Two of the cases were Type B, one was Type C, and the remaining three had been diagnosed as non-A non-B in the 1980s.

It may be confirmed in the figure that at several places, foci are so formed as to involve a portal vein and at the same time a neighboring hepatic vein. As necrotic areas are collapsed and scarring advances, such foci will change into an interstitium harboring a PC bridging. However, it has to be reiterated that the necrosis is essentially focal and randomly distributed. PC bridgings do occur, but their position and distribution suggest that bridging is not inherent in this lesion, arising only as the result of stochastic hitting process. None of the necrotic areas is extensive enough to involve multiple hepatic lobules.

#### The development of P-C bridging (Figs. 6-12, 6-13, 6-14)

The liver from another patient with chronic hepatitis is shown in Fig. 6-12, a non-A non-B case. Some of the portal tracts appear widened with fibrosis extending into

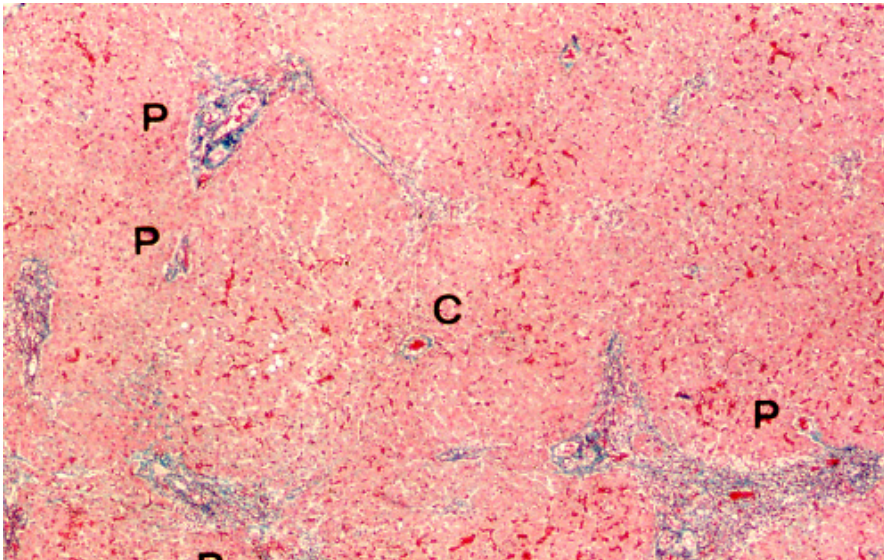


Fig. 6-12. Another case of chronic hepatitis (non-A non-B; the material was obtained in 1980s). Portal (P) and central (C) veins are discernible, and as yet the original lobular structure seems to be retained, a picture that would possibly have been classified as chronic persistent hepatitis in the previous classification. Elastica-Goldner stain.

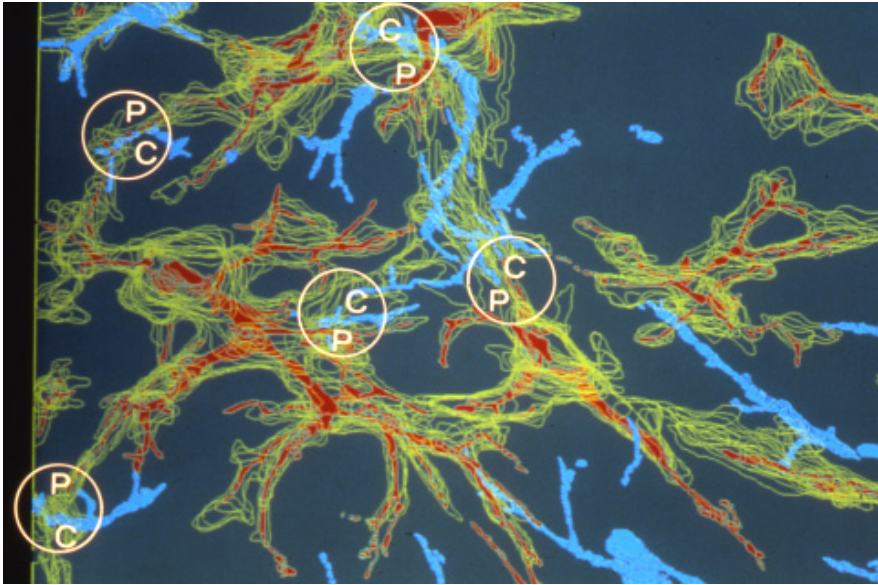


Fig. 6-13. Computer-aided 3-D reconstruction of the liver of Fig. 6-12. The yellow wireframes denote the profiles of fibrotic areas. Despite the impression of not so much advanced disease on the 2-D microscopic picture, there are already fibrosis with P-C bridging at several places.

the surroundings, but seemingly, the lobular structure looks well sustained with portal tract (P) and central veins (C) positioned at a distance. The picture may correspond to what previously was classified as chronic persistent hepatitis (CPH), a type of chronic hepatitis considered to take a comparatively benign course (DeGroot *et al.*, 1968).

Figure 6-13 is a 3-D reconstruction of the liver shown above (Fig. 6-12) and betrays the impression given by the microscopic picture. While in the 2-D section the lobular structure seemed likely to be retained, in this 3-D picture one can find fibrosis, as denoted by yellow wireframes, extending mostly around the portal veins but sometimes involving the hepatic veins. As the result, P-C bridging is demonstrated at several places, suggesting that already, lobular disorganization has started and advanced to a certain degree. Why such a discrepancy can occur between the 2-D and 3-D findings will be understood in the next figure.

Figure 6-14 is a microscopic picture taken from one of the serial sections of the above liver (Figs. 6-12 and 6-13). It demonstrates a picture corresponding to an area of fibrosis possibly resulting from organized focal necrosis, where on 3-D reconstruction, a PC bridging was demonstrated to exist. One can see a portal tract having a small portal vein (P), and this portal tract appears widened due to what has been regarded as inflammatory reaction and fibrosis. Conventionally, this sort of picture has been interpreted as a small fibrosis resulting from piecemeal necrosis which advanced so as to injure the periportal hepatocytes in a piecemeal fashion. However, the fibrosis that seems to be only a minute “periportal fibrosis” has, in reality, a far more massive extension. It contains a small vessel, denoted by C, which is a central (hepatic) vein. Therefore, the seemingly “periportal” fibrosis has to be considered a sectional picture

of focal necrosis occupying an area extending over a half of hepatic lobule from the portal tract to beyond the central vein. Its extension is apt to be underestimated because of shrinkage after postnecrotic collapse. That the small vessel is certainly a central vein has been confirmed while visualizing the 3-D vasculature by reconstruction. It should be stressed that without performing 3-D analysis, differentiation is impossible between small portal and hepatic veins in such fibrotic areas.

This sort of fibrosis is found very often in biopsies of patients having chronic hepatitis. After making reconstruction analysis on several cases of chronic hepatitis, we are convinced that in fact, such “periportal” fibrosis are sequelae of focal necrosis that is collapsed, shrunk, and presenting on section as a tiny mass of collagen.

### **Skeleton formation and transformation (Figs. 6-15, 6-16, 6-17)**

As focal necroses occur in increasing number, more and more they come into contact with the neighboring ones, while at the same time they are collapsed into fibrous interstitial zones. Thus, with time, the skeleton of interstitium is constructed in the form of 3-D network. As explained, the parenchymal tissue that was exempted from necrosis comes to be molded into another network that is intertwined with the interstitial network.

Now, based on this, let us consider how we can explain the morphogenesis of cirrhosis and its progression. While having a skeleton common to cirrhosis, the structural pattern of chronic hepatitis is different from cirrhosis. Before the liver reaches the state of cirrhosis, some secondary changes have to be added, modifying the picture. The first such changes may be nodular regeneration that the parenchymal zones

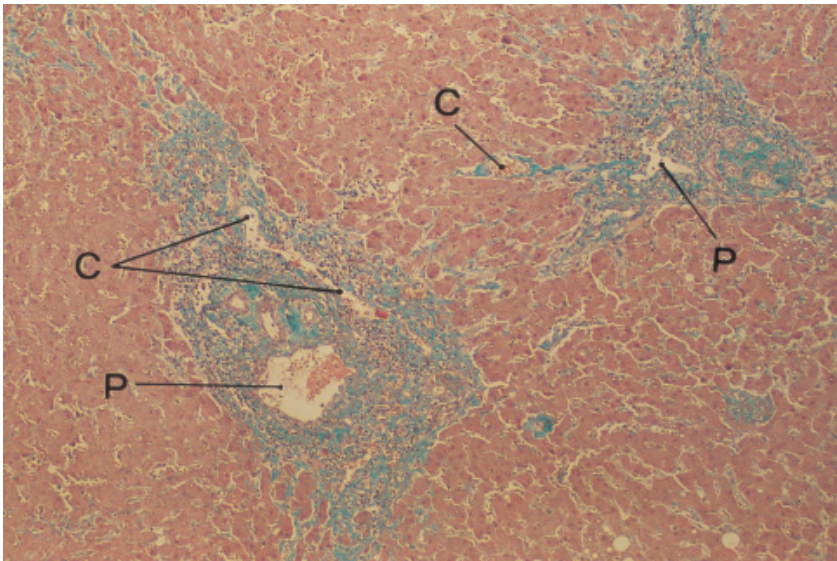


Fig. 6-14. A focal necrosis leaving PC bridging, in the liver shown in Figs. 6-12 and 6-13. There is fibrosis that may seem, at first glance, mild fibrous extension of portal tract (P: portal vein). However, this fibrosis is considered to be the product of focal necrosis that must have been far more massive than expected from this picture, because it contains a central vein (C). That this is indeed a central vein has been confirmed since the picture is a part of serial sections reconstructed in Fig. 6-13.



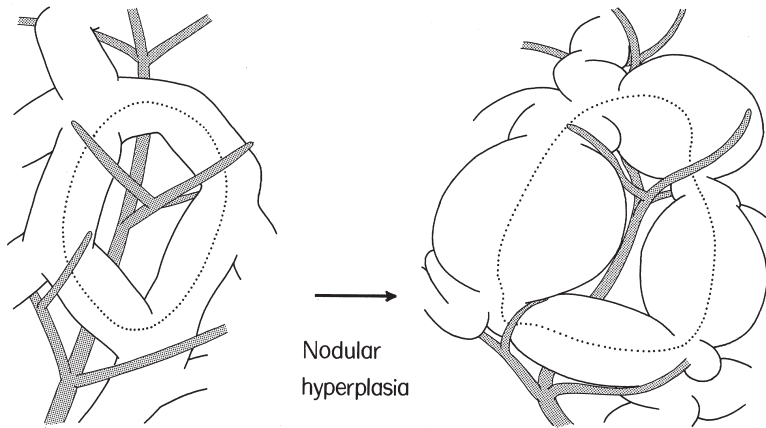


Fig. 6-15. Continuous transformation of network by nodular hyperplasia. With advancing regeneration of hepatocytes that survived necrosis, the parenchyma is gradually transformed into nodular network, but the skeleton maintains its topological properties with the holes of network retained as they were. Reproduced from Takahashi (1978); *Virchows Arch A Path Anat Hist* 377, pp. 190.

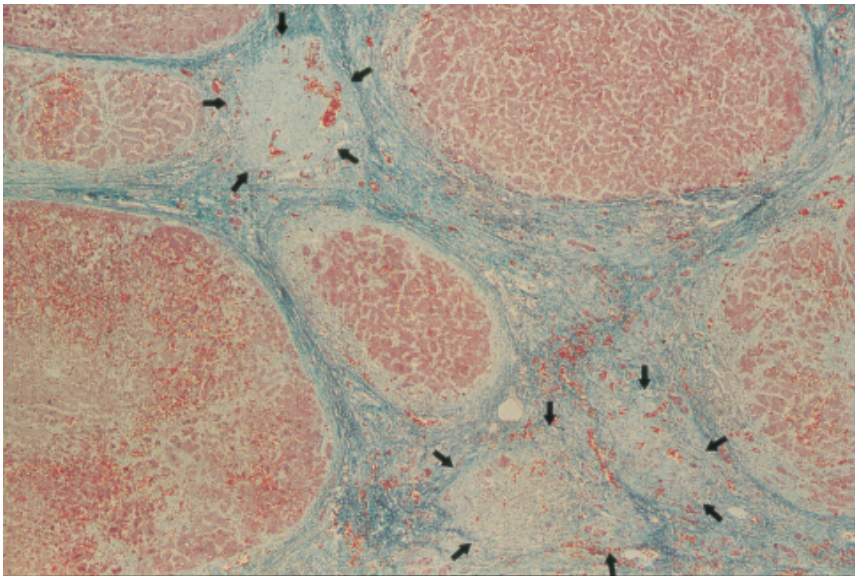


Fig. 6-16. Necrosis of hepatocytes involving whole regenerative nodules (arrows). Liver injury of this scale can sever the continuity of network, resulting in a radical reorganization of skeleton. Elastica-Goldner stain.

undergo. Let us assume therefore that as schematized in Fig. 6-15, cirrhosis may develop only through nodular swelling of parenchyma due to hepatocellular regeneration, while the network skeleton is sustained throughout the process. This is what may be called continuous transformation, with the whole geometric (topological) proper-

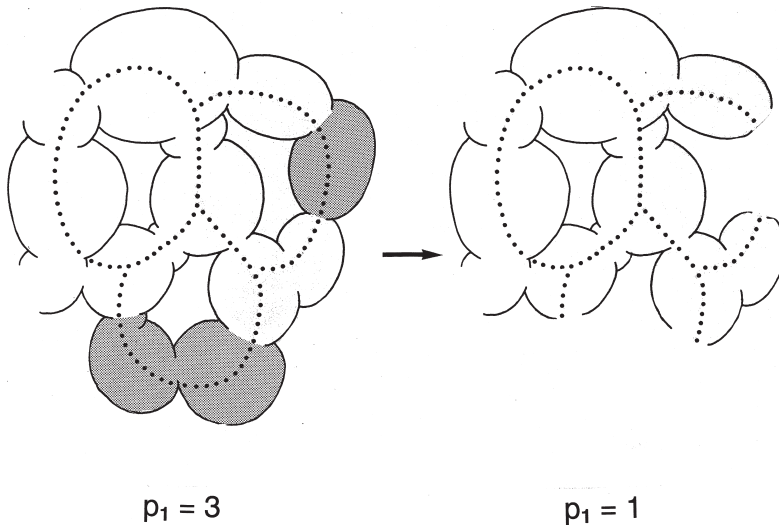


Fig. 6-17. Dehisence (crack) of loop due to hepatocellular necrosis of such an extension as shown in Fig. 6-16. The consequence is an reorganization of network skeleton, with the number of originally three holes reduced by two.

ties of network maintained. The skeleton might be subjected to distortion through the process, but the whole inner connecting relation would be preserved exactly as it has been.

The second factor that can affect the form of lesion is the hepatocellular necrosis that takes various extension. In Fig. 6-16, necrosis is shown developing in a cirrhotic liver, destroying some of the small nodules (arrows). This can happen in the form of recurrent focal necrosis, when the host immune system is reactivated against hepatocytes expressing virus-related antigens. However, one can also find necrosis attributable to parenchymal ischemia because, as shown above, parenchymal tissue becomes increasingly susceptible to impaired portal blood flow with the advancement of cirrhotic changes. In livers with alcoholic injury, alcohol abuse can also produce hepatocellular necrosis of sizable scale.

If parenchymal network is involved in necrosis of sufficiently large scale, the involved part of network is severed off, bringing about a dehisence (crack) of loop as in Fig. 6-17. Consequently, at every bout of necrosis, the network skeleton can undergo radical transformation. If so, the topological properties of the whole skeleton can gradually change with accumulation of cracks.

### Topological description of cirrhogenesis (Fig. 6-18)

In the foregoing chapter, a method was introduced with which we can compare the geometric properties among various networks. That was to quantify the inner connectivity of network with genus, a topological parameter, but its significance has to be explained in more accurate geometric terms, together with the method of its measurement.



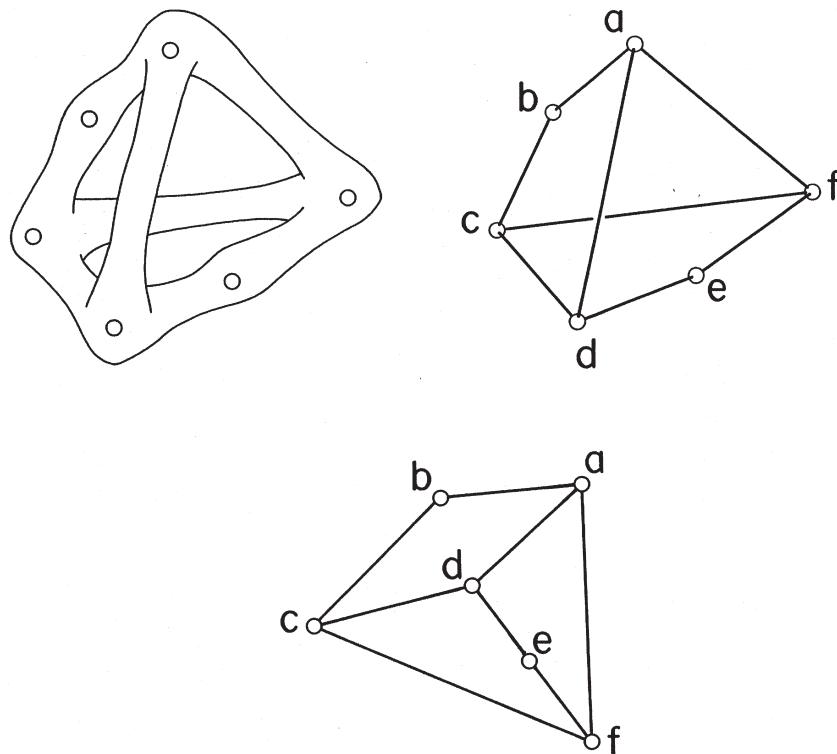


Fig. 6-18. Topological description of 3-D network with genus ( $p_1$ ). The inner connecting relation of a 3-D network made of closed surface (left) is simplified by replacing it with a node-branch system without changing the connectivity. Here, the number of nodes ( $n$ ) is six and that of branches ( $b$ ) is eight. The number of separate parts of network ( $p_0$ ) is one because the network is united. Then, on account of Euler-Poincaré formula  $n - b = p_0 - p_1$  we obtain that  $p_1$ , the number of holes the network contains (the genus), is three, as one can confirm in the lower figure.

Suppose, as in the left upper part of Fig. 6-18, a network made of closed surface and having several loops, or holes. It may serve as the simplest model of parenchymal (or interstitial) network of hepatic lesion. Now assume that arbitrary number of points (nodes) are placed in the trabecular network and, as in the right upper figure, are connected by branches, so that the network may be replaced with a node-branch system without changing the connecting relation. This procedure of replacement corresponds to the construction of the “deformation retract” of DeHoff *et al.* (1972). In this situation, let the number of nodes contained in the system be  $n$ , and that of the branches  $b$ . If the number of holes is  $p_1$  and that of the separate parts of network is  $p_0$ , then

$$n - b = p_0 - p_1$$

according to Euler-Poincaré principle, where  $p_1$  is called the genus. Let us attempt to apply this to the network of the figure. Then we obtain that  $n = 6$  and  $b = 8$ . The

number of separate parts of network is 1 because the figure is united as a whole. Then,

$$6 - 8 = 1 - p_1$$

and we obtain that  $p_1 = 3$ , which means that the network contains three holes. That there are three holes may be visualized if we transform the right upper, 3-D network into the lower, 2-D network. This is done only by transforming the holes and stretching and twisting the branches, which does not influence the connectivity. Now assume that a branch (for example ad) is taken away from the network. In this case  $b = 7$ , with  $n$  and  $p_0$  remaining as they have been. Then the number of holes  $p_1$  is calculated at 2, as confirmed in the figure. Accordingly, if we apply the formula to the parenchymal (or interstitial) network of the liver and compare the value of  $p_1$  among livers with different lesions, we will be able to know whether during cirrhogenesis, the skeleton of the lesion is maintained, or undergoes a radical reorganization.

### Measurement of genus on serial sections (Figs. 6-19, 6-20)

In measuring the  $p_1$  value contained in a certain volume of liver, we cannot rely on stereology, as explained in the foregoing chapter. This is because  $p_1$  is a quantity expressing the property of form which is non-metric and therefore not influenced by

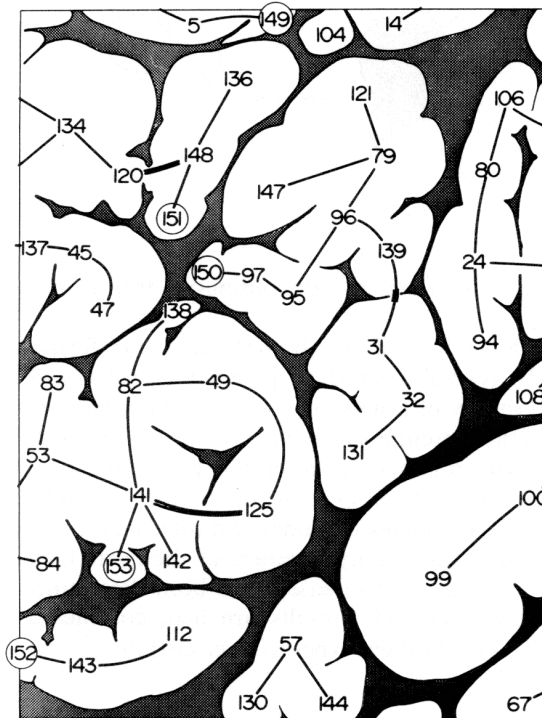


Fig. 6-19. Topological analysis of nodular network on serial sections of cirrhosis aimed at counting the number of genres ( $p_1$ ) in a certain volume. Nodules are registered with consecutive numbers. Also the internodular connections are checked at every step of serial sections. Reproduced from Takahashi (1978): *Virchows Arch A Path Anat Hist* 377, pp. 192.

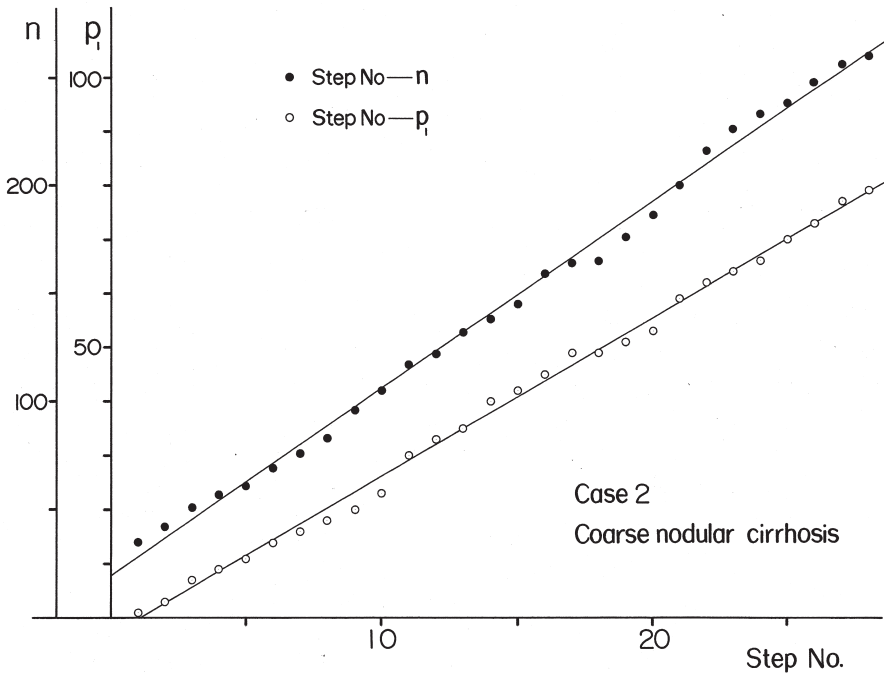


Fig. 6-20. The linear relation between the tissue volume (scanned with serial sections) and the number of genuses contained. The value of  $p_1$  increases with the advancement of serial sections treatment. The total  $p_1$  contained in the whole liver can be estimated by extending the regression line until it reaches the point corresponding to the liver volume. Reproduced from Takahashi (1978): *Virchows Arch A Path Anat Hist* 377, pp. 193.

distorsion, swelling or shrinkage. For this reason, manual 3-D measurement had to be performed to obtain the value of  $p_1$  contained in a certain volume of the liver. A sampling area was defined in one of the semiserial sections, where all the nodules were numbered and internodular connections were checked as in Fig. 6-19. This was done consecutively with semiserial sections, thereby checking the connectivity of nodules and counting the values of  $n$ ,  $b$  and  $p_0$ . The interval of semi-serial sections was set as large as  $50 \mu\text{m}$ , a coarseness which however gives no influence on the internodular connectivity obtained, because of the semi-gross nature of the object.

As increasing number of steps are processed, the number of nodules and that of holes accumulate, as in Fig. 6-20. This means that the larger the volume analyzed, the more do the holes emerge. In this way we obtain a regression between  $p_1$  and the volume of the tissue scanned. Thus, by extending the regression line to the volume of the whole liver, we obtain the total number of holes, or meshes, contained in the parenchymal network.

### Livers with chronic diseases: topological difference and its interpretation (Fig. 6-21)

The values of  $p_1$  thus obtained were compared among six livers with chronic diseases (Takahashi, 1978b) as in Fig. 6-21. In chronic hepatitis as well as subacute

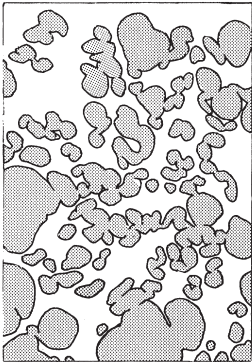
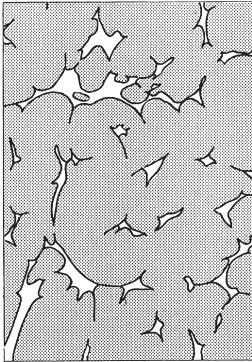

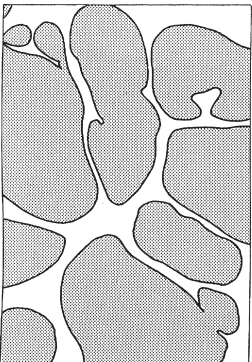
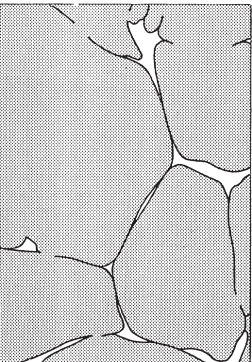

			
<b>Type</b>	<b>Subacute Hepatitis</b>	<b>Chronic Hepatitis</b>	<b>C(alcoholic)</b>
<b>Weight</b> (g)	<b>580</b>	<b>1270</b>	<b>1970</b>
<b>Total <math>p_1</math></b> ( $\times 10^4$ )	<b>501</b>	<b>610</b>	<b>635</b>
			
<b>Type</b>	<b>A'</b>	<b>B</b>	<b>B'</b>
<b>Weight</b> (g)	<b>1030</b>	<b>780</b>	<b>590</b>
<b>Total <math>p_1</math></b> ( $\times 10^4$ )	<b>37</b>	<b>10</b>	<b>23</b>

Fig. 6-21. The total number of genuses estimated in six autopsy livers. In the upper row are livers representing pre-cirrhotic and early cirrhotic lesions, including subacute hepatitis, chronic hepatitis and early alcoholic (portal) cirrhosis. In contrast, all the three cases arranged in the lower row exhibit advanced cirrhoses. Noteworthy is that in all the pre-cirrhoses and early cirrhosis, the total  $p_1$  is within about the same range, 5 to 6 million, whereas in the three advanced cirrhoses, the value is incomparably lower. Reproduced from Takahashi (1978): *Virchows Arch A Path Anat Hist* 377, pp. 195.

hepatitis, i.e., diseases that potentially can progress into cirrhosis, the total  $p_1$  of the liver is about the same and ranges from 5 to  $6 \times 10^6$ . In an early stage of alcoholic cirrhosis, it remains at about the same level. The other three livers entered in the lower frames are all cirrhosis, either Type A', Type B or Type B' of the classification used in Japan (Nagayo, 1914; Miyake, 1960). Of these, Type A' corresponds approximately to

the postnecrotic type and Types B and B' to the posthepatic type of Gall's classification (1960). It is shown that the total  $p_1$  of the liver in cirrhosis is much lower than the early lesions of the upper frames, ranging from 1/20 to 1/60 of the latter.

We can draw a conclusion from this. During the development of cirrhosis from precirrhotic lesions like chronic hepatitis, the skeleton once formed as a densely meshed 3-D network undergoes radical transformation where most of the segments are cut by hepatocellular necrosis. Perhaps the bout of necrosis recurs many times during a long course of disease, each time creating small number of connectivity changes. This assumption seems to match the actual clinical picture of chronic hepatitis, where, during a course of ten or more years, bouts of hepatocellular necrosis recur many times, gradually leading to the terminal stage of cirrhosis.

### Morphogenesis and advancement of cirrhosis (Fig. 6-22)

Figure 6-22 presents a schema of cirrhogenesis based on the above assumption. In an early pre-cirrhotic stage, the liver has a closely knit network with larger  $p_1$ . How-

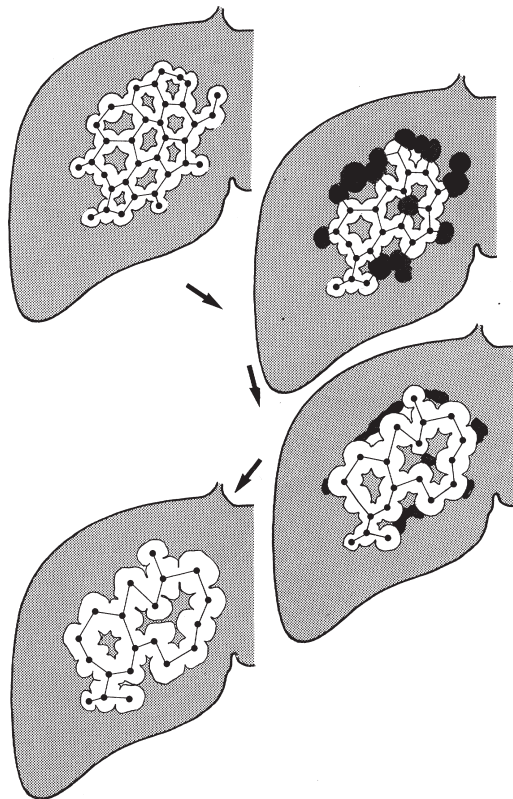


Fig. 6-22. A schema of morphogenesis from precirrhosis (or early cirrhosis) to advanced cirrhosis. In early lesions, the skeleton forms as a fine network with larger genres. With a bout of massive or submassive hepatocellular necrosis that frequently intervenes in the course of disease (black), the parenchymal network comes to be severed at several places, and the total genus number is reduced. Such an event recurs many times, reducing the  $p_1$  value at every recurrence, gradually transforming the skeleton into a network significantly coarser than the original one.



ever, with the bouts of parenchymal necrosis recurring again and again, the skeleton gradually changes into growingly coarser network. With time, the nodules that have survived necrosis will decrease in number while individual nodules enlarge due to continuing regeneration. This assumption seems giving support to the prospective study of Danish group reporting that in the alcoholics, the pattern of cirrhosis tends to be increasingly coarser with the advancement of disease (Fauerholdt *et al.*, 1983).

### **Viral antigen and its distribution (Figs. 6-23, 6-24, 6-25)**

We analyzed the origin and development of focal hepatocellular necrosis in livers with chronic hepatitis B (Endoh and Takahashi, 1997). As well documented, hepatocellular necrosis in this disease is attributable to host immune reaction against hepatocytes that have membrane-bound expression of HBcAg, the HB core antigen (Hsu *et al.*, 1987). Fig. 6-23 presents a liver section with chronic hepatitis B, immunostained for HBcAg. One can see that hepatocytes expressing HBcAg are not distributed diffusely or randomly, but clearly are forming foci, various in dimension but mostly less than 800  $\mu\text{m}$  in the largest diameter, the diameter of a single hepatic lobule.

On closer look, an HBcAg-positive focus contains positively reacting hepatocytes in mosaic fashion and the reaction is taking place in either the nuclei, cytoplasm or cell membrane (Fig. 6-24). Around the positive hepatocytes there are lymphocytes probably engaged in immune activities. There are also antigen-free hepatocytes among the antigen-positive ones, co-existing in “piecemeal” distribution. If such a focus is located in the periportal zone of lobule, a typical picture of so-called piecemeal necrosis can appear in a 2-D microscopic section. It seems to us that the piecemeal necrosis may correspond to a sectional picture of what has been described in the above as focal necrosis. Particularly when this sort of change takes place in the close vicinity of portal tract, it would present on 2-D section a typical picture of piecemeal necrosis.

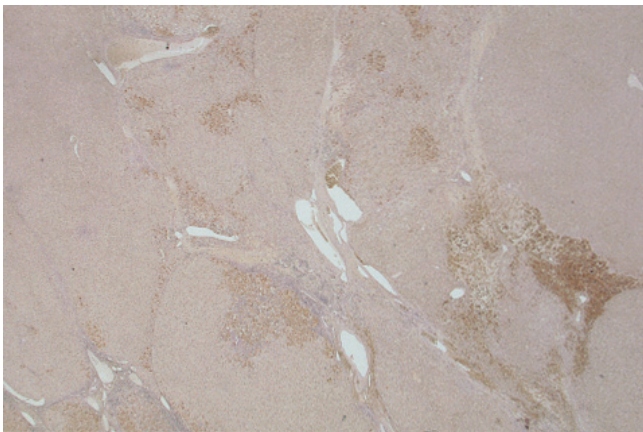


Fig. 6-23. Distribution of hepatitis B core antigen (HBcAg) in Type B chronic hepatitis. Note that the viral antigen is not uniformly distributed, but clearly forming positive areas. Immunostain for HBcAg.

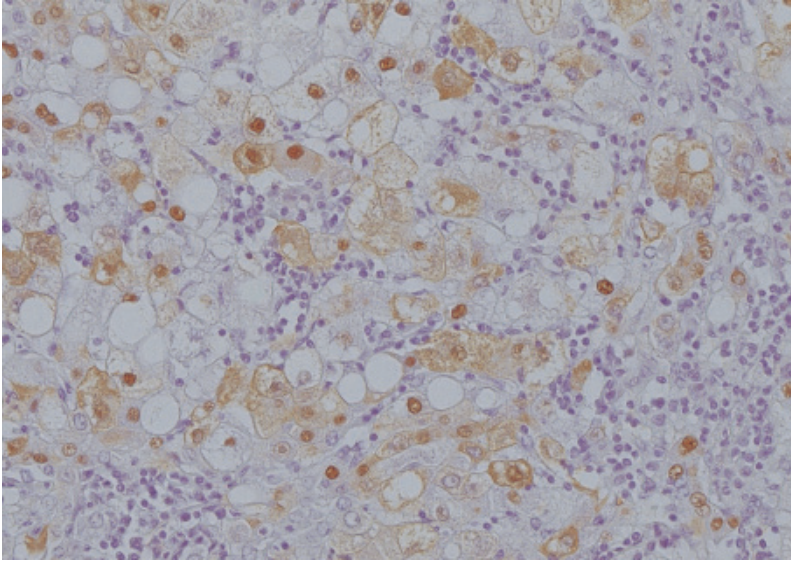


Fig. 6-24. High power microphotograph of HBcAg positive focus. There are positively reacting hepatocytes but the reaction is expressed variously: either upon the cellular membrane, or in the cytoplasm or in the nucleus. Dispersed among these are hepatocytes expressing no reaction. Also, lymphoid cells (presumably T-lymphocytes) are infiltrating in and around this positive area. If positioned around a portal tract, this would present as a typical "piecemeal necrosis." Immunostain for HBcAg.

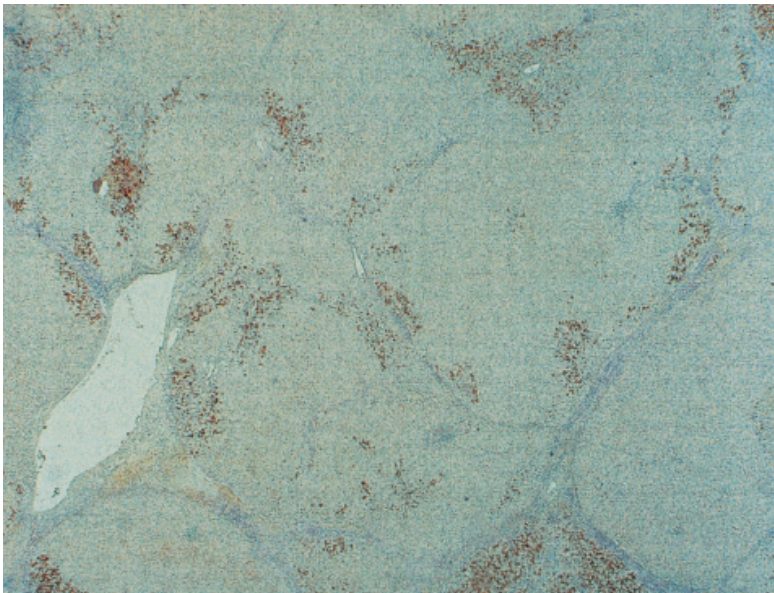


Fig. 6-25. Cirrhosis developing from chronic hepatitis B. Low power microphotograph of section immunostained for HBcAg. HBcAg+ hepatocytes are not distributed uniformly but forming a clearly demarcated foci. It may be intriguing that without exception, the foci are distributed along the interstitial septa. Immunostain for HBcAg.

Shown in Fig. 6-25 is a case of cirrhosis derived from chronic hepatitis B, immunostained for HBcAg. Antigen-positive areas are distributed as multiple foci, but it is particularly interesting that the interstitial septa have developed so as to link the positive areas. The message given by this picture may be clear: focal necroses occur in the antigen-positive areas, while new foci arise one after another. In such foci, however, some of the antigen-positive hepatocytes survive and proliferate, paving the way for future recurrence of necrosis in and around the sites. In the meantime, fibrosis is gradually deposited in the antigen<sup>+</sup> areas that extend with every recurrence and finally join with neighboring necrotic areas. On the other hand, the non-antigen-positive areas keep expanding by hepatocellular regeneration.

### Two-D distance distribution to locate the HBcAg<sup>+</sup> areas (Figs. 6-26, 6-27)

The idea of spatial distance distribution introduced in Chapter 3 was modified to demonstrate the close positional relation between the HBcAg-positive areas and the cirrhotic septa (Endoh and Takahashi, 1997). Figure 6-26 is a 2-D sectional picture of cirrhosis, where sampling points (six points in the figure) are set by tessellation. The points that fell in the interstitium (point No. 4) were omitted. Those falling in the nodules were divided according to whether they fell in an area positive (orange) or negative (white) for HBcAg. In the figure, two points (2, 5) fell in the positive, three (1, 3, 6) in the negative area, respectively. For each of the points, including those hitting the antigen-positive and those hitting the negative areas, the shortest distance from the point to the nearest septal border was measured.

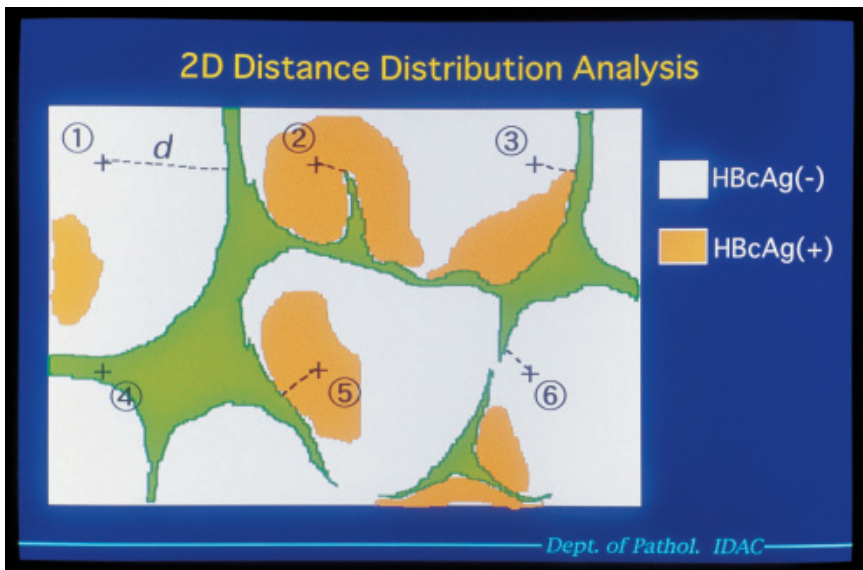


Fig. 6-26. Two-D distance distribution analysis. This is a method to test whether, in terms of position in the tissue, a lesion has affinity with a special structure, in this case HBcAg<sup>+</sup> areas with the interstitial septa. In the figure, six sampling points are randomly set by tessellation. For details see the text.

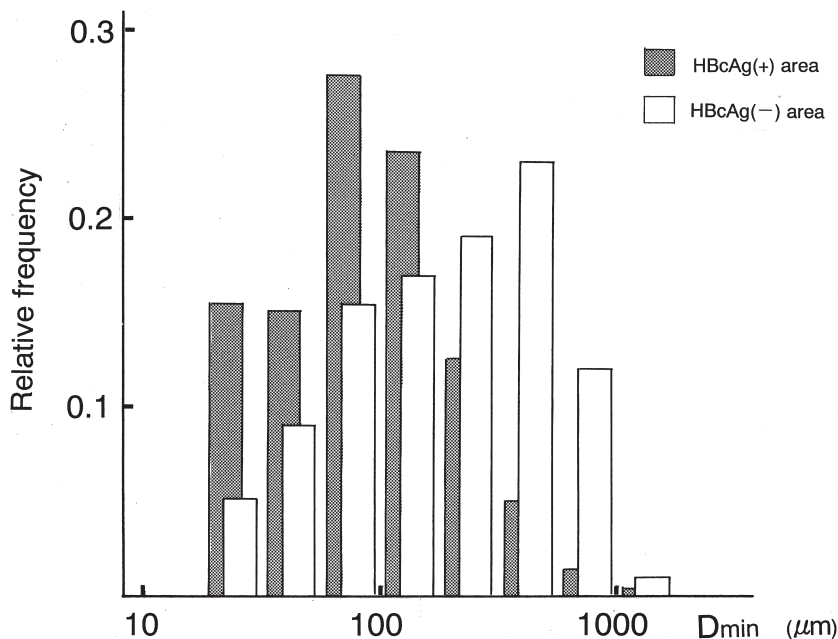


Fig. 6-27. Two-D distance distribution analysis. An example of application to a cirrhotic liver from chronic hepatitis B.  $D_{min}$ , the distance from the intranodular test points to the nearest septa, was shown on a log scale. Note that  $D_{min}$  from the points hitting HbAg<sup>+</sup> areas (hatched) is significantly smaller than those from HbAg<sup>-</sup> areas (non-hatched). Reproduced from Endoh, Takahashi, *et al.* (1997): *Tohoku J Exp Med* 182, pp. 183.

Liver specimens from 8 patients of cirrhosis developing from chronic hepatitis B were submitted to the 2-D distance distribution analysis. In each case, measurement was performed on 700 to 1,000 sampling points. Figure 6-27 is the result obtained in one of the livers and demonstrates that the distance from the points in the antigen-positive areas is smaller than those in the negative areas. Also in the remaining livers, quite the same results were obtained. In all cases, the difference in the distance proved to be significant on Mann-Whitney's test at  $p < 0.001$ . This allows us to conclude that the interstitial septa are likely to develop so as to link the necrotic areas.

### Model of cirrhogenesis from chronic hepatitis (Fig. 6-28)

From the above, the morphogenesis of cirrhosis from chronic hepatitis B can be schematized as in Fig. 6-28. HbAg-positive hepatocytes are distributed in the hepatic parenchyma forming multiple foci of sublobular dimension. The foci, dispersed in seemingly random fashion, appear to be representing something like viral colonies. In an active phase of hepatitis, antigen-positive hepatocytes in the foci undergo necrosis, while in each of the foci, at least some hepatocytes survive. They proliferate, extending the positive area, which again undergoes necrosis in the next recurrence. Fibrosis advances with the repetition of this cycle, and in the meantime, new necrotic foci add to the previous ones, where old and new foci gradually come to join, creating



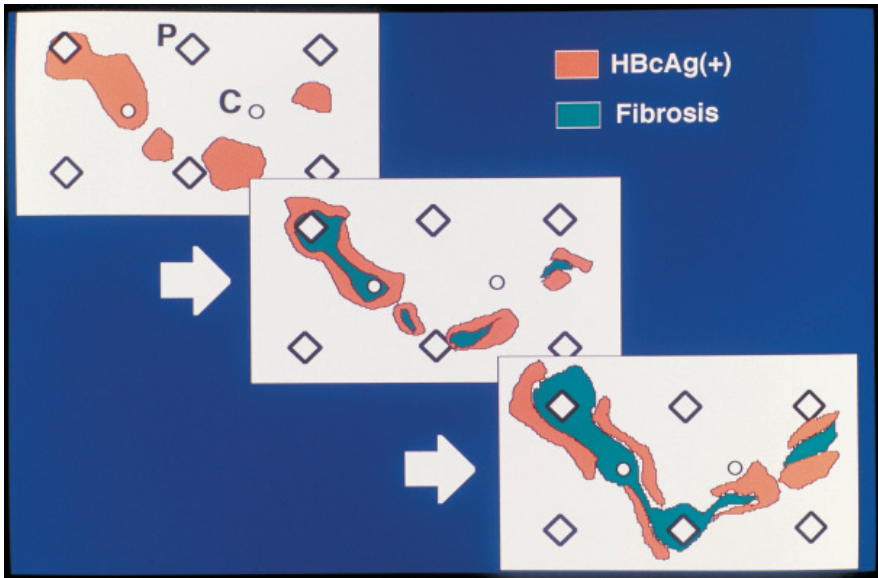


Fig. 6-28. A schema of cirrhogenesis from chronic hepatitis. Viral antigen-positive hepatocytes are distributed as multiple foci (brown) of sublobular dimension. While in an active phase, antigen<sup>+</sup> hepatocytes in the foci are mostly destroyed, some cells survive. They proliferate, extending the positive area, which again breaks down in the next recurrence. In the meantime, fibrosis (green) is left after every bout of necrosis and is added to the previous scars. While this cycle recurs again and again, there emerge new foci one after another. Thus the fibrotic areas continue spawning, each of which extends and joins with the neighboring ones, finally forming a network skeleton. Thus, slowly the basic pattern of cirrhosis comes into being.

interstitial septa in the form of network. Thus, slowly the basic pattern of cirrhosis comes into being.

Today, most patients of cirrhosis in Japan derive from Type C chronic hepatitis. We expect the same way of thinking may work again in studying the cirrhogenesis in such cases.



## **Some Other Topological Problems in Microscopic Pathology**

In making microscopic diagnosis of various organ changes, we often face problems that will better be approached if we are equipped with knowledge about the ABC of topology. Already, topological way of thinking has been introduced in Chapters 5 and 6, in the former of which it was pointed out that in distinguishing among variously differentiated adenocarcinoma and adenoma, changes of glandular skeleton serve as equally important a clue as changes of individual cells. However, so long as 2-D sectional images are examined, changes of structure in this aspect only provide the observers with a vague sense of abnormality. Only when visualized in 3-D pictures, the abnormalities of carcinomatous glands were disclosed so clearly as to allow us to define in accurate geometric terms how and to what degree the glandular structure is deviated from the norm. The deviation proved to involve the inner connectivity of normally tree pattern: generation of redundant branches that creates a network, or partial loss of branches causing the network to crumble into parts.

There are also similar aspects in the interpretation of 2-D microscopic images, and here too, we are assisted by applying the topological way of thinking. This is because sometimes in a 2-D section of diseased organs, structural changes of non-metric character play an essential role in creating the picture. Again, such changes have nothing to do with the length, area, volume or angle, but are associated with features sustainable during continuous transformation, as the number of holes contained in a network. All these features belong to the aspect of morphology where one can measure the grade of deviation by applying topological parameters. Added in this chapter are some other examples of such problems.

### **a) Changes of pattern from chronic hepatitis to cirrhosis**

#### **Cirrhosis, chronic hepatitis and intermediate stage (Figs. 7-1, 7-2)**

To be shown as the first example is the change of microscopic pattern from chronic hepatitis to cirrhosis. On what criteria do we differentiate between the two conditions microscopically? Nowhere we can draw a clear borderline. The whole process advances continuously, and we can only compare between arbitrarily chosen two livers and discuss, which of the two is more (or less) advanced. When we have a disease of an organ that shows a continuous transition of picture from one stage to another, its

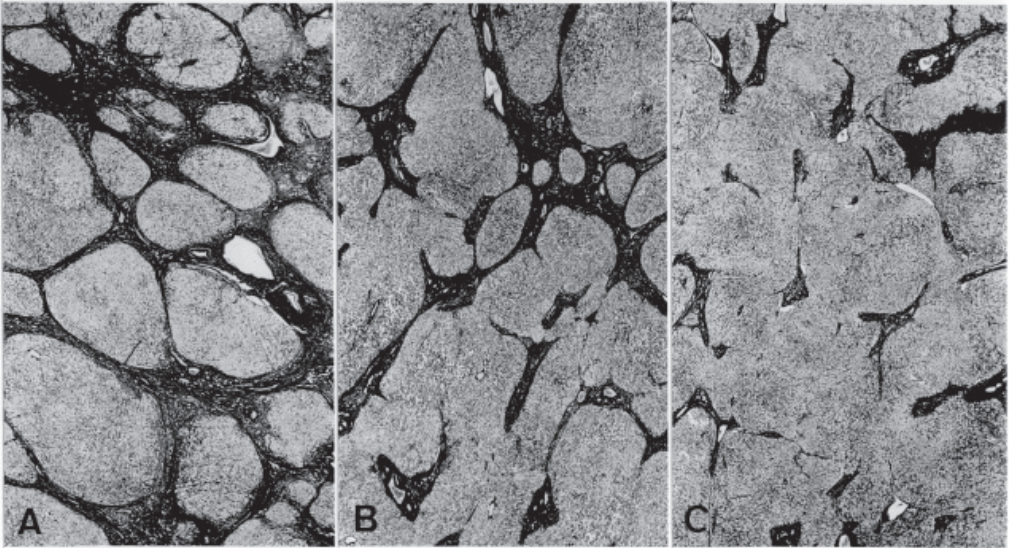


Fig. 7-1. Three different microscopic patterns of chronic liver diseases. A: advanced cirrhosis with completed nodulation. C: chronic hepatitis where nodules are not well separated. B: an intermediate pattern between A and C. Gomori's silver stain. Reproduced from Takahashi and Matsumoto: *Tohoku J exp Med* (1980), 131: pp. 322.

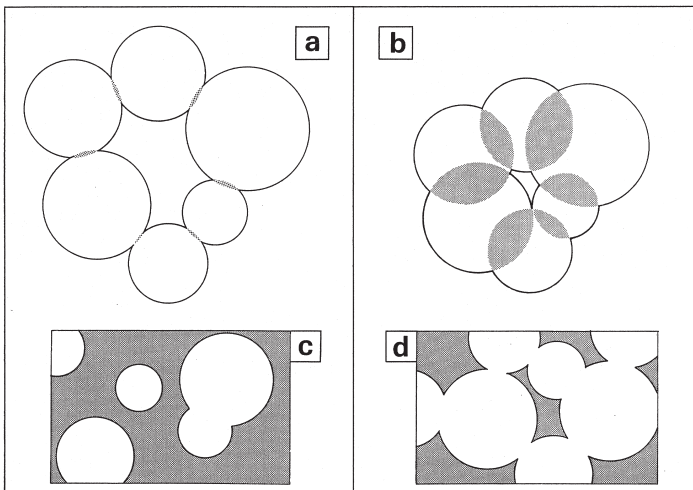


Fig. 7-2. Two-D topological difference between cirrhosis (c) and chronic hepatitis (d), related to their 3-D structure (a, b). Reproduced from Takahashi and Matsumoto: *Tohoku J exp Med* (1980) 131: pp. 315.

progression must be the very object to evaluate with a parameter, i.e., in terms of continuous quantity. Classification into separate groups is a time-honored method of study, that however works, strictly speaking, only when one can assume that the object comprises groups that in themselves are not continuous. To this problem, however, we will recur in the next chapter.

Now look at Fig. 7-1A. This is from an advanced cirrhosis where the microscopic section was silver-impregnated by Gomori method. One can find a typical two-phasic pattern, with the interstitial zones stained black and the regenerative nodules left unstained.

In Fig. 7-1C, a liver with chronic hepatitis is shown in order to compare with completed cirrhosis. In the parenchymal zone, there seems to be a tendency to swell with regeneration of hepatocytes, as shown by its partially rounded contour convex toward the interstitium. Still, the pattern of hepatic changes has yet to be qualified as cirrhosis, with quite incomplete nodulation. One can say at least that the pattern corresponds to a pre-cirrhotic condition, which cannot be expressed as real cirrhosis until necrotic foci have arisen one after another, adding to the preformed interstitial zone, and the parenchymal zone has undergone far more advanced nodular regeneration. The transition of pattern from chronic hepatitis to cirrhosis progresses along a continuous course, where morphologically no borderline exists separating the two conditions.

Then what is the difference in the above two patterns? By comparing the two, one may notice that it is the connectivity of the two phases that essentially differs. In cirrhosis (Fig. 7-1A), the interstitial phase is connected as a whole, separating the parenchymal zone into independent nodules. In contrast, we have a reversed state in chronic hepatitis of Fig. 7-1C, where it is the parenchymal zone that is connected over the entire picture, while the interstitial zone is split into separate parts.

There are of course a continuous series of intermediate stages. In the liver shown in Fig. 7-1B, both the parenchymal and the interstitial zones are halfway connected. Here the two phases seem to be embracing one another, forming an arabesque pattern. Pathologists may waver at this picture in deciding which diagnosis is more pertinent, chronic hepatitis or cirrhosis.

Three-dimensionally, as in Chapter 6, a liver with chronic hepatitis as well as cirrhosis has a parenchymal network as a common skeleton. Therefore the difference in 2-D pattern between the two conditions does not seem reflecting an essential difference in the skeleton. It appears that as in Fig. 7-2, the pattern of separate nodules in cirrhosis (c) is a 2-D section of nodules that in the three dimensions, are slightly connected (a). On the other hand, in chronic hepatitis the pattern of aggregated nodules (d) is likely to originate from a 3-D structure where the nodules are more deeply connected (b).

### **Various patterns related with angles subtended by interphasic curves (Fig. 7-3)**

As above, a liver with chronic hepatitis passes through a continuous series of 2-D microscopic pictures as it advances toward the terminal stage of cirrhosis, and now we are dealing with a connectivity change in a two-phasic pattern, a process that consists in a gradual separation of nodules from initially connected parenchymal zone. In fact, pathological diagnosis of cirrhosis solely depends on the grade of nodular separation in microscopic pictures. In the following, let us consider how we can describe the degree of advancement toward cirrhosis, establishing an index of connectivity with which to describe different 2-D patterns (Takahashi and Matsumoto, 1980; Takahashi, 1982).

Connectivity in a 2-D, 2-phasic pattern can be translated to the curvature of linear interphasic boundaries, or interphases. In Figs. 7-3a and 7-3b, we assume that the non-

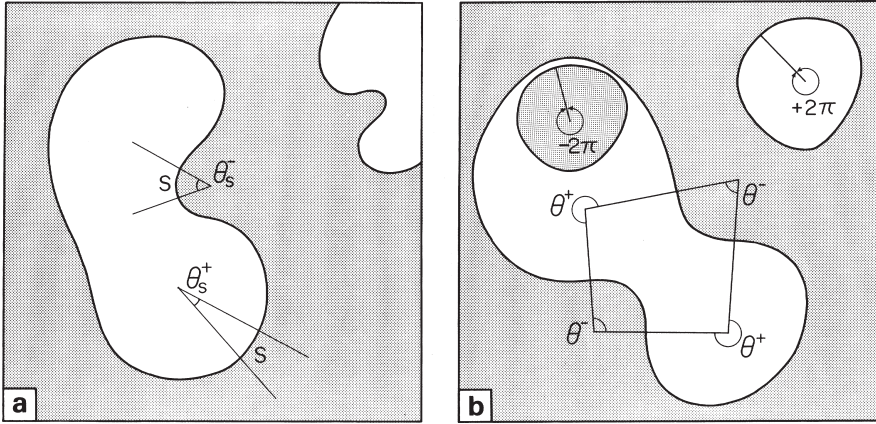


Fig. 7-3. **a**: definition of angle  $\theta_s$ , “subtended” by a minute segment S of interphasic boundary curve. The non-shaded areas are the parenchymal phase, the shaded the interstitial phase.  $\theta_s$  is defined as a plus angle if the segment S is convex toward the interstitium; it is minus if S is concave. **b**: three different figures surrounded by a closed curve are correlated to the total angle subtended by the perimeter. For details see the text. Reprinted from Takahashi and Matsumoto: *Tohoku J exp Med* (1980) 131: pp. 315.

shaded areas are parenchymal, and the shaded areas are interstitial phase. Pay attention to the curves delimiting the two phases. In Fig. 7-3a, we take a minute segment S of curving interphase, and define the angle  $\theta_s$  which is “subtended” by the segment. It corresponds to the angle between the normals drawn at the both ends of S. Here, plus and minus angles are to be distinguished according to whether, the interphase is convex or concave when viewed from the parenchymal phase. If S is convex toward the interstitium,  $\theta_s$  shall be plus and denoted by  $\theta_s^+$ , while it shall be minus ( $\theta_s^-$ ) if S is concave.

Now let us define  $\theta_A$ , the total sum of angles in an area A, in two different forms. One is the absolute sum  $\theta_A(\text{abs})$ , the sum of absolute values, in which we discard plus or minus. The other is the net sum  $\theta_A(\text{net})$ , in which  $\theta^-$  is added as minus angles. Accordingly,

$$\theta_A(\text{abs}) = \theta_A^+ + |\theta_A^-| = \theta_A^+ - \theta_A^-$$

and

$$\theta_A(\text{net}) = \theta_A^+ + \theta_A^-.$$

It may be clear from the definition of  $\theta_A^+$  and  $\theta_A^-$  that  $\theta_A(\text{abs}) \geq 0$ , and  $\theta_A(\text{abs}) \geq \theta_A(\text{net})$ .

To what values  $\theta(\text{abs})$  as well as  $\theta(\text{net})$  amounts is to be shown in various examples. In Fig. 7-3b, there is a nodule in the right upper part, where the contour is entirely convex along the circumference, and here, both  $\theta(\text{abs})$  and  $\theta(\text{net})$  are  $+2\pi$ , because there is no minus angle. In a “lobulated” pattern in the middle of the figure where two nodules are connected, minus angles develop at the places of constriction. In this pattern,  $\theta(\text{abs}) > 2\pi$  because lobulation generates redundant plus angles that

make the total  $\theta^+$  larger than  $+2\pi$  and moreover there are minus angles that are added as absolute values. But  $\theta(\text{net})$  remains always  $+2\pi$  in such an indented shape because the redundantly formed plus angles are exactly offset by the minus angles. Next, there is a hole in a nodule in the left upper part of the figure. If the interphase is concave toward the hole along the entire circumference, no plus angle exists. Therefore  $\theta(\text{abs}) = +2\pi$  and  $\theta(\text{net}) = -2\pi$ .

### The index of nodular separation $\rho_\theta$ (Fig. 7-4)

Based on the above, we define  $\rho_\theta$ , the index of nodular separation, as

$$\rho_\theta = \theta_A(\text{net}) / \theta_A(\text{abs}). \quad (7-1)$$

One can see in Fig. 7-4 how  $\rho_\theta$  describes a series of patterns that are different in terms of connectivity of the two phases. In the left upper figure (a) where all the nodules are round with the interphasic curve always convex toward the interstitium,  $\rho_\theta = +1.0$ , because  $\theta(\text{net})$  is  $+2\pi$  for each nodule and equal to  $\theta(\text{abs})$ . With beginning "lobulation" of nodules due to aggregation as in the right upper figure (b),  $0 < \rho_\theta < +1.0$

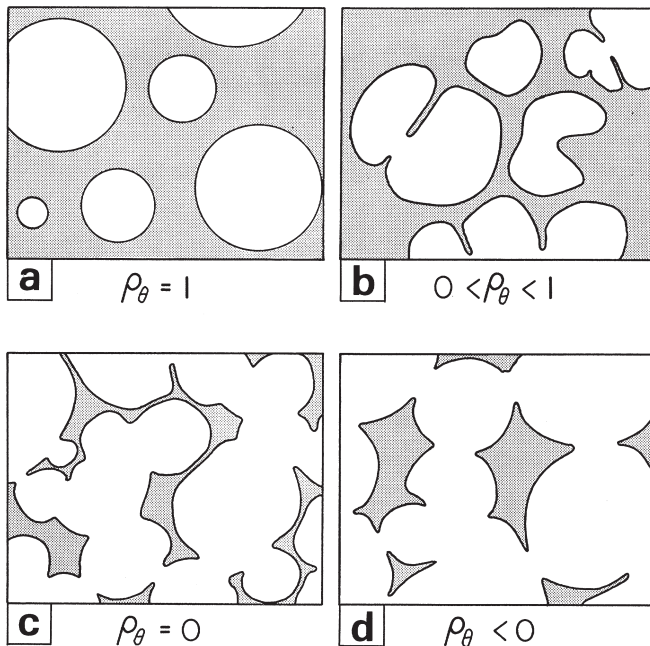


Fig. 7-4. Various patterns described with the index of nodular separation  $\rho_\theta$ . When  $\rho_\theta$  is  $+1.0$  (upper left), the nodules are constantly convex toward the outside. As internodular connection begins (upper right),  $\rho_\theta$  becomes smaller. When  $\rho_\theta$  is 0, it describes an arabesque, where the parenchymal and interstitial phases embrace one another (lower left). A negative  $\rho_\theta$  implies a reversed pattern (lower right) with the interstitial phase disconnected into separate parts. Reproduced from Takahashi and Matsumoto (1980): *Tohoku J Exp Med* 131, pp. 318.



because minus angles, developing at the places of constriction, make  $\theta_A(\text{abs})$  larger than  $\theta_A(\text{net})$ . As aggregation advances,  $\rho_\theta$  becomes smaller, and when it reaches 0, the pattern corresponds to “arabesque” as in the left lower figure (c), in which the two phases are embracing one another. If nodular connection advances further, we get a pattern of separate interstitium (d: right lower), or a reversed pattern, where  $\rho_\theta < 0$ .

Thus, the parameter describes a series of differently connected patterns as a continuous variable. If applied to liver diseases, the larger the value of  $\rho_\theta$ , the more advanced the cirrhotic changes, and vice versa.

### Determination of $\rho_\theta$ by tangent counting (Fig. 7-5)

$\rho_\theta$  is calculated by the equation (7-1), but how to estimate the total angles  $\theta_A^+$  and  $\theta_A^-$  in an area A? These are obtained very easily by applying the tangent counting method proposed by DeHoff (1968, 1970). Consider, as in the upper part of Fig. 7-5, a rectangular area A which we assume to be sufficiently large and contain interphasic curves randomized with regard to their orientation. Let the shadowed area be the interstitial, and the non-shadowed area the nodular phase, respectively. Here we attempt to “sweep” the area with a line, for example the upper side of the rectangular, that is to be translated downward as the test line. With “sweeping,” this line comes to contact at many places with the interphasic curves, generating tangents as denoted by symbols  $\circ$  and  $\times$ . It may be clear that the more meandering the curves, the larger the number  $T_A$  of tangents generated, which means, the more  $\theta_A$  is contained in the area A.

Statistically, a tangent occurs at every  $\pi$  of angles “subtended” by the interphasic curves, if the area A is sufficiently large and the curves are randomized in their orientation. This would be understood intuitively as follows. We assume, as in the lower part of Fig. 7-5, that the linear interphasic boundaries in A are entirely split into a large number of sufficiently minute, elementary arcs, each of which subtends a minute angle  $d\theta$ . Let us pay attention to an elementary arc and consider the expected number  $dT$  of tangents that occur at the arc (of interest) when the area A is swept by a test line. Suppose that all  $d\theta_s$  in A, together with the arcs, are collected by parallel translation to a point as in the right part of the figure. Then we can see a circle having an angle of  $2\pi$  may be formed many times. Because sweeping generates a tangent at every hemisphere ( $\pi$ ), the probability that it occurs at the arc (of interest) subtending  $d\theta$  is  $d\theta/\pi$ . Accordingly, if the total expected number of tangents in A is  $T_A$ ,

$$T_A = \int_A dT = \frac{1}{\pi} \int_A d\theta = \frac{1}{\pi} \theta_A(\text{abs}),$$

and we obtain

$$\theta_A(\text{abs}) = \pi \cdot T_A.$$

An accurate mathematical derivation will be found in the literature (DeHoff, 1968; Takaki and Arai, 1993). The estimate of  $\theta_A^+$  and that of  $\theta_A^-$  are obtained by distinguishing between the tangents generated at convex ( $\circ$ ) and concave parts ( $\times$ ) of curves. If the tangent number at convex and concave curves are denoted as  $T_A^+$  and  $T_A^-$ , respectively,

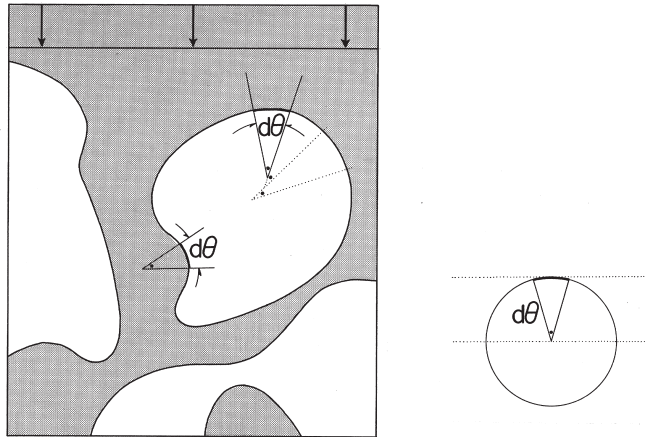
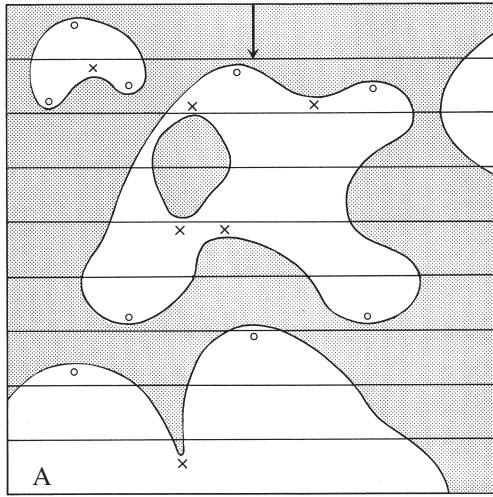


Fig. 7-5. Measurement by tangent counting of  $\theta_A$ , the total angles subtended by the curving interphasic borders in an area A. For explanation see the text. Reproduced from Takahashi and Matsumoto: *Tohoku J exp Med* (1980), 131: pp. 319 and 321.

$$\theta_A^+ = \pi \cdot T_A^+$$

and

$$\theta_A^- = -\pi \cdot T_A^-.$$

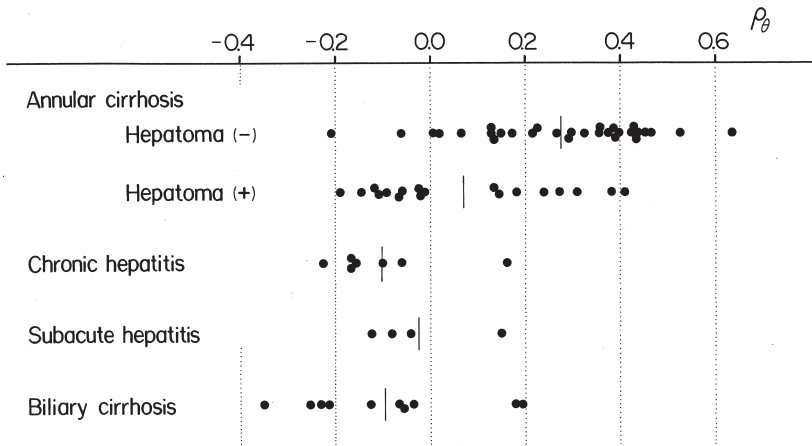


Fig. 7-6. Index of nodular separation  $\rho_\theta$  estimated in various liver diseases. Reproduced from Takahashi and Matsumoto: *Tohoku J exp Med* (1980), 131: pp. 323.

### $\rho_\theta$ estimated in various liver diseases (Fig. 7-6)

$\rho_\theta$  was obtained by measurement on seventy autopsy livers with different types of chronic diseases, including cirrhosis with or without hepatoma (hepatocellular carcinoma), chronic hepatitis, subacute hepatitis and biliary cirrhosis (Fig. 7-6). These diagnoses were given microscopically by a number of pathologists in advance of morphometry. In cirrhosis, the obtained values of  $\rho_\theta$  range from  $-0.21$  to  $+0.64$ . That even the highest value is far lower than  $+1.0$  may be understood by taking into account the 3-D structure of cirrhosis where the nodules are mutually joined to form chains (see Figs. 6-4, 6-5 and 6-9), producing indented contour of nodules. Cirrhoses were divided according to whether or not harboring hepatoma. In the group with hepatoma the mean  $\rho_\theta$  is  $+0.07$ , a value much lower than  $+0.27$  in the group without hepatoma, and the difference is significant at  $p < 0.01$ . Thus, seemingly less completed cirrhosis is likely to be rather more prone to cancer development. The mean  $\rho_\theta$  was negative in all the remaining groups;  $-0.102$  in chronic hepatitis,  $-0.023$  in subacute hepatitis and  $-0.095$  in biliary cirrhosis.

## b) Two types of glandular tumors: papillary and tubular

### Intraductal papilloma of breast: papillary and tubular types (Figs. 7-7, 7-8)

The glandular epithelium is a generic term for the epithelium that consists of glandular or secreting cells. If we introduce a term “glandular tumors” to express tumors developing from glandular epithelia, it includes a wide range of various tumors like adenoma, papilloma, adenocarcinoma and so on, totaling in frequency up to the largest share of tumors pathologists encounter in their routine diagnostic practice. Looking through the various pictures of glandular tumors, one may notice that there are basically two types, i.e., “tubular” and “papillary” types.

Figures 7-7 and 7-8 present typical microscopic pictures. These are tumors of the

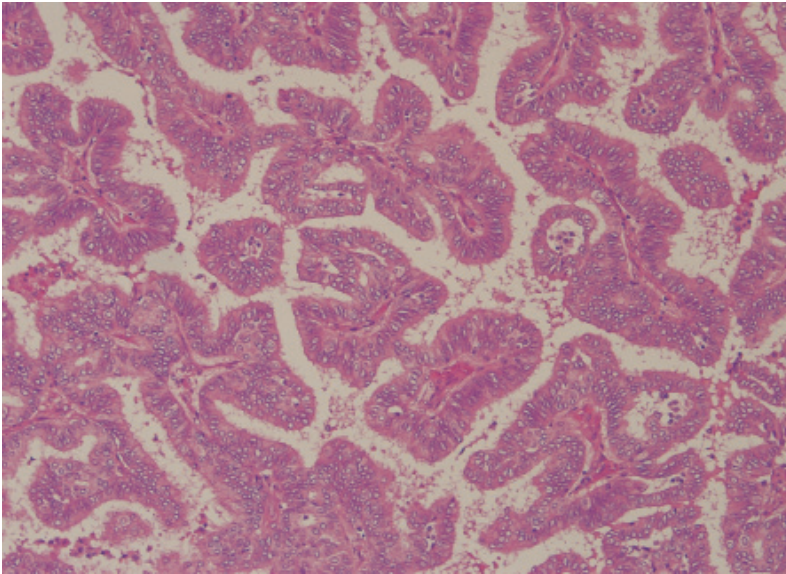


Fig. 7-7. Intraductal papilloma of the breast: papillary pattern. The tumor consists of finger-like rods, all having fibrovascular stroma and covered by a monolayer of epithelial tumor cells. Extending around the tumor cells is the void space, into which the glandular epithelia secrete their products. Hematoxylin-eosin stain.

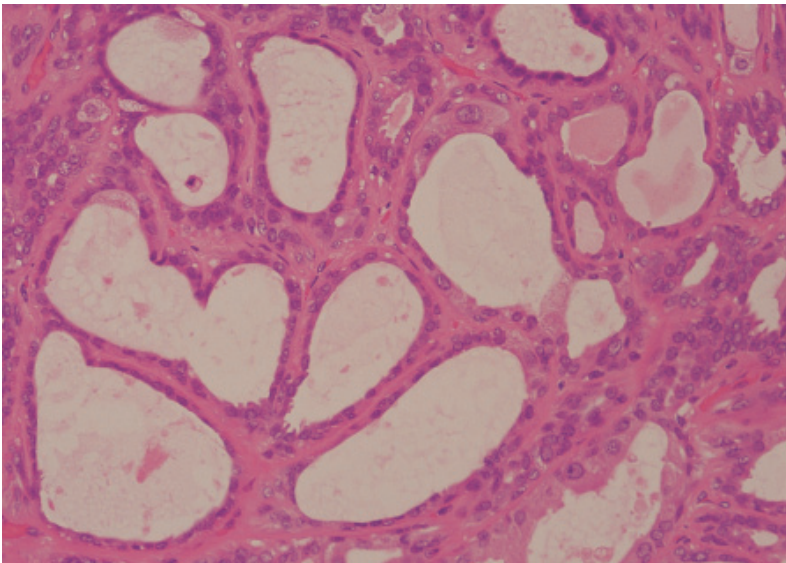


Fig. 7-8. Intraductal papilloma: tubular pattern. Here one can find multiple tubes that penetrate the stromal phase. The inner surface of the tubes is covered by tumor cells. The products of tumor cells are secreted into the lumina of tubes which in this pattern are the phase of void. Hematoxylin-eosin stain.

breast, both designated as intraductal papilloma, about which we already discussed in Chapter 4. In Fig. 7-7, the tumor appears consisting of numerous finger-like rods, each having a stroma made of connective tissue which is covered by epithelial tumor cells, presenting a form that may adequately be called a papillary tumor.

In Fig. 7-8, however, one can find a different pattern. Formed here are multiple tubes. They are separated by connective tissue stroma, and the neoplastic glandular cells are extending so as to cover the inner surface of the tubes, a pattern that can be expressed as a tubular tumor. Although conventionally diagnosed as intraductal papilloma, this type of tumor seems to be found not infrequently on microscopic examination of intraductal tumors of the breast. There are also intermediate tumors in which papillary and tubular patterns co-exist in various proportion. Thus, we find here a lesion which can present a series of different patterns between the two extremes. As to be shown, these varying patterns can exactly be defined from a connectivity point of view.

### Topological difference between papillary and tubular patterns (Fig. 7-9)

Here again, we face the same problem as we saw in the foregoing section. Figure 7-9 is a schema explaining in what aspect the two patterns differ. Both papillary and tubular tumors consist of two phases, the stroma (shaded in the figure; one may also call interstitium) and the void (non-shaded). The proliferating tumor cells are lining along the interphasic border, while both of the phases are not in themselves a tumor. The stroma is an indispensable component of tumor because it contains blood vessels feeding the growing tumor cells. The void corresponds to the exterior spaces where products secreted by the tumor cells flow in, stay and are carried through.

Now, let us examine the connecting relation of the two phases. First we realize

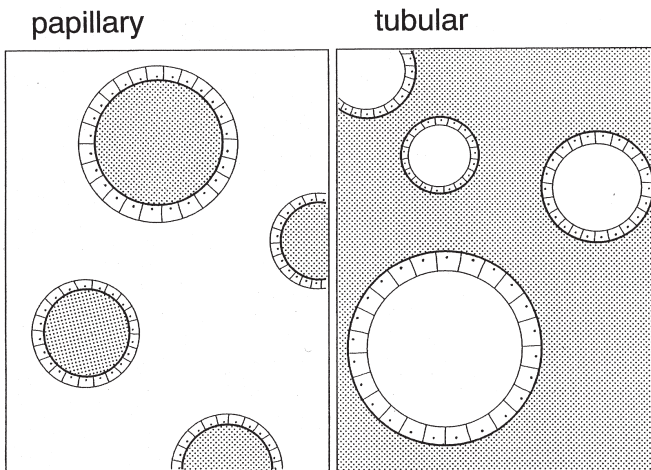


Fig. 7-9. Papillary vs. tubular tumors: their topological difference. In the papillary tumor (left), the void phase (non-shaded) is connected, separating the stromal phase (shaded) into pieces. The tubular tumor (right) corresponds to the reversed state, where the stromal phase is totally connected, disuniting the void phase. Thus the difference underlying the two patterns is reduced to that of topology.



that in the papillary tumor, the void phase is connected as a whole, separating the stromal phase into many pieces. In contrast, in the tubular tumor the connecting relation is reversed: the stroma is totally connected, and inevitably the void is disconnected into separate tunnels. Thus we understand that the difference between the two patterns is defined by connectivity, i.e., which of the two phases is connected, containing the other.

The situation is quite the same as what we saw in the livers with chronic hepatitis and those with cirrhosis. Consequently, also in the intraductal tumors of breast, we can apply the quantitative expression with  $\rho_\theta$  to measure the degree to which a given tumor is papillary or tubular. This will help us correlate the grade of “papillarity” or “tubularity” with clinical or biological features of glandular tumors. Recently, Sasaki *et al.* attempted to evaluate the pattern of intraductal papillomas with  $\rho_\theta$  by micromorphometry on surgically excised breast from 40 patients.

### Morphometry of intraductal papillomas (Fig. 7-10)

Morphometry was performed on silver-impregnated sections. Figure 7-10 is an example of tubular tumor where the interstitial phase, comprising collagen, is stained black. As the interphasic border, we defined the basement membranes of the proliferating glandular cells, disregarding the tumor cells which were included in the void. Measurement was made with a microscope equipped with tessellated eyepiece of grid-type as entered in the figure, where the parallel transverse lines allowed the observer to find the places where a tangent with basement membranes would occur. Using the grid, point counting was performed at the same time to estimate the volume density of the stromal phase  $V_v(s)$ , as illustrated in Chapter 2 (Figs. 2-1, 2-2, 2-3).

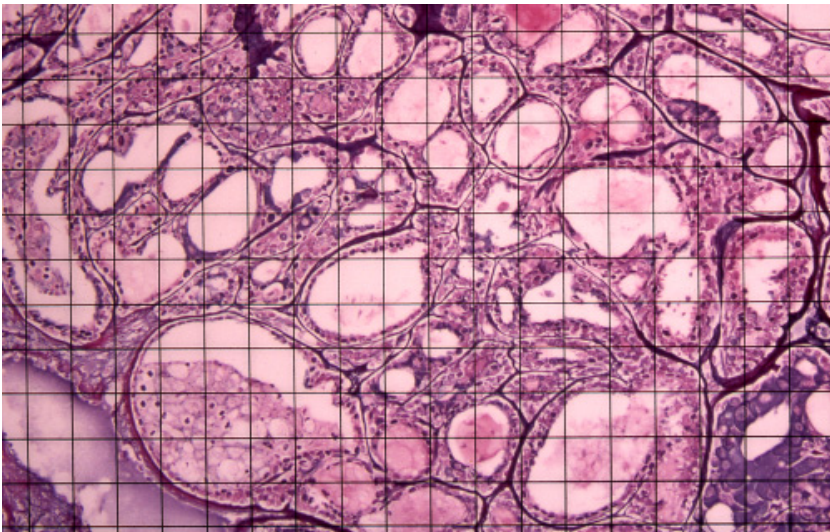


Fig. 7-10. Microscopic tangent counting for the pattern analysis of intraductal papilloma. The places where a tangent occurs between the interphasic border and the transverse parallel lines, are detected as the picture is slowly moved in the direction vertical to the lines.  $V_v(s)$ , the volume density of stroma, can simultaneously be estimated by point counting. Gomori's silver stain.

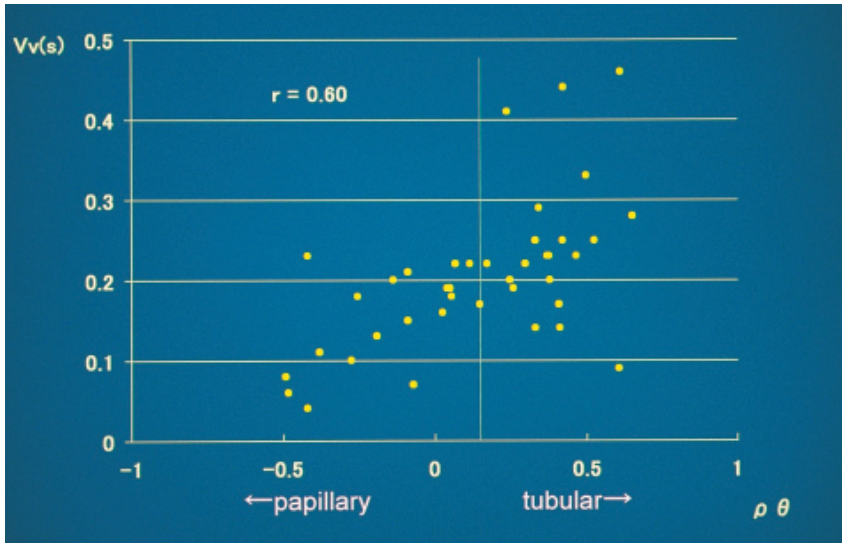


Fig. 7-11. Index of tubularity  $\rho_\theta$  estimated in 40 intraductal papillomas.  $\rho_\theta$  is presented in the abscissa, and  $V_v(s)$  in the ordinate. The mean  $\rho_\theta$  is  $+0.14$ , showing that in the microscopic pictures, tubular pattern dominates over papillary, betraying the term “papilloma.” Interestingly, there is a significant correlation between  $\rho_\theta$  and  $V_v(s)$ , showing that the more tubular the tumor, the more stromal component it contains.

### Obtained values of $\rho_\theta$ and its correlation with $V_v(s)$ (Fig. 7-11)

Figure 7-11 presents the result of measurement, with  $\rho_\theta$  in the abscissa and  $V_v(s)$  in the ordinate. This time,  $\rho_\theta$  was defined as an index of tubularity: the larger the value, the more tubular the pattern, and the smaller, the more papillary. When  $\rho_\theta = 0$ , the pattern consists of a mixture with tubular and papillary components, each having an equal share. As shown,  $\rho_\theta$  ranges from  $-0.5$  to  $+0.7$ , with a mean of  $+0.14$ . A mean value that proved to be plus demonstrates that in intraductal papilloma as a whole, tubular pattern predominates over papillary. Therefore, strictly speaking, “intraductal tubular adenoma” may be a more appropriate term than intraductal papilloma.

There is another finding which is more intriguing. One can see a positive correlation between  $\rho_\theta$  and  $V_v(s)$ , the volume density of the stromal zone. The correlation coefficient, calculated at  $+0.60$ , is significant at  $p < 0.01$ . It demonstrates that, of the intraductal tumors of the breast, the more tubular the pattern, the larger the volume ratio of stroma contained in the tumor, and *vice versa*. We think this is a result quite significant in studying the morphogenetic difference between the two types of glandular tumors.

### Morphogenesis for tubular and papillary tumors (Figs. 7-12, 7-13)

Figure 7-12 is a schema illustrating an assumption on the morphogenesis of tubular and papillary tumors. The figure in the upper part means a normal mucosa of mammary duct where a monolayer of epithelial cells are lining along the surface. The cells are laid on a basement membrane covering the stroma (shaded), the connective tissue that lies beneath and holds the membrane. The right lower figure expresses a

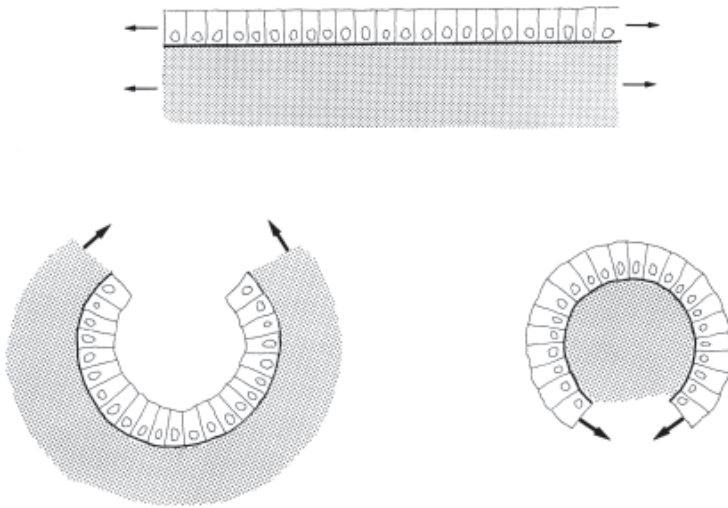


Fig. 7-12. A schema of morphogenetic difference between tubular and papillary tumors. For explanation see the text.

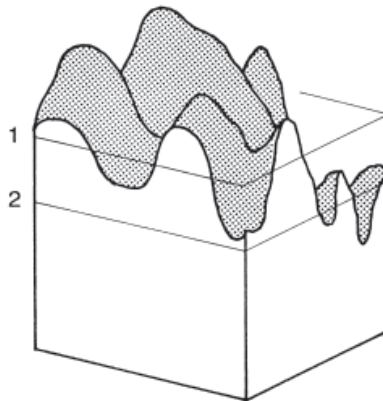


Fig. 7-13. Papillary and tubular tumors: difference in their 3-D structures. Consider that the cubic space contains an interphasic basement membrane covering the stromal phase that is under the membrane. The upper part of the space corresponds to the void. The membrane forms several mountains and depressions, and if the cube is cut at Level 1, a papillary pattern emerges in the section, while at Level 2, a tubular pattern will be produced.

papillary tumor. Here the epithelial tumor cells, proliferating so as to extend the epithelial surface, grow faster than the connective tissue of stroma, and as the result, the stroma gradually comes to be wrapped by the superficial tumor cells, resulting in the formation of papilloma pattern. Quite the opposite is found in the morphogenesis of tubular tumor, as in the left lower. In this tumor, the stroma grows at a speed higher

than the epithelial tumor cells, and this makes the void phase being contained by faster-growing stromal phase. The result will be the formation of tubular tunnels.

It is often said that with regard to the morphogenesis of various tumors, it is the stromal tissue rather than the tumor cells themselves that determines the form (Sakakura *et al.*, 1976). The present study seems to be giving a support to this concept.

In the above, the difference between papillary and tubular tumors has been discussed solely on 2-D sectional pictures. Then, what difference is there in the 3-D? Figure 7-13 is a schema correlating the 2-D patterns with the corresponding 3-D structure. Imagine a form like geographical configuration which is meant to express the basement membrane of glandular tumor. We assume that the membrane is covering the stroma that lies beneath. Now one can see the membrane is elevated at several places and is depressed between the neighboring mountains. Suppose that this configuration is sectioned with a plane parallel to the ceiling. At Level 1, several sections of mountains appear in the 2-D picture creating a papillary pattern, while at Level 2, the ground depressions emerge as cavities, and this is equivalent to a tubular pattern. After all, no critical point seems to exist in the 3-D structure corresponding to the transition of connectivity in a 2-D section where the value of  $\rho_\theta$  changes plus and minus.

### c) Hepatocellular carcinoma: cord and plate types

#### Normal hepatocytes and sinusoids (Fig. 7-14)

As another example, the microscopic feature of hepatocellular tumor is to be

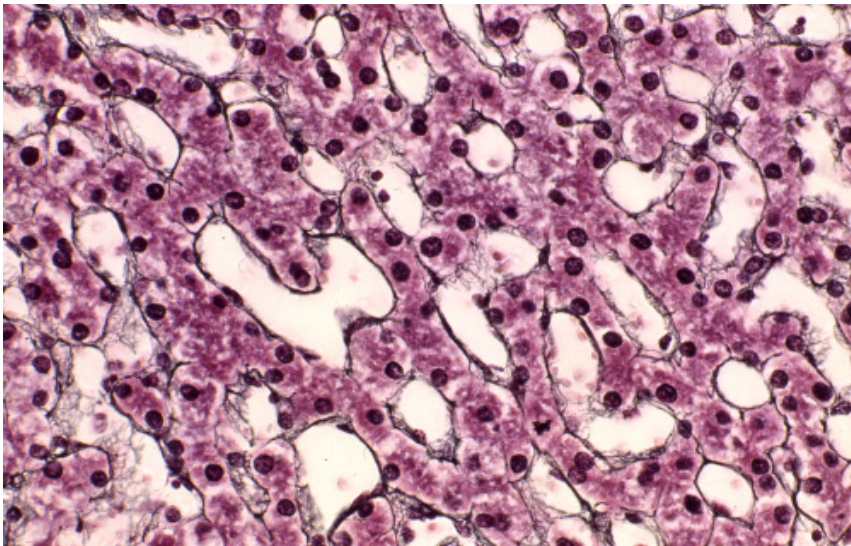


Fig. 7-14. Microscopic appearance of normal liver parenchyma. The hepatocytes seem forming continuous cords one cell breadth. The void spaces surrounded by the cords are the capillaries (sinusoids). Note that the hepatocytes are continuous throughout the picture, while the sinusoids are all split apart by hepatocytes, presenting a topological question of form. Gomori's silver stain.



added as a case for the application of  $\rho_\theta$ . In Fig. 7-14 we revisit the normal intralobular parenchyma of the human liver (also see Figs. 3-26 and 3-27). The section is silver impregnated, with the hepatocytes stained wine red, their basement membranes black, and the capillaries (sinusoids) left as void spaces. Here again we find in the hepatic parenchyma a two-phasic structure comprising hepatocytes and capillaries, with the basement membrane delimiting the two phases. Now let us consider what a basic 3-D structure the hepatocytes are forming. The cells seem arranged in the form of continuous rows one-cell thick. Previously, an expression “liver cell cord” had been coined to describe this arrangement of hepatocytes. Though used for a long time, this term was abandoned after Elias (1949) pointed out its inadequacy from a structural viewpoint. Pay attention to the connecting relation between the two phases, and it may be clear that the capillaries are all separated into pieces, while on the other hand, hepatocytes are all connected over the whole picture, forming a continuum. Then what a 3-D structure should be assumed for each of them? It may be understood that the capillaries that are not united in a 2-D section, if integrated into 3-D by reconstruction from serial sections, will certainly present a linear structure, or in other words, a system of cords. However, the hepatocytes that are all continuous in a section cannot be a cord in the 3-D. Instead, they make plates, or “muralium,” to use an expression by Elias. Though having curved surfaces and finely anastomosed, the aggregates of hepatocytes are certainly a plate facing the sinusoids with both of the sides, so long as a small part of the aggregate is concerned. Today, hepatocytes are correctly said to form “liver cell plates.”

### Hepatocellular carcinoma: plate and cord types (Fig. 7-15)

Figure 7-15 presents two microscopic types of hepatocellular carcinoma. These are from the study of M. Nakamura *et al.* (1996) who noticed that there are a variety of

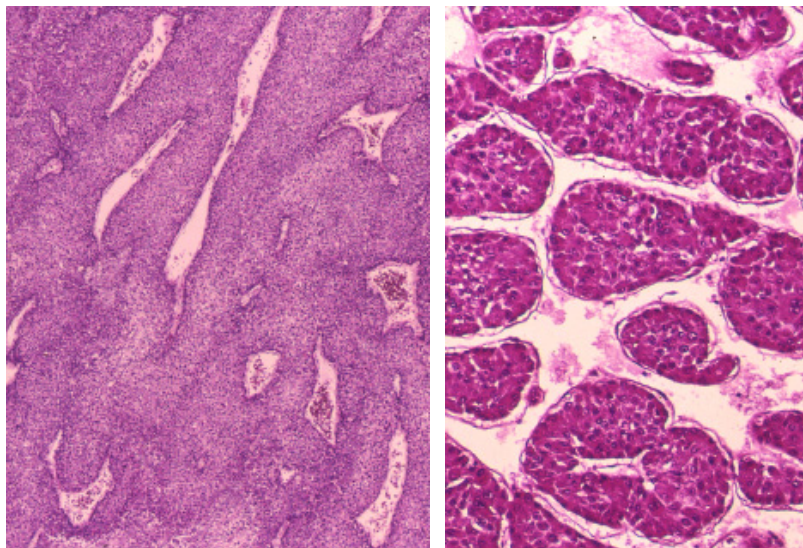


Fig. 7-15. Two patterns of hepatocellular carcinoma: the plate pattern (left) and the cord pattern (right).



tumors ranging over such a difference in the microstructural pattern. In the left, the carcinoma cells are forming plates. Although cells making up the tumor are stacked into a multilayer, the basic relation of the cell masses with the blood spaces is quite the same as in normal hepatic parenchyma. We call this the plate type tumor.

In the right, we can find a reversed pattern which corresponds to the papillary type of intraductal breast tumor. This may be called the cord type tumor. What we actually experience in most hepatocellular carcinomas is a mixture where the two patterns are co-existing in a tumor in various proportion. For some unknown reason, these two types have been described commonly as “trabecular type” in conventional classifications of hepatocellular carcinoma despite their apparently different patterns. It may be clear that one can apply without any modification the above quantification to these hepatocellular tumors.

#### **d) The pattern of zonal hepatocellular necrosis: Is the acinar theory tenable?**

It was shown in the above examples that in 2-D, 2-phasic patterns, there is an aspect in which the connectivity of phases plays a decisive role in the characterization of pattern. The different connectivity was measurable by “sweeping” the pictures with a test line where the number of tangents gave the estimates of total angles “subtended” by the interphasic border curves contained in an area, which then were correlated with the connectivity of phases. In reality, this methodology can be extended to the 3-D as proposed by DeHoff (1968). In this section, we show an application of this technique to the pattern analysis of zonal hepatocellular necrosis of the liver. The aim of this study is to examine whether or not the acinar theory of Rappaport is tenable, based on the shape and distribution of necrosis. The following is the summary of an attempt performed by Y. Nakamura and Takahashi (1996, 1998).

#### **Centrilobular necrosis in acute intoxication and chronic ischemia (Figs. 7-16, 7-17)**

The zonal necrosis of the liver implies a confluent injury of hepatocytes involving a certain anatomical zone. For example, sometimes at autopsy, we find in the liver a necrosis of hepatocytes extending in the centrilobular zone or Zone 3 of Rappaport’s acinus, although it remains a matter of question whether both of the zones are identical. Look at Fig. 7-16. This is a microphotograph of the autopsy liver from a patient dying of acute cresol intoxication on the third day. There are areas of coagulation necrosis (deeply stained), and clearly, these have a central vein at the center (C). On the other hand, there are areas in which hepatocytes are sustained without signs of necrosis, and these areas are connected as a whole, having portal tracts along the axis. On this pattern, it may be reasonable to say that this is a centrilobular necrosis.

Figure 7-17 presents another liver with centrilobular necrosis. This is from a patient who died of chronic cardiac failure due to aortic insufficiency. In this case there are necrotic areas, faintly stained but strongly congested, and their distribution seems to be essentially the same as in the foregoing case, having central veins along the congested axis (C). There is however a difference; the zone of parenchyma exempted from necrosis tends to have a rounded contour convex toward the necrotic

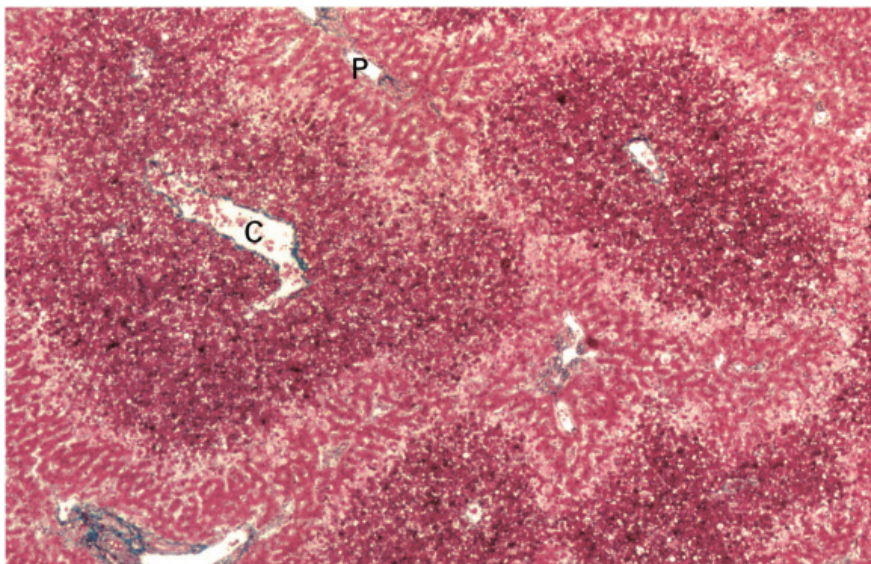


Fig. 7-16. Necrosis of liver from a patient dying in an acute stage of cresol intoxication. The hepatocytes in the central zone of lobules are uniformly destroyed as evidenced by the presence of central vein (C), the terminal hepatic venule, that is found at the center of necrotic area. The problem is whether, in geometric terms, the necrotic area sufficiently coincides with the form of what was defined as Zone 3 of Rappaport's acinus. Elastica-Goldner stain.

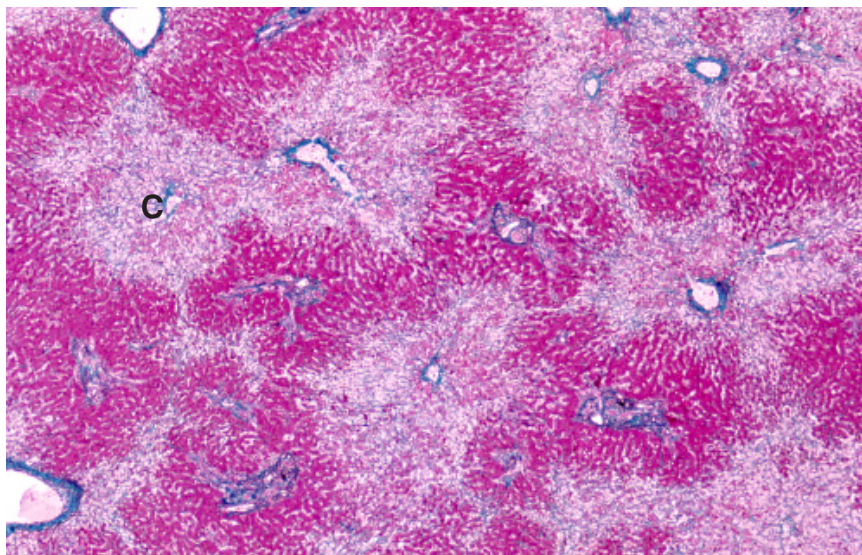


Fig. 7-17. Microscopic appearance of the liver in a patient who died of chronic congestive heart failure. Here too, necrosis is confined to the zone around the central vein (C). However, the shape of the necrotic areas is different from the cresol case, with the surviving parenchyma having a rounded contour because of nodular hepatocellular regeneration. Mallory's stain.

zone, perhaps because of nodular hepatocellular regeneration progressing during the long course of disease, for a matter of years. Here too, the areas that have survived are continuous, with terminal portal tracts positioned along their axis. In a patient in whom the liver has undergone severe ischemia but only for a terminal short period, the pattern of necrosis is quite the same as in the cresol cases.

### The acinar model (Fig. 7-18)

The acinar model of Rappaport, illustrated in Chapter 3 (Fig. 3-6), is to be briefly revisited, because it is the very pathogenesis of zonal hepatic necrosis due to intoxication or ischemia that this hypothesis was proposed to explain. Using the schema of Fig. 7-18, Rappaport maintained that the structural unit of the liver must be defined as what he called acinus, a clump of parenchyma centered with a terminal portal venule and flanked by terminal hepatic venules (THV; synonymous to the central veins). The model is so illustrated that an acinus may comprise three zones, Zones 1, 2 and 3, which Rappaport says are arranged in the order of blood irrigation from the periportal to areas around the THV. Thus, Zone 3 (painted in pink) is assigned a position least advantageous from a sustenance of hepatocytes point of view, irrigated with blood delivering the lowest density of oxygen and nutrients that were already consumed in Zones 1 and 2. Hence, hepatocytes in Zone 3 are said to be the most liable to necrosis, in case of ischemia as well as intoxication. The problem with this theory is that with regard to the distribution, Zone 3 was defined so that it may extend from around the

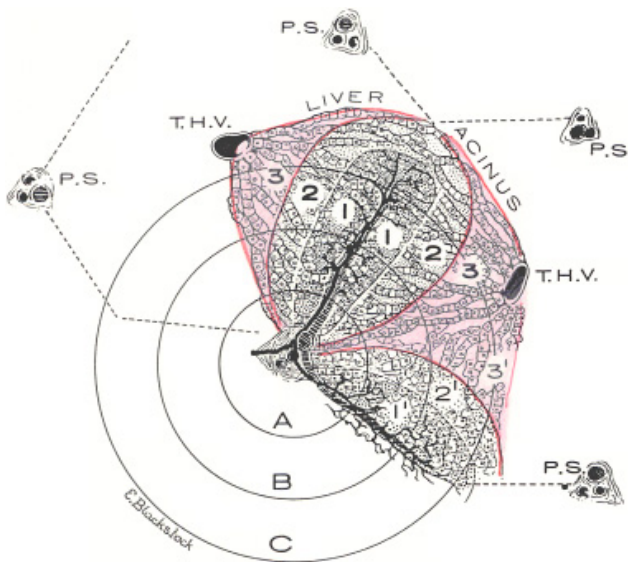


Fig. 7-18. The schema of an acinus given by Rappaport. The acinus is defined as a parenchymal clump that has a terminal portal venule at the center and is flanked by terminal hepatic venules (central veins). The parenchyma in an acinus is divided into Zones 1, 2 and 3. Of these, the hepatocytes in Zone 3 (pink), situated farthest apart from the afferent portal venule and consequently, are said to be most vulnerable to toxic or ischemic injuries. Reproduced from Rappaport *et al.* (1954): *Anat Rec* 119, pp. 11.

THV toward the portal tract in a “sleeve-like” fashion and reach the place where the three terminal portal venules come to join. This setting, particularly the assumption of “sleeves,” seems to have been necessary in devising this model because otherwise, an acinus would not be separable even in a liver with Zone 3 necrosis, making it impossible to define the acinus as an independent unit. Accordingly, what we have to do is to examine in livers with acute and uncomplicated zonal necrosis whether or not an acinus discloses itself as a parenchymal clump independent from the neighboring ones. If it really does, then inevitably it ensues from the model that each of the non-necrotic part of acini, Zones 1 and 2, be demarcated from the necrotic Zone 3 with a plane that is convex toward the exterior over the entire surface.

In the hepatic lesions shown in Figs. 7-16 and 7-17 we have a 2-phasic structure: the phase of necrosis and that of parenchyma that has survived. In the following, let us consider how we can examine the geometric nature of the curved interfaces extending between the two areas.

**The three types of surfaces (Fig. 7-19)**

In solid geometry, surfaces are classified into three types: convex, concave and saddle, as in the lower part of Fig. 7-19. In case of zonal hepatic necrosis, let us take

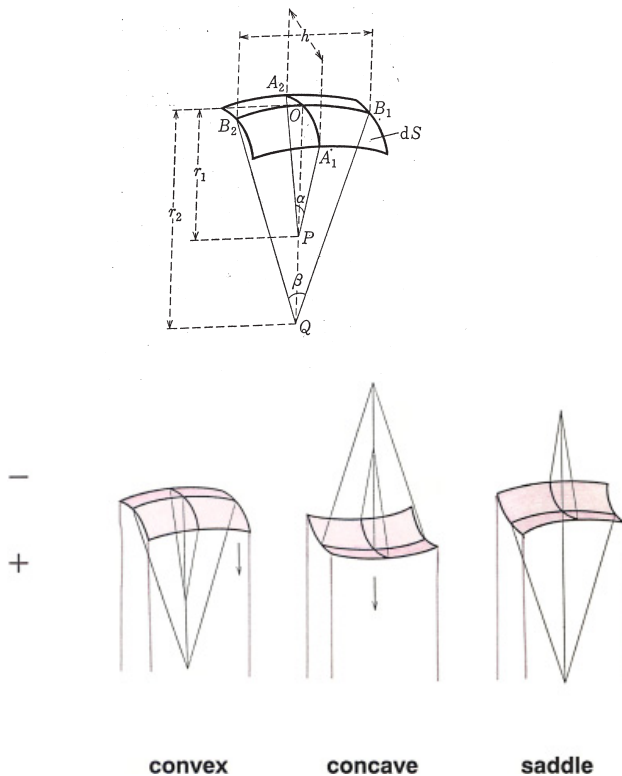


Fig. 7-19. (Upper) The curvature of surface at  $O$  is defined by a pair of principal radii  $r_1$  and  $r_2$ . (Lower) Three types of surfaces; convex, concave and saddle.

the surviving parenchyma as the structure of interest, which is enveloped by a continuous surface where the three types are considered to be co-existing as small patches assembled in mosaic. Assume as in the upper part of the figure, that we take a point  $O$  in a small patch of surface convex toward the outside. Then, a pair of principal radii of curvature  $r_1$  and  $r_2$ , the minimum and the maximum radii, are defined so that both of the radii extend from  $O$  along the normal toward the inside of parenchyma. When the surface is cut by a plane that contains the point  $O$  and the normal, the surface appears on the section as a curve convex toward the outside. In contrast, when  $O$  is taken at a concave surface as in the center of the lower figure, both of the principal radii of curvature turn out to be extending toward the outside. Here, if the parenchyma is cut with a plane containing one of the principal radii, and then with another plane containing the other, the surface will emerge in each of the sections as a curve concave toward outside. Besides, we have the third type of surface, the saddle surface, as in the right. In this type, one of the principal radii of curvature occurs toward the inside, while the other toward the outside of the parenchymal surface. In reality, in the interphasic membrane of zonal necrosis we are going to study, the saddle parts have the largest share in the total solid angle produced by the interphase (see below). Such being the circumstances, in a 2-D section, we cannot simply regard the convex interphasic curve as being a section of convex surface. Either, the concave curve in section does not always mean that it originates from a concave surface. Thus, it is unavoidable for us to study the matter from a 3-D geometry point of view.

### The solid angle $\omega$ (Fig. 7-20)

The problem we are going to approach is whether the surface of the parenchymal zone that has survived is convex toward the necrotic zone so uniformly as to make the liver unit definable in the form of Rappaport's acinus.

The surface curvature of the surviving areas can be defined with the solid angle  $\omega$ , as follows. This is an expansion into 3-D of the 2-D relation which we confirmed to hold between the curvature of an interphasic curve and the angle "subtended" by it (see Figs. 7-3a and 7-3b). In the left part of Fig. 7-20, a circle,  $r$  in radius, is shown. If

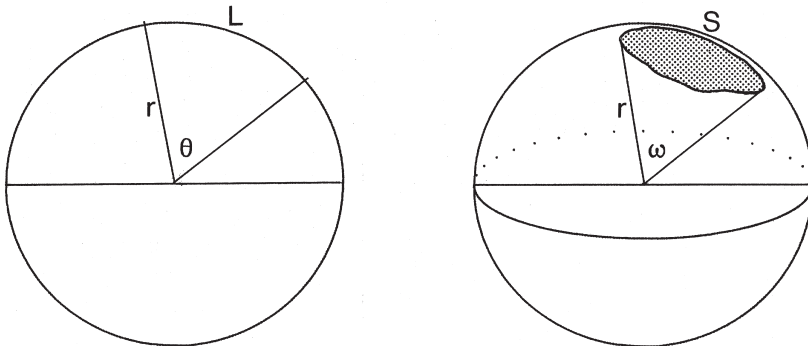


Fig. 7-20. The solid angle.



we take an arc  $L$  in length, the curvature of the arc is measured with the angle  $\theta$  it subtends at the center of the circle. Therefore

$$\theta = L/r.$$

The right part of the figure demonstrates its 3-D counterpart. Here we suppose a sphere of  $r$  in radius and a patch of surface on it with an area of  $S$ . Also here, the patch makes a curvature corresponding to the solid angle  $\omega$  it subtends at the center of the sphere. The angle is given, as in the case of 2-D, by

$$\omega = S/r^2.$$

For a whole sphere,  $\omega = 4\pi$  because  $S = 4\pi r^2$ . Thus the solid angle expresses the spread of space from a point in the form of cone.

### Generalization of $\omega$ into common surface (Fig. 7-21)

This is generalized into any small patch of surface taken arbitrarily from an object of complicated form. In general, in a minute patch  $dS$  arbitrarily cut from a non-spherical surface, for example from a spheroid shown in the left part of Fig. 7-21, the normals erected along the contour do not converge at a point. Still, we can define  $d\omega$  by replacing the normals with unitary vectors of the same direction which then are brought so as to converge at a point by parallel translation in the space, as in the right part of Fig. 7-21. The tips of the vectors come to enclose a transformed surface on a sphere, thus defining  $d\omega$ . This is a process of projecting  $dS$  from an arbitrary patch onto a spherical surface.

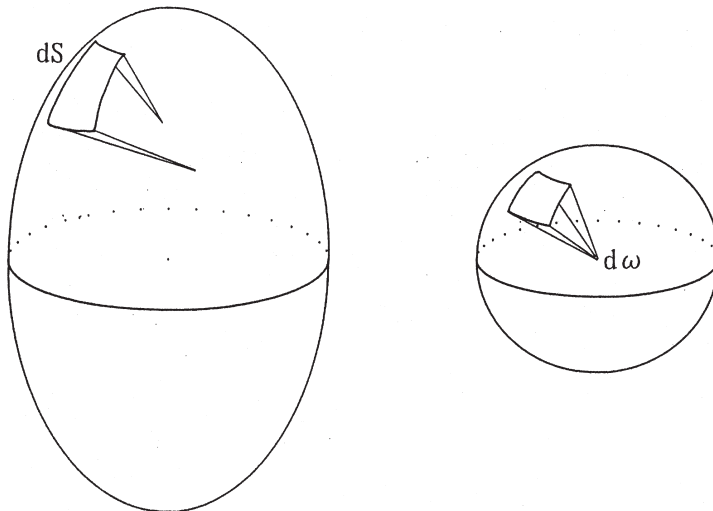


Fig. 7-21. Solid angle of a common surface.

Now we go back to Fig. 7-19 and imagine, as in the upper part of the figure, a small square patch in the surface of parenchymal zone with edges of  $h$  in length. If the normal at point  $O$  is  $OQ$ , we can define the radius of curvature for each of a pair of orthogonal arcs  $A_1A_2$  and  $B_1B_2$ , as  $r_1$  and  $r_2$ , respectively. It is known that as the arcs are turned around  $OQ$ , at the moment when  $r_1$  comes to be the smallest, then  $r_2$  is the largest. In other words, in this situation the curvature  $k_1$  of the arc  $A_1A_2$  is the largest, and  $k_2$  of  $B_1B_2$  is the smallest. The pair of curvatures  $k_1$  and  $k_2$  are called the principal curvatures of the surface at point  $O$ . Of course, if the angle subtended by  $A_1A_2$  is  $\alpha$ , and that by  $B_1B_2$  is  $\beta$ , then

$$k_1 = \alpha/h$$

$$k_2 = \beta/h.$$

According to principles of solid geometry, we can describe  $d\omega$  at an arbitrary point  $O$  in terms of Gaussian curvature  $K$ , as

$$d\omega = h^2K,$$

where

$$K = k_1 k_2 = 1/r_1 r_2.$$

In the definition of Gaussian curvature  $K$ , plus and minus  $rs$  are to be discriminated. Consider that the radius of curvature  $r$  is a vector originating at  $O$ . Let  $r$  be plus when the vector extends toward the inside of parenchyma, and minus when it extends toward the outside (see Fig. 7-19). Thus, both in convex and concave surfaces,  $\omega$  is plus because  $r_1 r_2$  is  $++$  in the former and  $--$  in the latter. In a saddle surface, however,  $\omega$  is minus on account of the combination  $+--$ .

### **$\omega$ in a constricted surface (Fig. 7-22)**

Let us consider in some 3-D surfaces what the solid angle  $\omega$  amounts to. As shown,  $\omega$  is  $+4\pi$  for a sphere. This holds true not only for a sphere but for any convex bodies like an ellipsoid, where  $\omega$  is constantly  $+4\pi$ .

Next, consider a shape of two spheres partially united as in the left part of Fig. 7-22. Because both the upper and lower spherical parts are larger than a hemisphere,  $\omega$  created by each of the convex parts can be described as  $[+2\pi + \alpha]$  and  $[+2\pi + \beta]$ , respectively ( $\alpha > 0$ ,  $\beta > 0$ ). However, there is a circumferential zone of saddle surface between the two spheres, which produces a minus  $\omega$  corresponding to  $-\alpha - \beta$ . Consequently, as a whole,  $[\alpha + \beta]$  is offset, and we have a total net  $\omega$  of  $+4\pi$ . No matter how many spheres are united into a single closed surface, the result is the same, leading to the conclusion that a closed surface of any complicated shape has a net solid angle of  $+4\pi$ , so long as there is no hole. A saddle surface occurs at places of transition between convexity and concavity, at a constriction, or as in the following, along the margin of hole.

The right part of Fig. 7-22 demonstrates the surface of an open pot. It has an

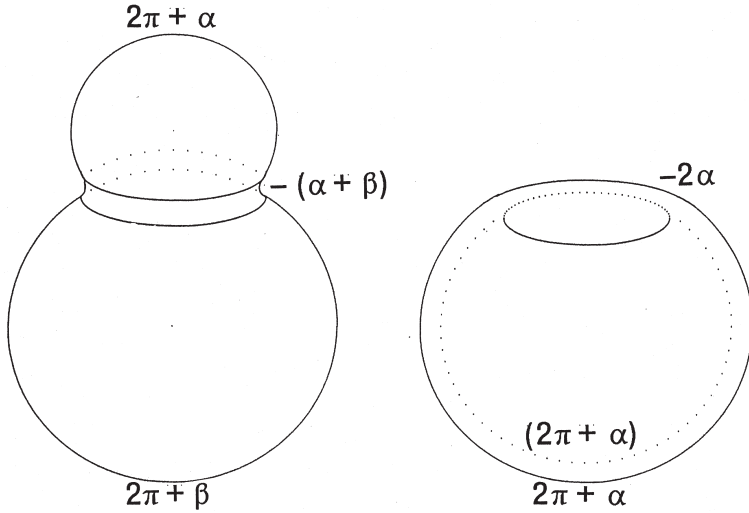


Fig. 7-22. Solid angle of constricted surfaces.

external convex surface which is larger than a hemisphere, with an  $\omega$  of  $2\pi + \alpha$ . The internal surface is entirely concave and therefore creates an  $\omega$  of  $2\pi + \alpha$  as well. Along the margin of opening there is a round belt of saddle surface and this creates a negative  $\omega$  of  $-2\alpha$ . Thus, here too, the total  $\omega$  amounts to  $2 \times (2\pi + \alpha) - 2\alpha = +4\pi$ , and we find the above conclusion holds true.

**$\omega$  in a torus: relevance to 3-D topology (Fig. 7-23)**

In the next place, let us consider a torus, as in Fig. 7-23 right. There is a belt of saddle along the inner surface of the hole, generating a negative  $\omega$  of  $-4\pi$ . It offsets an  $\omega$  of  $+4\pi$  which, if there were no hole, would have been generated by the closed surface.

This will be understood by making a simple ideal experiment. We consider a torus with a circular hole of  $r$  in radius, as in the figure. Here suppose that we close the hole by putting a sphere which also has a radius of  $r$ . In this situation,  $\omega$  for the whole body must be  $+4\pi$ , because there is no longer a hole. Next, assume that we take away the sphere and restore to the original state of torus. The sphere that was separated from the body has an angle of  $+4\pi$ , and through this procedure no other surface was added or subtracted, which is equivalent to saying that no  $\omega$  was added or subtracted. Which shows that for the torus,  $\omega$  is 0 because a solid angle of  $+4\pi$  was taken away from a body of  $+4\pi$ .

Thus,  $\omega = 0$  for a torus with one hole. If a surface contains two holes, then the total solid angle amounts to

$$\omega = +4\pi + 2(-4\pi) = -4\pi.$$

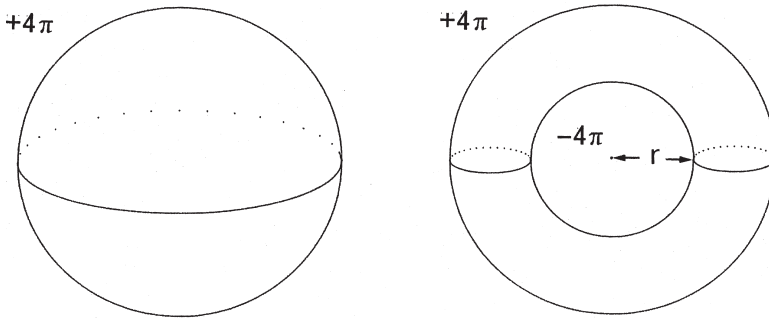


Fig. 7-23. Solid angle of a torus (right).

This can be generalized into

$$\omega = 4\pi(m - c), \quad (7-3)$$

where  $\omega$  is the total angle generated in the space,  $m$  is the number of closed surfaces in the space and  $c$ , the number of holes. A closed surface having several holes is nothing but a membrane, or an interface, covering a 3-D network. An example of this sort of surface was already found in cirrhotic livers where the interphase between the nodular and interstitial phases presents as a continuous surface with many holes (see Fig. 6-9). In the above equation, one can see how closely the solid angle generated by surfaces correlates with the connectivity of network the surfaces are covering.

### 3-D tangent counting by sweeping the space (Figs. 7-24, 7-25)

Here too, we can apply tangent counting method to the estimation of total solid angles contained in a space (DeHoff, 1968). The principle is the same as we have seen in 2-D pictures, where angles “subtended” by linear boundaries were estimated by tangent counting, i.e., sweeping the sample area with a line. In dealing with the problem of curved surfaces, however, sweeping has to be done in the 3-D, requiring to “sweep” by translating a plane through the space. This is a procedure of scanning the space with serial sections. In the schema of Fig. 7-24, we assume that a rectangular space contains surfaces of various shape. Imagine that we slowly move the ceiling ABCD of the space downward by parallel translation, thus sweeping the space. Then the plane comes to touch the surfaces at various points, each time generating a tangent.

Statistically, a tangent occurs at every  $+2\pi$  of solid angle at convexity as well as at concavity, while at a saddle, it occurs at an angle of  $-2\pi$ . This may be understood in Fig. 7-25 where, in the left, sweeping of sphere generates two tangents, each corresponding to an angle of  $+2\pi$ , while in a torus, two tangents add at the saddle, each producing  $-2\pi$ . Therefore if, in a sample space containing a sufficient amount of curving interfaces, we count the number  $n$  of tangents and at the same time discriminate among the tangents occurring at convex, concave and saddle surfaces separately, the total  $\omega$  generated by each of the three different surfaces is given by

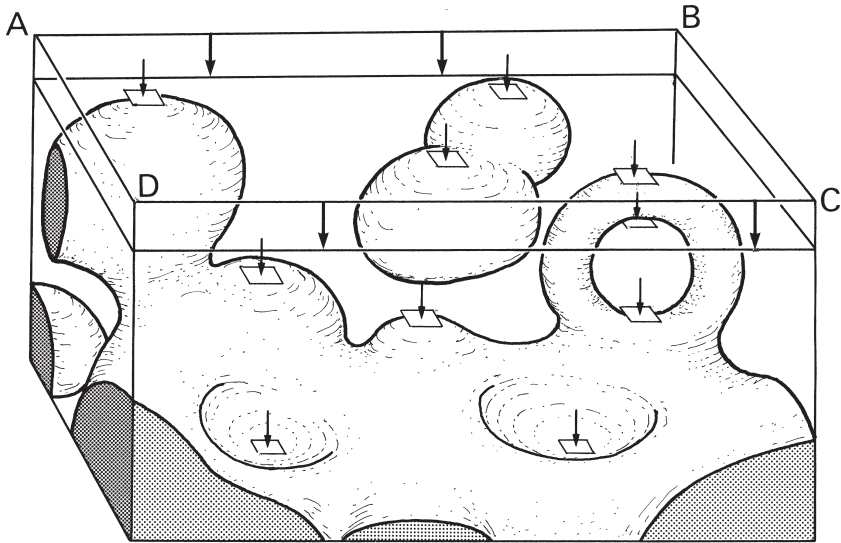


Fig. 7-24. A schema of 3-D tangent counting. Imagine a rectangular space containing surfaces of various shape. Then consider that the ceiling ABCD of the rectangle is moved downward by parallel translation. While moving, the plane comes to touch the surfaces at various points (small arrows), each time generating a tangent. Reproduced from Nakamura and Takahashi: *Tohoku J Exp Med* (1998) 184: pp. 217.

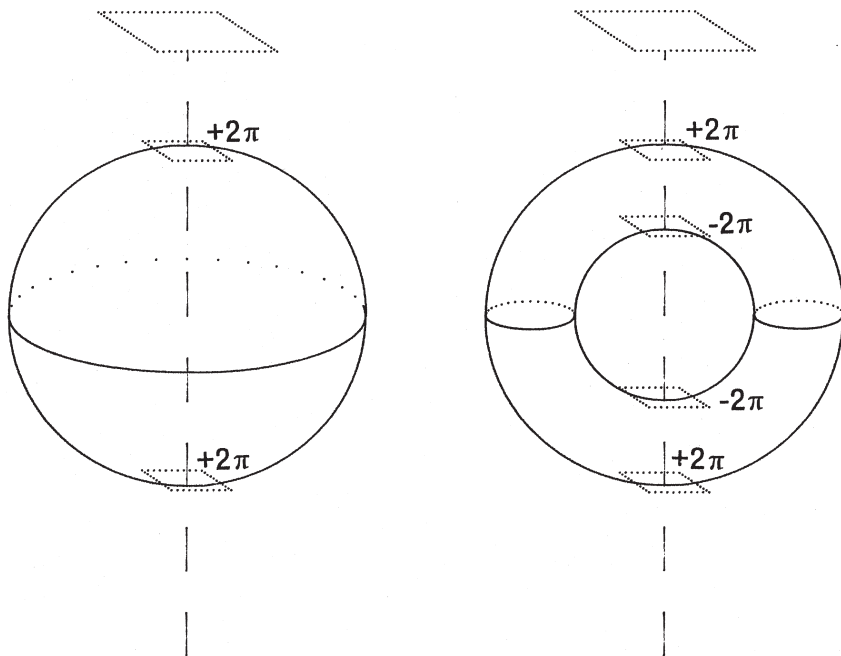


Fig. 7-25. Sweeping: the cases of sphere and torus.



$$\omega(\text{cvx}) = +2\pi n(\text{cvx})$$

$$\omega(\text{ccv}) = +2\pi n(\text{ccv})$$

$$\omega(\text{sdl}) = -2\pi n(\text{sdl})$$

where  $n(\text{cvx})$ ,  $n(\text{ccv})$  and  $n(\text{sdl})$  denote the number of tangents generated at convex, concave and saddle parts of interface. Thus the total  $\omega$  contained in the space amounts to

$$\omega = 2\pi \{n(\text{cvx}) + n(\text{ccv}) - n(\text{sdl})\}.$$

### Tangent counting on serial sections (Fig. 7-26)

Three-D tangent counting by sweeping a sample volume was performed on serial sections of livers with zonal necrosis. As usual, serial 2-D images of the interphasic border between the necrotic and surviving zones were inputted consecutively into a computer, together with the portal and hepatic veins. While scanning the sampled



Fig. 7-26. Counting of 3-D tangents between the test plane and the interphasic surfaces in the liver with hepatocellular necrosis due to cresol intoxication. Counting is performed upon the computer display as 3-D reconstruction advances, as in the figure where the test plane for sweeping is the display itself that is moved in the direction vertical to the section. The green wireframes express the interphasic borders between the necrotic and surviving areas. Red are the portal, and blue are the hepatic veins. Reconstruction was designed so as to progress at a large between-steps interval of  $16 \mu\text{m}$ . In the figure one can recognize several points where a tangent has occurred, for example at A and B. One can recognize that at B, both of the two tangents were generated at a saddle plane. Whether the surface is convex or concave at a point like A can be determined by observing how the nearby surface changes with the advancement of reconstruction. Reproduced from Nakamura and Takahashi: *Tohoku J Exp Med* (1998) 184: pp. 227.

volume in a computer display by advancing reconstruction, the places where a tangent occurs could easily be recognized. Whether a tangent arose at a convex, concave or saddle part of interphase was judged by comparing the nearby contour lines, as shown in Fig. 7-26, where a tangent (A) was confirmed arising at convex surface, and two (B) at saddle. Whether the surface like A corresponds to a mountain top or a bottom of depression could be determined by observing what a 3-D form develops in the surroundings as reconstruction progresses.

### The result of 3-D tangent counting (Table 7-1)

The result of measurement is listed in Table 7-1. Studied were autopsy livers from five patients. Cases 1 and 2 were selected to represent livers with acute necrosis, both from patients dying of cresol intoxication, 60 and 90 hours after ingestion, respectively. The other three patients had suffered from chronic cardiac failure including cardiac amyloidosis (Case 3), primary pulmonary hypertension with right ventricular failure (Case 4) and aortic regurgitation (Case 5), in all of whom zonal hepatocellular injuries were considered attributable to chronic ischemia and/or congestion. Signs of cardiac failure had lasted 2 years and 8 months (Case 3), 10 months (Case 4) and 4 years and 3 months (Case 5).

Here, the numbers of tangents,  $n(ccv)$ ,  $n(cvx)$  and  $n(sdl)$ , can directly be translated into the share of the corresponding solid angles  $\omega(ccv)$ ,  $\omega(cvx)$  and  $\omega(sdl)$  in the total solid angle contained in the sampled volume, because, as shown, the value of  $\omega$  is proportional to the number of tangents. First of all, it is noteworthy that in the acute cases, the share of tangent number at convex surface was only 6% and 3%, while the share at concave surface was as high as 25% and 22%. In contrast, in the chronic cases, this ratio is reversed, with the number of tangents occurring at the convex surface exceeding those at the concave sites. Why, with time, the pattern has changed in such a way may be clear. Within a matter of years, with recurrent bouts of necrosis followed by regeneration of hepatocytes that survived, the pattern of lesion has gradually come to undergo secondary transformation due to nodular hepatocellular hyperplasia and collapse of necrotic areas. Accordingly, in examining whether the acinar theory can really hold as an anatomical and functional unit, it is crucial to study the

Table 7-1. The result of 3-D tangent counting in 5 livers with zonal hepatocellular injuries.

	Liver weight (g)	Sample volume(mm <sup>3</sup> )	Number of tangents			$\omega$ in sample	Total genus
			n(ccv)	n(cvx)	n(sdl)		
<b>Acute</b>							
Case 1	1,180	31.0	59(25%)	14(6%)	169(69%)	-192 $\pi$	1.83 $\times 10^6$
Case 2	990	17.5	26(22%)	4(3%)	91(75%)	-122 $\pi$	1.73 $\times 10^6$
<b>Chronic</b>							
Case 3	830	25.6	16(4%)	89(24%)	222(70%)	-234 $\pi$	1.90 $\times 10^6$
Case 4	1,140	29.2	23(4%)	158(27%)	415(70%)	-468 $\pi$	4.57 $\times 10^6$
Case 5	946	21.7	23(4%)	136(22%)	467(75%)	-616 $\pi$	6.71 $\times 10^6$

pattern of liver lesion fresh from injury. In chronic cases, we find the original shape of injury modified with additional and secondary changes, where the liver has already started advancing toward cirrhosis. In the acute cases of cresol intoxication, there remains no doubt about the shape of parenchyma surviving zonal necrosis. The surviving areas are cast into a shape where the surface concave toward the necrotic zone far exceeds the convex surface. Clearly, this must be quite the opposite to what has been maintained by those supporting the acinar concept.

### 3-D structure of acute zonal necrosis (Fig. 7-27)

Figure 7-27 presents a 3-D reconstruction of the liver in acute cresol intoxication (Case 1). Clearly, the surface of the surviving parenchyma, presenting as green masses, comprises concave, convex and saddle parts but concavity is likely to be more common than convexity. At no place, necrosis (void) is extending as a sleeve-like flap reaching the portal tract. The parenchymal areas that survived necrosis are only uniformly surrounding the segments of terminal portal veins (pink), without being separated into “acini” demarcated from each other. These are findings least expectable from the acinar model. At several places, one can find connections between adjacent areas of necrosis, disclosing that the overall shape of necrosis, and also that of the surviving parenchyma, are a loose 3-D network.

Thus, the geometry of the interface between the necrotic and surviving phases is a 3-D network. As shown in Chapters 5 and 6, how densely the network is knit can be given by the number of holes (meshes) it contains. This is given by the value of  $c$  in

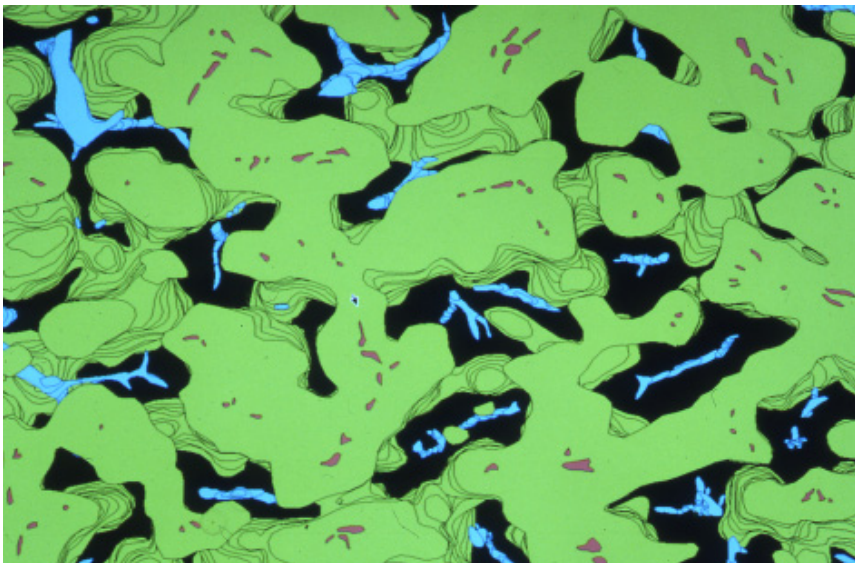


Fig. 7-27. Computer-assisted 3-D reconstruction of the liver with acute injury due to cresol intoxication. The viable parenchyma is painted in green, with the necrotic zones left as void spaces. When viewed from the parenchymal side, the interphasic surface seems mostly to be concave, a situation not compatible with the model proposed in the form of acinar schema. Reproduced from Nakamura and Takahashi: *Tohoku J Exp Med* (1998) 184: pp. 227.

equation (7-3), which corresponds to the genus given in the descriptions in the foregoing chapter (see Fig. 6-18). Assuming that the specific gravity of the liver is 1.0, the total number of meshes contained in the liver was calculated based on the ratio of the sampling volume to the whole liver. As in Table 7-1, the total number of genus proved to be within a comparatively narrow range from 1.7 to  $1.9 \times 10^6$  in both of the cresol cases. In the three cases with chronic heart failure, the number was shown comparatively larger in Cases 4 and 5. In Case 5 where the disease lasted as long as four years and 3 months, the network proved to be so dense as to have a genus number of  $6.71 \times 10^6$ . It is interesting that this is a value close to the number of holes in chronic hepatitis, where the total genus number ( $p_1$ ) was estimated at  $6.10 \times 10^6$ , showing that the two livers share a skeleton that is topologically quite similar (Fig. 6-21). Perhaps there may be some reason for the hepatic microvasculature to deliver a network skeleton of this density, but this belongs to what is to be studied in the future.

After all, the 3-D distribution and shape of acute zonal necrosis turned out to be something quite different from what one would expect to see based on the acinar model. Nowhere "sleeve-like" projection of necrosis was confirmed extending from around the THVs and reaching the portal venule where three terminal portal twigs come to join. The surviving parenchyma was being covered by an interphase where concavity toward necrosis was overwhelmingly predominant over convex surface. All these are not consistent in any respect with the pattern of necrosis which has to be induced from the acinar model.

Then, what a unitary structure of the liver one should assume? Our conclusion is that from a 3-D structure point of view, any unitary concept is not necessary in understanding the structure-function correlation in the liver. We think, the principle of the hepatic microstructure lies in the isodistance between the terminal afferent and efferent vessels, which is realized in the liver in a typical and perfect way compared with other organs.

## The Adequate Classification of Form in Pathology

We pathologists are engaged in making diagnosis of diseases by examining the form of cells, tissues and organs microscopically and macroscopically. During the past 20 years, various technique including immunohistochemistry and molecular biology has been introduced, greatly contributing to improved accuracy of diagnosis. To the credit of these methods is *reproducibility* with which we have become capable to confirm the presence of specific molecules in the cells or tissues. But even now, morphology, the study of form, remains to be the core of what pathologists are required to perform, train themselves in, and develop. The importance of morphology in clinical pathology will not be reduced even in the future. However, pathologists over the world do not always appear to have managed to improve the accuracy and reproducibility of morphological diagnosis.

### Normal, cancer and intermediate cells (Fig. 8-1)

Look at Fig. 8-1. Imagine that the cell in the upper left part of the figure is a normal cell, and that in the right upper, a carcinoma cell. The difference is definable in purely morphological terms: a carcinoma cell is characterized with what is called a severe cellular atypia. However, we so often experience cells with a form quite intermediate between the normal and carcinoma, as shown in the lower part of the figure. Already in the foregoing chapters we have seen such quasi-carcinoma cells in adenomas of the colon and stomach, and in dysplasia of the hepatohilar bile ducts. When faced this sort of cells, sometimes pathologists may waver in determining the diagnosis, and visit their colleagues to discuss. It often happens however that they all fail to reach a conclusion, with different opinions not tending to converge. What should be done on such an occasion? Pathologists then seem likely to think that it may be the one who has the largest experience that could deliver the most correct diagnosis.

I do not think this tradition should be changed. We have to bear social responsibilities, and often it is necessary to have our diagnosis strengthened with experience as much as possible. Only from a scientific viewpoint, however, there may be problems if this sort of decision-making covers the entire aspect of pathological research. Science requires a decision to be a reproducible one, and reproducibility cannot be ensured by personal experience alone. I have to confess that even after having been engaged for many years in the practice of diagnostic pathology, it remains beyond my power to reproduce 100% of diagnosis I made in the past. Much less, among different pathologists who have their own standard of judgment based upon their experience, and it seems almost a daunting task to bring their personal standards to a common



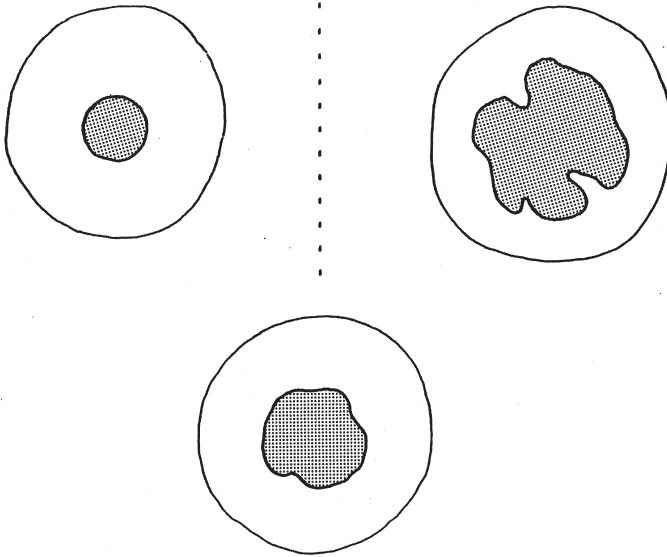


Fig. 8-1. The difference of cancer cell (upper right) from normal cell (upper left) is apparent, but pathologists often encounter cells that assume quite an intermediate form (lower).

level. How to find a solution? Obviously, this requires us to introduce some methods with which to deal with various forms in an objective way. And objectivity can be attained only by introducing quantitative way of thinking into the domain of morphology.

In the following, attempts will be shown to establish a reproducible classification of cellular or tissue changes, mostly led by R. Chiba of our team. Making a morphological diagnosis of an object is, after all, equivalent to deciding, into which of the categories, the object in question is to be classified.

### What is classifiability? (Fig. 8-2)

A question has to be answered. Whether or not the disease in question is classifiable at all, and if it is, how to classify. Let us assume in Fig. 8-2 that a large number of subjects were examined for a certain property  $x$ , for example, the mean blood pressure. Classification of subjects into two or more groups with regard to  $x$  may be justified when, and only when, we have a multimodal distribution as in the upper figure. If tendency to separate did not prove to exist as in the lower, what one can do is only to divide the population in an arbitrary way: at the peak into two groups (1), or into three groups (2) at the levels of plus and minus standard deviation, and so forth. Apparently, this means that the population has been non-classifiable in the first place. Although classification has been and remains the most widely used method of study in pathology, this question of classifiability has never been examined.

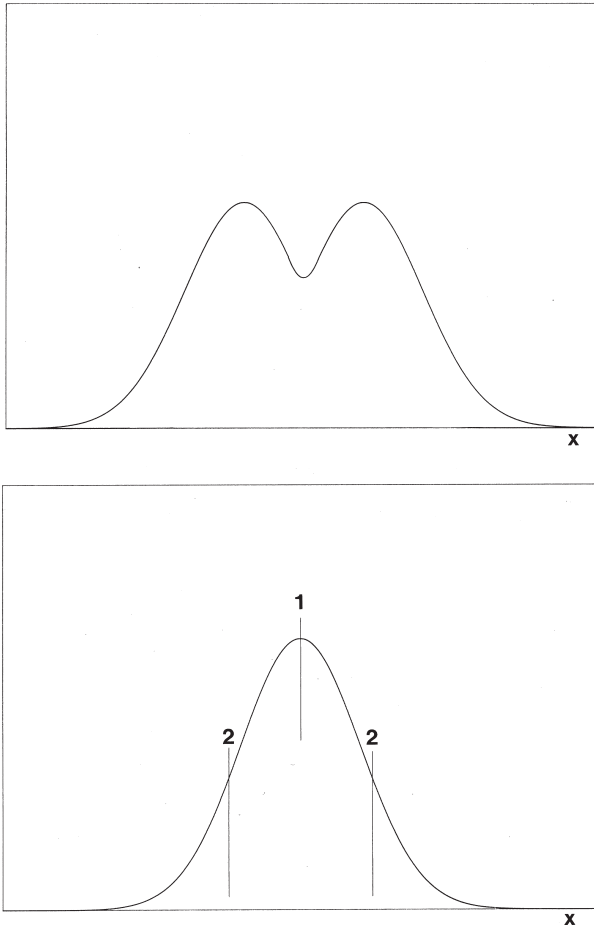


Fig. 8-2. The classifiability with regard to a single property  $x$ . The subjects are classifiable into groups when, and only when, multimodal distribution was proved as in the upper figure. When the distribution fails to separate as in the lower, the subjects have to be assumed non-classifiable. Reproduced from Chiba and Takahashi: *Pathol Int* (1994) 44: pp. 672.

### a) Adequate classification of liver cirrhosis

#### Two cirrhotoses with different patterns (Fig. 8-3)

Let us begin with the computerized classification of cirrhosis performed by Chiba and Takahashi (1994a,b). Of the two cirrhotic livers exhibited in Fig. 8-3, the left corresponds to Type A and the right to Type B, according to Nagayo's classification (1914) widely used in Japan. In Gall's classification (1960), the former may be expressed as the postnecrotic and the latter, the posthepatitic type.

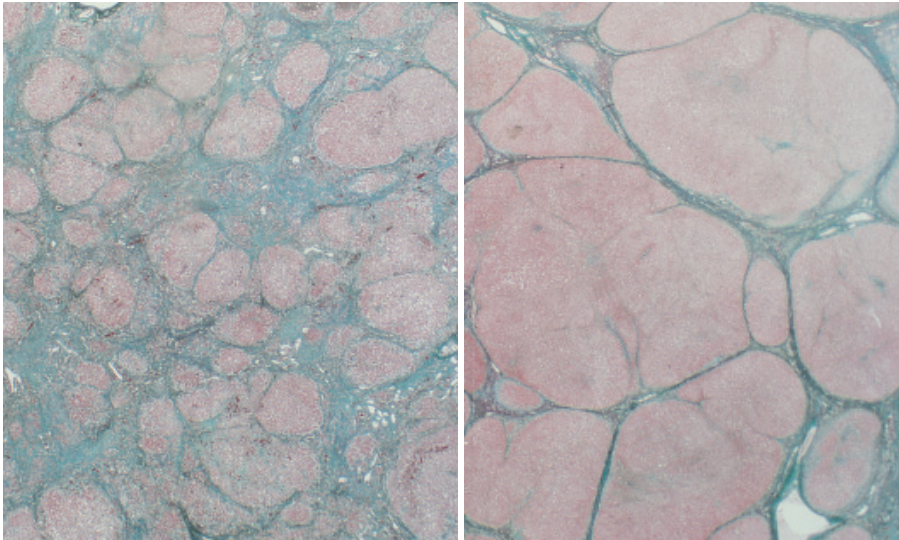


Fig. 8-3. Two cases of cirrhosis with different microscopic pattern. Left: Type A of Nagayo's classification, or postnecrotic type of Gall's, with small nodules and broad interstitial zones. Right: Type B, or posthepatic type, with coarse nodules and thin, membranous interstitium. Elastica-Goldner stain.

### The rationale of classification involving multiple factors of form (Fig. 8-4)

One of the difficulties inherent in the examination of classifiability for lesions like cirrhosis is that the microscopic pattern usually comprises several factors of form instead of a single factor  $x$ . As will be shown, in our attempt at computerized classification of cirrhosis, the morphological feature in each case was reduced into a combination of four parameter values. In another series of attempts at classifying carcinomatous and dysplastic cells, we used twelve parameters. Figure 8-4 is a schema explaining the rationale for multiparameter classification, taking as an example the simplest case of two parameters.

Suppose we have five patients, in whom we measured features  $x$  and  $y$ . The result is depicted in a scatter diagram in the left part of the figure. If we are dealing with cirrhotic livers, then for example  $x$  could be the mean radius of nodules and  $y$ , the mean thickness of the interstitial septa. At a glance, we immediately realize that in the figure, Cases 1, 2 and 3 form a group or a cluster, whereas Cases 4 and 5 form another. What makes us recognize this grouping? To conclude, it is the difference in the distances among the five cases.

Imagine that the distance was calculated for all possible pairs among the cases in a "round robin." Here we have five cases and consequently, there are ( ${}_5C_2=$ ) 10 pairs. The Euclidean distance between Case  $i$  and Case  $j$ , if written as  $d(i, j)$ , is defined on the  $xy$ -plane as

$$d^2(i, j) = (x_i - x_j)^2 + (y_i - y_j)^2.$$

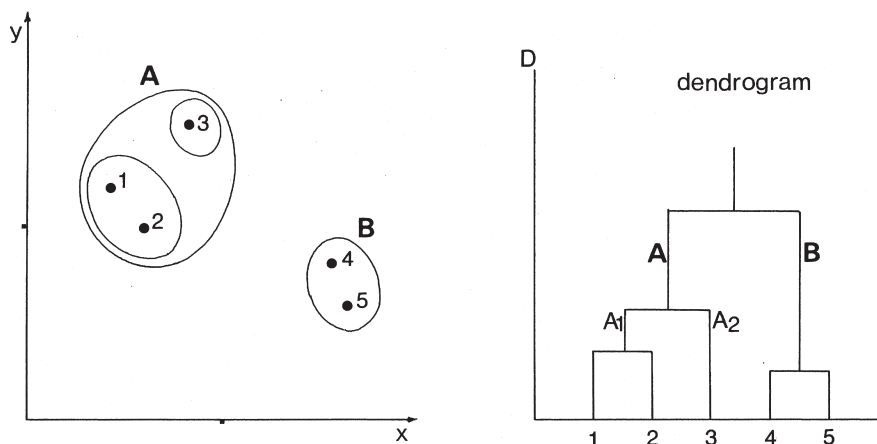


Fig. 8-4. Rationale of cluster analysis for the classification involving multiple factors of form. The left figure presents a simple example of five cases and with two factors  $x$  and  $y$ . It is clear by inspection that there are two clusters [Cases 1, 2, 3] and [Cases 4, 5]. This grouping is defined by the between-cases distances (see the text). The right figure is the dendrogram drawn based on the distance analysis. Reproduced from Chiba and Takahashi: *Pathol Int* (1994) 44: pp. 672.

In the figure, one may realize instantly that the distance between the pair of Cases 4 and 5 is the smallest among the 10 pairs, which means that in this pair, one can find the highest similarity. Accordingly, we put these two cases together into Cluster [4, 5]. Next, we compare among the other pairs and confirm the pair of Cases 1 and 2 to be the next nearest, and define Cluster [1, 2]. Then we examine which of the two clusters is nearer to Case 3, and find that Cluster [1, 2] is the case. Thus, finally, the five cases come to be categorized into either two clusters [1, 2, 3] and [4, 5], or three clusters [1, 2], [3] and [4, 5]. The process is visualized in a dendrogram in the right part of the figure. This is the basic principle of cluster analysis, a technique of multivariate statistics, which allows us to determine an order of hierarchy within a large population according to the grade of similarity among the individuals. In the attempt at quantifying the pattern of cirrhosis, a set of four parameters  $x$ ,  $y$ ,  $z$  and  $u$  were used in expressing the form. Therefore the between-individuals difference was defined as a four-dimensional Euclidean distance, as

$$d^2(i, j) = (x_i - x_j)^2 + (y_i - y_j)^2 + (z_i - z_j)^2 + (u_i - u_j)^2.$$

Of course, a space of more than three dimensions is no longer visible, but the distance is definable in whatever dimensions, at least in mathematical terms. Here it only has to be added that in calculating the between-individuals distance  $d(i, j)$  in cirrhosis, standardization is necessary for each parameter with the corresponding variance  $\sigma$ , as

$$d^2(i, j) = (x_i - x_j)^2/\sigma_x^2 + (y_i - y_j)^2/\sigma_y^2 + (z_i - z_j)^2/\sigma_z^2 + (u_i - u_j)^2/\sigma_u^2.$$

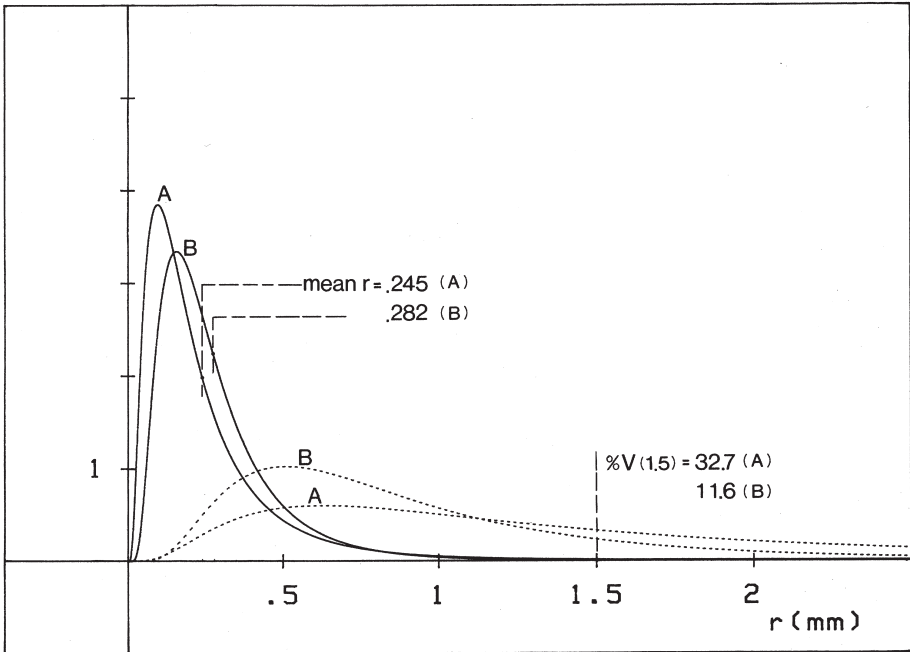
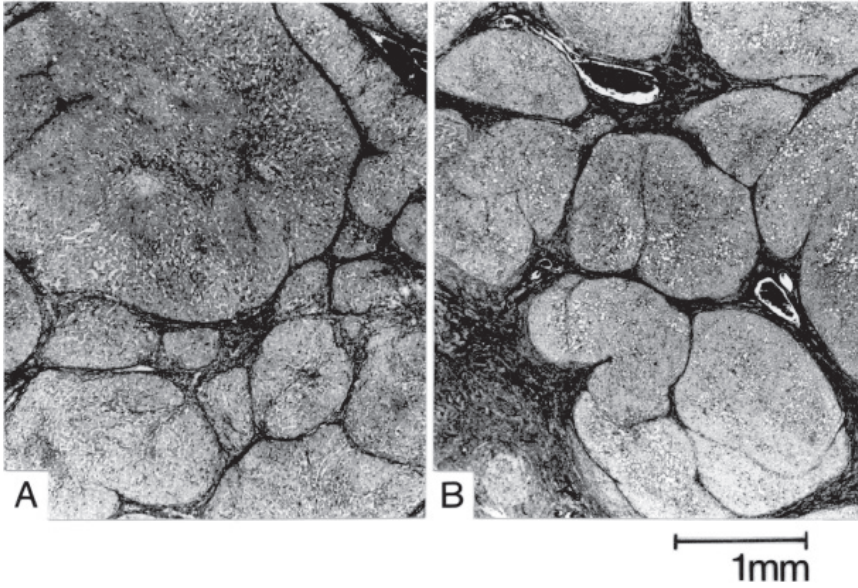


Fig. 8-5. Numerical and volume distribution of nodules in two cirrheses, Cases A and B. The mean radius in Case B is larger than in Case A, but the numerical curves cross, and in the larger range of  $r$ , Case A comes higher. This brings about a difference in %V(1.5) which is larger in Case A. The difference in the pattern between Cases A and B is shown in the upper microphotographs, where Case A gives an impression of cirrhosis coarser than Case B. Reproduced from Chiba and Takahashi: *Pathol Int* (1994) 44: pp. 666.



Of the various methods for defining the distance between clusters, we employed the Ward method (1963) which gave the clearest separation in comparison with other methods of clustering. Computation was performed using a mainframe.

### Parameters employed for characterization of cirrhosis (Table 8-1, Fig. 8-5)

In this study, the morphological feature of cirrhotic liver was reduced to four quantities listed in Table 8-1. A total of 70 cirrhotic livers were entered.

The form of cirrhosis was assimilated to the geometric model of dispersed spheres already explained in Chapter 2 where the islets of Langerhans were studied. There, islets were assumed to spheres of various radius  $r$  dispersed in the space. While Weibull distribution was assumed for the radius of islets, this time the radius  $r$  of cirrhotic nodules was considered to follow logarithmic normal distribution. In cirrhosis too, as schematized in Chapter 2 (Fig. 2-6), nodules appear in a section as circles of various dimension. If a test line of sufficient length is randomly drawn on the section, it traverses nodules and generates chords of different lengths  $\lambda$ . The length  $\lambda$  was measured under microscope for about 200 consecutive chords. For the rationale of stereological method, see the original articles.

Of the parameters,  $\%V(1.5)$  means the volume % of nodules larger than 1.5 mm in radius. In Fig. 8-5, volume distribution of nodules (the dotted curves) in two cirrhotoses, Cases A and B, is added to the numerical distribution (the solid curves). The mean  $r$  is 0.245 mm in A and 0.282 mm in B. However, the numerical distribution curves cross, showing that although the mean  $r$  is larger in Case B, the curve of Case A trails over Case B in the larger range of  $r$ . This brings about a clearer difference between the two cirrhotoses in the volume distribution as shown by  $\%V(1.5)$ . It expresses the share of area under the volume distribution curve in the range of  $r \geq 1.5$  mm, which in Case A is calculated at 32.7%, while it remains 11.6% in Case B. Roughly speaking, a coarsely nodular pattern is represented by a curve trailing far toward the larger  $r$ , giving a higher  $\%V(1.5)$ ; there is no need for the mean  $r$  also to be large. In fact, the pattern of Case A gives an impression of cirrhosis coarser than Case B, as shown in the b & w pictures.

The thickness of the interstitium  $D_s$  was defined as a 3-D quantity. For this, the plate model used to determine the thickness of alveolar septa was available without any modification. The model was introduced in Chapter 2 (see Fig. 2-26).

In some cirrhotoses, nodules were seemingly well separated in section, while in others they were mutually aggregated. Thus, the degree of nodular separation was

Table 8-1. The four parameters employed for the cluster analysis of cirrhosis.  $\%V(1.5)$ : the volume % to the total of nodules larger than 1.5mm in radius, serving as a parameter of nodular coarseness.  $D_s$ : the thickness of interstitium defined as a 3-D quantity.

---

mean $r$ :	the mean radius of nodules as assimilated to spheres of various dimension
$\%V(1.5)$ :	parameter of nodular coarseness, defined by the volume % of nodules larger than 1.5mm in $r$ to the total nodular volume
$D_s$ :	the mean 3-D thickness of the interstitium.
$\rho_\theta$ :	the grade of nodular separation ( $-1.0 \leq \rho_\theta \leq +1.0$ )

---

considered to be an important factor of form. To this,  $\rho_\theta$  defined in Chapter 7 as the index of nodular separation was directly applicable.

**Cluster analysis of 70 cirrhotoses (Figs. 8-6, 8-7, Table 8-2)**

The result of cluster analysis for 70 cirrhotic livers is exhibited in the dendrogram of Fig. 8-6. This is the optimal clustering that satisfies the condition defined above. Of course, the classification thus brought about by computer is reproducible. It is

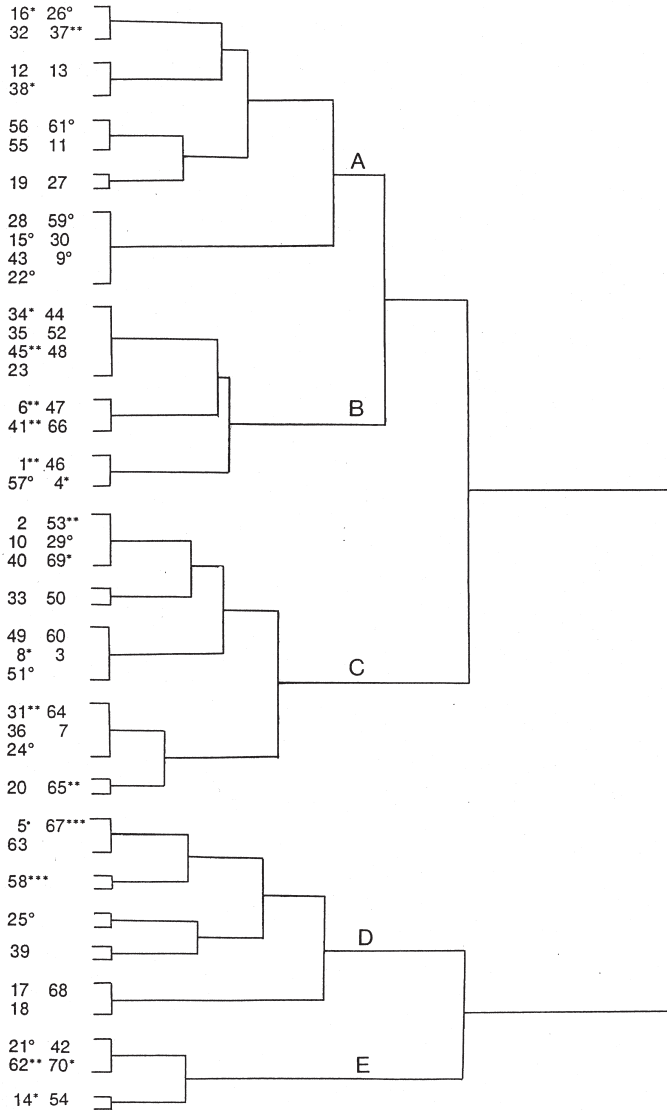


Fig. 8-6. The dendrogram obtained by cluster analysis of 70 cirrhotoses. Five clusters, A, B, C, D and E proved to form. Reproduced from Chiba and Takahashi: *Pathol Int* (1994) 44: pp. 676.

based only upon the form of the objects. In the above process, the objects have assembled or divided themselves only according to their form. We think this can be called the natural classification, discriminating from the conventional, artificial classification.

Five clusters, A, B, C, D and E were obtained. Mean parameter values for each cluster are listed in Table 8-2. Shown in Fig. 8-7 are the microscopic appearances, each of which seems representing the cluster it belongs to, with the parameter values closest to the cluster mean. In Cluster A, the pattern is characterized by membranous interstitium that is the thinnest of all, a mean nodular radius that is also small, and a remarkable fineness of pattern as expressed by a small %V(1.5). A moderately high  $\rho_\theta$  implies that the nodules are well separated. The pattern may be a typical feature of nutritional (or septal) cirrhosis of Gall's classification. Cluster B also has relatively thin septa, while in this cluster the nodules are much larger as revealed by both the mean  $r$  and %V(1.5). This combination of coarse nodules and thin septa is considered to reflect the pattern of posthepatic cirrhosis of Gall, or Type B cirrhosis of Nagayo. In Cluster C, the nodules are small with both the mean  $r$  and %V(1.5) being the lowest of the five clusters, while the septa are thick and the nodules are well separated. Apparently, this describes the pattern of postnecrotic type, or Nagayo's Type A. Cluster D consists of cases where both the mean  $r$  and %V(1.5) are extraordinarily large, representing cases with extremely advanced coarsening of nodules. Cluster E is similar to Cluster A in mean  $r$ , but it has the largest %V(1.5) and, most uniquely, a value of  $\rho_\theta$  which is the smallest of the five clusters. In other words, this is a type with incomplete separation of nodules, corresponding to what was designated as quasi-B type in the classification of Miyake (1960), a modification of Nagayo's.

In examining the result of computer-assisted classification, we were struck by the close resemblance of the result to the outline of Gall's classification. It is quite interesting that Gall's classification should be imitated in a trial independently made by a computer. Also, the result is, on the whole, consistent with the classification of Nagayo or that of Miyake. Small discrepancy from their classifications, if present, may be related to the natural history of cirrhosis in Japan: the decrease in the number of Type A and increase in that of Type F (nutritional) during these 40 years.

In any event, it does not seem coincidental that a computer-aided classification should agree so well with the proposals made by prominent pathologists. However, this does not mean at all that any pathologist can attain the same conclusion without fail. Not every pathologist can experience the tremendous number of pictures the

Table 8-2. The mean parameter values of cirrhoses assigned to the five clusters.

Cluster	No. cases	Mean $r$ ( $\mu\text{m}$ )	%V1.5	Ds ( $\mu\text{m}$ )	$\rho_\theta$
A	20	282.1 $\pm$ 61.6	14.2 $\pm$ 9.5	134.7 $\pm$ 45.6	0.42 $\pm$ 0.17
B	15	430.2 $\pm$ 75.9	26.5 $\pm$ 5.8	228.5 $\pm$ 50.8	0.47 $\pm$ 0.09
C	20	275.3 $\pm$ 71.3	9.0 $\pm$ 6.6	307.0 $\pm$ 59.4	0.54 $\pm$ 0.11
D	9	706.3 $\pm$ 145.2	41.8 $\pm$ 12.0	318.9 $\pm$ 97.7	0.36 $\pm$ 0.17
E	6	403.0 $\pm$ 75.7	44.8 $\pm$ 3.7	146.3 $\pm$ 41.6	0.06 $\pm$ 0.10

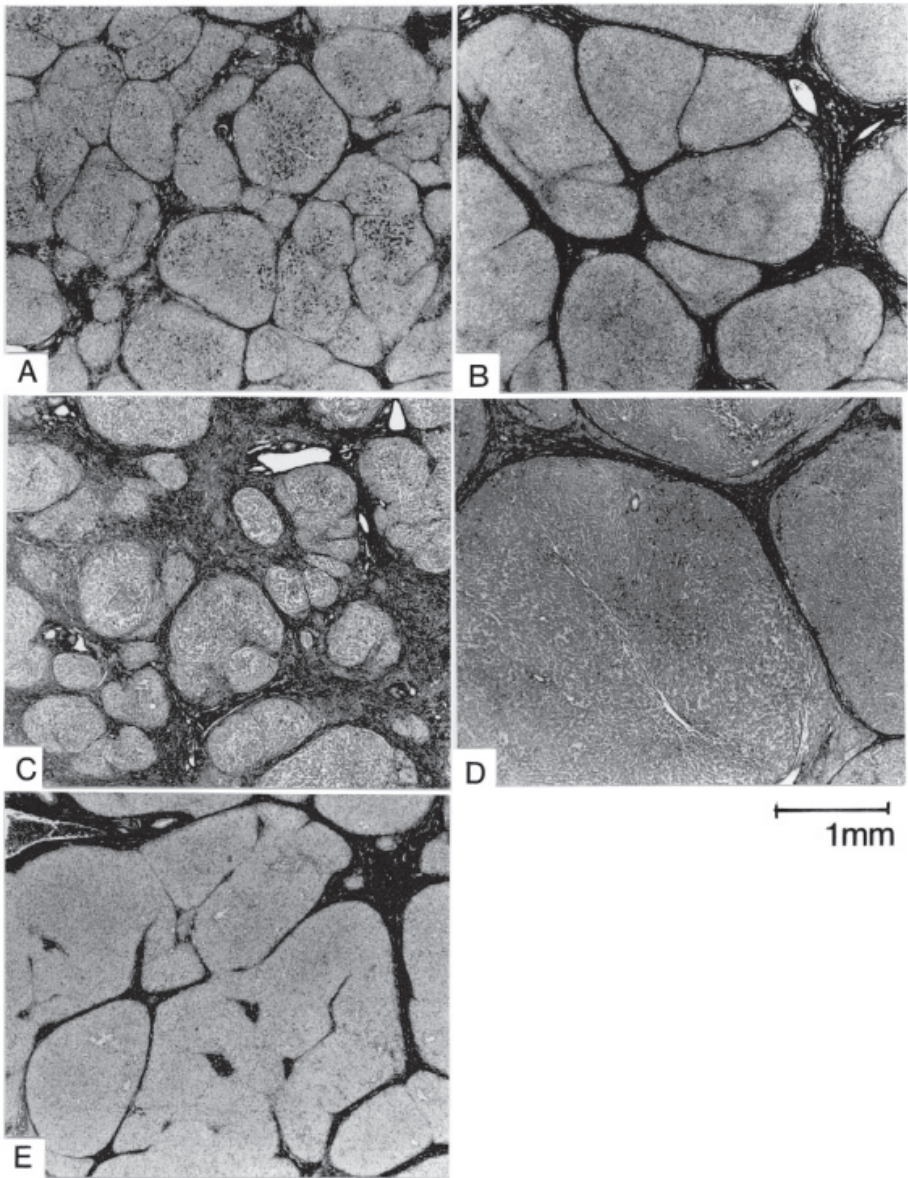


Fig. 8-7. Microscopic pictures of the cases representing the five clusters.

founders of these classifications must have studied. We think therefore, the merit of computerized classification lies in that, the conclusion reached only by a few authorities, is reproducible by common pathologists no matter how much he or she may be experienced in the field.

**b) Adequate classification of carcinomatous and precarcinomatous cells****i) Adenocarcinoma of lung and its precursor****Pulmonary adenocarcinoma and AAH (Figs. 8-8, 8-9)**

Of the various adenocarcinomas arising from the lung, Clara cell type (Fig. 8-8 upper left) and Type-II pneumocyte-type (Fig. 8-8 upper right) are two major varieties, both in the classification proposed by Shimosato (1989). The former type was coined as such on account of hobnail-shaped carcinoma cells reminiscent of Clara cells. In the latter, the cuboidal shape of cells was considered analogous to Type II pneumocytes which in normal lung secrete surfactant. In the early, pre-invasive stages of development, both types of carcinoma cells grow so as to extend along the surface of alveolar septa, replacing the pre-existing epithelial cells. Recently, attention has been paid to a lung lesion considered to be a forerunner of adenocarcinoma. Called atypical adenomatous hyperplasia, or AAH, the lesion resembles the picture of non-invasive adenocarcinoma but differs from carcinoma in the grade of atypia that appears somewhat lower. Exhibited in the lower part of Fig. 8-8 are two examples of what were diagnosed by our team as AAH before morphometric analysis. However, the degree of atypia is not the same; the lesion in the right seems more atypical, with the atypical nuclei arranged at a higher density than in the left. Its difference from non-invasive

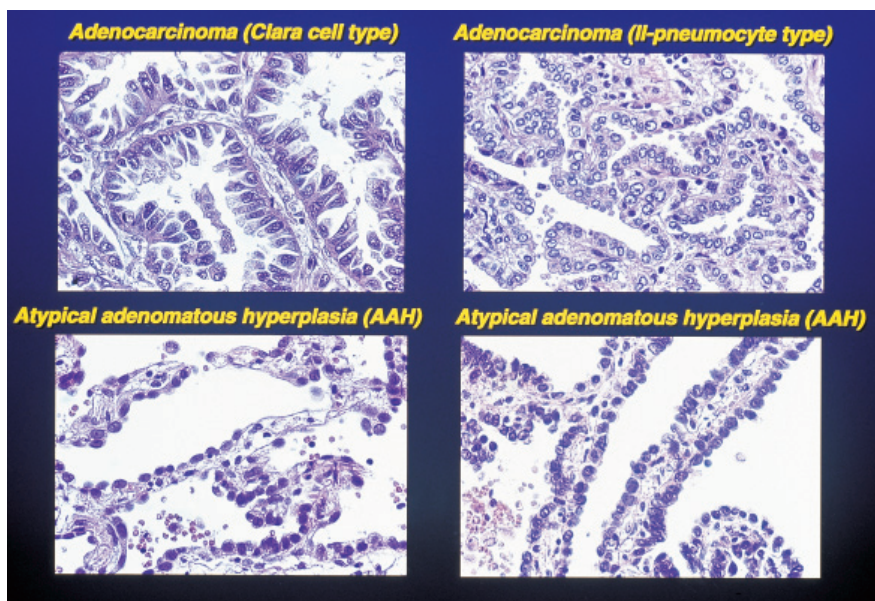


Fig. 8-8. Microphotographs of pulmonary adenocarcinoma and its related lesions. The upper left: adenocarcinoma of Clara cell type. The upper right: adenocarcinoma of Type II pneumocyte type. Both of the pictures in the lower half are from the lesions diagnosed as atypical adenomatous hyperplasia (AAH) before morphometry, where however the cells in the right seem more atypical than those in the left. Hematoxylin and eosin stain.



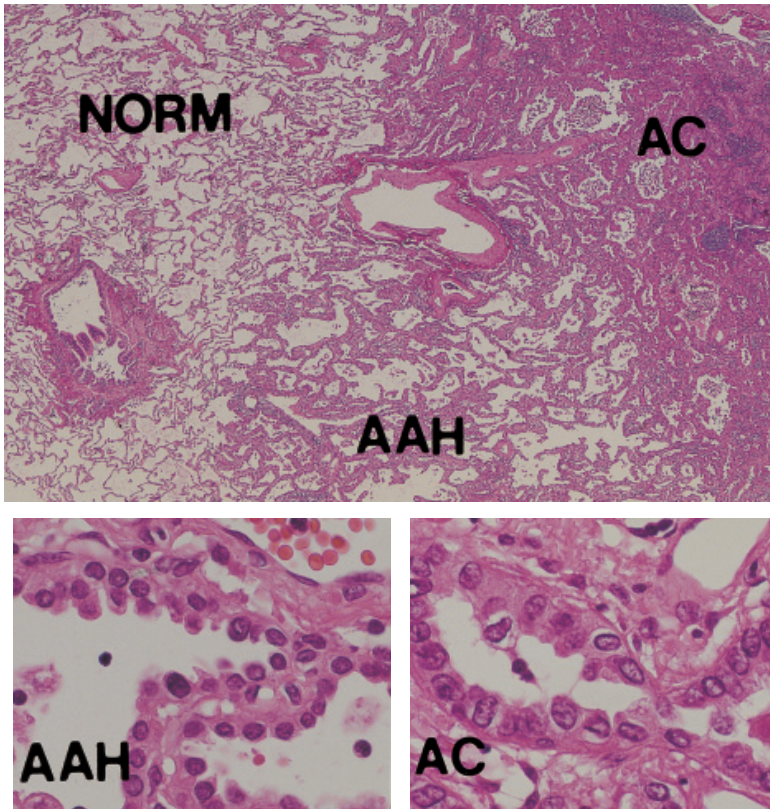


Fig. 8-9. Microscopic picture of an adenocarcinoma of lung (AC), surrounded by a zone of atypical adenomatous hyperplasia (AAH). Hematoxylin and eosin stain.

carcinoma, particularly the Type II pneumocyte-type, seems so delicate as to make us unsure about whether we can reproduce our diagnosis without fail. In view of this, Mori *et al.* (1993, 1996ab) attempted to apply cluster analysis to AAH and the two types of adenocarcinoma.

It is well evidenced that the AAH corresponds to one of the steps preceding the development of adenocarcinoma, both for the Clara cell type and Type-II pneumocyte-type (Nakanishi, 1990). In Fig. 8-9, a zone of AAH is shown surrounding a non-invasive adenocarcinoma, a finding often encountered while examining lungs surgically resected for carcinoma. This reminds us of the concentric zonation of different atypia already shown in the adenoma-carcinoma sequence of colon (Fig. 4-36) and dysplasia-carcinoma sequence of bile ducts (Fig. 4-44).

#### **Parameter expression of cellular atypia (Figs. 8-10, 8-11)**

In studying the difference among the adenocarcinomas and AAH by cluster analysis, the feature of atypical cells has to be reduced to several parameters. An atypical cell is recognized as such based on a series of factors constituting its form. In the

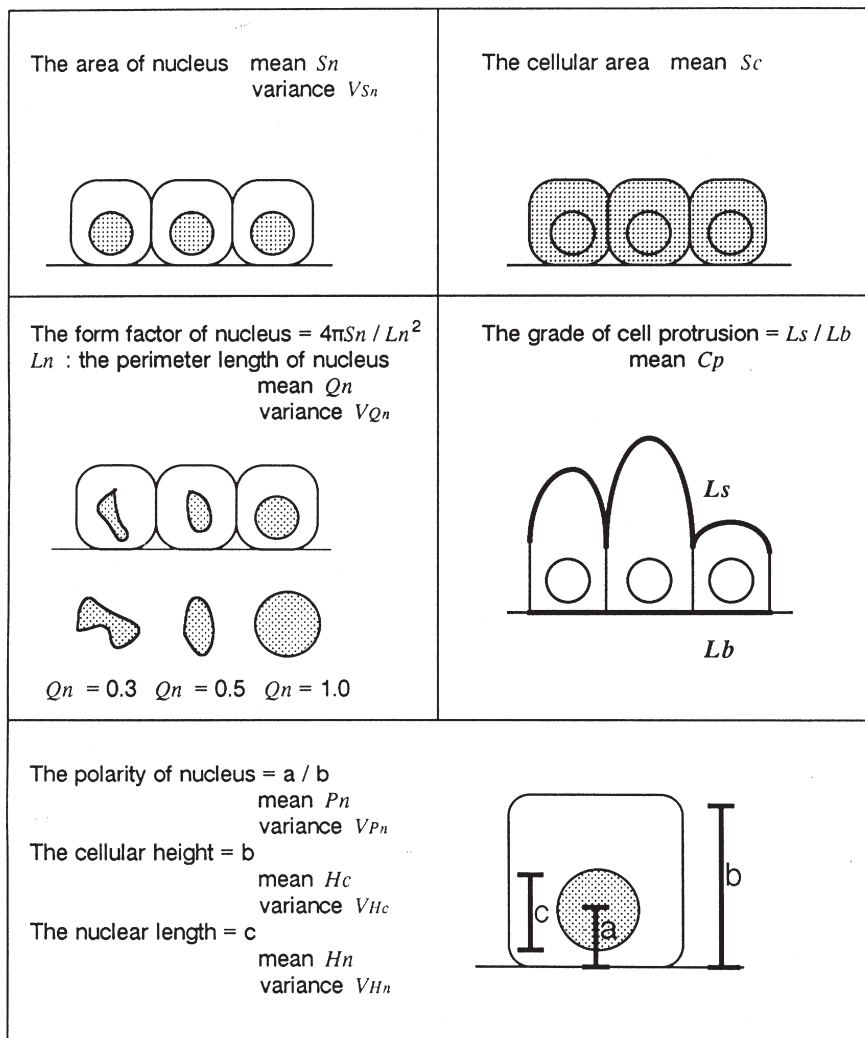


Fig. 8-10. Parameters employed to express the grade of cellular abnormality in quantitative terms. Reproduced from Mori, Takahashi *et al.*: Cancer (1993) 72: pp. 2334.

present study, twelve factors of cell form were taken as atypia-associated, each defined quantitatively as in Fig. 8-10. These include the nuclear area ( $S_n$ ), the form factor ( $Q_n$ ) of nucleus and the cellular area ( $S_c$ ), all with the mean and variance, and the grade of cell protrusion ( $C_p$ ). To these, the polarity of nucleus ( $P_n$ , positioning at the cell base), cellular height and the nuclear length were added as secondary parameters. Of these, the form factor of nucleus ( $Q_n$ ) is defined as

$$Q_n = 4\pi \cdot S_n / L_n^2 \quad (0 \leq Q_n \leq 1.0)$$

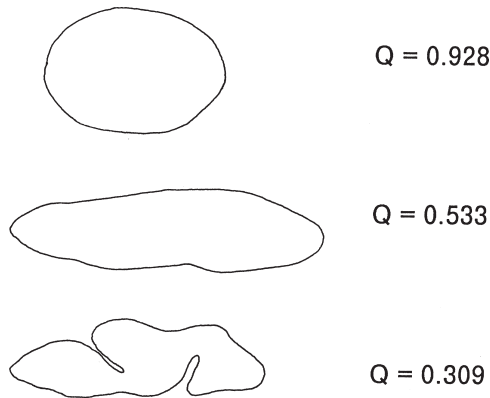


Fig. 8-11. The form factor of nucleus  $Q_n$  applied to three examples of closed profiles.

where  $L_n$  is the perimeter length of nucleus. As schematized in Fig. 8-11, the value of  $Q_n$  is 1.0 when the nucleus is exactly circular. The more elongated or indented the nuclear shape, the smaller does the value become, thus serving as a measure of irregularity in the shape of nucleus.  $C_p$ , the grade of cell protrusion was introduced to express the “hobnail” pattern, a rugged contour of apical surface, which characterizes Clara cell type adenocarcinoma with cells having high-positioned nuclei.

The material was a total of 97 lesions selected from surgical lung specimens. Pre-morphometry microscopic diagnosis was: Clara cell type adenocarcinoma in 35 lesions, Type II pneumocyte-type adenocarcinoma in 22, and AAH in 40. In each lesion, b & w microphotographs were taken from ten fields at a magnification of  $\times 1,200$  with a Polaroid camera attached to the microscope. The photographs were placed on a digitizer, and the contours of typical lining cells and their nuclei were inputted into a digital image analyzer by tracing with a cursor. About 100 non-fragmented cells with complete nuclear outlines were sampled for each lesion.

### Cluster analysis of AAHs and adenocarcinomas (Figs. 8-12, 8-13)

Figure 8-12 demonstrates the result of cluster analysis for the 97 lesions. Clearly, the lesions proved to be classifiable into three clusters. Entered along the lower margin of the dendrogram are the microscopic diagnoses of the lesions given before morphometry: “C” (yellow) denotes Clara cell type adenocarcinoma, “2” (blue) Type II pneumocyte type adenocarcinoma, and “AAH” (red) atypical adenomatous hyperplasia. It is shown that the lesions diagnosed as Clara cell carcinoma were classified into Cluster 3 without exception. Of the lesions diagnosed as Type II pneumocyte carcinoma, a single lesion each was found astray into Cluster 2 and Cluster 3, but the remaining 20 lesions were all classified into Cluster 1. Thus it may be clear that Cluster 3 is a group of Clara cell type and Cluster 1, that of Type II pneumocyte-type carcinoma.

However, most intriguing was the separation into two groups of the 40 lesions that were given a pre-morphometry diagnosis of AAH: 25 of them were classified into

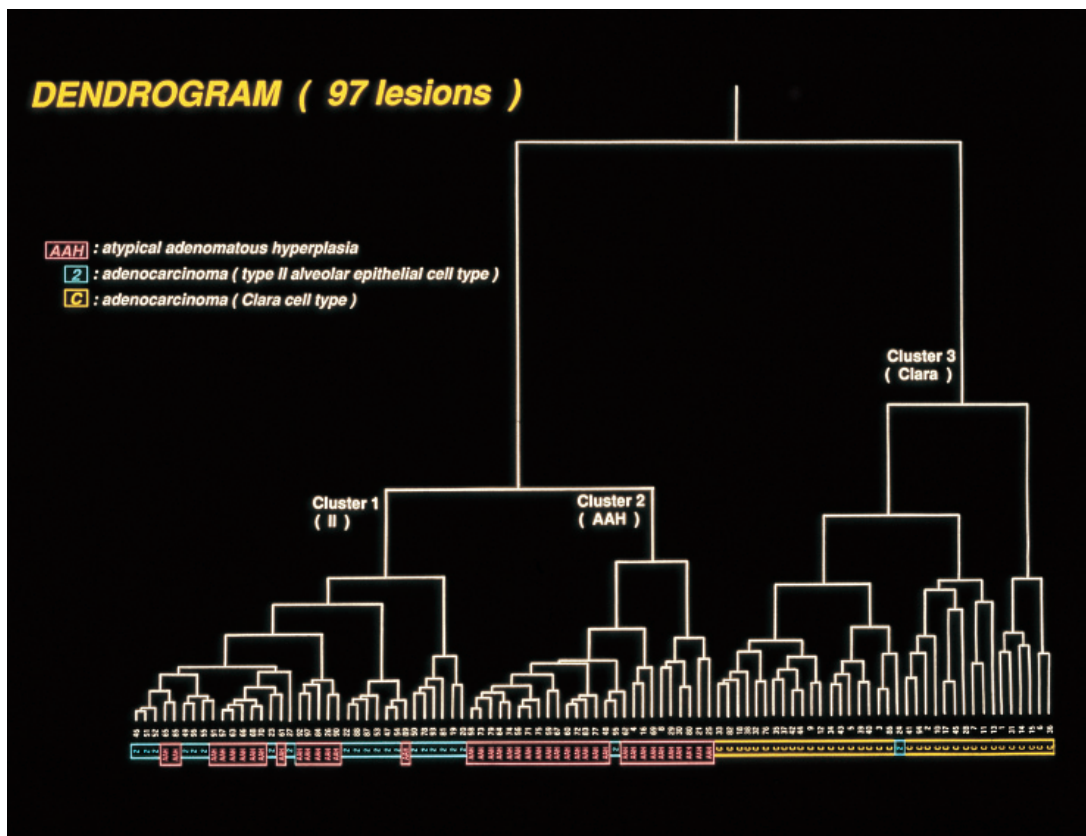


Fig. 8-12. A dendrogram showing the result of cluster analysis for 97 lung tumors. Arranged along the lower margin are the microscopic diagnoses given before morphometry. “C” (yellow): Clara cell type adenocarcinoma. “2” (blue): adenocarcinoma of Type II pneumocyte type. “AAH” (red): atypical adenomatous hyperplasia. The lesions proved to group themselves into three clusters. Of these, Cluster 3 appears to be representing Clara cell type adenocarcinomas and Cluster 1 Type II pneumocyte adenocarcinomas. However, the 40 cases diagnosed as AAH were split into Clusters 1 and 2. Reproduced from Mori, Takahashi *et al.*: *Cancer* (1993) 72: pp. 2337.

Cluster 2, and 15 into Cluster 1. Allotted to Cluster 2 were 26 lesions, of which as many as 25 were those diagnosed as AAH, with only one additional lesion diagnosed as Type II cell carcinoma. This seems suggesting that Cluster 2 is the very group proper to AAH. While a pre-morphometry diagnosis of AAH was given to the remaining 15 lesions, they were shown forming Cluster 1 together with Type II cell carcinoma. In a re-examination of microscopic pictures after the cluster analysis, it was confirmed that in the 25 lesions grouped into Cluster 2, the form of cells were typical of AAH, while in the 15 lesions classified into Cluster 1, the cell shape may not have been so much like AAH as Type II pneumocyte-type carcinoma.

This seemed to be urging us to reconsider the way we had been making microscopic diagnosis. After this study, our stance changed into such a way as to consider,

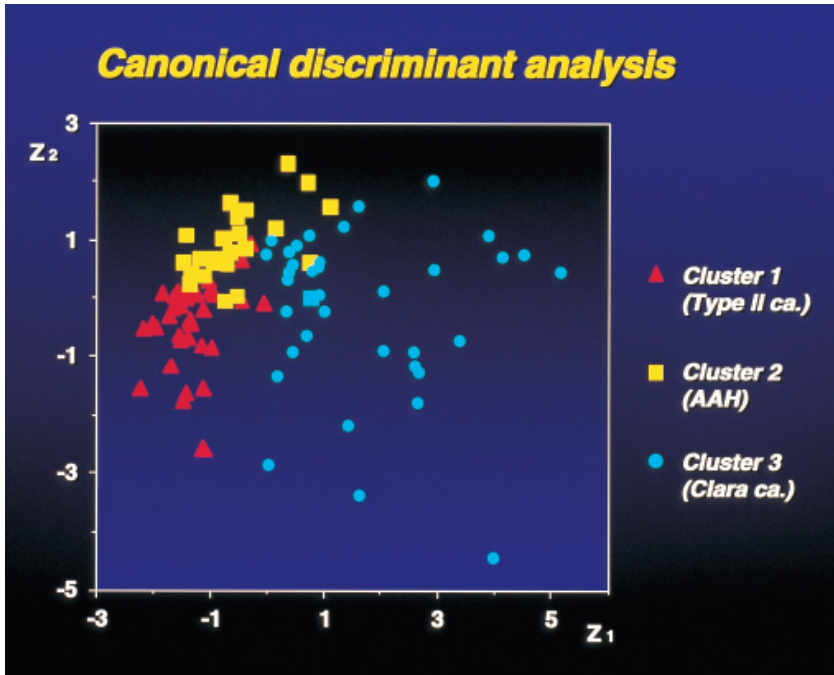


Fig. 8-13. Scattergram showing the result of canonical discriminant analysis for the 97 lesions.  $z_1$ , the first, and  $z_2$ , the second canonical variate. Note that the cases classified into Cluster 2 (AAH) form a group that is positioned between Clusters 1 and 3, suggesting that in the development of adenocarcinoma, AAH corresponds to a common progenitor. Reproduced from Mori, Takahashi *et al.*: *Cancer* (1993) 72: pp. 2339.

while examining a lesion like AAH, whether the lesion is to be classified into the group of adenocarcinoma (Cluster 1) or AAH (Cluster 2). When the lesion is evaluated as being high-grade, we think we should not hesitate in making a diagnosis of (Type-II pneumocyte-type) adenocarcinoma.

Figure 8-13 is the result of canonical discriminant analysis, where the result is expressed in a 2-D scattergram. The abscissa ( $z_1$ ) is the first, and the ordinate ( $z_2$ ) the second canonical variate. Here the distribution of individual lesions faithfully reflects the result of cluster analysis shown in the dendrogram: the lesions assigned to the three clusters are well separated, but the lesions classified into Cluster 2 (AAH) are, as a whole, positioned between Cluster 1 and Cluster 3. This seems to be suggesting that in the development of adenocarcinoma, AAH corresponds to a common progenitor that has a potential to develop into either type of carcinoma.

## ii) Carcinoma and dysplasia of pancreatic duct

### Intraductal papillary adenoma of pancreas (Figs. 8-14, 8-15)

Carcinoma of the pancreas is considered to originate from epithelia lining the pancreatic duct in various level of ductal tree. Sometimes, papillary tumor arises in



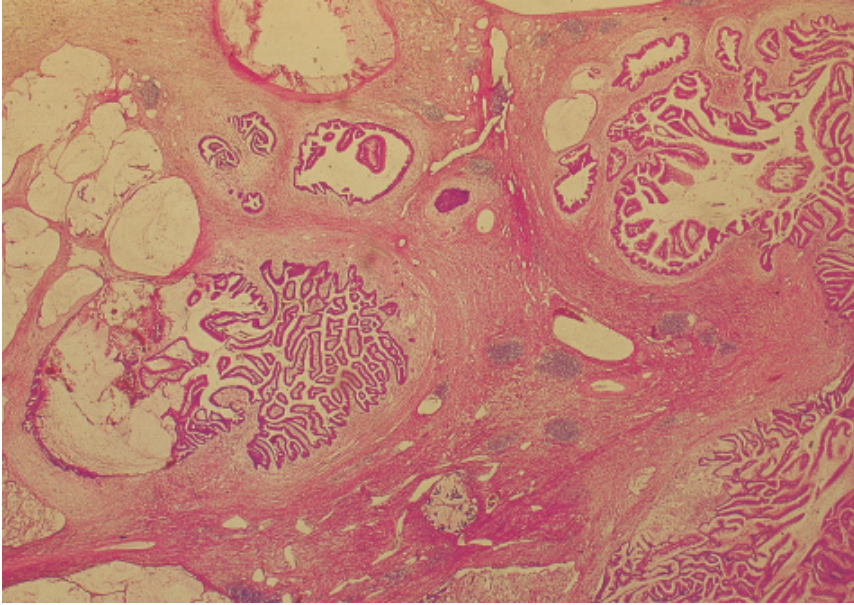


Fig. 8-14. Intraductal papillary adenoma of pancreas. Low power microphotograph. There are multiple cystic lesions, all lined with adenoma cells producing mucinous products into the tubular lumina. Hematoxylin-eosin stain.

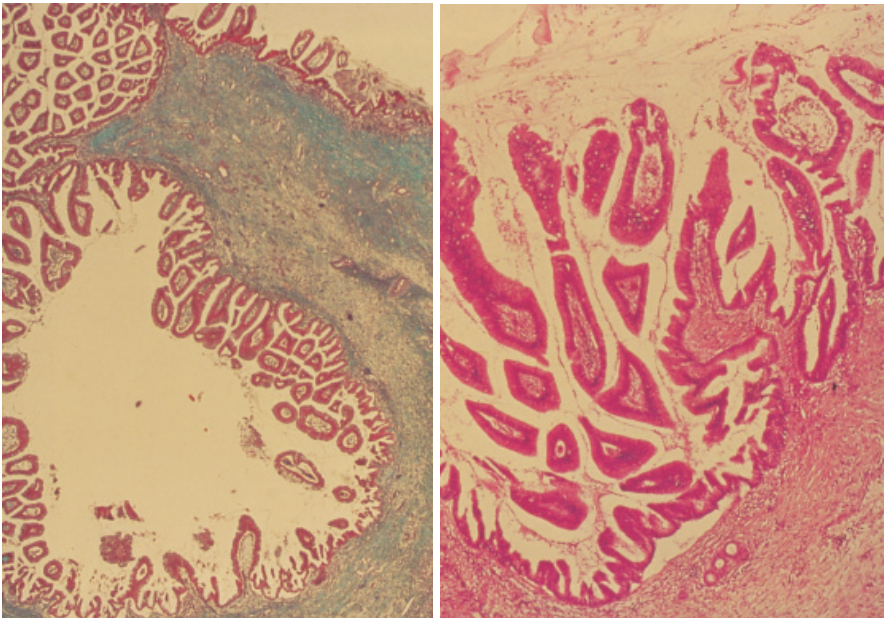


Fig. 8-15. Intraductal papillary adenoma of Fig. 8-14 shown at a higher magnification. The adenoma cells lining the inner surface of the cystic lumina are mildly atypical and with markedly papillary contour. Elastica-Goldner (left) and hematoxylin-eosin stain (right).

larger pancreatic ducts. Given various expressions as intraductal papillary adenoma, mucus-hypersecreting tumor or cystadenoma, the tumor is regarded as representing one of the multiple steps in the carcinogenesis of pancreatic duct (Klöppel, 1980; Pour *et al.*, 1982). As shown in Fig. 8-14, this tumor extends in the ductal tunnels and emerges in a section as multiple intraductal masses.

At a higher magnification, papillary growth of the lining cells is prominent (Fig. 8-15). In this picture the cells look moderately atypical, but among the cases, the grade of atypia is variable. Also within a case, pictures with different grades of atypia ranging from mild nuclear atypia to overt carcinoma *in situ* (CIS), can co-exist forming a mosaic of mucosal patches. Here we are likely to have a situation similar to the development of adenocarcinoma in adenoma of the large bowel, hepatohilar bile duct carcinoma and pulmonary adenocarcinoma. In view of this, Furukawa *et al.* (1992) performed a 3-D mapping of various grades of atypia in 12 surgical specimens of pancreas with this tumor.

### Grade of cell atypia (Fig. 8-16)

Figure 8-16 presents examples of lining cells with various grades of atypia, each diagnosed before morphometry and cluster analysis. In the left upper part one can see ordinary epithelia of pancreatic duct. In the right upper, hyperplastic cells are shown with papillary projections and single row of slightly enlarged nuclei. Demonstrated in the left lower was diagnosed as dysplasia with moderately atypical nuclei arranged along the basal side but in slight disorder. The right lower was considered to be CIS with marked irregularity in nuclear size and shape and loss of polarity.

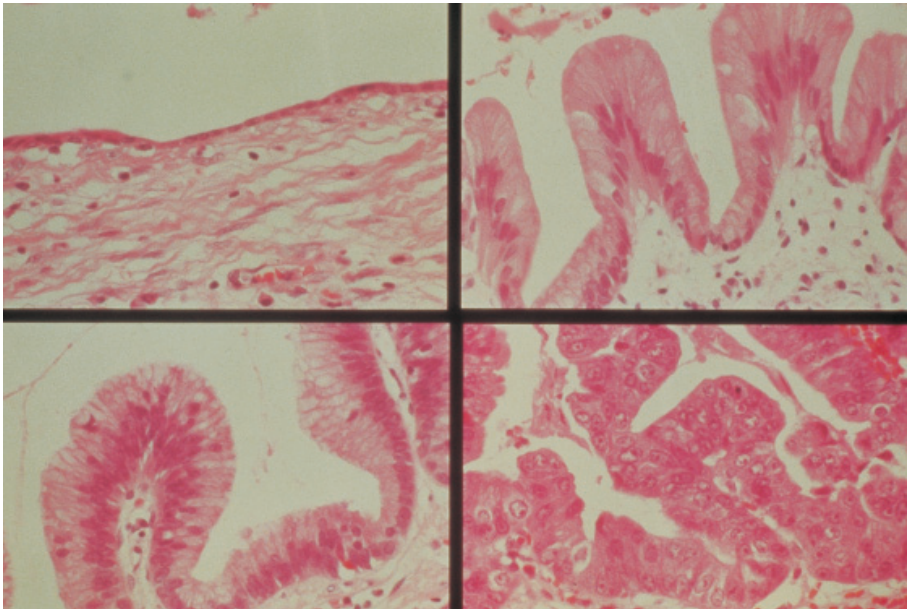


Fig. 8-16. Various grades of atypia found in the adenoma cells. Hematoxylin-eosin stain.

**3-D mapping of intraductal tumors using “macroserials” (Figs. 8-17, 8-18)**

Figure 8-17 demonstrates a surgical specimen of pancreas harboring intraductal papillary adenoma, which was “gelatin embedded” and reduced to “macroserials” using a ham slicer, in the same way as we applied to the slicing of livers (Chapter 4; Fig. 4-42). All the slices were re-embedded in paraffin, and their sectional pictures were subjected to 3-D reconstruction.

Figure 8-18 demonstrates the result of 3-D mapping in a case of intraductal papillary tumor. The main pancreatic duct and several primary subbranches dividing from

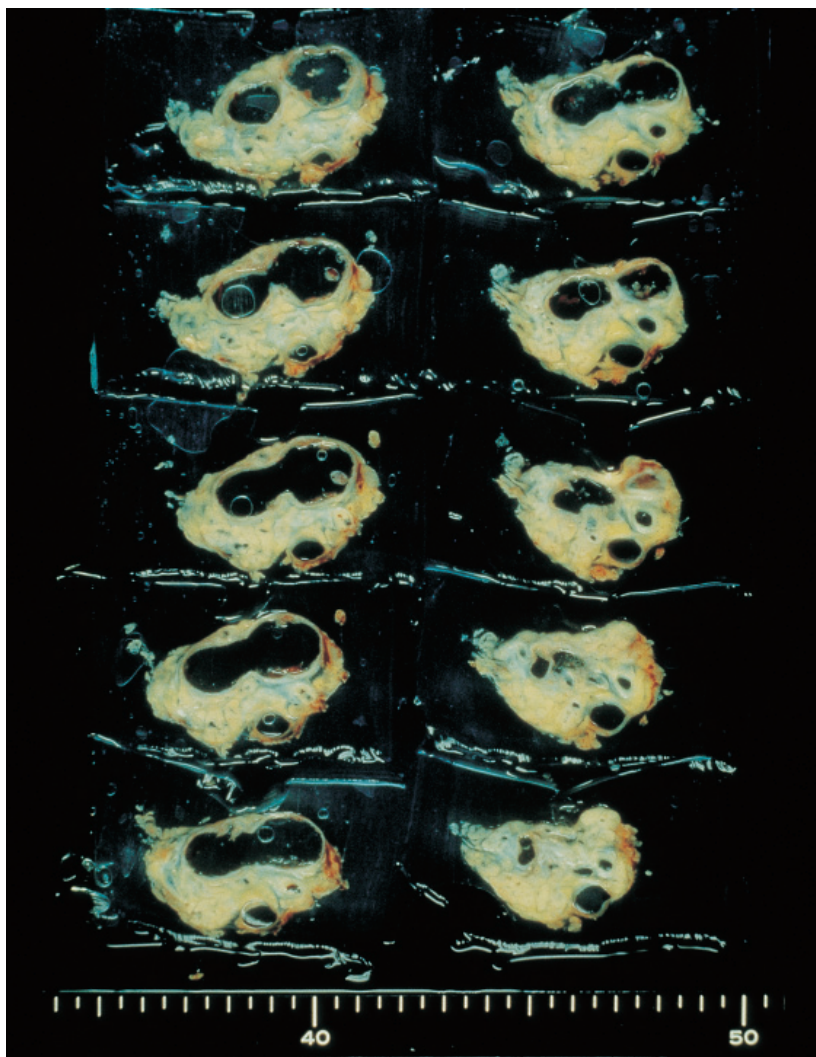


Fig. 8-17. “Macroserials” of surgically excised pancreas harboring intraductal papillary adenoma. The pancreas was embedded in gelatin and serially sliced with a ham slicer. Reproduced from Furukawa, Takahashi *et al.*: *Cancer* (1992) 70: pp. 1507.



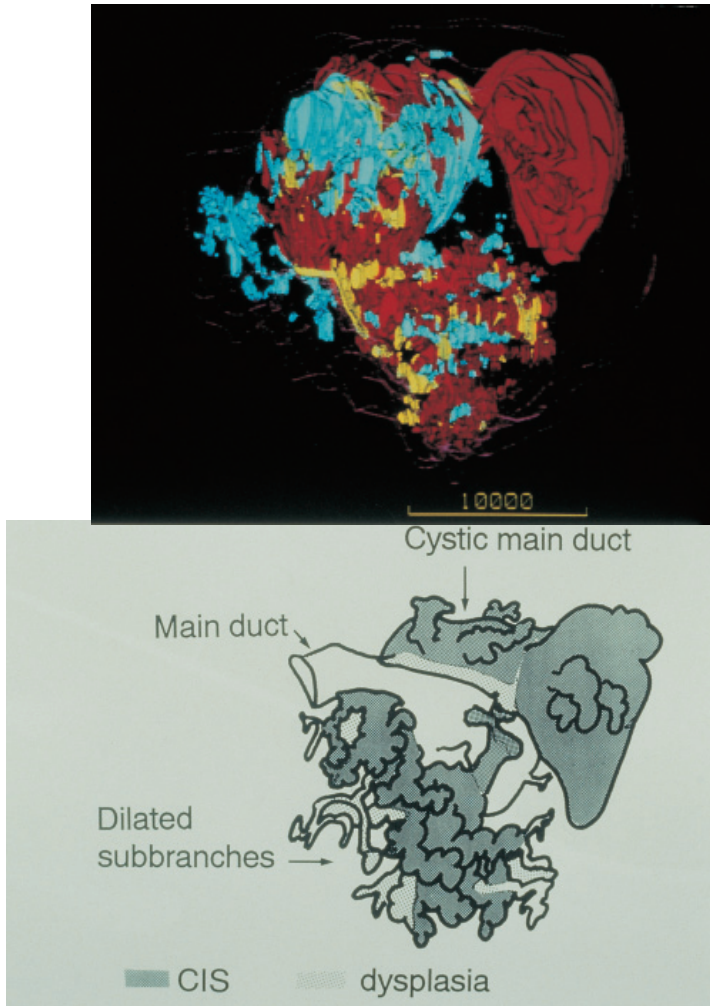


Fig. 8-18. Computer-assisted 3-D mapping of intraductal papillary adenoma in the pancreatic ducts. The main duct is dilated focally in the upper right part, corresponding to a major cyst, which is lined with non-invasive carcinoma cells (CIS) as painted in red. Painted in light blue are areas with normal duct epithelia. Around the CIS, small patchy areas having dysplasia are dispersed (yellow). Reproduced from Furukawa, Takahashi *et al.*: *Cancer* (1992) 70: pp. 1507.

the main duct are strongly dilated due to intraductal growth of tumor. Of the ectatic ducts, those painted in red contain CIS, those yellow are ducts lined by dysplastic cells, and light blue are ducts having ordinary lining cells. Although the arrangement of the three areas seems complicated and intertwined, it seems at least that around the areas of carcinoma are zones of dysplasia, justifying also here to assume progression of multistep carcinogenesis.

**Cluster analysis for atypical ductal cells of pancreas (Fig. 8-19)**

Based on the above, Furukawa attempted at applying cluster analysis to atypical cells lining the pancreatic ducts (1994). The form of atypical cells was reduced to a combination of nine parameters, all defined in basically the same way as in lung adenocarcinomas. The material included microscopic sections of pancreas from 53 patients subjected to partial or total pancreatectomy. The pathological diagnosis of the pancreatic disease was adenocarcinoma, intraductal papillary adenoma, chronic or acute pancreatitis. Of the 53 pancreases, a total of 78 areas with ductal epithelia were selected for morphometry, with some of the pancreases harboring within-case variation in the grades of atypia. The 78 areas were so sampled as to cover the whole range of changes from ordinary epithelia to hyperplastic epithelia to dysplasia to cells with severe atypia consistent with a diagnosis of CIS, and to invasive adenocarcinoma. A sampled area was divided into five parts, from each of which a microphotograph was taken at a high-power magnification of  $\times 1,200$  so that more than 150 nuclei may be included for each of the sample areas. The microphotographs were placed on a digitizer, and the cellular as well as nuclear contours were inputted into a computer by tracing with a cursor.

Exhibited in Fig. 8-19 is the result of cluster analysis in the form of dendrogram.

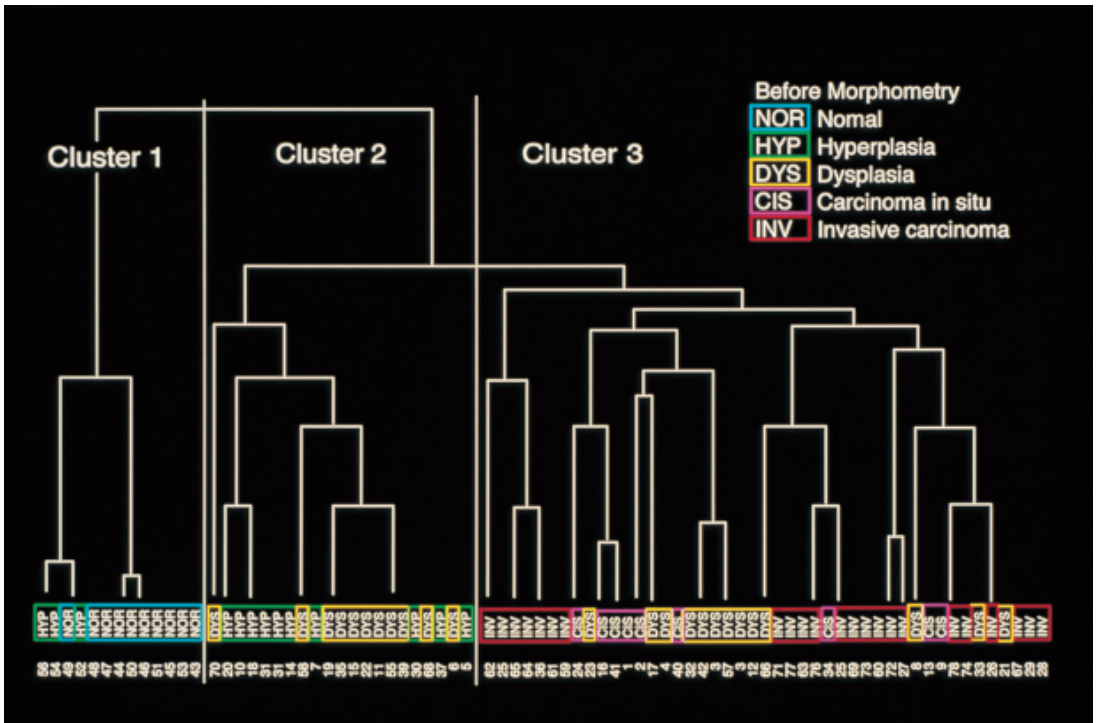


Fig. 8-19. A dendrogram showing the result of cluster analysis of pancreatic duct cells from the 78 lesions with epithelial atypia. Note the clear separation into Clusters 1, 2 and 3. NOR indicates ordinary epithelia; HYP, lesion diagnosed as hyperplasia; DYS, dysplasia; CIS, carcinoma in situ; INV, invasive carcinoma. Reproduced from Furukawa, Takahashi *et al.*: Arch Pathol Lab Med (1994) 118: pp. 230.



The numbers arranged along the lower margin are those of the samples, and arranged upon these are the diagnoses given before morphometry to each of the samples: NOR, normal epithelia; HYP, hyperplastic cells; DYS, dysplasia; CIS, carcinoma in situ; INV, invasive carcinoma. As shown, the 78 samples were separated into three clusters. Cluster 1, comprising 10 areas diagnosed as having normal cells and 3 with hyperplastic cells, was definable as the cluster of ordinary cells. On the other hand, all the areas, to which a pre-morphometry diagnosis of invasive or in situ carcinoma was given, were classified into Cluster 3 without exception. Accordingly, this cluster may well be definable as a cluster of carcinoma. Twenty areas were assigned to Cluster 2, with 9 of them having a diagnosis of hyperplasia and the remaining 11 that of dysplasia, suggesting that this is a cluster of benign lesion with mild atypia. However, there were another 13 samples diagnosed as having dysplasia but classified into Cluster 3, the cluster of carcinoma. Thus, here again, it has been shown that the lesions that seemed to be dysplasia before morphometry were, in reality, not a single category, but contained heterogeneous groups of atypical cells. Cluster analysis made it clear that they have to be separated further into mild and severe dysplasias, the latter being indistinguishable from carcinoma in terms of cellular morphology. For us, this study was a lesson, and according to what was shown, we have changed our standard of microscopic diagnosis.

#### **Analysis of *ki-ras* mutation related with clusters (Fig. 8-20, Table 8-3)**

After cluster analysis was performed, some of the samples were selected for PCR and dot blot analysis of mutations at codon 12 of *ki-ras*.

Fifty of the 78 samples were subjected to analysis (Table 8-3). The remaining 28 samples were omitted because of limited amount of cells available and/or, of inadequate state of samples in terms of fixation. In this study, the 50 samples were divided according to the result of cluster analysis, ordinary cells (Cluster 1), cells with mild dysplasia (benign atypical lesions; Cluster 2) and cells with severe dysplasia (malignant atypical lesions; Cluster 3). It was shown that in Cluster 3 including severe dysplasia and carcinoma, as many as 86% of samples were harboring mutation, while even in Cluster 2 which was thought to comprise only cells with benign lesions, the mutation proved to exist in 82%, a ratio comparable to the cluster of carcinoma.

Data like this may be found in many reports, but the point is that in the present study, DNA analysis was performed for atypical cells that were classified in a *reproducible* way. Usually in this sort of DNA analysis, pathologists are asked to determine, on inspection basis, whether the studied cells are dysplasia or carcinoma.

Table 8-3. The result of *ki-ras* analysis for atypical cells subjected to classification by cluster-analysis.

Morphology	Number of samples	Mutations
Ordinary cells (Cluster 1)	11	0
Mild dysplasia (Cluster 2)	17	14 (82%)
Severe dysplasia (Cluster 3)	22	19 (86%)

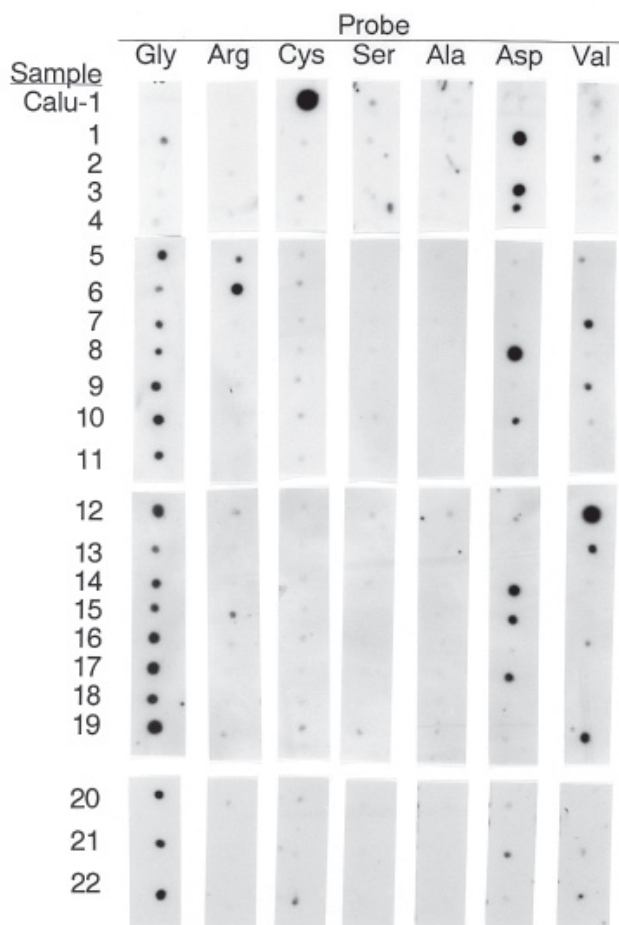


Fig. 8-20. Dot-blot analysis for point mutation at codon 12 of *ki-ras* using the materials classified by cluster analysis shown in Fig. 8-19.

If reproducibility is not ensured in the microscopic differentiation of atypical cells, a firm reliable basis cannot be provided for the DNA analysis either.

On closing this chapter, it should be added that in our team, cluster analysis found application to still other studies. Of such studies, small comment is to be given to that of Tezuka *et al.* and M. Nakamura *et al.*

In a series of studies dealing with endometrial carcinoma and related lesions, Tezuka *et al.* (1994) subjected the cell pattern of smear preparations to 5-variate cluster analysis. The material was aspirated samples from 70 cases. In 10 of the cases the diagnosis before morphometry was well differentiated adenocarcinomas and in 4 cases, endometrial hyperplasia. Besides, there were 56 normal controls. Cellular pictures from the 70 cases proved to separate squarely into three clusters: Cluster C including

10 cases of adenocarcinoma and 2 cases of atypical hyperplasia, Cluster B including 39 normal cases and 2 cases of adenomatous hyperplasia, and Cluster A including 17 cases which were all histopathologically normal. Thus, the study indicated that morphometric-statistical classification could be of great help in improving the cytodiagnostic validity and reproducibility of endometrial carcinoma.

M. Nakamura *et al.* (1996) attempted to re-examine the histological classification of hepatocellular carcinoma based on cluster analysis. To the parameters of atypia they added a quantity corresponding to the mean breadth (D) of cell nests and thus expressing structural abnormality. Cluster analysis resulted in the separation of the sampled 47 cases into Clusters 1, 2a and 2b, with the picture increasingly atypical in this order. The difference of D-value among the cases proved to be most contributing to the separation of clusters. On DNA ploidy analysis which was performed on the same samples, aneuploid and tetraploid nuclei were shown to increase in the above order, suggesting that this may also be reflecting the growing order of malignancy.

## A Stereological Method of Granulometry

In the domain of pathology, we often face spherical bodies of various size dispersed in the organ. Though a classic subject of stereology, the quantitative treatment of particles has been a matter of extreme difficulty, and the estimation of sphere number in a unit volume  $N_V$  (the numerical density) still remains a hardest problem of biometry. In the above, Langerhans islets and metastatic nodules in the liver (Chapter 2) and cirrhotic nodules (Chapter 8) were treated applying the stereological method developed by Suwa *et al.* (1976). In the following, the algorithm of this method is to be outlined, taking the study of pancreatic islets as an example.

**Fig. A-1 Dispersed spheres and chord length measurement** (Chapter 2, p. 32)

**Fig. A-2  $N(r)$ , the distribution of sphere radius** (Chapter 2, p. 39)

We consider a space in which spheres of different radius  $r$  are dispersed as in Fig. A-1. Let the number of spheres in a unit volume (the numerical density) be denoted as  $N_V$ . Besides, we assume that the sphere radius  $r$  follows a distribution function  $N(r)$ . If the number of spheres in a unit volume with radius between  $r_1$  and  $r_2$  is denoted as  $N_V(r_1, r_2)$ ,

$$N_V(r_1, r_2) = \int_{r_1}^{r_2} N(r) dr$$

as shown in Fig. A-2.

Any function may be assumed, so long as its integration from 0 to infinity is definite and equal to  $N_V$ . In this study of islets, Weibull distribution was employed, but logarithmic normal distribution and gamma distribution may also be useful. The Weibull distribution is written as

$$N(r) = N_V m \alpha (\alpha r)^{m-1} \cdot \exp\left[-(\alpha r)^m\right].$$

The advantage of employing this function has been described in Chapter 2 (see Fig. 2-7).

The analysis starts with sampling of islets on microscopic sections, where we employed chord length measurement by line sampling. As shown in Fig. A-1, suppose that on a section we randomly draw a test line, which in the figure is being drawn on the frontal face of the cube. Spheres emerge in the face as circles of various dimen-

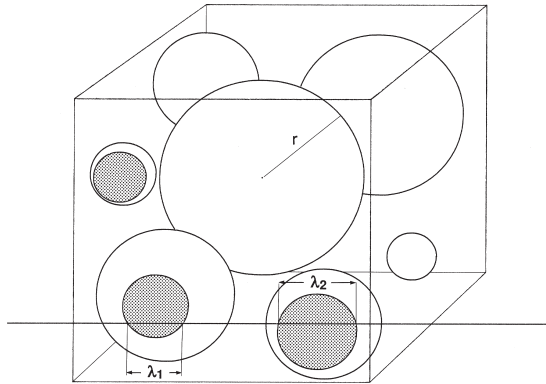


Fig. A-1. The geometric model of dispersed spheres with varying radius  $r$ . Measurement of chord length  $\lambda$  generated by a sampling line randomly drawn on a section.

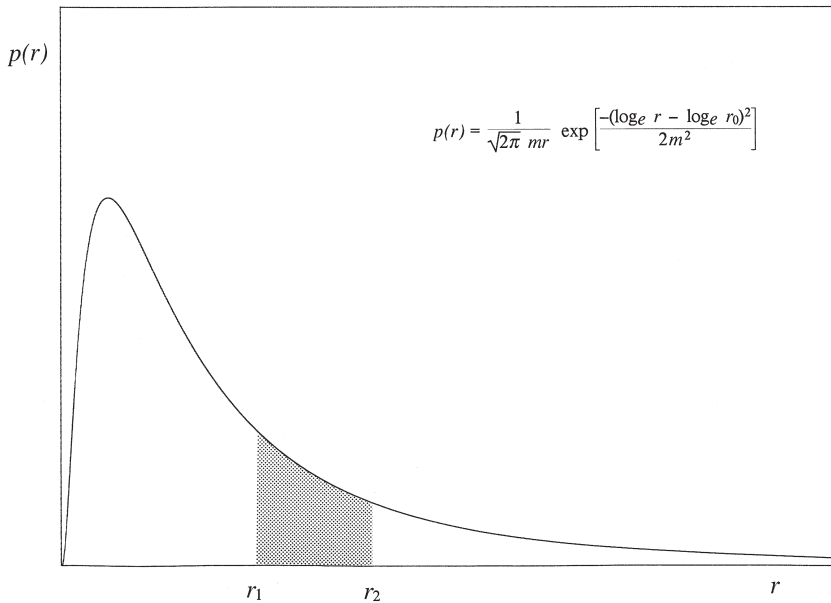


Fig. A-2.  $N(r)$ , the distribution of sphere radius. The total area below the curve and delimited by  $r$ -axis corresponds to  $N_v$ , the number of spheres in a unit volume (numerical density). The number, in a unit volume, of spheres with radius ranging from  $r_1$  to  $r_2$  is given by the area hatched in the figure.

sion, and if the line is sufficiently long, it comes to intersect a series of circles and at each intersection, generates a chord of length  $\lambda$ . By measuring the length  $\lambda$  for about 200 chords consecutively, we obtain its sample distribution. The problem is how to estimate the distribution of sphere radius  $r$  and its parameters (mean, variance, etc.) from this.



### Fig. A-3. Hitting of a single sphere

Suppose that a single sphere,  $r$  in radius, is randomly hit and penetrated by a test line as in Fig. A-3 left. We assume that with this, a chord of  $\lambda$  in length is generated at a distance  $x$  from the sphere center. Here let us try to find the probability that at a trial of penetration, a chord with length between  $\lambda$  and  $\lambda + d\lambda$  is generated. If the probability is  $dP(\lambda, \lambda + d\lambda)$ ,

$$dP(\lambda, \lambda + d\lambda) = \frac{2\pi x}{\pi r^2} dx. \quad (\text{A1})$$

This would be understood by referring to the schema in the right part of the figure, which expresses the equatorial plane of the sphere from a viewpoint along the penetrating line. The sampling line can hit evenly any corner of this circular plane, and a chord of length  $(\lambda, \lambda + d\lambda)$  is generated when the narrow concentric belt,  $dx$  in breadth, is hit by the line. Therefore  $dP(\lambda, \lambda + d\lambda)$  corresponds to the area of the belt divided by the total area of the equatorial plane, as in the above.

On the other hand

$$\frac{\lambda^2}{4} + x^2 = r^2. \quad (\text{A2})$$

By differentiating (A2)

$$\frac{\lambda}{2} d\lambda = -2x dx. \quad (\text{A3})$$

From (A1) and (A3) we obtain

$$dP(\lambda, \lambda + d\lambda) = \frac{\lambda}{2r^2} d\lambda. \quad (\text{A4})$$

by discarding the negative sign.

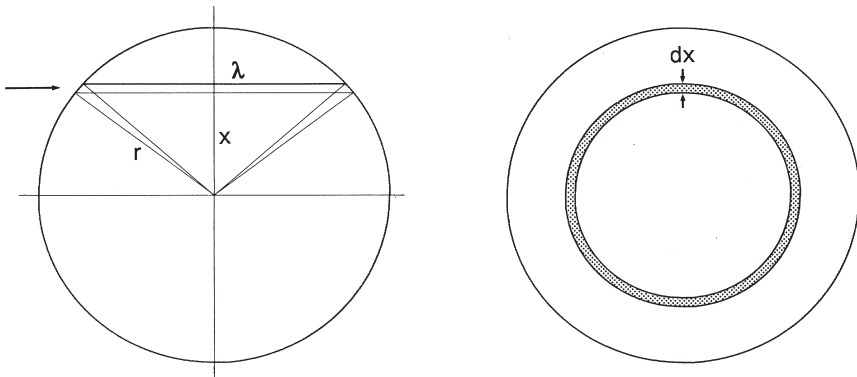


Fig. A-3. (Left) Hitting of a single sphere with a sampling line. (Right) The probability  $P(\lambda, \lambda + d\lambda)$  that the line generates a chord ranging  $[\lambda, \lambda + d\lambda]$  is given by the ratio of the hatched area to the whole circle.

**Fig. A-4. Sampling of spheres by penetrating the space with a line**

Now let us extend the discussion to a space in which a number of spheres are dispersed. Suppose a cubic space as in Fig. A-4, where a cube with edges of unit length contains a number of spheres with different radius  $r$ . Of course we assume that  $r$  follows  $N(r)$ . The number of spheres contained in the cube is  $N_V$  because the cube is of a unit volume.

Now we consider that the cube is penetrated by a random test line which is parallel to one of the edges. A number of spheres would be hit by the line as shown in the figure. In this situation, we try to find the expected number  $dN(r, r + dr)$  of spheres that are hit by the line and are between  $r$  and  $r + dr$  in radius. If the number of spheres between  $r$  and  $r + dr$  contained in the cube is expressed as  $dN_V(r, r + dr)$ ,

$$dN_V(r, r + dr) = N(r)dr.$$

For a sphere  $r$  in radius, the area of the equatorial plane is  $\pi r^2$ , which therefore means that the probability that the sphere is hit by the line is  $\pi r^2$  (note that the area of the side of the cube is 1). Accordingly,

$$dN(r, r + dr) = \pi r^2 N(r)dr. \tag{A5}$$

A chord of  $\lambda$  can emerge from spheres of various  $r$ , and a sphere of  $r$  can generate various length of chords. Therefore in the next place, we try to define the expected number of chords between  $\lambda$  and  $\lambda + d\lambda$  in length that are generated from the spheres between  $r$  and  $r + dr$  in radius. If the expected number of such chords is  $dF'[(\lambda, \lambda + d\lambda)|(r, r + dr)]$ , it is obtained by multiplying  $dN(r, r + dr)$  and  $dP(\lambda, \lambda + d\lambda)$ . Hence, from (A4) and (A5),

$$dF'[(\lambda, \lambda + d\lambda)|(r, r + dr)] = \frac{\pi}{2} \lambda N(r) dr d\lambda. \tag{A6}$$

A chord  $\lambda$  in length can arise from spheres of any radius equal to or larger than  $\lambda/2$ .

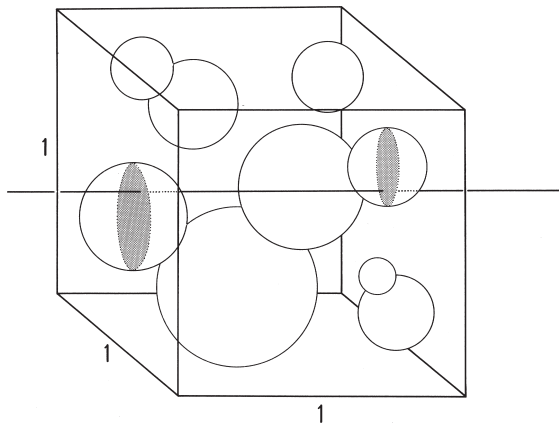


Fig. A-4. Sampling of spheres by penetrating the space with a sampling line. For explanation see the text.

Accordingly, we obtain the total number of chords  $dF(\lambda, \lambda + d\lambda)$  that are generated by line sampling if we integrate (A6) with regard to  $r$  from  $\lambda/2$  to infinity, as

$$dF(\lambda, \lambda + d\lambda) = \left[ \frac{\pi}{2} \int_{\frac{\lambda}{2}}^{\infty} \lambda N(r) dr \right] d\lambda.$$

One can find in this equation that  $dF(\lambda, \lambda + d\lambda)$  is expressed as a product of  $d\lambda$ . Thus we obtain

$$F(\lambda) = \frac{\pi}{2} \int_{\frac{\lambda}{2}}^{\infty} \lambda N(r) dr \quad (A7)$$

which relates the distribution function of sphere radius  $N(r)$  with that of chord length  $F(\lambda)$ . Based on this, now we can calculate the parameters of  $N(r)$ .

We define  $I_n(\lambda)$ , the  $n$ -th moment of  $\lambda$ , as

$$I_n(\lambda) = \int_0^{\infty} \lambda^n F(\lambda) d\lambda. \quad (A8)$$

On account of (A7), the equation contains parameters of  $N(r)$ . Now consider the 0th, 1st and 2nd moments. According to the definition of  $I_n(\lambda)$ , the 0th moment  $I_0(\lambda)$  corresponds to the expected number of chords, the 1st moment  $I_1(\lambda)$  to the sum of  $\lambda$ , and the 2nd moment  $I_2(\lambda)$  to the sum of  $\lambda^2$ , each per a unit length of sampling line. Thus,

$$I_0(\lambda) = \int_0^{\infty} F(\lambda) d\lambda = N(\lambda)_L$$

$$I_1(\lambda) = \int_0^{\infty} \lambda F(\lambda) d\lambda = \Sigma(\lambda)_L$$

$$I_2(\lambda) = \int_0^{\infty} \lambda^2 F(\lambda) d\lambda = \Sigma(\lambda^2)_L.$$

If  $N(\lambda)_L$ ,  $\Sigma(\lambda)_L$ , and  $\Sigma(\lambda^2)_L$  are replaced with the corresponding measurement data, we have a set of simultaneous equations.

The equation (A8) can be re-written by replacing  $F(\lambda)$  with (A7), as

$$I_n(\lambda) = \frac{\pi}{2} \int_0^{\infty} \int_{\frac{\lambda}{2}}^{\infty} \lambda^{n+1} N(r) dr d\lambda. \quad (A9)$$

By solving the above simultaneous equations, the parameters of  $N(r)$  can be obtained. Fortunately, if we assume Weibull distribution, the integration in (A9) is analytically soluble as follows.

In (A9), we exchange the sequence of integration taking in account that  $r \geq \lambda/2$ .

Thus,

$$\begin{aligned} I_n(\lambda) &= \frac{\pi}{2} \int_0^\infty N(r) dr \int_0^{2r} \lambda^{n+1} d\lambda \\ &= \frac{2^{n+1} \pi}{n+2} \int_0^\infty r^{n+2} N(r) dr. \end{aligned}$$

Here we replace  $N(r)$  with Weibull distribution function, as

$$I_n(\lambda) = \frac{2^{n+1} \pi}{n+2} N_V \int_0^\infty m \alpha r^{n+2} (\alpha r)^{m-1} \exp[-(\alpha r)^m] dr. \quad (\text{A10})$$

Make a substitution of

$$(\alpha r)^m = t$$

and on account of

$$r = \frac{t^{1/m}}{\alpha}$$

and

$$dr = \frac{1}{\alpha m} t^{(1-m)/m} \cdot dt,$$

(A10) can be re-written into

$$I_n(\lambda) = \frac{2^{n+1} \pi N_V}{(n+2) \alpha^{n+2}} \int_0^\infty t^{\frac{m+n+2}{m} - 1} \cdot e^{-t} dt. \quad (\text{A11})$$

Now we find that in (A11), the integration has been transformed into the form of gamma function:

$$\Gamma(x) = \int_0^\infty t^{x-1} \cdot e^{-t} dt.$$

With this, (A11) is reduced to:

$$I_n(\lambda) = \frac{2^{n+1} \pi N_V}{(n+2) \alpha^{n+2}} \Gamma\left(\frac{m+n+2}{m}\right). \quad (\text{A12})$$

Further, (A12) can be transformed into

$$I_n(\lambda) = \frac{2^{n+1} \pi N_V}{\alpha^{n+2} m} \Gamma\left(\frac{n+2}{m}\right) \quad (\text{A13})$$

on account of the basic property of gamma function,

$$\Gamma(x) = (x-1)\Gamma(x-1).$$

Thus, the above set of simultaneous equations are reduced to

$$I_0(\lambda) = \frac{2\pi N_V}{\alpha^2 m} \Gamma\left(\frac{2}{m}\right) = N(\lambda)_L$$

$$I_1(\lambda) = \frac{4\pi N_V}{\alpha^3 m} \Gamma\left(\frac{3}{m}\right) = \Sigma(\lambda)_L$$

$$I_2(\lambda) = \frac{8\pi N_V}{\alpha^4 m} \Gamma\left(\frac{4}{m}\right) = \Sigma(\lambda^2)_L.$$

By substituting the measurement data for  $N(\lambda)_L$ ,  $\Sigma(\lambda)_L$  and  $\Sigma(\lambda^2)_L$ , respectively, we can calculate the parameter values  $N_V$ ,  $\alpha$  and  $m$ .



## Literature

- Bach G. (1963) Gründung einer internationalen Gesellschaft für Stereologie. *Z wiss Mikroskop* 65: 190-195.
- Baddeley AJ, Gundersen HJG, Cruz-Orive LM. (1986) Estimation of surface area from vertical sections. *J Microsc* 142: 259-276.
- Baggenstoss AH, Summerskill WHJ, Ammon HV. (1974) The morphology of chronic hepatitis. In: *The Liver and its Diseases* (Schaffner F *et al.*, ed), Intercontinental Medical Book Corp., N. Y., pp.199-206.
- Beck J, Nordin B. (1960) Histological assessment of osteoporosis by iliac crest biopsy. *J Path Bact* 80: 391-410.
- Beck JSP, Berg BN. (1931) The circulatory pattern in the islands of Langerhans. *Am J Pathol* 7: 31-35.
- Cameron RB, Macintosh JK, Rosenberg SA. (1988) Synergistic antitumor effects of combination immunotherapy with recombinant interleukin-2 and a recombinant hybrid  $\alpha$ -interferon in the treatment of established murine hepatic metastases. *Cancer Res* 48: 5810-5817.
- Chiba R, Takahashi T. (1994a) Quantitative morphology of human cirrhotic livers. Part I: Parameter expression of pattern as a basis for computerized classification. *Pathol Internat* 44: 662-671.
- Chiba R, Takahashi T. (1994b) Quantitative morphology of human cirrhotic livers. Part II: The statistically adequate morphological classification of liver cirrhosis. Multivariate analysis from quantified data of form. *Pathol Internat* 44: 672-681.
- Capowski JJ. (1977) Computer-aided reconstruction of neuron trees from several serial sections. *Computer and Biomed Res* 10: 617-629.
- DeHoff RT. (1968) Curvature and the topological properties of interconnected phases. In: *Quantitative Microscopy* (DeHoff RT, Rhines FN, ed), McGraw-Hill, New York, pp. 291-325.
- DeHoff RT, Aigeltinger EH. (1970) Experimental quantitative microscopy with special applications to sintering. In: *Perspectives in Powder Metallurgy* (Hirschhorn JS *et al.* ed), Vo. 5, Prentice Hall, N. Y., pp. 81-137.
- DeHoff RT, Aigeltinger EH, Craig KR. (1972) Experimental determination of the topological properties of three-dimensional microstructures. *J Microsc* 95: 69-91.
- DeHoff RT. (1982) Quantitative serial sectioning analysis: preview. *J Microsc* 131: 259-263.
- Ebina M, Yaegashi H, Takahashi T, Motomiya M, Tanemura M. (1990a) Distribution of smooth muscles along the bronchial tree. *Am Rev Respir Dis* 141: 1322-1326.
- Ebina M, Yaegashi H, Chiba R, Takahashi T, Motomiya M, Tanemura M. (1990b) Hyperreactive site in the airway tree of asthmatic patients revealed by thickening of bronchial muscles. *Am Rev Respir Dis* 141: 1327-1332.
- Ebina M, Takahashi T, Chiba T, Motomiya M. (1993) Cellular hypertrophy and hyperplasia of airway smooth muscles underlying bronchial asthma. *Am Rev Respir Dis* 148: 720-726.

- Elias H. (1949) A re-examination of the structure of the mammalian liver. I. Parenchymal architecture. *Am J Anat* 84: 311-334.
- Endoh M, Chiba R, Takahashi T. (1997) Two-D distance distribution analysis: An application to HBcAg-positive hepatocytes and its relation to septum formation in cirrhosis. *Tohoku J Exp Med* 182: 181-184.
- Fauerholdt L, Schlichting P, Christensen E *et al.* (1983) Conversion of micronodular cirrhosis into macronodular cirrhosis. *Hepatology* 3: 928-931.
- Furukawa T, Takahashi T, Kobari M, Matsuno S. (1992) The mucus-hypersecreting tumor of the pancreas: development and extension visualized by three-dimensional computerized mapping. *Cancer* 70: 1505-1513.
- Furukawa T, Chiba R, Kobari M, Matsuno S, Nagura H, Takahashi T. (1994) Varying grades of epithelial atypia in the pancreatic ducts of humans. *Arch Pathol Lab Med* 118: 227-234.
- Furuyama M. (1962) Histometrical investigation of arteries in reference to arterial hypertension. *Tohoku J exp Med* 76: 388-414.
- Gall EA. (1960) Posthepatic, postnecrotic and nutritional cirrhosis. *Am J Pathol* 36: 241-271.
- Grundmann E. (1975) Histologic types and possible initial stages in early gastric carcinoma. *Beitr Pathol* 154: 256-280.
- Gundersen HJG, Jensen EB. (1985) Stereological estimation of the volume-weighted mean volume of arbitrary particles observed on random sections. *J Microsc* 138:127-142.
- Gundersen HJG. (1986) Stereology of arbitrary particles. *J Microsc* 143: 3-45.
- Gundersen HJG, Bendtsen TF, Korbo L, Marcussen N, Moller A, Nielsen K, Nyengaard JR, Pakkenberg B, Sorensen FB, Vesterby A, West MJ. (1988) Some new, simple and efficient stereological methods and their use in pathological research and diagnosis. *APMIS* 96: 379-394.
- Heath D, Edwards JE. (1958) The pathology of hypertensive pulmonary vascular disease. A description of six grades of structural changes in the pulmonary arteries with special reference to congenital cardiac septal defects. *Circulation* 18: 533-547.
- Hedlung LR, Gallagher JC. (1988) Vertebral morphometry in diagnosis of spinal fractures. *Bone and Mineral* 5: 59-67.
- Hennig A. (1956) Bestimmung der Oberfläche beliebig geformter Körper mit besonderer Anwendung auf Körperchen der menschlichen Bereich. *Mikroskopie*, 11: 1-20.
- Hogg JG, Macklem T, Thurlbeck WM. (1968) Site and nature of airway obstruction in chronic obstructive lung. *N Engl J Med* 278: 1355-1360.
- Hossain S. (1973) Quantitative measurement of bronchial muscle in men with asthma. *Am Rev Respir Dis* 107: 99-109.
- Hsu HC, Su IJ, Lai MY *et al.* (1987) Biologic and prognostic significance of hepatocyte hepatitis B core antigen expression in the natural course of chronic hepatitis B virus infection. *J Hepatol* 5: 45-50.
- Japanese Society for Cancer of the Colon and Rectum. (1997) Japanese classification of colorectal carcinoma (1st English edition). Kanehara, Tokyo.
- Japanese Research Society for Gastric Cancer. (1974) The general rules for the gastric cancer study in surgery and pathology. 9th ed., Kanehara, Tokyo.
- Kaiho T, Masuda T, Sasano N, Takahashi T. (1986) The size and number of Langerhans islets correlated with their endocrine function: A morphometry on immunostained serial sections of adult human pancreas. *Tohoku J Exp Med* 149: 1-10.
- Kasai M, Kimura S, Asakura Y, Suzuki H, Taira Y, Ohashi E. (1968) Surgical treatment of

- biliary atresia. *J Pediatr Surg* 3: 665-675.
- Kitaoka H, Takaki R, Suki B. (1999) A three-dimensional model of the human airway tree. *J Appl Physiol* 87: 2207-2217.
- Klöpffel G, Bommer G, Rückert K, Seifert G. (1980) Intraductal proliferation in the pancreas and its relationship to human and experimental carcinogenesis. *Virchows Arch A Pathol Anat Histopathol* 387: 221-233.
- Langer JC, Langer B, Taylor BR, Zeldin R, Cummings B. (1985) Carcinoma of extrahepatic bile ducts: Results of an aggressive surgical approach. *Surgery* 98:752-758.
- Lewis FT. (1923) The typical shape of polyhedral cells in vegetable parenchyma and the restoration of that shape following cell division. *Proc Am Acad Arts Sci* 58: 537-552.
- Lewis FT. (1933) The significance of cells revealed by their polyhedral shapes, with special reference to precartilage, and a surmise concerning nerve cells and neuroglia. *Proc. Am. Acad. Arts Sci* 68: 251-284.
- Like AA, Orci L.(1972) Embryogenesis of the human pancreatic islets: a light and electron microscopic study. *Diabetes* 21(suppl): 511-534.
- Linzbach J. (1958) Die Bedeutung der Gefäßwandfaktoren für die Entstehung der Arteriosklerose. *Verh Dtsch Ges Pathol* 41: 24-41.
- Luis M, Cruz-Orive LM, Howard V. (1990) Estimating the length of a bounded curve in three dimensions using total vertical projections. *J Microsc* 163: 101-113.
- Matsuki K, Takahashi T, Mouri T. (1994) The number and density of hypertensive vascular lesions of lung in advanced pulmonary hypertension. A computer-aided 3-D morphometry in autopsy lung specimens of five patients with congenital cardiac anomaly. *J Jpn Assn Thorac Surg* 42: 346-353. (Japanese with English summary)
- Miura H, Ohi R, Tseng SW, Chiba R, Takahashi T. (1995) Quantitative morphology of Auerbach's plexus with special reference to the transitional zone in the colon of patients with Hirschsprung's disease. *Pathol Clin Med* 13: 1447-1454. (Japanese with English summary)
- Miura H, Ohi R, Tseng SW, Takahashi T. (1996) The structure of the transitional and aganglionic zones of Auerbach's plexus in patients with Hirschsprung's disease: a computer-assisted three-dimensional reconstruction study. *J Pediatr Surg* 31: 420-426.
- Miyake H. (1960) Pathology of the liver. *Tr Soc Path Jap* 49: 589-632. (Japanese)
- Mori M, Chiba R, Takahashi T. (1993) Atypical adenomatous hyperplasia of the lung and its differentiation from adenocarcinoma: characterization of atypical cells by morphometry and multivariate cluster analysis. *Cancer* 72: 2331-2340.
- Mori M, Tezuka F, Chiba R, Funae Y, Watanabe M, Nukiwa T, Takahashi T. (1996a) Atypical adenomatous hyperplasia and adenocarcinoma of the human lung. *Cancer* 77: 665-674.
- Mori M, Chiba R, Tezuka F, Kaji M, Kokubo T, Nukiwa T, Takahashi T. (1996b) Papillary adenoma of type II pneumocytes might have malignant potential *Virchows Arch* 428: 195-200.
- Morson BC, Sobin LH, Grundmann E, *et al.* (1980) Precancerous conditions and epithelial dysplasia in the stomach. *J Clin Pathol* 33: 711-721.
- Nadel JA. (1980) Autonomic regulation of airway smooth muscle. In: *Physiology and pharmacology of airways* (ed. Lenfant C), Vol 15, Lung biology in health and disease. Marcel Dekker, N.Y., pp. 217.
- Nagayo M. (1914) Referat über Leberzirrhose (Pathologisch-anatomischer Teil). *Verh Jap Path Ges* 4: 3-72.

- Nagayo T. (1966) Atypical epithelial growth in the gastric mucosa. *Jpn J Cancer Clinics* 12: 400-405. (Japanese)
- Nakamura M, Chiba R, Ohi R, Tezuka F, Hayashi T, Takahashi T. (1996) Computer-assisted classification of hepatocellular carcinoma based on quantitative analysis of cellular and structural atypia. *Pathol and Clin Med* 14: 369-377. (Japanese with English summary)
- Nakamura Y, Takahashi T. (1996) A re-examination of the acinar concept of the liver based on a 3-D structural analysis of zonal necrosis in two autopsy cases of acute cresol intoxication. *Pathol and Clin Med* 14: 93-98. (Japanese with English summary)
- Nakamura Y, Takahashi T. (1998) A computer-aided 3-D geometry of acute and chronic zonal necrosis: Three-D tangent counting applied in an attempt to re-examine the structure of the human liver. *Tohoku J Exp Med* 184: 207-227.
- Nakanishi K. (1990) Alveolar epithelial hyperplasia and adenocarcinoma of the lung. *Arch Pathol Lab Med* 114: 363-368.
- Nio M, Takahashi T, Ohi R. (1987) Changes of intrahepatic portal veins in biliary atresia: Formation and development of medial smooth muscles correlated with portal hypertension. *Proceedings of the 4th International Symposium on Biliary Atresia* (Ohi R, ed.), Professional Postgraduate Services, Tokyo, 1987, pp. 243-250.
- Oguma S, Zerbe T, Banner B, Belle S, Starzl TE, Demetris AJ. (1989) Chronic liver allograft rejection and obliterative arteriopathy: possible pathogenic mechanisms. *Transplant Proc* 21: 2203-2207.
- Oh-i R, Kasai M, Takahashi T. (1969) Intrahepatic biliary obstruction in congenital bile duct atresia. *Tohoku J Exp Med* 99: 129-149.
- Ohuchi N, Abe R, Takahashi T, Tezuka F. (1984a) Origin and extension of intraductal papillomas of the breast: A three-dimensional reconstruction study. *Breast Cancer Res Treat* 4: 117-128.
- Ohuchi N, Abe R, Kasai M. (1984b) Possible cancerous change of intraductal papillomas of the breast. A 3-D reconstruction study of 25 cases. *Cancer* 54: 605-611 .
- Ohuchi N, Abe R, Takahashi T, Tezuka F, Kyogoku M. (1985) Three-dimensional atypical structure in intraductal carcinoma differentiating from papilloma and papillomatosis of the breast. *Breast Cancer Res Treat* 5: 57-65.
- Okuyama K, Yaginuma G, Takahashi T, Sasaki H, Mori S. (1988a) The development of vasa vasorum of the human aorta in various conditions. *Arch Pathol Lab Med* 112: 721-725.
- Okuyama K, Yaegashi H, Takahashi T, Sasaki H, Mori S. (1988b) The three-dimensional architecture of vasa vasorum in the wall of the human aorta. *Arch Pathol Lab Med* 112: 726-730.
- Ota K. (1964) Development of gastric cancer. *Trans Soc Jap Pathol* 53: 3-14. (Japanese)
- Popper H, Elias H. (1955) Histogenesis of hepatic cirrhosis studied by the three-dimensional approach. *Am J Pathol* 31: 405-441.
- Pour PM, Sayed S, Sayed G. (1982) Hyperplastic, preneoplastic and neoplastic lesions found in 83 human pancreases. *Am J Clin Pathol* 77: 137-152.
- Rappaport AM, Borowy ZJ, Lougheed WM, Lotto WN. (1954) Subdivision of hexagonal liver lobules into a structural and functional unit. *Anat Rec* 119: 11-34.
- Rappaport AM. (1963) Acinar units and the pathophysiology of the liver. In: *The liver* (Ch. Rouiller, ed), Vol. I, Academic Press, pp. 265-328.
- Saito K, Iwama N, Takahashi T. (1978a) Morphometrical analysis on topographical difference in size distribution, number and volume of islets in the human pancreas. *Tohoku J Exp*

Med 124: 177-186.

- Saito K, Takahashi T, Yaginuma N, Iwama N. (1978b) Islet morphometry in the diabetic pancreas of man. *Tohoku J Exp Med* 125: 185-197.
- Saltykov SA. (1958) *Stereometric metallography*. 2nd ed., Metallurgizdat, Moscow.
- Sakakura T. *et al.* (1976) Mesenchyme-dependent morphogenesis and epithelium-specific cytodifferentiation in mouse mammary gland. *Science* 194: 1439-1441.
- Sasaki K, Takahashi T, Satomi S. Parameter expression of papillary and tubular tumors. Its application to intraductal tumors of the breast. To be submitted to *Anal Quant Cytol Histol*.
- Sawai T, Fujiyama J, Takahashi M, Takahashi T. (1994) The site of elevated vascular resistance in early paraquat lungs: A morphometric study of pulmonary arteries. *Tohoku J Exp Med* 174: 129-140.
- Scheil E. (1931) Die Berechnung der Anzahl und Größenverteilung kugelförmiger Kristalle in undurchsichtigen Körpern mit Hilfe der durch einen oben Schnitt erhaltenen Schnittkreise. *Z anorg allg Chem* 201: 259.
- Schwartz HA. (1934) The metallographic determination of the size distribution of temper carbon nodules. *Metals Alloys* 5: 139.
- Seggev JS, Mason UG III, Worthen S. *et al.* (1983) Bronchiolitis obliterans: report of three cases with detailed physiologic studies. *Chest* 83:169-174, 1983.
- Shimizu H, Yokoyama T. (1993) Three-dimensional structural changes of hepatic sinusoids in cirrhosis providing an increase in vascular resistance of portal hypertension. *Acta Path Jpn* 43: 625-634.
- Shimizu H, Suda K, Yokoyama T. (1996) Difference in the three-dimensional structure of the sinusoids between hepatocellular carcinoma and cirrhotic liver. *Pathol Internat* 46:992-996.
- Shimosato Y. (1989) Pulmonary neoplasms. In: *Diagnostic Surgical Pathology* (Sternberg SS ed), New York, Raven Press, pp. 785-827.
- Smith P, Heath D, Kay JM. (1974) The pathogenesis and structure of paraquat-induced pulmonary fibrosis in rats. *J Pathol* 114: 58-67.
- Sugawara I, Ise Y, Mori K, Takahashi T. (2003) A study of changes of bone trabeculae in osteoporosis by morphometry and 3-D graphic reconstruction of vertebral bodies. *Igaku-Kensa*, 52: 200-206. (Japanese with English summary)
- Suwa N, Niwa T, Fukasawa H, Sasaki Y. (1963) Estimation of intravascular blood pressure gradient by mathematical analysis of arterial casts. *Tohoku J exp Med* 79: 168-198.
- Suwa N, Takahashi K, Fujimoto R, Sasaki Y. (1966) Derivation of expiratory mechanics of normal and emphysematous lungs on anatomical basis. *Tohoku J exp Med* 90: 77-96.
- Suwa N, Sasaki Y, Takahashi K, Fujimoto R. (1966) Estimation of expiratory efficiency of emphysematous lungs on the basis of anatomical findings. *Tohoku J exp Med* 90: 137-168.
- Suwa N, Takahashi T. (1971) Morphological and morphometrical analysis of arteries in hypertension and ischemic kidney. *Urban & Schwarzenberg, München*.
- Suwa N, Takahashi T, Saito K, Sawai T. (1976) Morphometrical method to estimate the parameters of distribution functions assumed for spherical bodies from measurements on a random section. *Tohoku J Exp Med* 118: 101-111.
- Suwa N. (1981) Supracellular structural principle and geometry of blood vessels. *Virchows Archiv A Pathol Anat* 390: 161-179.
- Suzuki M, Takahashi T, Ohuchi K. (1988) Three-dimensional reconstruction of semi-gross



- biostructures using "macroserials": 1-mm-thick serial organ slices. *J Microsc* 149:175-183.
- Suzuki M, Takahashi T, Ohuchi K, Matsuno S. (1989) The development and extension of hepatohilar bile duct carcinoma. *Cancer* 64: 658-666.
- Suzuki M, Takahashi T, Fukuhara K, Unno M, Endo K, Takeuchi H, Matsuno S. (1998) Intrahepatic extension of hepatohilar cholangiocarcinoma visualization by 3-D biliary tract mapping. In: *Carcinoma of the pancreas and biliary tract* (Wakui A *et al.* ed). Tohoku Univ. Press, Sendai, pp. 319-334.
- Tabuchi Y, Nakamura T, Saitoh Y. (1991) Liver metastases induced by implantation of VX2 cancer into the gastrointestinal. *J Surg Res* 50: 216-222.
- Takahashi T, Orii T, Kaneda M. (1968) Precancerous condition of the human liver. *Tohoku J exp Med* 94: 203-224.
- Takahashi T. (1970) The lobular structure of the human liver from the viewpoint of hepatic vascular architecture. *Tohoku J Exp Med* 101: 119-140.
- Takahashi T. (1978a) Three-dimensional morphology of the liver in cirrhosis and related disorders. *Virchows Arch A Pathol Anat Histol* 377: 97-110.
- Takahashi T. (1978b) Topological analysis of the morphogenesis of liver cirrhosis. *Virchows Arch A Pathol Anat Histol* 377: 189-201.
- Takahashi T, Suwa N. (1978c) Stereological and topological analysis of cirrhotic livers as a linkage of regenerative nodules connected in the form of three-dimensional network. *Lecture Notes in Biomathematics* 23: 85-92, Springer.
- Takahashi T, Matsumoto J. (1980) Pattern analysis of chronic liver diseases from the viewpoint of structural connectivity. *Tohoku J Exp Med* 131: 313-325.
- Takahashi T. (1982) Indexing of connectivity in a 2-D, 2-phasic pattern with its relevance to the 3-D structure: An application to the evaluation of advancement of chronic liver diseases. In: *Morphometry in Morphological Diagnosis* (Collan Y *et al.* ed), Kuopio Univ. Press, Kuopio, pp. 135-143.
- Takahashi T, Wagenvoort N, Wagenvoort CA. (1983) The density of muscularized pulmonary arteries in normal lungs. A morphometric study. *Arch Pathol Lab Med* 107: 19-22.
- Takahashi T, Iwama N. (1984a) Atypical pattern of gastric adenocarcinoma. A 3-dimensional reconstruction study. *Virchows Arch A Pathol Anat Histol* 403: 127-134.
- Takahashi T, Iwama N. (1984b) Atypical glands in gastric adenoma. Three-dimensional architecture compared with carcinomatous and metaplastic glands. *Virchows Arch A Pathol Anat Histol* 403: 135-148.
- Takahashi T, Iwama N. (1984c) Three-dimensional morphology of gastric adenocarcinoma. Atypical glands as a basis for histopathologic diagnosis. *Tohoku J Exp Med* 143: 451-465.
- Takahashi T, Iwama N. (1985) Three-dimensional microstructure of gastrointestinal tumors. Gland pattern and its diagnostic significance. In: *Pathology Annual* (ed. Sommers SC *et al.*) Vol. 20 (part I), Appleton-Century-Crofts, Norwalk, pp. 419-440.
- Takahashi T, Yaginuma N. (1985) Ischemic injury of the human pancreas. Its basic patterns correlated with the pancreatic microvasculature. *Path Res Pract* 179: 645-651.
- Takahashi T, Yaegashi H, Ito M. (1986) A microcomputer system for 3-D reconstruction of tissue microstructures. Its application to histopathological studies. *Proc Roy Microsc Soc* 21 (Suppl): S64.
- Takahashi T, Chiba T. (1990) Three-D computational geometry: The "form" of vascular tree as expressed by the distribution of distance in the space, its organ difference and significance

- in blood flow. In: Science on Form II (ed. Ishizaka S), KTK-Reidel, Tokyo, pp. 17-30.
- Takahashi T, Kikuchi T, Chiba T. (1992) Three-D computational geometry: The pattern of vasculature in normal and diseased livers as expressed by the distribution of distance in space. *Acta Stereol* 11: 41-49.
- Takahashi T, Takahashi Y, Nio M. (1994) Remodeling of the alveolar structure in the paraquat lung of humans. *Human Pathol* 25: 702-708.
- Takahashi T. (1994) The pathology of pulmonary fibrosis revealed by the study of paraquat lung. In: Basic and Clinical Aspects of Pulmonary Fibrosis (ed. Takishima T *et al.*), CRC Press, Boca Raton, pp. 3-13.
- Takahashi T, Chiba R, Mori M, Furukawa T, Suzuki M, Tezuka F. (1995) Computer-assisted pathology of intraepithelial adenocarcinoma and related lesions: 3-D distribution, structural aberration and discrimination. *J Cell Biochem (Suppl)* 23: 25-32.
- Takahashi T, Endoh M. (2000) The morphology and morphogenesis of cirrhosis. 3D visualization of the reorganization process. XXIII International Congress of IAP, CM-08 handout, pp. 31-34.
- Takaki R, Arai Y. (1993) Integral method for estimation of connectivity of elements in 2-dimensional gray patterns. *Forma* 8: 147-155.
- Takemura M, Oguma S, Mori S, Ishii M, Starzl TE, Demetris AJ, Takahashi T. (1991) Peribiliary vascular diseases in rejected livers; computer-aided three-dimensional reconstruction and morphometry. *Transplant Proc* 23: 1409-1412.
- Takizawa T, Thurlbeck WM. (1971) Muscle and mucous gland size in the major bronchi of patients with chronic bronchitis, asthma and asthmatic bronchitis. *Am Rev Respir Dis* 104: 331-336.
- Tezuka F, Chiba R, Takahashi T. (1994) Morphometric and multivariate statistical detection of cancer cells in endometrial cytology. *Analyt Quant Cytol Histol* 16:332-338.
- Thaler H. (1952) Über die formale Pathogenese der posthepatitischen Lebercirrhose. *Beitr path Anat* 112: 173-186.
- Thoma R. (1911) Über die Histomechanik des Gefäßsystems und die Pathogenese der Angionekrose. *Virchows Arch path Anat* 204: 1-74.
- Vogelstein B, Fearon ER, Hamilton SR *et al.* (1988) Genetic alterations during colorectal tumor development. *N Engl J Med* 319: 525-532.
- Wagenvoort CA, Wagenvoort N. (1977) Pathology of pulmonary hypertension. John Wiley & Sons, N.Y.
- Ward JH Jr. (1963) Hierarchical grouping to optimize an objective function. *J Am Statist Assoc* 58:236-244.
- Watanabe T, Yaegashi H, Koizumi M, Toyota T, Takahashi T. (1997) The lobular architecture of the normal human pancreas: a computer-assisted three-dimensional reconstruction study. *Pancreas* 15: 48-52.
- Watanabe T, Yaegashi H, Koizumi M, Toyota T, Takahashi T. (1999) Changing distribution of islets in the developing human pancreas: a computer-assisted three-dimensional reconstruction study. *Pancreas* 18: 349-354.
- Weibel ER. (1962) Morphometrische Analyse von Zahl, Volumen und Oberfläche der Alveolen und Kapillaren der menschlichen Lunge. *Z. Zellforsch*, 57:648-666, 1962.
- Weibel ER. (1963) Morphometry of the human lung. Springer, Berlin.
- Whitehous FR, Kernohan JW. (1948) Myenteric plexus in congenital megacolon. *Arch Intern Med* 82: 75-115.

- Yaegashi H, Takahashi T, Kawasaki M. (1987) Microcomputer-aided reconstruction: A system designed for studies in histology and histopathology. *J Microsc* 146: 55-65.
- Yaegashi H, Takahashi T. (1994a) The airway dimension in ordinary human lungs. *Arch Pathol Lab Med* 118: 969-974.
- Yaegashi H, Takahashi T. (1994b) The site, severity and distribution of bronchiolar obstruction in lungs with chronic obstructive pulmonary disease. *Arch Pathol Lab Med* 118: 975-983.
- Yaegashi H, Zhang Y, Tezuka F, Takahashi T, Fukumoto M. (2000) Computer-assisted 3-D mapping and morphometry of dysplastic zones in endoscopically resected colonic adenomas. *J Pathol* 191: 143-149.
- Yaginuma G, Mohri H, Takahashi T. (1990) Distribution of arterial lesions and collateral pathways in the pulmonary hypertension of congenital heart disease: a computer aided reconstruction study. *Thorax* 45: 586-590.
- Yaginuma N, Takahashi T, Saito K, Kyogoku M. (1986) The microvasculature of the human pancreas and its relation to Langerhans islets and lobules. *Path Res Pract* 181: 77-84.
- Yamaki S, Wagenvoort CA. (1981) Plexogenic pulmonary arteriopathy. Significance of medial thickness with respect to advanced pulmonary vascular lesions. *Am J Pathol* 105: 70-75.
- Yamanami H, Chiba R, Kobari M, Matsuno S, Takahashi T. (1999) Total number and size distribution of hepatic metastases of carcinoma. *Analyt Quant Cytol Histol* 21: 216-226.
- Zhang Y, Yaegashi H, Tezuka F, Takahashi T. (1994) A clinicopathological study of protuberant adenomas and adenocarcinomas of the colon based on a computer-aided 3-D distribution analysis and volumetry of atypical glands. *Pathol Clin Med* 12: 1395-1402. (Japanese with English summary)

## Acknowledgment

The Author is indebted to the following publishers (and/or editors) of journals and books for their generous permission to reuse the figures listed below which the author and his co-workers had previously submitted for publication. For each of the figures, the Author(s), Publication title, Volume number, Pages No. and Publication date (year) are included in the caption.

Figs. 1-7, 1-8, 1-9 and 1-10: 1971 Elsevier GmbH Urban & Fischer Verlag, Jena.

Figs. 4-50, 4-51, 4-54 and 4-55: 1985 Elsevier GmbH Urban & Fischer Verlag, Jena.

Figs. 4-52 and 4-53: 1986 Elsevier GmbH Urban & Fischer Verlag, Jena

Figs. 2-20, 2-25, 2-26, 2-27: 1994 Elsevier Inc.

Figs. 4-27, 4-28 and 4-29: 1996 Elsevier Inc.

Figs. 4-10, 4-11 and 4-12: 1988 American Medical Association.

Figs. 1-20, 1-22, 1-23, 4-32, 8-19: 1994 American Medical Association.

Fig. 4-48: 1984 American Cancer Society.

Figs. 4-42 and 4-44: 1989 American Cancer Society.

Figs. 8-17 and 8-18: 1992 American Cancer Society.

Figs. 8-10, 8-12 and 8-13: 1993 American Cancer Society.

Figs. 1-12, 1-16, 1-17: 1990 American Lung Association.

Figs. 6-4, 6-6, 6-8, 6-15, 6-19, 6-20 and 6-21: 1978 Springer Verlag.

Figs. 4-47, 4-49, 5-4, 5-5, 5-10 and 5-12: 1984 Springer Verlag.

Fig. 4-56: 1997 Lippincott-Raven Publishers.

Figs. 4-57, 4-58, 4-59: 1999 Lippincott-Raven Publishers.

Figs. 2-11, 2-12, 2-14, 2-15 and Table 2-1: The International Academy of Cytology.

Figs. 1-11 and 4-7: 1987 The Royal Microscopic Society.

Figs. 8-2, 8-4, 8-5 and 8-6: 1994 Japanese Society of Pathology.

Fig. 5-15: 1986 KTK Scientific Publishers.

Fig. 3-19: 1990 KTK Scientific Publishers.

Figs. 2-36, 2-37, 2-38, 2-39 and 2-40: 1968 Tohoku University Medical Press.

Figs. 3-8, 3-15, 3-16, 3-17, 3-18, 3-21, 3-23, 3-24 and 3-25: 1970 Tohoku University Medical Press.

Fig. 2-8: 1976 Tohoku University Medical Press.

Figs. 2-9 and 2-10: 1978 Tohoku University Medical Press.

Figs. 7-1, 7-2, 7-3, 7-4, 7-5 and 7-6: 1980 Tohoku University Medical Press.

Figs. 5-16 and 5-17: 1984 Tohoku University Medical Press.

Fig. 6-27: 1997 Tohoku University Medical Press.

Figs. 7-24, 7-26 and 7-27: 1998 Tohoku University Medical Press.